DUDLEY KNOX LIBRARY
NAVAL [illegible]
[illegible] [illegible]IA 93943

NPS68-84-001

NAVAL POSTGRADUATE SCHOOL
Monterey, California

THESIS

THE SPACE-TIME SCALES OF VARIABILITY
IN OCEANIC THERMAL STRUCTURE OFF
THE CENTRAL CALIFORNIA COAST

by

Laurence Coates Breaker

December 1983

Thesis Advisor: C.N.K. Mooers

Approved for public release; distribution unlimited.

Prepared for:

NPS Research Foundation and
Office of Naval Research
Environmental Sciences Directorate (Code 420)
Arlington, VA 22217

T214351

NAVAL POSTGRADUATE SCHOOL
Monterey, California

Commodore Robert H. Shumaker
Superintendent

David A. Schrady
Provost

This thesis prepared in conjunction with research supported in part by the Naval Postgraduate School Foundation Research Program which is funded by the Chief of Naval Research, and by sponsored funds from the Chief of Naval Research.

Reproduction of all or part of this report is authorized.

Released as a
Technical Report by:

REPORT DOCUMENTATION PAGE

READ INSTRUCTIONS BEFORE COMPLETING FORM

1. REPORT NUMBER: NPS68-84-001

2. GOVT ACCESSION NO.:

3. RECIPIENT'S CATALOG NUMBER:

4. TITLE (and Subtitle): The Space-Time Scales of Variability in Oceanic Thermal Structure Off the Central California Coast

5. TYPE OF REPORT & PERIOD COVERED: Ph. D. Thesis; December 1983

6. PERFORMING ORG. REPORT NUMBER:

7. AUTHOR(s): Laurence Coates Breaker

8. CONTRACT OR GRANT NUMBER(s):

9. PERFORMING ORGANIZATION NAME AND ADDRESS: Naval Postgraduate School, Monterey, California 93943

10. PROGRAM ELEMENT, PROJECT, TASK AREA & WORK UNIT NUMBERS: 61152N:RR00-01-10; N0001484WR41001

11. CONTROLLING OFFICE NAME AND ADDRESS: Naval Postgraduate School, Monterey, California 93943

12. REPORT DATE: December 1983

13. NUMBER OF PAGES: 483

14. MONITORING AGENCY NAME & ADDRESS(if different from Controlling Office): Chief of Naval Research, Arlington, VA 22217

15. SECURITY CLASS. (of this report): Unclassified

15a. DECLASSIFICATION/DOWNGRADING SCHEDULE:

16. DISTRIBUTION STATEMENT (of this Report): Approved for public release; distribution unlimited

17. DISTRIBUTION STATEMENT (of the abstract entered in Block 20, if different from Report):

18. SUPPLEMENTARY NOTES:

19. KEY WORDS (Continue on reverse side if necessary and identify by block number): Pt. Sur Upwelling Center; Coastal Upwelling Regime; Bathymetry; Infrared Satellite Imagery; Wind Stress; Empirical Orthogonal Functions; Spectral Analysis; Autocorrelation Function; Spring Transition; El Nino; Sea-Surface Temperature; Space-Time Scales

20. ABSTRACT (Continue on reverse side if necessary and identify by block number):

The space-time scales of variability in ocean thermal structure are examined off the Central California coast. In the active coastal upwelling regime off Pt. Sur, there was an equatorward surface jet 15 to 40km offshore, and a weaker poleward undercurrent near the continental slope. Based on tendency analyses of a set of quasi-synoptic hydrographic surveys, both upwelling and mixing were important in lowering sea-surface temperature (SST). The coastal bathymetry influenced the in situ property

#20 - ABSTRACT - (CONTINUED)

distributions around Pt. Sur, and the satellite-derived SST patterns. Based on the satellite data, the upwelling frontal boundary meandered with space and time scales of about 80km (alongshore) and 30 to 40 days, respectively.

Over several months, the major upwelling frontal boundary gradually moves the order of 50km offshore. This movement often commences in May, a month or so following the spring transition to coastal upwelling; it may be caused by both cumulative offshore Ekman transport and Rossby wave dispersion. Consequently, the offshore region influenced by the coastal upwelling regime exceeds the Rossby radius of deformation.

The major abrupt decreases in coastal SST (of order 3C) in certain years were attributed to the spring transition to coastal upwelling. The four El Nino episodes of the past 12 years were evident in coastal SST. El Nino events may initiate, and apparently strengthen, the spring transitions.

Based on daily surface and subsurface temperature, correlation time scales ranged from several days (subsurface) to almost ten days (surface). The vertical temperature field was statistically homogeneous with correlation scales of at least 60m. Based on empirical orthogonal function analysis of vertical temperature profiles acquired on a mesoscale grid, the limiting horizontal and vertical scales were of the order of 20km and 40m, respectively. These scale estimates provide guidance for the design of observational studies and numerical models.

Approved for public release; distribution unlimited.

THE SPACE-TIME SCALES OF VARIABILITY IN OCEANIC THERMAL STRUCTURE OFF THE CENTRAL CALIFORNIA COAST

by

Laurence Coates Breaker
B.S.M.E., Bucknell University, 1961
M.S., University of Miami, 1969

Submitted in partial fulfillment of the
requirements for the degree of

DOCTOR OF PHILOSOPHY

from the

NAVAL POSTGRADUATE SCHOOL
December 1983

DUDLEY KNOX LIBRARY
NAVAL POSTGRADUATE SCHOOL
MONTEREY, CALIFORNIA 93943

ABSTRACT

The space-time scales of variability in ocean thermal structure are examined off the Central California coast. In the active coastal upwelling regime off Pt. Sur, there was an equatorward surface jet 15 to 40km offshore, and a weaker poleward undercurrent near the continental slope. Based on tendency analyses of a set of quasi-synoptic hydrographic surveys, both upwelling and mixing were important in lowering sea-surface temperature (SST). The coastal bathymetry influenced the *in situ* property distributions around Pt. Sur, and the satellite-derived SST patterns. Based on the satellite data, the upwelling frontal boundary meandered with space and time scales of about 80km (alongshore) and 30 to 40 days, respectively.

Over several months, the major upwelling frontal boundary gradually moves the order of 50km offshore. This movement often commences in May, a month or so following the spring transition to coastal upwelling; it may be caused by both cumulative offshore Ekman transport and Rossby wave dispersion. Consequently, the offshore region influenced by the coastal upwelling regime exceeds the Rossby radius of deformation.

The major abrupt decreases in coastal SST (of order 3C) in certain years were attributed to the spring transition

to coastal upwelling. The four El Nino episodes of the past 12 years were evident in coastal SST. El Nino events may initiate, and apparently strengthen, the spring transitions.

Based on daily surface and subsurface temperature, correlation time scales ranged from several days (subsurface) to almost ten days (surface). The vertical temperature field was statistically homogeneous with correlation scales of at least 60m. Based on empirical orthogonal function analysis of vertical temperature profiles acquired on a mesoscale grid, the limiting horizontal and vertical scales were of the order of 20km and 40m, respectively. These scale estimates provide guidance for the design of observational studies and numerical models.

TABLE OF CONTENTS

I. INTRODUCTION ---------- 28

A. SCIENTIFIC OBJECTIVES---------- 28

B. BACKGROUND---------- 31

C. PLAN OF THE DISSERTATION---------- 5Ø

II. PHYSICAL CHARACTERISTICS OF THE CENTRAL CALIFORNIA COAST REGION AND THE PT. SUR UPWELLING CENTER------- 53

A. INTRODUCTION---------- 53

B. OCEANOGRAPHIC STUDIES OFF THE CENTRAL CALIFORNIA COAST---------- 55

C. THE PT. SUR UPWELLING CENTER---------- 61

1. Background---------- 61

2. Experimental Plan---------- 63

3. Observations from the Pt. Sur Upwelling Center Study---------- 66

a. Winds---------- 66

b. *In Situ* Oceanographic Measurements------ 71

c. Geostrophy---------- 94

d. Frontal Analysis---------- 1Ø3

D. SUMMARY OF RESULTS FROM THE PT. SUR UPWELLING CENTER STUDY---------- 114

III. ANALYSIS OF THE SATELLITE DATA---------- 121

A. INTRODUCTION---------- 121

B. COMPARISON OF THE SATELLITE AND *IN SITU* DATA---- 126

C. FRONTAL STATISTICS---------- 135

D. IMAGE SEQUENCES---------- 165

1. Sequence from June 6 to June 14, 1980------- 166

2. Seasonal Sequences------------------------- 177

E. OFFSHORE MOVEMENT OF THE MAJOR UPWELLING FRONTAL BOUNDARY---------- 193

1. Offshore Ekman Transport------------------- 193

2. Rossby Wave Dispersion--------------------- 200

3. Comparison Of Results---------------------- 207

F. SUMMARY OF RESULTS------------------------- 207

IV. TIME-SCALE ANALYSIS OF OCEAN TEMPERATURES OFF THE CENTRAL CALIFORNIA COAST---------- 214

A. INTRODUCTION------------------------------- 214

B. THE SOURCES OF DATA------------------------ 218

C. TRENDS IN THE DATA------------------------- 225

D. CYCLIC FIT AND DECOMPOSITION OF THE DATA-------- 227

E. GLOBAL FIT AND CYCLIC COMPONENTS---------- 232

F. EXAMINATION OF THE RANDOM COMPONENT, $\varepsilon(t)$------- 246

G. THE COMPLETED MODEL------------------------ 254

H. THE SAMPLING PROBLEM---------- 257

I. TIME SCALES---------- 264

J. OCEANOGRAPHIC ASPECTS OF THE DATA---------- 287

1. Spring Transitions---------- 287

2. The Annual and Other Cycles---------- 295

3. El Nino Events---------- 298

4. Additional Periodic and Non-Periodic Effects 302

K. SUMMARY AND DISCUSSION OF RESULTS---------- 305

V. SPATIAL ANALYSIS OF THE <u>IN SITU</u> TEMPERATURE DATA---- 314

A. INTRODUCTION---------- 314

B. SPATIAL AUTOCORRELATIONS AND PATTERN CORRELATION ANALYSIS---------- 317

C. PATTERN CORRELATIONS---------- 323

D. EOF CALCULATIONS---------- 344

1. Preliminary EOF Calculations---------- 345

2. X-Z EOF Calculations---------- 350

3. Vertical Profile EOF Analysis---------- 369

E. SUMMARY OF RESULTS---------- 392

VI. A SUMMARY, COMPARISONS, CONCLUSIONS, AND RECOMMENDATIONS---------- 400

A. INTRODUCTION---------- 400

B. SUMMARY---------- 400

1. The Physical Characteristics---------- 400

2. The Space-Time Scales: Techniques and Results---------- 407

C. COMPARISONS---------- 416

D. CONCLUSIONS AND RECOMMENDATIONS---------- 420

1. Conclusions---------- 420

2. Recommendations---------- 424

APPENDIX A: EMPIRICAL ORTHOGANAL FUNCTIONS---------- 429

APPENDIX B: CALCULATION OF THE BAROCLINIC ROSSBY RADIUS OF DEFORMATION FROM CONTINUOUS VERTICAL PROFILES OF DENSITY---------- 437

APPENDIX C: IMPLEMENTATION AND COMPARISON OF TWO METHODS OF TWO-DIMENSIONAL INTERPOLATION---------- 456

LIST OF FOOTNOTES---------- 466

LIST OF REFERENCES---------- 468

INITIAL DISTRIBUTION LIST---------- 482

LIST OF TABLES

TABLE		PAGE
1.	Frontal statistics for temperature, salinity, and density from the Pt. Sur upwelling center study----------	106
2.	Lag-correlation analysis for the Mean Frontal Boundary (MFB) and the first 4 EOFs for 1980 versus the 100, 500, and 1000m isobaths.------	164
3.	Estimated correlation coefficients for second residuals and estimated autoregressive coefficients for p = 1, 2, 3,and 4.----------	244
4.	Partitioned sample variances for Granite Canyon sea-surface temperature data.----------	244
5.	Summary of parameters associated with cyclic components----------	248
6.	Completed model including coefficients associated with linear trend, the cyclic components, and autoregression.----------	255
7.	Simulation results for sampling every observation. ----------	261
8.	Simulationresults for sampling every second and every third observation.----------	263
9.	Partitioned variances for Granite Canyon, Pacific Grove, and the Farallons.----------	267
10.	Estimated time scales for Granite Canyon, Pacific Grove, and the Farallons.----------	278
11.	Spring transitions at Granite Canyon between March 1, 1971 and March 1, 1983.----------	288
12.	Spatial correlation scales for Phase 1A temperature data at 0, 50, and 100m.----------	322
13.	Variances associated with first three eigenvalues for each phase.----------	346

14. Horizontal scales and locations of most prominent EOF structures for first 6 EOFs.---- 364

15. Vertical profile EOF parameters for detrended data.---------- 379

16. Comparison of variance distributions for detrended (X-Z), and non (X-Z) detrended data. 389

17. Overall recommended spatial and temporal sample spacings for the Central California coast and other coastal upwelling regions at similar latitudes.---------- 425

18. Calculated and estimated first mode baroclinic radii of deformation for Pt. Sur study area for depths of 1000, 1500, and 2000m.---------- 435

19. Density differences for two-layer approximation for R_{bc}.---------- 436

LIST OF FIGURES

FIGURE		PAGE
1.	Locations of the Pt. Sur upwelling center study area0, sea-surface temperature station locations, and the subsurface temperature location (i.e., moored array).	54
2.	The June 1980 synoptic study domain, which extends 90 km offshore, and 120 km alongshore from Pt. Pinos south to Pt. Piedras Blancas. Salinity-temperature-depth (STD) stations are indicated by solid circles and expendable bathythermograph (XBT) stations by solid circles and stars for each phase (1A, 1B, 3A, and 3B, respectively). Dashed lines are isobaths. ----	64
3.	Coastal winds. Panels A and B are wind stick diagrams at Pt. Sur and Pt. Piedras Blancas, respectively, for June 1980. Wind sticks show direction toward which wind is blowing, with north up. These coastal observations, taken every 3 hours, were provided by the National Weather Service. Panel C shows time histories of wind stress magnitude, Ekman transport, and upwelling index, based on computed synoptic-scale winds every 6 hours at Pt. Sur (Bakun, 1980). --------	67
4.	Mean offshore profiles of alongshore wind stress for each phase. Wind stress values from shipboard observations along each trackline were averaged in the alongshore direction. ----------	69
5.	Maps of sea-surface temperature in degrees C (upper left), surface salinity in parts per thousand (upper right), surface sigma-t (lower left), and mixed layer depth in 10m intervals (lower right), for Phase 1A. SSTs were derived from the XBT and STD data, surface salinities from the shipboard thermalsalinograph, sigma-t from XBT and STD temperatures and STD salinities, and mixed layer depth from the XBT and STD temperature profiles. ----------	72
6.	Maps of temperature for Phase 1A. Upper left panel: temperature at 10m, upper right panel: temperature at 50m, lower left panel: temperature at 100m, and lower right panel: temperature at 200m. ----------	74
7.	Maps of sea-surface temperature for each phase. ------	76

8. Vertical property sections for temperature, salinity, and sigma-t, for Phase 1A, Leg B. Each tick mark along the horizontal axis represents 5km, and along the vertical axis, 33m. ---------- 77

9. Mean vertical section for temperature averaged over all four phases. Data were initially averaged alongshore for each phase in corridors 15km wide (vertical dashed lines) before the four-phase mean was calculated. The total number of temperature profiles averaged along each corridor are enclosed by boxes at the top of the figure. ---------- 79

10. Mean temperature-salinity profiles averaged along corridors approximately parallel to the coast and 15km wide, for Phase 1B. ---------- 81

11. A water mass mixing diagram showing percentages of Subarctic and Equatorial waters. Two temperature-salinity profiles from Phase 3A, Leg C, are superimposed. The solid curve represents a station approximately 90km offshore and the dashed curve, a station approximately 10km offshore. ---------- 83

12. Map of sea-surface temperature tendency between Phases 1A and 3A. Random stippling indicates areas of increased SST; horizontal stippling indicates areas of decreased SST. The contour interval is 0.5C. -------- 85

13. Maps of temperature tendency between Phases 1A and 3A at four depths. Upper left panel: 10m upper right panel: 50m, lower left panel: 100m, and lower right panel: 200m. ---------- 87

14. Map of mixed layer depth tendency between Phases 1A and 3A. Contours are in meters and cross-hatching represents shoaling areas. ---------- 88

15. Tendency for mean vertical sections of temperature for Phases 1A and 3A. Cross-hatching represents areas of significant temperature change. Positive values indicate warming. ---------- 90

16. Map of mean thermocline depth (MTD) tendency between Phases 1A and 3A. Random stippling indicates areas of increased MTD; horizontal stippling indicates areas of decreased MTD. The contour interval is 10m. --------- 92

17. Maps of thermocline thickness (defined as the difference in depth between the 9 and 11C surfaces) for each phase. The contour interval is 10m. -------- 95

18. Map of thermocline thickness tendency between Phases 1A and 3A. Random stippling indicates areas of increased thickness; vertical stippling indicates areas of decreased thickness. The contour interval is 10m. 96

19. Maps of dynamic height in dynamic cm. for each phase. The different reference levels used in eah case are indicated. ---------- 98

20. Mean offshore geostrophic velocity profiles in cm/sec for each phase for the surface relative to 300m. Individual profiles along each leg were averaged alongshore to obtain the mean profiles shown. Negative values indicate southward flow (assuming a negligible barotropic component). Horizontal bars indicate +1 standard deviation about the mean. ------- 100

21. Vertical sections of geostrophic velocity (cm/sec) for Leg C of each phase. The vertical resolution is 25m, and areas of cross-hatching imply poleward geostrophic flow. ---------- 102

22. Location of the mean upwelling frontal boundary fom IR satellite imagery and from the in situ temperature data, for Phases 1A and 1B. Symbols associated with the satellite data represent the position of the frontal boundary taken from individual images. The solid line corresponds to the mean boundary position from the in situ data for both phases. The dotted region corresponds to the estimated region where the pycnocline broke the surface along each track leg. --- 127

23. A comparison of frontal boundary locations obtained from an AVHRR IR satellite image acquired on June 6, 1980 and temperature/salinity frontal crossings obtained from the thermalsalinograph (T/S) data acquired during Phase 1B. Frontal crossings from the T/S data are labeled with the observed temperatures and salinities at the beginning and end of each encounter, along with the distance over which the front persisted. ---------- 129

24. A comparison of frontal boundary locations obtained from an AVHRR IR satellite image acquired on June 14, 1980, and T/S frontal crossings obtained during Phase 3A. ---------- 130

25. Temperature frontal crossing transects from the thermalsalinograph data for Phase 1B superimposed on the June 6, 1980 AVHRR IR satellite image. Transect

distances are only approximate (1 inch 30km), and lighter gray shades correspond to cooler temperatures. 131

26. Superposition of the surface relative to 200m dynamic height field from Phase 1B, on the June 6, 1980 AVHRR IR satellite image. Dynamic height contours are in dynamic cm., with a contour interval of 2 dynamic cm. 134

27. Mean position of the major upwelling frontal boundary obtained from a sequence of 31 AVHRR IR satellite images starting on May 2, 1980 and ending on June 13, 1980. Individual images were digitized at a grid spacing of 2km. Two boundaries representing the mean and standard deviations were required because of ambiguities that arose occasionally from double valued boundary locations. ---------- 138

28. Normalized number density contour analysis. Images from the May 2, 1980, to June 13, 1980 sequence were composited to obtain probabilities of encountering water within the major upwelling frontal boundary. --- 140

29. Distribution of eigenvalues for the EOFs calculated from the digitized frontal locations taken from the sequence of AVHRR IR satellite images starting on May 2, 1980 and ending on June 13, 1980. Upper panel is a linear plot of the variance associated with the first 14 eigenvalues versus eigenvalue index, and the lower panel is the corresponding plot with a natural log ordinate (over 23 eigenvalues). In the lower panel, the eigenvalue index corresponding to the intersection of eigenvalue slopes represents the approximate number of signal-like EOFs (Craddock, 1972). ---------- 143

30. Same as preceeding figure except that these eigenvalues correspond to the 1981 image sequence from April 4, 1981 to July 14, 1981. ---------- 144

31. Upper panel represents the satellite - derived mean frontal boundary (MFB) and the first EOF, with respect to the 100, 500, and 1000m isobaths, and the coastline. MFB and first EOF have been rescaled by multiplying by standard deviation. First EOF has also been multiplied by . Value in percent indicates percent variance accounted for by the first EOF. Lower panel represents the distribution of principal components versus time (in days) associated with the first EOF. ---------- 147

32. Same as Figure 31, except for second EOF. ---------- 148

33. Same as Figure 31, except for third EOF. ---------- 149

34. Same as Figure 31, except for fourth EOF. ---------- 150

35. Same as Figure 31, except for fifth EOF. ---------- 151

36. Same as Figure 31, except for sixth EOF. ---------- 152

37. Same as Figure 31, except for 1981 data. ---------- 154

38. Same as Figure 37, except for second EOF. ---------- 155

39. Same as Figure 37, except for third EOF. ---------- 156

40. Same as Figure 37, except for fourth EOF. ---------- 157

41. Same as Figure 37, except for fifth EOF. ---------- 158

42. Same as Figure 37, except for sixth EOF. ---------- 159

43. Advanced Very High Resolution Radiometer (AVHRR) infrared (IR) satellite image acquired on June 6, 1980 at 1517 Pacific Standard Time (PST). ---------- 167

44. AVHRR IR satellite image acquired on June 7, 1980 at 1505 PST. ---------- 168

45. AVHRR IR satellite image acquired on June 7, 1980 at 1937 PST. ---------- 169

46. AVHRR IR satellite image acquired on June 9, 1980 at 1443 PST. ---------- 170

47. AVHRR IR satellite image acquired on June 9, 1980 at 1853 PST. ---------- 171

48. AVHRR IR satellite image acquired on June 12, 1980 at 1949 PST. ---------- 172

49. AVHRR IR satellite image acquired on June 12, 1980 at 1550 PST. ---------- 173

50. AVHRR IR satellite image acquired on June 12, 1980 at 1927 PST. ---------- 174

51. AVHRR IR satellite image acquired on June 14, 1980 at 1843 PST. ---------- 175

52. AVHRR IR satellite image acquired on May 2, 1980 at 0344 PST. ---------- 178

53. AVHRR IR satellite image acquired on May 29, 1980 at 1507 PST. ---------- 179

54. AVHRR IR satellite image acquired on June 5, 1980 at 1528 PST. ---------- 180

55. AVHRR IR satellite image acquired on June 13, 1980 at 0414 PST. ---------- 181

56. AVHRR IR satellite image acquired on June 25, 1980 at 1503 PST. ---------- 182

57. AVHRR IR satellite image acquired on July 10, 1980 at 1535 PST. ---------- 183

58. AVHRR IR satellite image acquired on August 1, 1980 at 1926 PST. ---------- 184

59. AVHRR IR satellite image acquired on September 20, 1980 at 1509 PST. ---------- 185

60. AVHRR IR satellite image acquired on April 4, 1981 at 0834 PST. ---------- 186

61. AVHRR IR satellite image acquired on June 10, 1981 at 0817 PST. ---------- 187

62. AVHRR IR satellite image acquired on June 21, 1981 at 1908 PST. ---------- 188

63. AVHRR IR satellite image acquired on July 7, 1981 at 1922 PST. ---------- 189

64. AVHRR IR satellite image acquired on September 19, 1981 at 1431 PST. ---------- 190

65. A comparison of coastal and geostrophic winds and surface upwelling areas obtained from IR Satellite Data for Pt. Sur. 65A: Integrated wind stress (i.e., the corresponding upwelling indices) versus time starting on 1 May 1980. The upper curve, b, corresponds to the time integral of the geostrophic wind stress and the middle curve, a, corresponds to the time integral of the coastal winds averaged between Pt. Sur and Pt. Piedras Blancas. t for each series is 6 hours. The line of constant slope labeled c, represents the time integral of u H. 65B: Linear regression between upwelling surface area obtained from the satellite data, and time starting 1 May 1980. This area is defined as the area separating the mean frontal boundary (MFB) offshore and the coast

and bounded to the north and south by the approximate latitudes of Cypress Point and Pt. Piedras Blancas, respectively. 65C: Linear regression of Area vs Integrated Wind Stress (IWS) from the averaged coastal winds, a, and the geostrophic winds, b. ---------- 196

66. Distribution of mean low cloudiness along coast of California. Upper panel shows the location of the boundary that separates stratus and strato-cumulus cloud types. Lower panel shows percentile distributions of mean low cloudiness obtained from satellite imagery for July 1975 (Simon, 1976). ------- 205

67. Sea-surface temperatures at Granite Canyon, Pacific Grove, and the Farallons. Observations acquired with immersion thermometers (+0.2C) daily at approximately 0800 local time. These 12-year records start on March 1, 1971 and end on February 28, 1983. ---------- 219

68. Sea-surface temperatures at Diablo Canyon (dashed) and Granite Canyon (solid) for the year 1980. ---------- 220

69. Sea-surface temperatures at Pacific Grove (dashed) and Granite Canyon (solid) for 1980. ---------- 222

70. Sea-surface temperatures at the Farallons (dashed) and Granite Canyon (solid) for 1980. ---------- 223

71. Sea-surface temperature at Granite Canyon, and subsurface temperatures approximately 8km off Cape San Martin (see Fig. 1). Subsurface temperatures acquired at 113, 186, 311, and 510m. Sample period extends from March 5, 1980 to April 7, 1980. ---------- 224

72. Scatter plot of sea-surface temperature versus day number at Granite Canyon. A least squares linear trend is superimposed. ---------- 226

73. Upper panel shows a 13-term cyclic fit to the linearly detrended data at Granite Canyon. Lower panel shows the second residuals created by subtracting the detrended data with cyclic fit, from the original data. ---------- 233

74. Autocorrelogram of linearly detrended data (first residuals). ---------- 234

75. Upper panel shows a Log_e periodogram of the first residuals out to 325 cycles per 4380 days. Maximum (0.99) and individual (0.025, 0.975) confidence limits have been included. Lower panel shows the entire periodogram out to 2190 cycles per 4380 days. -------- 237

76. Smoothed periodograms of first residuals at Granite Canyon. Middle and lower panels show smoothed versions of the raw periodogram (upper panel). Middle panel shows periodogram smoothed by non-overlapping groups of five (10 DOFs) and lower panel shows smoothing by groups of 15 (30 DOFs). 95% confidence limits have been included in each case. ---------- 239

77. Upper panel shows an expanded periodgram (325 cycles) for second residuals with a theoretical spectrum for an AR(2) process superimposed. The lower panel shows the corresponding full spectrum out to 2190 cycles. -- 241

78. Estimated and theoretical autocorrelations for second residuals out to 50 lags. The theoretical autocorrelations were calculated using the Yule-Walker equations (Chatfield, 1980). ---------- 242

79. Upper panel shows third residuals (first residuals less an AR (2) process). Lower panel shows the autocorrelogram of third residuals with 95% confidence limits superimposed. ---------- 245

80. Periodogram of third residuals. Upper panel shows an expanded version with maximum and individual confidence limits superimposed. Lower panel shows full periodogram. ---------- 247

81. Fourth residuals (upper panel) and autocorrelogram of fourth residuals (lower panel). Autocorrelogram of fourth residuals has 95% confidence limits included. - 250

82. Periodograms of fourth residuals. Upper panel shows full periodogram of fourth residuals and lower panel shows a cumulative periodogram of fourth residuals with confidence limits included. Cumulative periodogram lying completely within confidence bands indicates that fourth residuals possess a white (noise-like) spectrum. ---------- 252

83. Distribution of fourth residuals. Upper panel shows a histogram of fourth residuals with slight skewness and significant kurtosis. Lower panel shows a cumulative probability plot of the fourth residuals with the ordinate scaled such that normally-distributed data produce a straight line. ---------- 253

84. One year extrapolation of SST at Granite Canyon from model simulation. Upper panel shows original 12-year series, and the lower panel shows the 13-year simulation (original 12 years plus one additional year). ---------- 258

85. One year simulated projection at Granite Canyon (expanded from previous figure). ---------- 259

86. Standard deviations of selected harmonic amplitudes from simulated series versus sample interval in days for Granite Canyon. The one year fundamental (A_{12}), and the 6 month (A_{24}) and 46 day (A_{94}) harmonics are included. ---------- 265

87. Time scale analysis of autocorrelograms for second residuals for Granite Canyon. Upper panel shows autocorrelogram out to 100 lags with e-folding, first zero-crossing, and integral scales included. Lower panel shows autocorrelogram out to 500 lags with corresponding integral scale included. ---------- 270

88. Cumulative periodogram of second residuals for Granite Canyon. Samples taken every 6.5 and 4.5 days capture 90 and 95% of the cumulative variance, respectively. 273

89. Time scale analysis of autocorrelograms for second residuals for Pacific Grove. Upper panel shows autocorrelogram out to 50 lags with e-folding and integral scales included. Lower panel shows autocorrelogram out to 500 lags with corresponding integral scale included. ---------- 274

90. Time scale analysis of autocorrelograms for second residuals for the Farallons. Upper panel shows autocorrelogram out to 100 lags with e-folding scale included. Lower panel shows autocorrelogram out to 500 lags. ---------- 275

91. Cumulative periodogram of second residuals for Pacific Grove. Samples taken every 4.5 and 3.2 days capture 90 and 95% of the cumulative variance, respectively. - 276

92. Cumulative periodogram of second residuals for the Farallons. Samples taken every 4.8 and 3.0 days capture 90 and 95% of the cumulative variance, respectively. ---------- 277

93. Autocorrelograms for second residuals at Granite Canyon. Upper panel shows autocorrelogram for first six years of the 12-year record and lower panel shows autocorrelogram for second six-year period. E-folding time scales are almost identical even though autocorrelograms differ markedly beyond lags of about 10 days. ---------- 280

94. Sea-surface temperature (SST) at Granite Canyon and temperature at 175m off Cape San Martin. Observation period starts on November 25, 1978 and ends on January 15, 1979. Subsurface temperatures were acquired once per hour. ---------- 282

95. Third-order polynomial least squares fits to the Granite Canyon SST data (upper panel), and to the 175m temperature data (lower panel). ---------- 284

96. Autocorrelogram for the second residuals at Granite Canyon for the period between November 25, 1978 and January 15, 1979. E-folding time scale is about 30 hours. ---------- 285

97. Autocorrelograms for second residuals for 175m temperature data. Upper panel shows autocorrelogram out to a maximum lag of 100 hours. Lower panel shows an expanded version out to 20 lags. E-folding time scale from the autocorrelogram in the lower panel is about 2 hours. ---------- 286

98. One-year time series at Granite Canyon from January 1, 1980 to January 1, 1981. Major decrease in SST around day number 70 corresponds to the spring transition to coastal upwelling. ---------- 289

99. Upwelling index time-series for 1980 at 27, 30, 33, and 36N. Index values are directly proportional to alongshore wind stress, and are obtained from 6-hourly synoptic-scale winds calculated from sea level pressure (Bakun, 1980). March 11, 1980 corresponds to the date when the 1980 spring transition was first detected at Pt. Sur. ---------- 291

100. AVHRR IR satellite images showing coastal region off Pt. Sur just before, and during, the 1980 spring transition. Upper left panel shows an image from March 3, 1980. Upper right panel shows an image from March 8, 1980. Lower left panel shows an image from March 12, 1980, and lower right hand panel shows an image from March 16, 1980. ---------- 293

101. Sea surface temperature arrival time differences with respect to Granite Canyon at eight locations along the California coast between 35 and 42N. Along the abscissa, to the left is southward, and to the right, northward. A linear least squares fit to the data yields a poleward speed of 64.1km/day. ---------- 294

102. Mean annual temperature cycles at Granite Canyon and at an open ocean location (36N, 140W). The 12-year record at Granite Canyon was averaged to obtain the mean (dotted) annual cycle. The smoothed version was obtained by using a low-pass filter with a cosine taper and 49 weights. The open ocean data were obtained from Robinson, 1977. ---------- 296

103. Comparison of spectra for upwelling and non-upwelling portions of the year at Granite Canyon. Upwelling period is defined from 15 March to 30 June, and non-upwelling period from 1 September to 16 December. Individual spectra for each period were averaged over the entire 12 years to obtain the plots shown. ------- 299

104. Comparison of sea-surface temperatures at Granite Canyon for period of March 1, 1982 to March 1, 1983 with a smoothed 12-year mean (the dashed curve represents the actual observations). ---------- 301

105. Partial spectrum of second residuals for temperature at Granite Canyon. Periodogram from 100 to 2000 cycles has been smoothed to show the constant slope that occurs over this range of frequencies. An estimated slope of -1.8 was obtained, and is similar to the -5/3 slope predicted by classical homogeneous turbulence theory. ---------- 304

106. Autocorrelogram of second residuals for SST at Granite Canyon out to 1000 lags is shown in the upper panel. Lower panel shows the sum of autocorrelation coefficients versus selected lag numbers out to 1000 lags. The sum of the autocorrelation coefficients tends to converge to a value of about 5.0. This value agrees favorably with the previous time-scale estimate of 6.0 days obtained by using the e-folding criterion. 310

107. Spatial autocorrelation contours at the surface for Phase 1A. Values have been plotted at the mid-points of corresponding x/ y range increments. ---------- 319

108. Spatial autocorrelations for Phase 1A at 50 meters. -- 320

109. Spatial autocorrelations for Phase 1A at 100 meters. - 321

110. Spatial grid used to interpolate temperature data for each phase. Grid spacing is 5km (alongshore) x 5km (offshore). ---------- 324

111. Comparison of contour maps for sea-surface temperature for Phase 1B. Lower panel shows machine-produced map using the MQS algorithm; upper panel shows hand-drawn version. ---------- 326

112. Temperature contour maps for Phase 3A at the surface, produced using the MQS algorithm for two-dimensional interpolation. Panel on R.H.S. shows original temperature field. Upper left panel shows the bilinear trend surface used to detrend original data. Lower left panel shows temperature residuals created by removing bilinear trend surface from original data. 329

113. Same as Figure 112 except for a depth of 25m. --------- 330

114. Same as Figure 112 except for a depth of 50m. -------- 331

115. Same as Figure 112 except for a depth of 75m. -------- 332

116. Same as Figure 112 except for a depth of 100m. ------- 333

117. Same as Figure 112 except for a depth of 150m. ------- 334

118. Same as Figure 112 except for a depth of 200m. -------- 335

119. Comparisons of temperature and density maps for Phase 1B, at the surface and at 50m. Maps were produced using the TPS algorithm for two-dimensional interpolation (see Appendix C). ---------- 336

120. Upper panel shows percent variance in the temperature field accounted for by a bilinear trend versus depth for Phases 1A and 3A. Lower panel shows corresponding alongshore and offshore linear regression coefficients or slopes as a function of depth. ---------- 337

121. Pattern correlation profiles (PCPs) for Phase 1A. PCPs for reference levels of 0, 25, 50, 75, and 100 meters are shown for detrended surfaces, and for one non-detrended profile (0 meter reference). A 95% confidence limit is included. ---------- 339

122. Same as Figure 121 except for Phase 3A. ---------- 340

123. Mean pattern correlation profiles for Phases 1A and 3A. The previous PCPs have been adjusted to a common reference level (0m) and then ensemble-averaged for each phase. E-folding scales are estimated assuming that the previous confidence limits have been sufficiently reduced, through averaging, to allow significant scale estimates to be obtained. ---------- 343

124. First three EOFs for 53 deep temperature profiles from Phase 3A. An overall mean X-Z transect was first removed from the data. ---------- 348

125. Principal component maps for first EOF for each phase. Principal components are plotted at the respective station locations. ---------- 349

126. Distribution of variance versus eigenvalue index for X-Z EOFs. Upper panel is a linear plot of variance (i.e., eigenvalues) and the lower panel is the same except with a natural log ordinate. Signal-like EOFs extend over approximately the first 6 EOFs, from the locus of slope intersections. ---------- 353

127. Mean temperature field in X-Z plane from all phases. This field is used to detrend the temperature profiles before calculating the X-Z EOFs. ---------- 354

128. First X-Z EOF (upper panel) and principal components (lower panel). Principal components are both a function of alongshore location, and time. ---------- 355

129. Same as Figure 128 except for second EOF. ---------- 356

130. Same as Figure 128 except for third EOF. ---------- 357

131. Same as Figure 128 except for fourth EOF. ---------- 358

132. Same as Figure 128 except for fifth EOF. ---------- 359

133. Same as Figure 128 except for sixth EOF. ---------- 360

134. Run tests applied to X-Z principal components to test for statistical independence. Based on run tests for each mode, the principal components for modes 2 and 4 are not statistically independent, at the Ø.Ø5 level of significance. ---------- 368

135. Distribution of variance versus eigenvalue index for the vertical EOFs, with X-Z detrending. Lower panel shows that about the first six EOFs are signal-like. 371

136. First vertical EOF (upper panel) and principal components (lower panel) with X-Z detrending. Principal components in this case are a function of alongshore and offshore location and time. ---------- 372

137. Same as Figure 136 except for second EOF. ---------- 373

138. Same as Figure 136 except for third EOF. ---------- 374

139. Same as Figure 136 except for fourth EOF. ---------- 375

140. Same as Figure 136 except for fifth EOF. ---------- 376

141. Same as Figure 136 except for sixth EOF. ---------- 377

142. Periodograms for first six vertical EOFs with X-Z detrending. Ordinate is the frequency component times the appropriate eigenvalue. Abscissa is the wavenumber in cycles per 3ØØ meters. ---------- 381

143. Individually-scaled periodograms for first six vertical EOFs with X-Z detrending. ---------- 382

144. Principal component variance associated with the vertical, X-Z detrended EOFs as a function of offshore distance. ---------- 385

145. Principal component maps for first vertical EOF for each phase. Principal components are plotted at the appropriate grid point locations. ---------- 386

146. Same as Figure 135 except without X-Z detrending. --- 388

147. First six eigenvectors without X-Z detrending plotted with respect to global mean profile. ---------- 391

148. Same as Figure 144 except without X-Z detrending. --- 393

149. Individual Brunt-Vaisala frequency squared profiles for each phase for a location approximately 40km off Lopez Point. Profiles have been extended to the bottom by catenating an exponential "tail" in each case. ---------- 432

150. Four-phase mean Brunt-Vaisala frequency squared profile. Same exponential tail has been catenated in this case as in Fig. 149. ---------- 433

151. Mean temperature profiles for Phases 1A and 1B. Only deep (300m) profiles from each phase are included. --- 439

152. Offshore correlation transect of temperature profile residuals for Phase 1A along Leg C. Numbers in parentheses indicate the vertical depth lag at which the maximum correlation occurred. ---------- 441

153. Offshore correlation transect of temperature profile residuals for all Legs (A through E) of Phase 3A. Correlation coefficients in this case correspond to zero depth lag. ---------- 443

154. Temperature profile residual correlation times for stations re-occuppied (to within 1km) between Phases 1A and 1B, and 3A and 3B. Maximum correlations and correlations at zero depth lag are included. --------- 445

155. Interprofile correlation map of temperature profile residuals for Phase 3A. These correlation coefficients were obtained by cross-correlating adjacent profiles along each leg and plotting the result at the station mid-points. Values shown are for zero vertical depth lag. ---------- 447

156. Contoured space-time correlation map of temperature profile residuals. Values have been averaged in 5km x 5hour blocks before being contoured. ---------- 450

157. Contoured space-time correlation map of temperature profiles residuals. Means in this case have been calculated using a non-linear weighted average favoring higher correlations. Also the block size in this case is 4km x 4 hours. ---------- 451

158. Space-time temperature profile residual correlations averaged over time to isolate range dependence. ------ 453

159. Space-time temperature profile residual correlations averaged over space to isolate time dependence. ------ 454

160. Two-dimensional interpolation of surface temperature data from Phase 1A using the Modified Quadratic Shepard (MQS) algorithm. Data are scaled equally in the X and Y directions, yielding poor results because data were not acquired with equal spacing in both directions. ---------- 460

161. Same as Figure 161 except that the input data have been expanded by a factor of 3 in the offshore direction to more closely approximate the actual data acquisition alongshore/offshore aspect ratio. -------- 462

162. Two-dimensional interpolation of surface temperature data from Phase 1A using the Thin Plate Spline (TPS) algorithm. This map is satisfactory. ---------- 463

ACKNOWLEDGEMENTS

Many individuals assisted the author in various ways during the course of this study. It is impossible to acknowledge all of them here. However, the author wishes to thank the members of his Dissertation Committee and his Dissertation Supervisor, Professor C.N.K. Mooers, for their continued guidance and their patience throughout the study. Also the author wishes to acknowledge Professor P.A.W. Lewis and the IBM Watson Research Center for making available an experimental APL software package called GRAFST3, which was used extensively in producing many of the figures. Funding for the initial phases of this study was provided by the Naval Postgraduate School (NPS) Research Foundation and by the Office of Naval Research. The efforts of Captain Woodrow Reynolds and the crew of the R/V ACANIA in making it possible to acquire much of the data used in this study are greatly appreciated. The subsurface temperature data were provided by Mr. J.B. Wickham and Dr. S.P. Tucker of the Oceanography Department at the NPS. The sea-surface temperature data from Granite Canyon were kindly provided by Mr. Earl Ebert and his staff at the Granite Canyon Marine Culture Laboratory. Satellite imagery was provided by the NOAA/NESDIS Satellite Field Services Station in Redwood City, CA.

Finally, the author would like to acknowledge the untiring efforts of Mrs. Magge Lazanoff for her typing and re-typing this document many times over.

I. INTRODUCTION

A. SCIENTIFIC OBJECTIVES

The first objective of this study is to establish a regional oceanographic framework within which to evaluate and interpret the space-time scales of variability investigated. This framework will be established by combining the results of previous oceanographic studies in the region with the results of a recent oceanographic study of the physical characteristics of the Pt. Sur upwelling center based on shipboard measurements of temperature, salinity, surface winds, and frontal data acquired from a continuously recording thermalsalinograph. These data were acquired over an area extending from Carmel Bay to Pt. Piedras Blancas on four occasions. These results, plus sea-surface temperatures (SSTs) acquired at three locations along the Central California coast and subsurface temperature acquired at a moored array south of Pt. Sur, are used to establish an oceanographic setting for the area. Infrared (IR) satellite data also help to establish this setting. Processes and features are identified which may contribute to the observed variability.

The second objective of this study is to estimate the space-time scales of variability in ocean thermal structure off the Central California coast. The space-time variability of SST will be examined in part using IR satellite data. Initially, the validity of IR satellite data is established for use in estimating space-time variability by comparison with the *in situ* data. In particular, the space-time variability of the upwelling frontal boundary is examined. Space-time variations of the upwelling center *per se* are also examined through several image sequences. Dynamical scales for the offshore width of the coastal upwelling zone are evaluated. The influence of local bathymetry on the surface temperature field is also examined.

Time scales of variability for coastal observations along the Central California coast are estimated statistically from 12-year time-series of SST at Granite Canyon (13 km north of Pt. Sur), Pacific Grove, and the Farallon Islands. Subsurface temperatures from a moored array off Cape San Martin are also used to estimate time scales in the thermocline for comparison with the time scales estimated for the coastal SST's. Because the techniques of space-time scale analysis are not fully established, this objective includes an evaluation of the existing techniques for estimating these scales. The problem of specifying adequate sampling rates is also

considered using simulation techniques. The data are interpreted physically to provide additional oceanographic background for the study. Particular attention is given to the recently identified spring transition phenomenon along the Central California coast and the present El Nino warming.

The spatial scales of variability are estimated from the *in situ* data acquired during the Pt. Sur upwelling center study in June 1980. Particular objectives include (1) isolating the effects of space and time on the correlation properties of the internal temperature field, (2) estimating the offshore and alongshore scales (3) estimating the vertical coherence of the horizontal temperature field, (4) estimating the vertical scales *per se*, (5) examining the effects of different methods of detrending the data prior to scale estimation, and (6) examining the results for the possible influence of coastally-trapped waves.

Another objective is to compare the space-time scales of variability obtained here, (1) with similar results from other coastal regions, and (2) with similar results from the deep ocean.

The final objective is to provide a sampling plan for acquiring future observations along the Central California coast, and in other coastal upwelling regimes around the

world, based on the space-time scale analyses conducted herein. This sampling plan is also expected to provide strong guidance for numerical circulation models for such a regime.

B. BACKGROUND

Prior to the 1950's, oceanographic surveys usually covered relatively large ocean areas with measurements taken at standard depths and uniform spatial separations over time spans of several months. It was not until the mid-1950's that the oceanographic community became generally aware of the highly energetic mesoscale ocean circulation processes (e.g., Swallow, 1957). As awareness of the importance of mesoscale ocean processes increased, the focus of ocean surveys changed from being mainly geographical in scope to being more process-oriented (Baker, 1981). It became clear, because of higher frequency processes in the ocean, that it would be difficult to improve the statistical significance of the data being acquired. This was mainly due to the limitations of the approach to sampling in use at that time (Stommel, 1963). Stommel further asserted that measurement programs must be designed on the basis of what is known about the dynamics and the space-time spectral distributions of the processes involved. Within the past 15 years, important changes have taken place with regard to the

methodology used in designing and conducting at-sea measurement programs.

Because the acquisition of oceanographic data is usually time-consuming and expensive, it is important that the techniques employed in designing at-sea experiments provide an efficient methodology. On the one hand, oversampling provides redundant information, while on the other, undersampling provides either incomplete or contaminated information.

Modern techniques of experimental design have come in part from the theory of optimal estimation, which derives from Wiener's theory of optimal filtering (Liebelt, 1967). An important part of modern experimental design involves the calculation of the temporal and spatial covariance structures for sets of simultaneous observations (Davis, 1975). These techniques were first used in meteorology by Gandin (1963), and their use in estimating the space-time scales of variability has continually increased. These scales are estimated from the correlation properties of the data taken in space or time. With most geophysical data which are ordered with respect to space or time, correlation (or coherence) between observations decreases as separation increases, unless there are predominant periodic processes. Correlation analysis provides a quantitative method by which this temporal or spatial coherence can be estimated. Although many other

statistical measures of association exist, because of their Fourier transform relation to energy spectra, the use of correlation functions has become accepted as a basis for estimating space-time scales of variability in meteorology, oceanography, and other fields. Also, this approach is intimately related to the technique of optimum interpolation, which requires for its application the estimation of these same correlation functions.

The statistical tools described here are also used in the study of geophysical turbulence (Hinze, 1959; Panchev, 1970; Lumley, 1970). According to Hinze, higher order correlation functions can also be calculated from higher-order moments of the statistical process involved. These correlation functions are formed by triple and higher-order products and lead to very lengthy calculations and often difficult interpretations. Consequently higher-order correlations, although a natural extension of second-order correlations, are rarely calculated for observed meteorological and oceanographic observations.[1]

The treatment of space-time scales in the oceanographic literature has been extended since the pioneering work of Stommel (1963), cited above. Garrett and Munk (1972), for example, in developing an empirical model for the distribution of internal wave energy, use space-time scales to define the distribution and limits (in wavenumber-

frequency space) of internal waves in the ocean. Woods (1974), in describing the space-time characteristics of turbulence in the seasonal thermocline, applied the concept of scales to a dimensional analysis of the various forces which affect the spectral distribution of turbulence. Woods (1973), in studying the transfer of energy between the atmosphere and ocean and within the ocean itself, characterized scales of variability in both the space-time and wavenumber-frequency domains.

The following definition is proposed for the purposes of the present study. The space/time scale for a given realization corresponds to the total number of observations times the sample interval divided by the number of statistically independent observations in that realization. Obviously the quantity of interest is the number of statistically independent observations available in a given record. Correlation analysis provides a means for estimating this quantity. For a truly random process, the associated correlation scale approaches zero. Most geophysical data, however, are characterized by various degrees of persistence in space or time due to the space-time structure of the prevailing processes, and, as a result, they possess finite scales of variability.

In practice, several problems arise in estimating these scales. First, no single measure exists to establish the limiting separation over which adjacent values are taken to

be correlated at a specified level of confidence. Secondly, the interpretation of space-time scales estimated statistically is not necessarily straightforward.

These scales are not absolute since they usually depend on the particular sampling interval over which the data were acquired. Scales calculated for data acquired once an hour will not reveal the structure of fluctuations which occur over time periods shorter than an hour. (This problem is equivalent to the problem of aliasing in the frequency domain.) Fortunately with most geophysical data the fluctuation amplitudes decrease for shorter sampling intervals (this is equivalent to the "red" cascade in the frequency domain).

The removal of all major deterministic components from the data prior to calculating the actual correlation functions is also extremely important in estimating these scales for the random component. Scale estimates obtained from data which have not been adequately detrended will usually be excessive. It is emphasized once more that these techniques are used to characterize the random structure in the data and not the cyclic components. Finally several definitions exist for the correlation functions used to estimate these scales and a choice must be made as to which definition is to be used (Chapter IV).

Correlation techniques in experimental design were used by the Russians in the late 1960's in analyzing temperature data acquired from underway vessels equipped with thermistor chains (Navrotskiy, Kazachkina, and Navrotskaya, 1968; Navrotskiy, 1969; Navrotskiy, 1971). Navrotskiy et al. (1968), for example, found a spatial correlation distance of roughly 4km in the western equatorial Pacific at a depth of approximately 50 meters. They also found the temperature field to be non-isotropic due to the directionality of the significant internal wave activity in that region. In 1970, the Russians conducted a large-scale multi-buoy experiment in the tropical Atlantic (16.5N, 33.5W) called the "Polygon" experiment (Brekhovskikh et al., 1971). Although the techniques used in designing the Polygon Experiment were not explained in detail, Brekhovskikh et al. did indicate that experimental design was a point most seriously debated during the preparatory phases of the program. The final pattern of buoys was chosen to allow the use of advanced techniques in spectral analysis of the spatial data.

By the mid-1970's, two major ocean experiments had taken place in the western North Atlantic, both of which were designed using statistical methods: MODE 1 (1973) and POLYMODE (1974-1976). Spatial scales generally decreased with depth from the thermocline to deeper levels, ranging from 140 km at 500m to 55 km at 4000m (Richman et

al., 1977). Correlation time scales for temperature were 23 days at deeper levels but considerably longer in the thermocline. Much of the statistical analysis was devoted to using optimum interpolation techniques to construct synoptic maps of the velocity field over the study domain. These techniques were discussed at length by Bretherton, Davis, and Fandry (1976) with application to experimental design and the analysis of data from the MODE experiment. Two very important related aspects of experimental design considered during the planning of MODE-1 were selection of (1) a specific time period (i.e., season) including the overall duration of the experiment, (2) a specific domain, and (3) an optimal scale or size for the array.

Correlation techniques have been used to resolve the important space-time scales of variability in the North Pacific Ocean (Namias, 1972; White and Bernstein, 1979; Barnett, Knox, and Weller, 1977). In these studies the large-scale variability has been emphasized. Generally, coherence scales in the zonal direction are at least 50% greater than in the meridional direction. Also, spatial correlation scales are typically smaller in areas where eddies are influential (Bernstein and White, 1981). Noise-like variability in temperature near the bottom of the mixed layer in the Central Pacific, which had a spatial scale of 50 km, was considered important to the design of

an optimum sampling program for this region (Barnett et al., 1977).

Space-time scales of variability in SST were estimated using an Airborne Radiation Thermometer (ART) for the Ionian Sea (Saunders, 1972). Spatial analysis of SST from scales of 3 to 100km indicated greater variability at low wavenumbers, but the distribution of temperature variance observed did not fit any particular model of geophysical turbulence. The coherence of SST fluctuations over time was found to increase with increasing spatial scale. Coherence times of 8 to 16 days were associated with a spatial scale of $\sim$100 km, for example. Saunders associated the decorrelation of SST with advection, and not with local temporal changes.

Estimating adequate sampling rates is far more difficult in coastal areas than in the deep ocean. This difficulty is due in part to the variety, complexity, and interaction of physical processes that typically exist in coastal regions (Mooers, 1976). For example, in coastal areas the ocean may be more sensitive to local winds, tides, and boundary effects. Turbulence and internal waves undoubtedly contribute strongly to the field of variability in coastal areas.

In coastal upwelling regions, it is expected that turbulence may contribute significantly to the observed variability because the vertical density gradients are

generally reduced. According to Rooth (1973), "upwelling zones are likely candidates to carry the burden of cross isopycnal mixing maintenance far above oceanic averages." In particular, the decrease in stability due to a shoaling density field should lead to a continual deepening of the surface layer through turbulent mixing. However, the particular oceanic response to the surface wind field in an upwelling region, whether it be due to upwelling or turbulent mixing (or both), will depend in part on the magnitude and direction of the surface wind field itself (deSzoeke and Richman, 1981).

Internal waves are also expected to contribute to the variability in physical properties in coastal regions. Whether or not internal waves occur on the continental shelf will depend on the density stratification and on the possibility of local generation near the shelf (Huthnance, 1981). At low internal wave frequencies, tidal and inertial internal wave motions are often vigorous in continental shelf regions (Johnson, Van Leer, and Mooers, 1976).

In evaluating the sources of variability in a coastal upwelling region, it is difficult to distinguish the variability caused by turbulence from that caused by internal waves. According to Stewart (1969), there probably is no clear distinction between turbulence and

internal waves in a stratified medium because of the strong exchange of energy that occurs between these processes where they coexist.

Coastally-trapped long waves, generalizations of idealized internal Kelvin waves and continental shelf waves, also contribute to the field of variability in coastal upwelling areas. These waves with periods on the order of several days to weeks, and wave lengths of the order of 100's of km may influence coastal waters to 100km or so offshore at mid-latitudes (LeBlond and Mysak, 1978; Allen and Romea, 1980).

Frontal processes and eddies may be relatively more important in coastal upwelling regions than in the open ocean. Overall, it is expected that the combined effects of the processes mentioned above will result in considerably shorter space-time scales in coastal areas.

In coastal domains, it is probably not valid to assume that the ocean is isotropic, homogeneous, and stationary. For example, alongshore scales near the coast are expected to be several times greater than offshore scales (Allen, 1981). In coastal upwelling regions, a major frontal zone often separates offshore waters from recently upwelled waters near the coast. Consequently, such regions are most likely inhomogeneous. Because major changes in circulation usually take place on seasonal time scales in coastal regions, data acquired over a significant fraction of a

seasonal cycle are likely to be non-stationary unless seasonal trends are first removed.

Awareness of the sampling problem in upwelling studies has been demonstrated repeatedly in the Coastal Upwelling Ecosystems Analysis (CUEA) Program's literature (Mooers and Allen, 1973; Mooers et al., 1976; Mooers et al., 1978). The important space-time scales of variability in the Oregon upwelling area were identified through field measurements and from dynamical considerations. The important offshore length scale off the Oregon coast was found to be on the order of 10 to 20km and to correspond to the first baroclinic radius of deformation, or the continental shelf width (whichever is less). In the alongshore direction, it was estimated that the flow field was coherent over distances from 100 to 1000km at time scales of several days to several weeks.

The problem of adequate sampling in upwelling regions has also been addressed by Kelley (1971). He suggests using adaptive sampling procedures whereby the incoming data itself determines the local sampling rate. As an alternative, he suggests that the gradient of the incoming signal associated with the data being acquired be used as a basis for establishing an adequate sampling procedure.

In an investigation of the mesoscale variability of SST in the upwelling zone off the central coast of Oregon large

variance in SST was concentrated between wavelengths of 16 and 40km (Holladay and O'Brien, 1975). However, isotropy was assumed, and other data sets from the same area suggest that this assumption may not be valid (e.g., Allen, 1981).

A prime example of undersampling in the coastal region along California can be found in the California Cooperative Fisheries Investigation (CalCOFI) data. This data acquisition program has been in operation since 1947 with oceanographic data acquired systematically on a regular grid along the West Coast on a periodic basis. However, the spacing of these measurements - 25 km or greater offshore, and 100 km or greater alongshore - is such that in some areas the upwelling zone is completely missed and the energetic mesoscale field of variability is seriously undersampled.

Although much of the CalCOFI data is seriously aliased in space and time, one experimental study conducted by Defant (1950) using CalCOFI data along the central and southern coast of California is germane to the present study. Defant showed that the confounding effect of internal waves of tidal period on shipboard observations was important in this region. He further demonstrated that this effect could be minimized through a proper spacing of the observations, determined by taking account of the propagation characteristics of the waves in question.

Variability in ocean properties is generally a function of both space and time, and it is often difficult to separate these effects. For data acquired at a single fixed point (i.e., an Eulerian framework) it is only possible to ascertain the time dependence of the process involved. For data acquired from moving platforms the effects of both space and time may be important. For slow ships which progress at speeds comparable to baroclinic phase speeds, it is often difficult to separate space and time effects. For single-ship operation, the data must be acquired sequentially rather than synchronously, leading to the so-called "synopticity myth" (Kelley, 1976). Often the assumption is made that observed changes in ocean properties are purely space dependent as a ship moves from one location to another. This assumption corresponds to the Taylor hypothesis, where it is assumed that the time required for significant changes to occur within the medium is long compared to the time required to acquire the data. As pointed out by Woods (1975), however, the structure of the real ocean may change significantly during the time required to acquire the data. He cites such factors as rapid internal wave propagation relative to ship's speed, steady current shear, temporal changes resulting from internal interactions and external forcing, and advection. The problem of separating the effects of space and time is greater in coastal areas than in the deep ocean, because of

the short time scales associated with coastal ocean processes.

Another approach to estimating statistical scales of variability for oceanic properties involves the use of so-called structure functions (Yaglom, 1952 ; Ozmidov, 1962 ; Black, 1965). The structure function is similar to the autocorrelation function, and the two are equivalent for stationary processes (Yaglom, 1952). However, the structure function is less sensitive to non-stationarity; nevertheless, it will not necessarily provide better results than the autocorrelation function in estimating scales, if the data have been properly detrended before the correlation functions are calculated.

A slightly different approach to the design of geophysical surveys has been proposed and used by Davis (1974). He points out the difficulties in estimating the sampling errors associated with correlation functions, their sensitivity to non-stationarity, and the difficulty in propagating errors associated with such functions through linear systems. As a result, Davis' technique relies on the use of one and two-dimensional Fourier transforms applied to numerical models of the sampling process to estimate the mean square error, as well as the spectral content, of the sampling error. Although in general terms, this approach may appear to be similar to

the approach using correlation functions, it differs in the details of its application. In particular, the appropriate scale lengths of interest are estimated in the wavenumber-frequency domain rather than in the space-time domain. In cases where the density of samples is sufficient, and the area of coverage extensive, Davis' technique is preferable. This approach to survey design is now being used in a number of Navy-oriented disciplines including magnetic and gravity surveys (Davis, 1982).

Empirical Orthogonal Functions (EOF's) have been used to estimate scales of variability for oceanic properties (Barnett and Patzert, 1980). EOF analysis provides a method for decomposing a given field into a set of orthogonal modes. When the mean is removed, these modes represent independent modes of variability. Barnett and Patzert assert that the EOF analysis technique is not affected by spatial inhomogeneities, as would be a scale length analysis using correlation techniques. The application of EOF's to the problem of estimating scales of variability presents an interesting alternative to the correlation function approach and this technique will be used in portions of the present study (Chapters III and V).

Other scales exist in addition to the statistical scales. Observed scales may be defined by significant changes in mean property gradients. The depth of the mixed surface layer is an example of an observed scale. In a

discussion of the boundaries of upwelling regions, Tomczak (1978) refers to physical boundaries or natural scales. Tomczak's "natural scales" correspond closely to the observed scales indicated above. With respect to coastal upwelling regions Tomczak considers several natural vertical length scales including the surface Ekman layer depth, and the bottom Ekman layer depth at least in shallow shelf areas. Tomczak also proposes a natural alongshore scale which is equal to the distance traveled by newly upwelled water in the alongshore direction while it moves over a specified (scale) distance in the offshore direction. He suggests an offshore scale equal to the distance of the upwelling frontal boundary from the coast, where such a boundary can be identified. Otherwise, he suggests using the location of the maximum gradient in hydrographic properties in the offshore direction. Finally, Tomczak suggests that the ratio of offshore to alongshore scales can be used to characterize different upwelling regions.

Dynamical scales are derived from the equations of motion and provide another measure of similarity with respect to the processes involved. According to Huthnance (1981), seven independent length scales can be derived from the equations of motion. The significant length scale in any given situation is the one that provides the minimum

value. Along the coast of Oregon for example the most significant length scale (i.e., horizontal) is given by the two-layer internal Rossby radius of deformation, R_{bc}, (Huthnance, 1981), as

$$R_{bc} = f^{-1} \{ g h_1 h_2 (\rho_2 - \rho_1) / (h_1 + h_2) \rho_2 \}^{1/2} \qquad (1.1)$$

where

f = Coriolis parameter

g = Acceleration due to gravity

h_1 = upper layer thickness

h_2 = lower layer thickness

ρ_1 = upper layer density

ρ_2 = lower layer density

In proceeding from shallow to deep water, it is apparent from the expression above that R_{bc} will increase. Calculations at 36N indicate that R_{bc} increases from approximately 5km at the shelf margin to almost 20km at a depth of 1500m.[2] However, along the Central California coast, a topographic scale corresponding to the width of the continental shelf may provide a length scale smaller than that given by R_{bc} even in shallow water. Satellite data indicate that during the early part of the upwelling season (March-May), coastal upwelling is restricted to a

narrow coastal band of the order of 20km in width. As the upwelling season progresses, the upwelling front gradually expands seaward, extending as far as 100km off the coast by mid-summer. In this situation, it is obvious that neither R_{bc}, nor the width of the continental shelf, provides a realistic scale estimate for the offshore distance of the upwelling front.

Philander and Yoon (1982) present a time-dependent length scale for the offshore width of coastal upwelling based on Rossby wave dynamics. Their model of circulation in eastern boundary currents extends only as far north as 30N ; however it is reasonable and straightforward to apply their results as far north as Central California. Their calculations show that on time scales of 60 days or more, the offshore scale exceeds R_{bc} due to the Beta effect, i.e., the latitudinal variation of the Coriolis parameter, which in turn permits westward propagating Rossby waves to develop. The spatial scale associated with this motion is 400km at 15 degrees north for a period of 200 days. The relationship expressing this scale is given by Philander and Yoon as

$$R_r = \beta T / (\ell^2 + \lambda^{-2}) \qquad (1.2)$$

where $\beta = 2.0 \times 10^{-11} m^{-1} s^{-1}$, T = time period of interest, ℓ is the meridional wavenumber of variation taken to be 150km, and λ is R_{bc}. At 36N, equivalent conditions yield an offshore

scale of about 65km. Such a value is in order-of-magnitude agreement with the available satellite data.

Any theoretical discussion of space-time scales must include the inertial time scale $((2\,\Omega\,\sin\phi\,)^{-1})$, where Ω is the angular velocity of the earth and ϕ is the latitude. Oscillations of inertial period are common in coastal regions (Mooers, 1976). Internal tides are important in coastal regions and have wavelengths of the order of a few ten's of km. Major alongshore topographic scales are 100 to 200km along the Central California coast with scales of the order of 10km or so appropriate to the submarine capes and canyons in the region. The prevailing alongshore winds have length scales of the order of a 1000km whereas the local winds have length scales similar to those associated with the coastal orography (O(10km)).

Many other space-time scales based on theoretical considerations could be given; only those obviously important to the present study have been included. Statistically derived scales are distinguished from observed and dynamical scales in that they characterize a length over which the variability of a given property is similar. Although the main emphasis in this study is on estimating the statistical scales of variability, the corresponding observed and dynamical scales which are often

related, help to establish a useful framework within which to evaluate the statistical scales.

Scales derived from directly observed properties such as temperature and salinity will not necessarily be the same as the scales derived from dynamically related properties, such as pressure, dynamic height, or geostrophic velocity (Rhines, 1977). The scale relationships between these directly observed and dynamical properties are determined by their relationships through the equations of motion. Therefore, scales associated with the geostrophic velocity field will be related to the scales of the first spatial derivative of the pressure field, for example. The equations of motion thus provide the basis for deriving velocity scales based on initial scale estimates obtained from the mass field.

C. PLAN OF THE DISSERTATION

In Chapter II, a review of previous oceanographic studies along the Central California coast is presented. This review is followed in Chapter II by the presentation of new results from a study describing the physical characteristics of the Pt. Sur upwelling center. The second chapter is intended to (1) provide a regional oceanographic setting for the subsequent chapters of the study, and (2) identify the dominant features and processes that are most likely to influence the space-time scales of variability.

In Chapter III, IR satellite data acquired during the Pt. Sur upwelling center study and during several month periods in 1980 and in 1981 are analyzed. In addition to providing motivation for the subsequent space-time scale analyses, the satellite imagery is used to obtain preliminary estimates of the space-time scales associated with variations of the upwelling frontal boundary between Monterey Bay and Pt. Piedras Blancas. Also, dynamical scales indicating the offshore extent of coastal upwelling are evaluated and compared. Two possible explanations for the observed seasonal behavior of coastal upwelling along the Central California coast are presented.

In Chapter IV the time-scales of variability are estimated from 12-year time-series of SST acquired at Granite Canyon, Pacific Grove, and the Farallon Islands. These data allow examination of the problem of determining adequate temporal sampling rates. A subsurface temperature time series off Cape San Martin is also subjected to time-scale analysis and the results compared with an equivalent surface time scale estimate. These data are also examined for their oceanographic content to provide additional background for the various scale analyses.

In Chapter V, the spatial scales of variability are estimated. The spatial scales are more difficult to estimate than the temporal scales, because of the limited

number of observations available, and because the data used in estimating these scales were acquired aboard a moving ship. As a result space and time variability coexist. Consequently several approaches are used to estimate the spatial scales.

In Chapter VI, the scientific results are summarized. Results of the various temporal and spatial scale analyses are summarized and then compared with similar results from other regions, including other coastal and deep ocean areas. Finally, a list of conclusions and recommendations are presented. In particular, recommendations for sampling in space and time are given.

II. PHYSICAL CHARACTERISTICS OF THE CENTRAL CALIFORNIA COAST REGION AND THE PT. SUR UPWELLING CENTER

A. INTRODUCTION

The study presented in this thesis is concerned with the region off the Central California coast extending from approximately 34.5 to about 37.8N. These latitudes correspond to the limits of the coastal observations used in this study. The offshore limit extends approximately 100km and applies in particular, to the region off Pt. Sur where the *in situ* data used in this study were acquired (Fig. 1). With respect to satellite coverage, the overall region is somewhat larger, extending perhaps several hundred km further north, and 400-500km offshore. This chapter contains a summary of results from previous physical oceanographic studies in the region defined above (Section B.), and results from a recent study of the Pt. Sur upwelling center based on observations of temperature, salinity and surface winds acquired aboard ship (Section C.).

The study region includes Monterey Bay, but since the distribution of physical properties and circulation within the Bay are not fully representative of the physical properties and circulation along the open coast, the Bay is

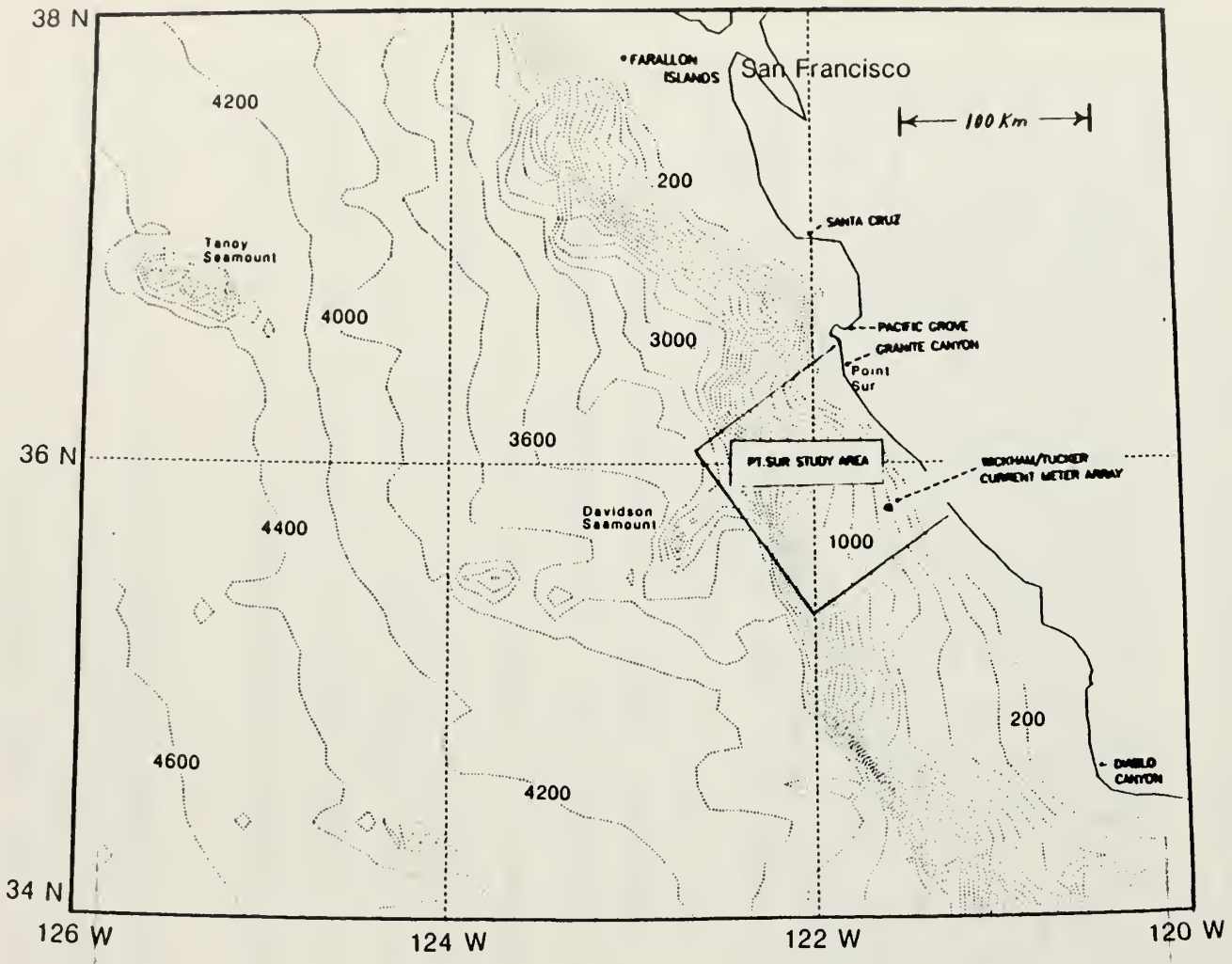

Figure 1. Locations of the Pt. Sur upwelling center study area, sea-surface temperature station locations, and the subsurface temperature location (i.e., moored array).

not generally included in the present study. However in Chapter IV., SST at Pacific Grove, which is inside Monterey Bay, is compared with temperatures at other locations outside the Bay.

Few studies have been conducted along the California coast that specifically address the problem of estimating the space-time scales of variability. However, a few studies do address the general topic of variability with respect to physical and dynamical properties. A number of studies also consider physical processes that are likely to contribute to the observed variability in the region. The results of these studies are now summarized.

B. OCEANOGRAPHIC STUDIES OFF THE CENTRAL CALIFORNIA COAST

Hughes (1975) used correlation techniques to estimate correlation length scales in sound speed gradient profiles in the area between 36 and 37N. Correlation length scales were found to vary between about 27 and 50km for observations acquired in different seasons. However, correlation coefficients from observations taken across ocean fronts were found to change sign over distances as short as 16 km.

Shepard (1970) refers to the heterogeneity of the coastal area between Monterey Bay and San Francisco with respect to the distribution of various physical and bio-optical properties, including chlorophyll a, particulates,

oxygen, and temperature. From his study, during May of 1970, four distinct regions were identified with respect to the distribution of these properties; the south end of Monterey Bay, the north end of the Bay near Santa Cruz, the region off Pt. Montara, and the region west of the entrance to San Francisco Bay. He also found considerable interannual variability between San Francisco and Monterey Bay.

From a frequency analysis of currents off Cape San Martin at depths between 100 and 500m during the winter of 1978, Dreves (1980) found spectral peaks in the range of 2 to 4 days, and at 10.7 days. He also found much greater current variability in the alongshore direction than in the offshore direction.

From hydrographic data acquired over a finely-spaced grid (5km offshore, 15km alongshore) off the coast at the latitude of Monterey Bay, Blumberg (1975) found significant spatial variations in physical properties over distances of 10 km or less from surveys taken at different times.

Based on geostrophic calculations from six surveys over a two year period, between 35.5 and 37.0`N., marked seasonal variability was found in the near-surface flow which included eddies and filaments. Bottom topography was found to influence the direction of flow offshore to a depth of about 2000m (Brown, 1974). In the same region,

alternating elements of poleward and equatorward flow were found based on geostrophic calculations and drogues (Greer, 1975). Individual flow elements were often less than 10km in width.

Anomalies in monthly averaged sea level were found to persist over periods of up to five months, based on autocorrelation analysis of sea level at Monterey (Bretschneider, 1980). Large variances in sea level at periods between 12 and 24 days were also found.

Based on the distribution of physical and optical properties in an area just north of Santa Cruz, an anticyclonic eddy was observed extending about 8km offshore (Labyak, 1969). Because of its apparant connection with circulation in Monterey Bay, it was implied that this feature should recur.

Based on satellite and in situ data, upwelling features around Pt Sur are recurrent with observed scales ranging from 10's to 100's of kms, with some features extending almost 300km offshore (Conrad, 1980). In this upwelling region, based on the association of shipboard measurements of physical properties with the magnitude and orientation of surface features observed in IR satellite imagery, subsurface temperature structures were similar in each of three comparisons (Johnson, 1980). Estimated time scales associated with these features, based on successive satellite images, were found to range from about 8 to 19

days. The dominant spatial scales were estimated to be: (1) alongshelf scale: O(100km), (2) across-shelf: O(10km), (3) depth: O(10m), and (4) frontal zone width: O(10km). The area of most intense upwelling was often located over Sur Canyon.

The locations of thermal features observed off Pt. Sur in IR satellite data, and the distributions of various biochemical properties have been found to be strongly associated (Traganza, 1980, 1981, and 1983). These upwelling-related features are frequently eddy-like.

Based on drogues, nearsurface currents from 10 and 110 km off Pt. Sur, generally flowed to the southeast between 19-26 March 1958 (Jennings and Schwartzlose, 1960). The flow was apparently diverted by the presence of the Davidson Seamount, in that higher speeds were observed just to the east and west of it. In about the same area, a drogue study in November of 1961 (at a depth of 250m) indicated northward flow seaward to about 65km, and southeasterly flow from 65 km to 160km, offshore (Reid, 1962). Reid associated northward flow within the first 65 km of the coast with the California Countercurrent. Based on nearsurface drogues during October 1958, coastal waters were just beginning to flow northward, whereas in January 1959, the northward flowing Davidson current, which

extended approximately 80 km offshore at 36N, was well-established (Reid and Schwartzlose, 1962).

Between 36.3 and 36.8N, flow in the California Countercurrent is complex, with large changes in water properties in the offshore direction over distances of 10's of km (Wickham, 1975). The vertical scale of these property variations was on the order of several hundred meters. There was a narrow band of poleward flow near the shelf edge, complex flow further offshore, and a broader poleward flow still further offshore at 40 to 50km off the coast. Drogue trajectories in the study area suggested eddy formation.

From moored current meters, prominent large amplitude changes in current speed at depths between 100 and 300m were observed over the continental slope just south of Pt. Sur (Wickham and Tucker, 1979). These "episodes" were observed at moorings 12km apart, and they had time scales of about one week.

From analyses of sea level data along the West Coast, variations in sea level south of San Francisco are caused mainly by anomalies of equatorial origin (Enfield and Allen, 1980; Bretschneider and McLain, 1983).

Based on CalCOFI charts of dynamic topography from 1949 to 1965, the region covered by the present study frequently contains both cyclonic and anticyclonic eddies (Burkov and Pavlova, 1980). Cyclonic eddies were generally

observed near the coast and anticyclonic eddies closer to the center of the California Current.

From drift bottle returns along the U.S. West Coast, exceptions to the general southeasterly flow observed during the spring and summer are found between San Francisco and Monterey Bay, where small countercurrents and/or eddies may occur (Schwartzlose, 1963). Based on CalCOFI dynamic topographies, there may be a permanent counterclockwise eddy south of San Francisco for all months of the year except April (Hickey, 1979).

CalCOFI dynamic height data frequently indicate the presence of a cyclonic eddy during July centered at approximately 100km off the coast between San Francisco and Monterey Bay (Schwartzlose and Reid, 1972).

Based on hydrographic data, and current meters on a satellite-tracked drifting buoy at about 175km west of Monterey Bay (36N, 124W), a 100km diameter, deep (1500m), anticyclonic eddy was found to rotate with a depth dependent period ranging from about 32 days at 150m to 15 days at 1500m (Broenkow, 1982).

From nearshore surface drifter returns between Ano Nuevo (30km north of Santa Cruz), and the Monterey Peninsula, flow is predominantly northward (3-13 cm/sec) in association with the Davidson Current, from November through February (Griggs, 1974). In March, flow reversed

to the south (5-12 cm/sec) until June. Between July and November there were no dominant flow patterns. LANDSAT satellite imagery was used to infer current patterns along the entire California coast, using suspended sediment from river discharge and shore erosion as a tracer (Pirie et al., 1975). Their results generally agree with those of Griggs, where they coincide, and indicate similar seasonal patterns over most of the present study area.

C. THE PT. SUR UPWELLING CENTER

1. Background

Coastal upwelling has been studied intensively off the coasts of Oregon, Northwest Africa, Peru, South Africa, Somalia, and elswhere for over a decade as part of such research programs as the Coastal Upwelling Ecosystems Analysis (CUEA) Program. However, few studies have been conducted off the coast of California where indicators of upwelling such as computed offshore Ekman transport (Bakun, 1975), and IR satellite imagery (Breaker and Gilliland, 1981), suggest that coastal upwelling occurs both extensively and intensively.

Based on IR satellite imagery off the West Coast, coastal upwelling apparently occurs more frequently and intensely at preferred locations or centers, viz., the major capes along the California coast. These centers are characterized by recurrent surface outcrops of relatively cold water, that may upon occasion extend several 100km

offshore in the form of elongated filaments. The remainder of Chapter II. pertains to a recent field study of the physical aspects of the coastal upwelling center off one such cape, Pt. Sur, California.

Coastal upwelling centers are a partially understood aspect of coastal upwelling, perhaps due to their complexity. However, upwelling is known to be intensified south of major capes and points along the California Coast (Reid et al., 1958). Upwelling is expected to be more intense equatorward of capes along eastern boundaries due to a local increase in cyclonic relative vorticity (Arthur, 1965). Upwelling may also be intensified around capes due to centrifugal forces associated with strong tidal currents (Garrett et al., 1976). Upwelling is greatly intensified over the heads of submarine canyons off Northwest Africa (Shaffer, 1976); these canyons are generally associated with capes. During summer, the extent of coastal upwelling off the southern tip of South Africa (Capes Peninsula and Columbine) is related to the local winds (Andrews and Hutchings, 1980). At this location the surface structure of the upwelling center varies considerably, but below the surface it was found to be less mobile. The surface cold anomaly in the upwelling center off Cabo Nazca, Peru is restricted to about the upper 60m of the water column (Brink et al.,

1980). Also, the surface area of the cold anomaly is directly related to the two-day averaged, local wind stress, and much of the perturbation displacement of the cold anomaly is due to the passage of poleward-propagating, coastal-trapped long (ca. 1,000 km) waves.

2. Experimental Plan

The primary goal of the Pt. Sur study was to obtain a better understanding of how the Pt. Sur coastal upwelling center behaves as a physical system with respect to the winds, local topography, eddies in the California Current, and coastal-trapped long waves. A secondary goal was to interpret, with respect to the primary goal, the high-resolution IR satellite imagery acquired during this study. The study area encompassed Pt. Sur, extending 90 km offshore and 120 km alongshore (Fig. 1).

The field study was conducted during three phases in June 1980: the first phase, 1 to 5 June; the second phase, 9 to 11 June; and the third phase, 15 to 19 June. The first and third phases each consisted of two halves during which one hydrographic mapping of the area was made (Fig. 2). The mappings are labelled 1A, 1B, 3A, and 3B, respectively.

The oceanographic measurements were made from the R/V ACANIA. Airborne Radiation Thermometer (ART) and Aircraft Expendable Bathythermograph (AXBT) measurements were made during the third phase from a Coast Guard C-130

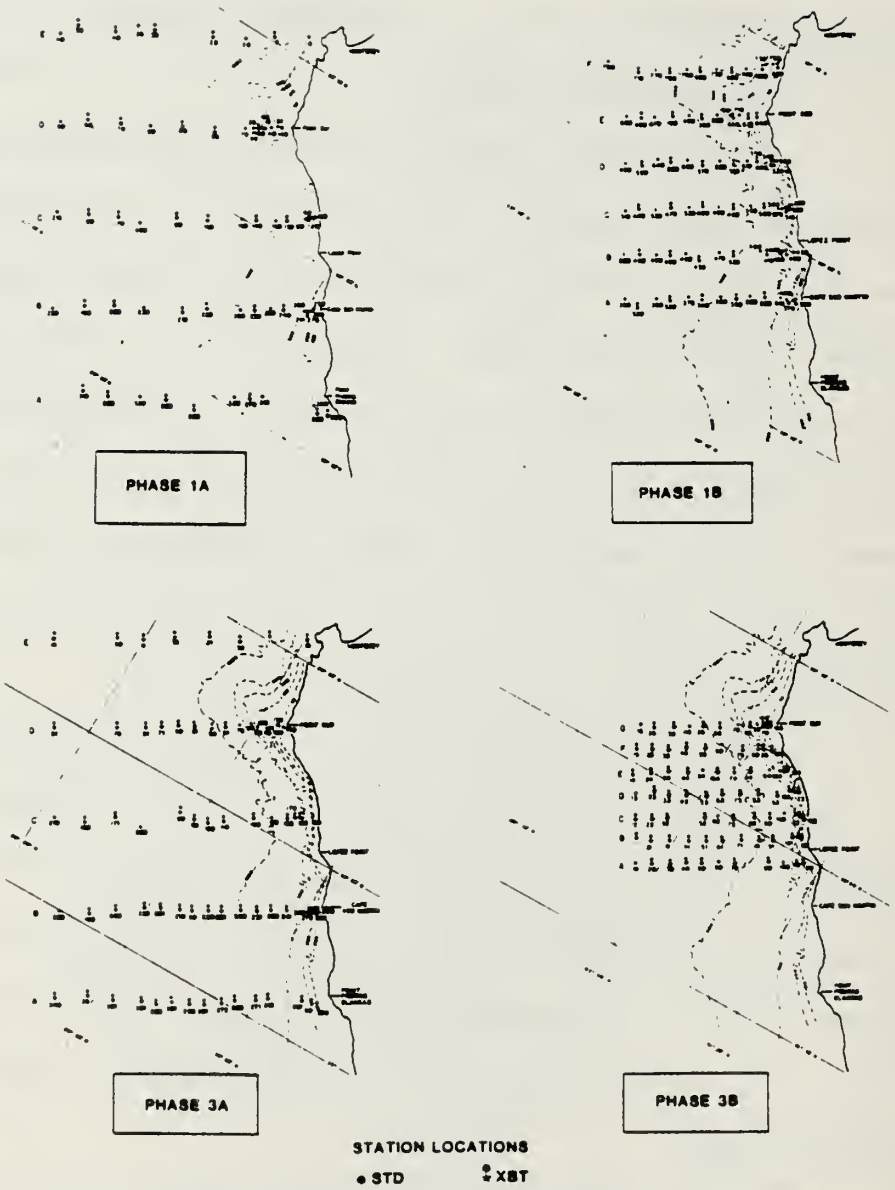

Figure 2. The June 1980 synoptic study domain, which extends 90 km offshore, and 120 km alongshore from Pt. Pinos south to Pt. Piedras Blancas. Salinity-temperature-depth (STD) stations are indicated by solid circles and expendable bathythermograph (XBT) stations by solid circles and stars for each phase (1A, 1B, 3A, and 3B, respectively). Dashed lines are isobaths.

aircraft. To estimate surface currents within 30 km of the coast, SRI International made high-frequency coastal radar measurements just south of Pt. Sur during the third phase. The NOAA/NESDIS Satellite Field Services Station in Redwood City, CA, provided twice-daily, high-resolution IR satellite coverage. IR satellite images were used to help design the hydrographic sampling grid, guide shipboard sampling in real-time, and aid in the subsequent data interpretation.

Shipboard observations included Expendable Bathythermograph (XBT) casts to 450m and Salinity/Temperature/Depth (STD) casts to 300m at regular intervals (Fig. 2). Records of temperature and salinity at a depth of 2m were obtained from a continuously recording thermalsalinograph. Casts were spaced to resolve the baroclinic radius of deformation (ca. 15km) in the offshore direction. Hence, offshore spacing was usually 10 km or less. Alongshore spacing was 30 km or less in order to resolve the principal bathymetric scales. A total of 210 XBT and 105 STD casts were made. Synoptic coverage of the area was a key sampling requirement; however, each mapping required 48 hours to complete. Coarse resolution of the typical synoptic wind event scale of one-to-two weeks was achieved.

3. Observations from the Pt. Sur Upwelling Center Study

a. Winds

The synoptic scale winds off Pt. Sur during summer are consistently favorable for coastal upwelling (Bakun, 1975 ; Nelson, 1977). Although large variations in wind speed occur, typically over periods of several days, winds rarely reverse direction. The constancy in wind direction is associated with the seasonal intensification and stationarity of the subtropical high pressure cell over the Northeast Pacific and the proximity of a fixed, and often steep, coastal boundary.

Based on coastal wind observations at Pt. Sur and at Pt. Piedras Blancas (90km to the south), wind speeds often approached 10m/sec during the month of June (1980) (Fig. 3). Mean wind directions at the two sites were slightly different, consistent with local differences in coastline orientation. Winds at Pt. Sur tended to be from the North-Northwest (NNW) whereas the winds at Pt. Piedras Blancas tended to be more from the Northwest (NW). Shipboard winds were mainly from the NNW. Because the Central California coast is mountainous, coastal orography undoubtedly influences the local wind field.

From upwelling indices computed at Pt. Sur (Fig. 3), variations in the alongshore wind stress occurred on roughly a weekly time scale, whereas wind direction

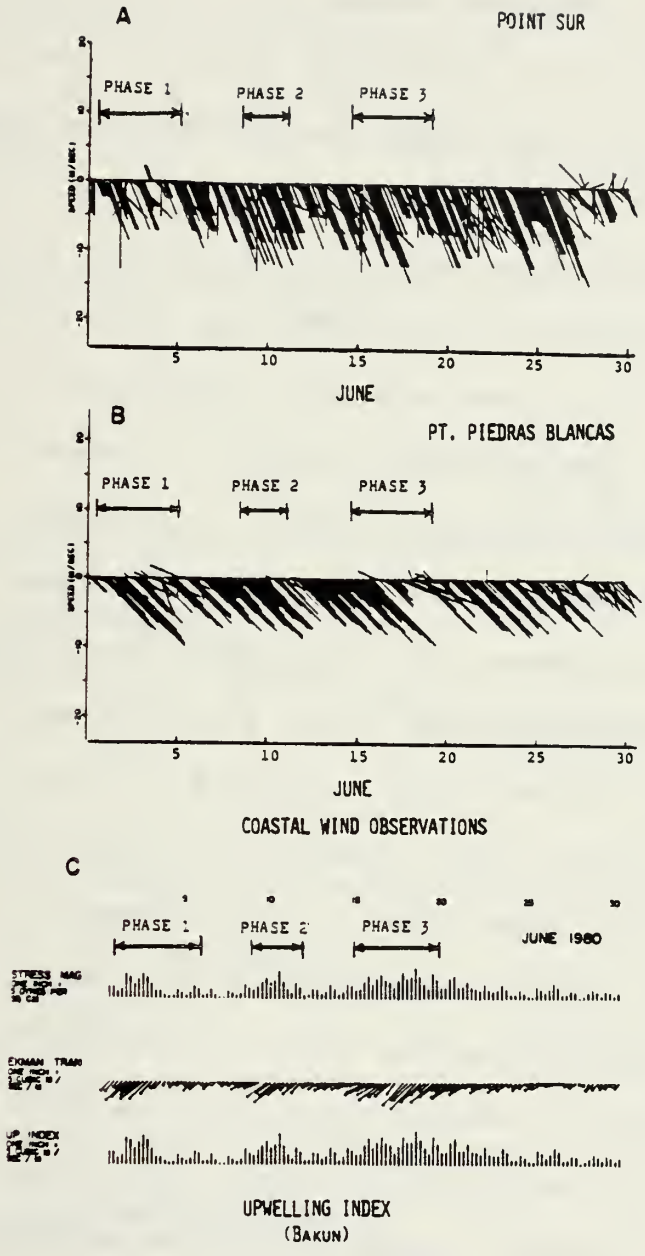

Figure 3. Coastal winds. Panels A and B are wind stick diagrams at Pt. Sur and Pt. Piedras Blancas, respectively, for June 1980. Wind sticks show direction toward which wind is blowing, with north up. These coastal observations, taken every 3 hours, were provided by the National Weather Service. Panel C shows time histories of wind stress magnitude, Ekman transport, and upwelling index, based on computed synoptic-scale winds every 6 hours at Pt. Sur (Bakun, 1980).

remained almost constant (Bakun, 1980). Periods of maximum winds coincided closely with the sea-going phases of the field study!

Winds observed aboard ship (at 10m) during each of the four phases were usually 10 m/sec or greater (Mooers et al., 1983). Wind direction was steady from about 320°T, in close agreement with similar observations by Pilie et al. (1978). Wind stress was also calculated from the wind observations acquired aboard ship for each phase using a quadratic law with a constant drag coefficient of 1.3×10^{-3}. The hourly wind observations were first rotated parallel to the coast and then interpolated to a standard grid with 10km spacing offshore and on station tracklines alongshore. The alongshore component of wind stress was highest during Phase 3A and lowest during Phase 1B. For each phase the interpolated values were averaged in the alongshore direction to obtain mean offshore profiles (Fig. 4). At least within the first 60km or so offshore, there was a slight tendency for the alongshore wind stress to increase in magnitude away from the coast; thus, the wind stress curl was positive. During Phase 3A, the wind stress and wind stress curl were both maximum, the wind stress curl averaging ca. $+2.3 \times 10^{-2}$ dynes/cm^2/km between the coast and the location where the .pa offshore wind stress reached its maximum value (ca. 70km offshore).

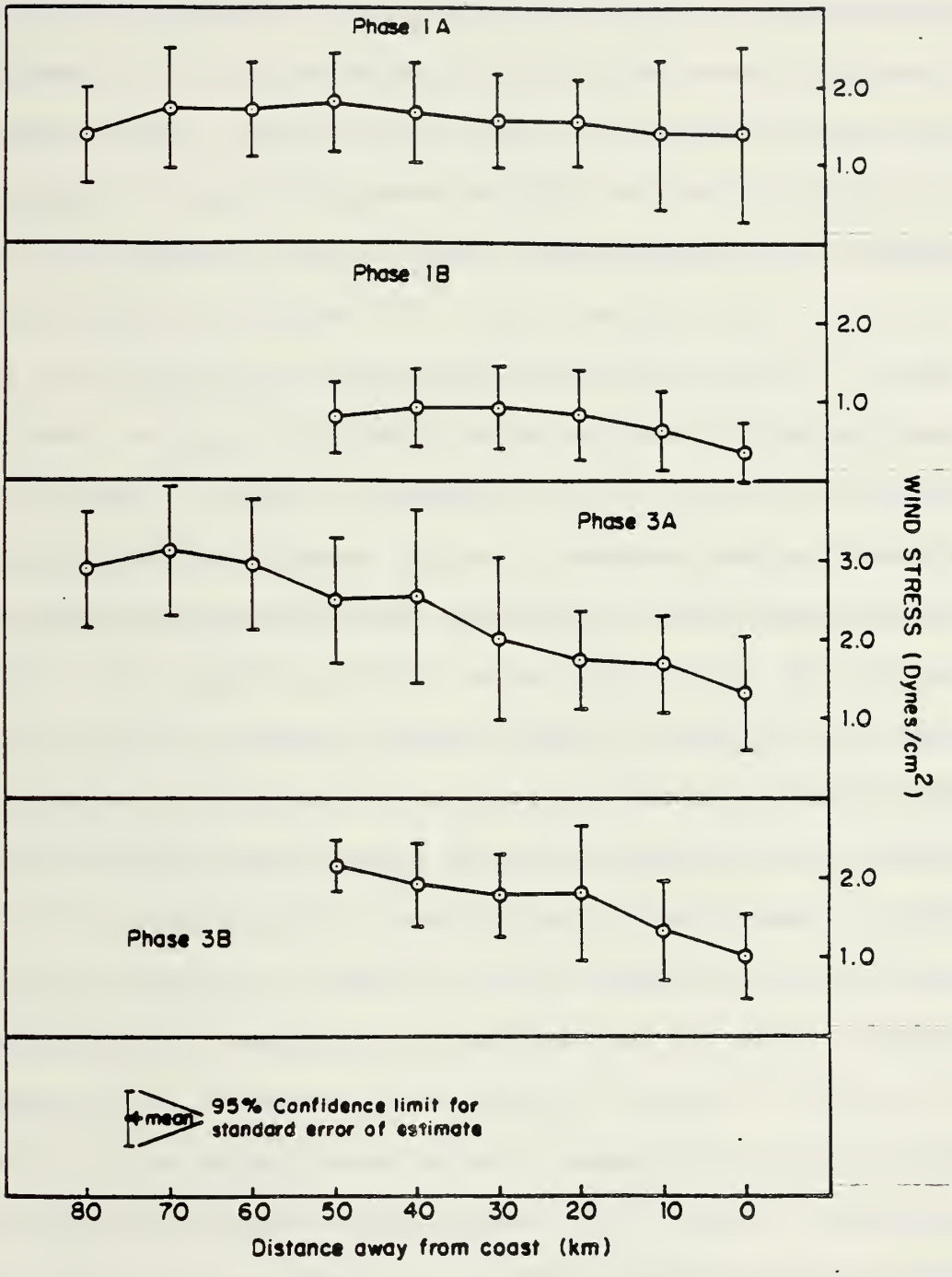

Figure 4. Mean offshore profiles of alongshore wind stress for each phase. Wind stress values from shipboard observations along each trackline were averaged in the alongshore direction.

The alongshore component of wind stress contained a relatively strong diurnal component with an amplitude of the order of one dyne/cm^2. The maximum alongshore wind stress occurred at approximately Ø3ØØL and the minimum at approximately 16ØØL. These times are not necessarily consistent with those expected for a sea-breeze circulation (Atkinson, 1981). Sea breeze circulations are frequently observed off the coast of Southern California (Edinger and Helvey, 1961; Angell et al., 1972) and further north off the Oregon coast (Johnson and O'Brien, 1973; Hawkins, 1977). Off the Oregon coast the influence of sea-breeze circulations has been observed out to at least 25km offshore (O'Brien and Pillsbury, 1974). However, the orientation and proximity of the coastal mountains in this region were found to deflect diurnal period onshore winds toward the south (Halpern, 1974). Along the coast of Northern California between Pt. Reyes and Pt. Arena, a region bounded with high coastal mountains, strong diurnal variations in alongshore wind stress were observed (Sauvel, 1983). These diurnal variations in alongshore wind stress, however, were attributed to diurnal variations in the height of the marine inversion, which in turn are thought to create a Venturi effect with respect to the surface winds near the coast. In areas where strong marine inversions exist, the coastal mountains can introduce important steering effects, forcing coastal winds around

(along) mountains rather than over them (Atkinson, 1981). Similar conditions may be present along the Central California coast between Pt. Sur and Pt. Piedras Blancas, where the steepness and height of the coastal mountains is even greater. Also nocturnal radiation from the marine boundary layer, and its destabilizing influence, could contribute to the diurnal variations in surface wind. The diurnal influence however has not been removed from the profiles shown in Fig. 4.

b. In Situ Oceanographic Measurements

First, the horizontal property distributions are examined. These include SST, surface salinity, surface sigma-t, and mixed layer depth.[3] Property maps from Phase 1A (1 to 3 June) are seen to have a high-gradient zone more-or-less parallel to, and within about 25km of, the coast (Fig. 5). The maximum gradient in SST just south of Pt. Sur, for example, was approximately 3C in 10km. Occasionally, significantly sharper gradients were detected in the continuous temperature records from the thermalsalinograph. (The nearshore, high gradient zones are generally taken as an indication of active coastal upwelling.)

A protrusion appears about 35km south of Pt. Sur, with SST lower, surface salinity higher, and surface density higher within the protruding region. This

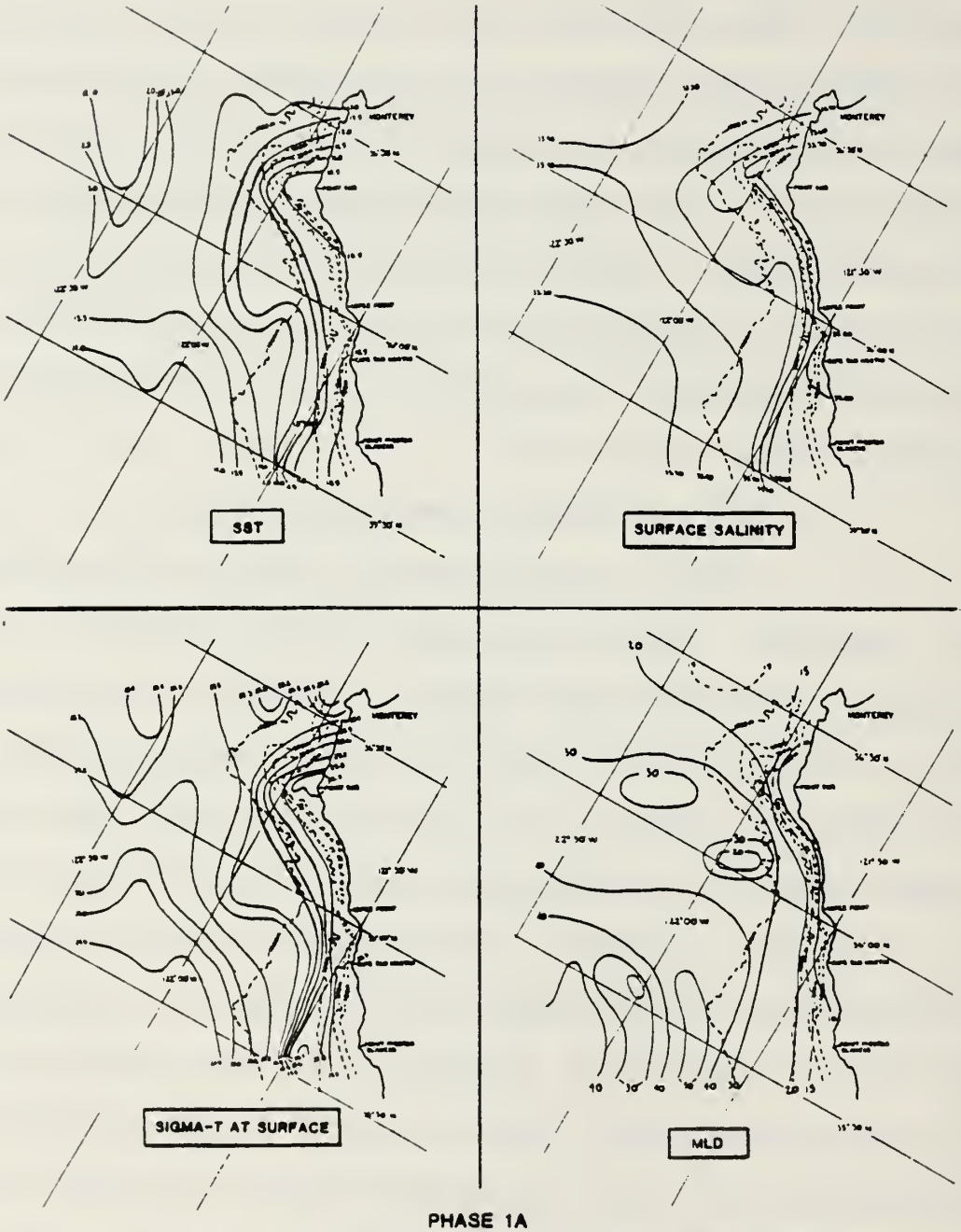

Figure 5. Maps of sea-surface temperature in degrees C (upper left), surface salinity in parts per thousand (upper right), surface sigma-t (lower left), and mixed layer depth in 10m intervals (lower right), for Phase 1A. SSTs were derived from the XBT and STD data, surface salinities from the shipboard thermalsalinograph, sigma-t from XBT and STD temperatures and STD salinities, and mixed layer depth from the XBT and STD temperature profiles.

protrusion of cold water can be traced vertically to a depth of at least 50m (Fig.6). This feature is consistent with intensified upwelling over Sur Canyon, which may contribute to the protrusion. IR satellite imagery has frequently shown this location to be anomalously cool with the area of cool water distending offshore.

In the southwest corner of the study area, SSTs were higher, surface salinities lower, surface density lower, and MLD deeper than in adjacent waters. These patterns are consistent with the anticyclonic circulation of a warm-core eddy, possibly associated with the Davidson Seamount, located 125 km South-Southwest (SSW) of Pt. Sur. The likely influence of this seamount on near-surface circulation was mentioned previously (Jennings and Schwartzlose, 1960).

The surface distributions of temperature and salinity are quite similar. The gradients of temperature and salinity were usually of opposite sign and thus acted jointly to produce an enhanced density gradient. Hence, the local circulation should include a strong baroclinic geostrophic component.

Temperature at 10m (Fig. 6) and SST (Fig. 5) are similar in Phase 1A since the MLD was usually deeper than 10m. The eddy-like feature in the SW corner of the area is clearly indicated at all depths from the surface to 200m.

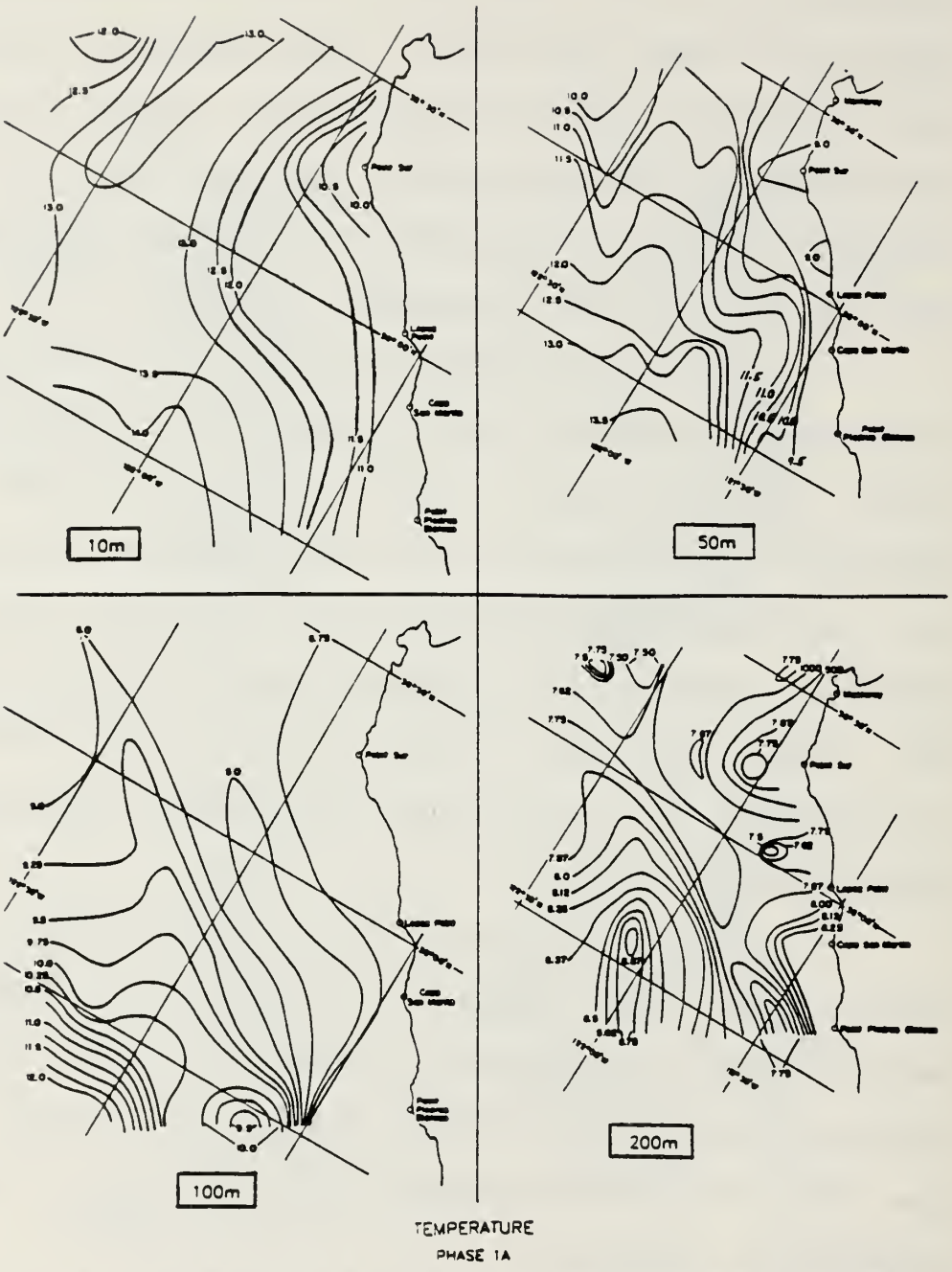

Figure 6. Maps of temperature for Phase 1A. Upper left panel: temperature at 10m, upper right panel: temperature at 50m, lower left panel: temperature at 100m, and lower right panel: temperature at 200m.

The protrusion of cool water south of Pt. Sur (Fig. 5), which was present during Phase 1A, is not as apparent during Phase 1B (Fig. 7).

From Phase 1A to 3A, the surface baroclinic zone moved seaward, particularly just south of Pt. Sur. Also the region nearest the coast cooled by about 1C between phases 1A and 3A. These changes indicate that upwelling intensified over the two-week period between phases. Again, probably due to fluctuations in upwelling and mixing, the variations in the SST patterns were almost as large between 1A and 1B, or 3A and 3B, as they were over the entire two-week period. Except for isolated areas where anomalies in surface salinity occurred, the maps of SST closely resembled those of surface sigma-t.

Individual isopleths in the vertical transects of temperature, salinity, and density in the offshore direction contain spatial perturbations with wavelengths of the order of a few 10's of km (Fig. 8). The local internal tide may contribute to these variations. The variability contained in these transects is typical of that observed in other transects not shown. To examine the nature of this variability, individual temperature profiles were grouped by distance offshore in corridors approximately 15km in width (of the order of 1 R_{bc}), and then averaged. These mean profiles were then averaged again in the alongshore

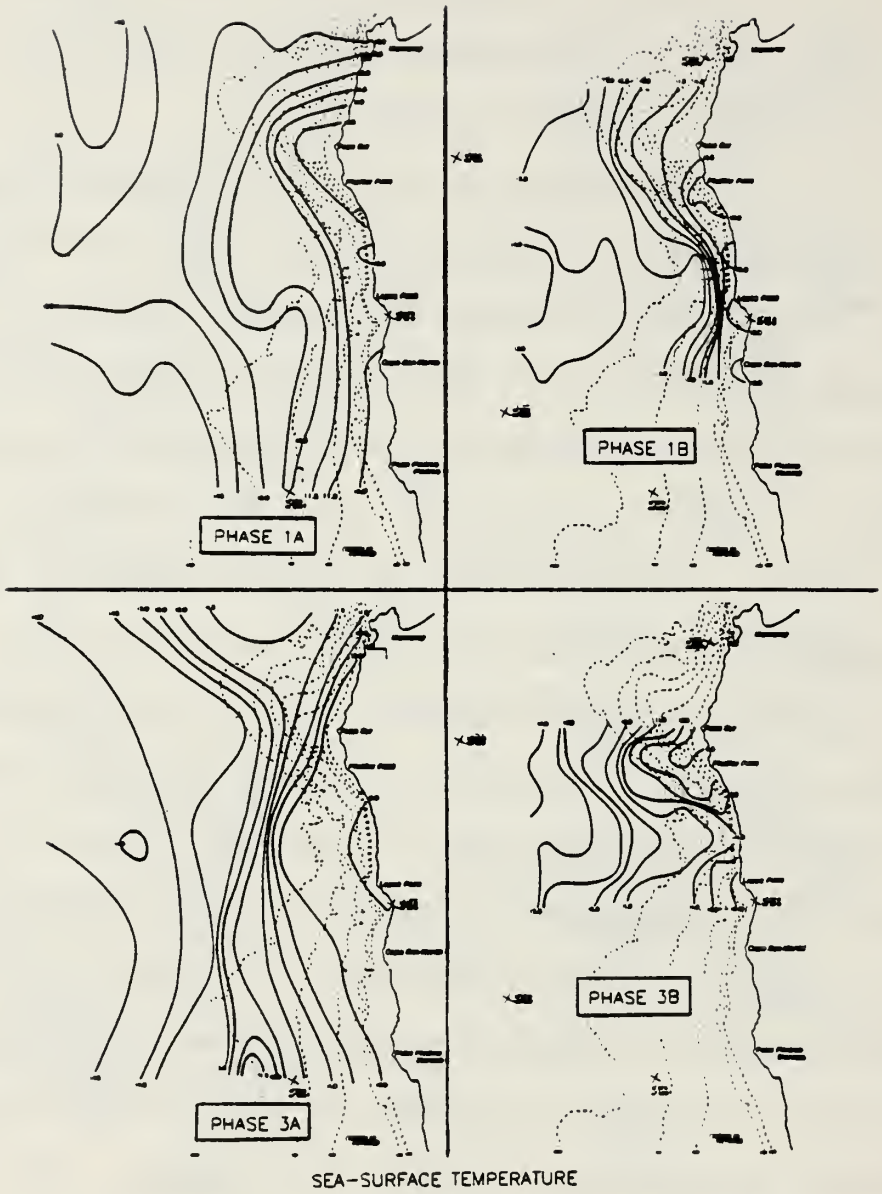

Figure 7. Maps of sea-surface temperature for each phase.

Figure 8. Vertical property sections for temperature, salinity, and sigma-t, for Phase 1A, Leg B. Each tick mark along the horizontal axis represents 5km, and along the vertical axis, 33m.

direction for each corridor, producing a mean transect for each phase. An overall mean transect was then calculated by averaging the individual mean transects for each phase (Fig. 9). Through alongshore averaging most of the variability seen in the individual transects has been removed. The overall mean transect clearly shows the expected characteristics of a coastal upwelling regime. Both equatorward flow at the surface and poleward flow below 150m and within 20km of the coast are implied. The maximum temperature gradient and the pycnocline are located at a depth of about 70m, beyond 50km off the coast. Nearer the coast, the region of maximum gradient rises and intersects the surface approximately 15km offshore. This distance offshore corresponds approximately to the Rossby radius of deformation (APPENDIX A) and suggests that coastal upwelling per se may occur within one R_{bc} of the coast. However, subsequent observations in Chapter III. show that the offshore area apparently influenced by coastal upwelling usually extends much farther off the coast.

Individual temperature-salinity (T-S) diagrams have been constructed for each STD profile acquired during the study. Most individual T-S curves displayed considerable fine-scale variability. In addition, curves for stations near the shelf margin indicated significantly higher temperatures and salinities (following isentropic

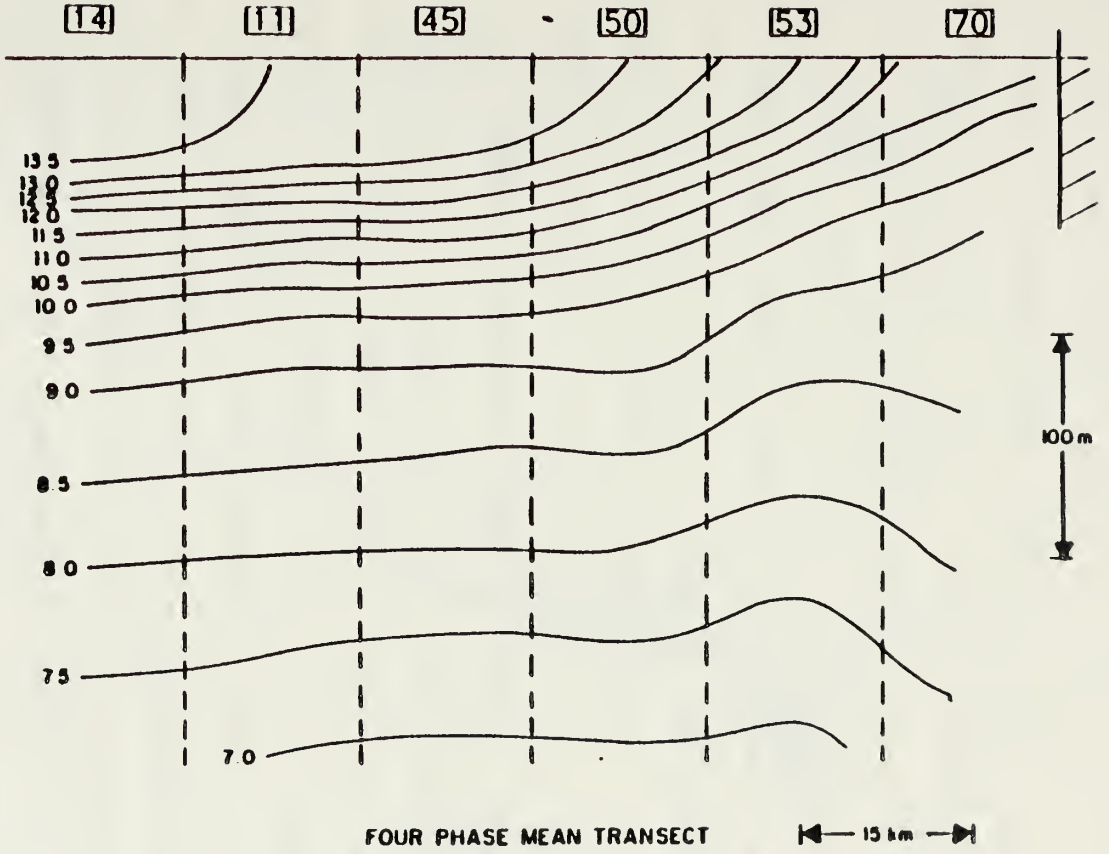

Figure 9. Mean vertical section for temperature averaged over all four phases. Data were initially averaged alongshore for each phase in corridors 15km wide (vertical dashed lines) before the four-phase mean was calculated. The total number of temperature profiles averaged along each corridor are enclosed by boxes at the top of the figure.

surfaces) than further off the coast. The higher values of temperature and salinity near the shelf margin indicate higher concentrations of Equatorial Water associated with the California Undercurrent (CU).

At two stations near the shelf margin, temperature and salinity, particularly between 100 and 200m, increased from 1A to 3A. Such an increase may be associated with an intensification of poleward flow in the CU. Intensification of the CU could result from the increase in upwelling favorable winds and wind stress curl which took place between 1A and 3A (Pedlosky, 1974).

In addition to higher T-S values near the shelf margin the profiles generally showed a larger-scale systematic trend in the offshore direction. To help clarify this trend, T-S profiles from Phase 1B (Phase 1B provided the highest density of STD profiles) were averaged alongshore over the same corridors used in constructing the mean transects. Through this averaging procedure, the average offshore trend becomes somewhat clearer (Fig. 10). In particular, salinity and temperature tend to decrease for a given density proceeding offshore at depths less than about 150m. At depths greater than 200m the mean T-S profiles converge to a common water mass. The T-S dependence shown in Fig. 10 is consistent with higher concentrations of Subartic Water further offshore, a

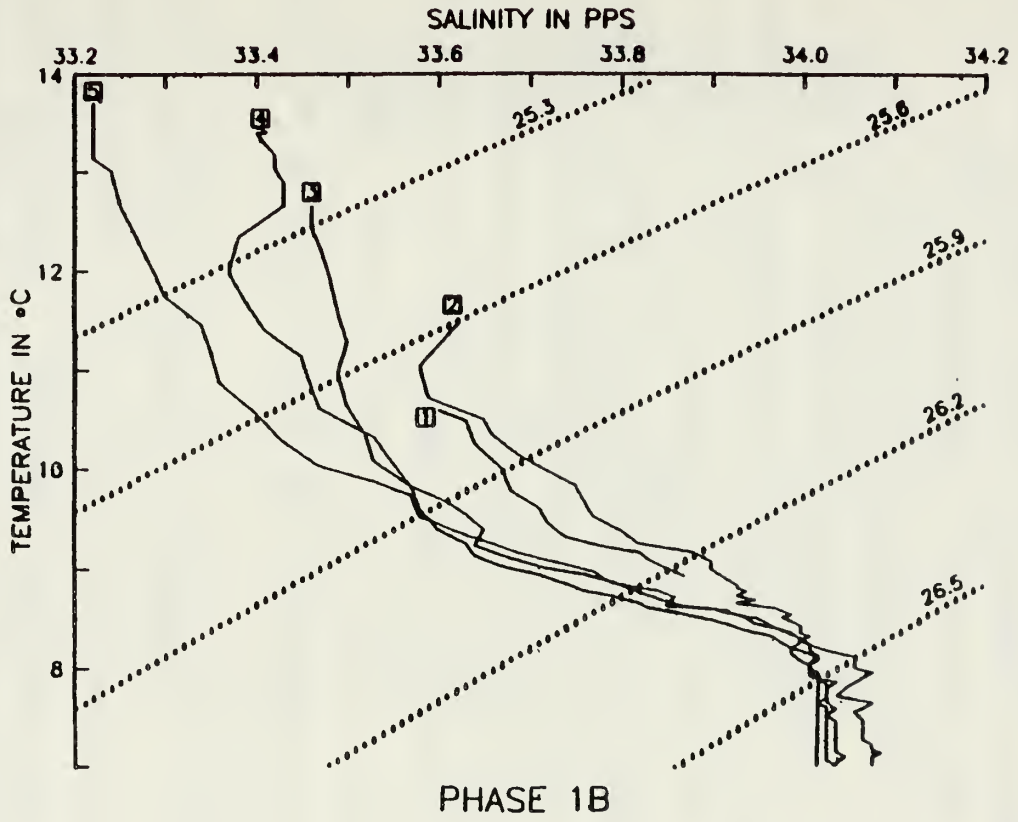

Figure 10. Mean temperature-salinity profiles averaged along corridors approximately parallel to the coast and 15km wide, for Phase 1B.

condition to be expected as the main body of the California Current is approached. To help quantify the influence of Subarctic and Equatorial waters on the T-S structure off Pt. Sur, two T-S profiles, one near the coast and the second near the offshore limit of the study area (Phase 3A - Line C) have been plotted on a diagram showing percentages of Equatorial Water, assuming that mixing takes place along surfaces of equal sigma-t (Fig. 11). Such an analysis, as pointed out by Tibby (1941), is only valid at depths roughly greater than 100m since vertical mixing related to the effects of wind and local changes due to absorption of solar radiation will invalidate the requirement that mixing take place along surfaces of equal sigma-t near the surface. At depths greater than 100-150m, both T-S profiles are seen to lie in the 50-60% Subarctic Water category. The mean T-S profiles from Fig. 10 generally lie in the same region but tend to slightly higher concentrations of Subarctic Water at shoaler depths (not shown).

To examine variations in property distributions between phases, tendencies (i.e., first differences) were taken for selected mappings. Tendency analysis is a commonly used tool in meteorology, where atmospheric fields are usually available at successive synoptic times (Duthie, 1968). Care must be taken in the interpretation of tendency analyses however. In constructing a tendency

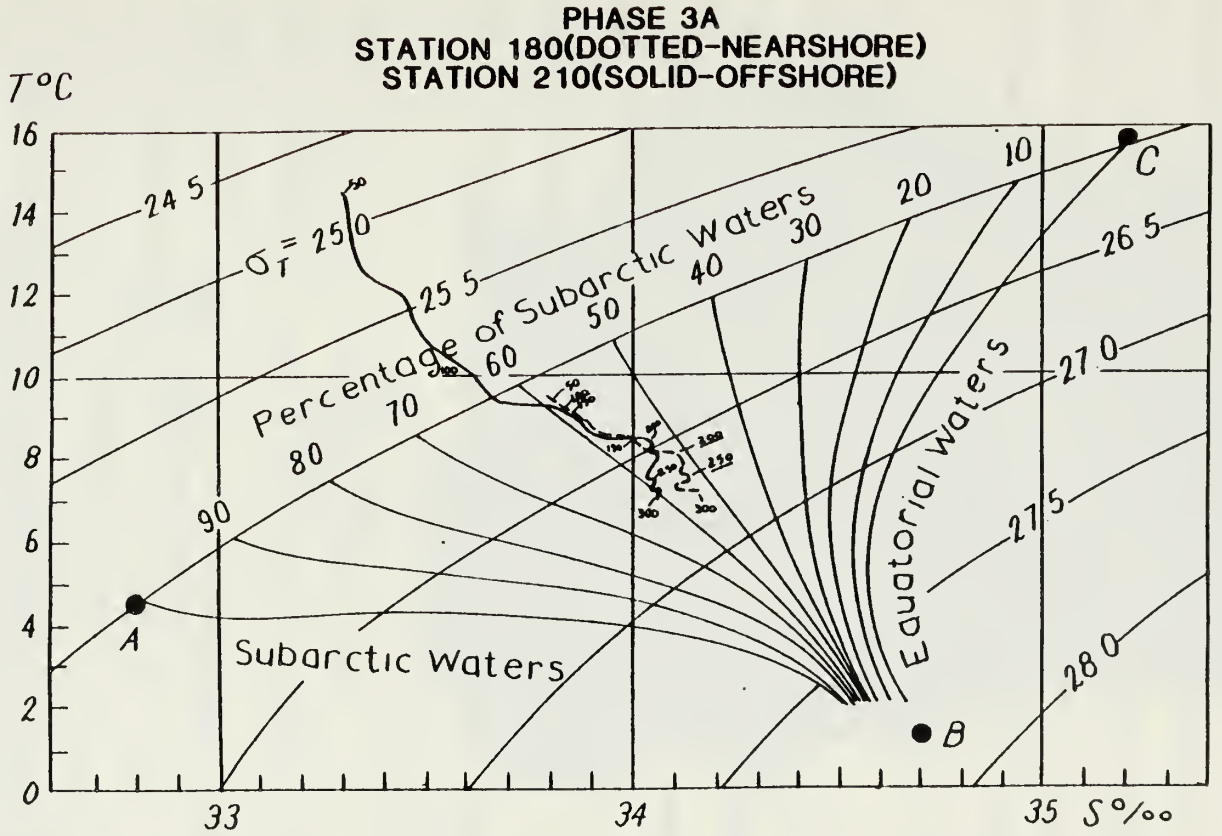

Figure 11. A water mass mixing diagram showing percentages of Subarctic and Equatorial waters. Two temperature-salinity profiles from Phase 3A, Leg C, are superimposed. The solid curve represents a station approximately 90km offshore and the dashed curve, a station approximately 10km offshore.

analysis it is implicitly assumed that the time interval between mappings is short enough that only unidirectional changes in properties have taken place. In oceanography this technique has been used to a much lesser extent. A notable exception is an analysis by Jones (1972), where tendencies were constructed in the vertical-offshore plane for hydrographic data acquired in the coastal upwelling region near Cap Blanc off NW Africa.

Based on SST tendencies between 1A and 1B (ca. 2 days), there was a warming trend over most of the area. The warming was apparent near Sur Canyon and particularly off Lopez Pt. Warming continued near Pt. Sur, but farther south there was strong cooling between 1B and 3A (ca. 12 days). The trend from 1B to 3A almost reversed between 3A and 3B (ca. 2 days), with cooling near Pt. Sur and warming by 3C or more near Lopez Pt.

Over the two-week period between 1A and 3A, there was a warming trend west of Pt. Sur, perhaps due to onshore displacement of the California Current or an eddy (Fig. 12). South of Pt. Sur (near Lopez Pt.), there was significant cooling (ca. 2.5C), due partially, as will be shown, to increased mixing. Noteworthy were the rapid two-day trend reversals off Pt. Sur between 3A and 3B, and south of Pt. Sur between 1A and 1B and between 3A and 3B. These results indicate that sampling intervals of two days

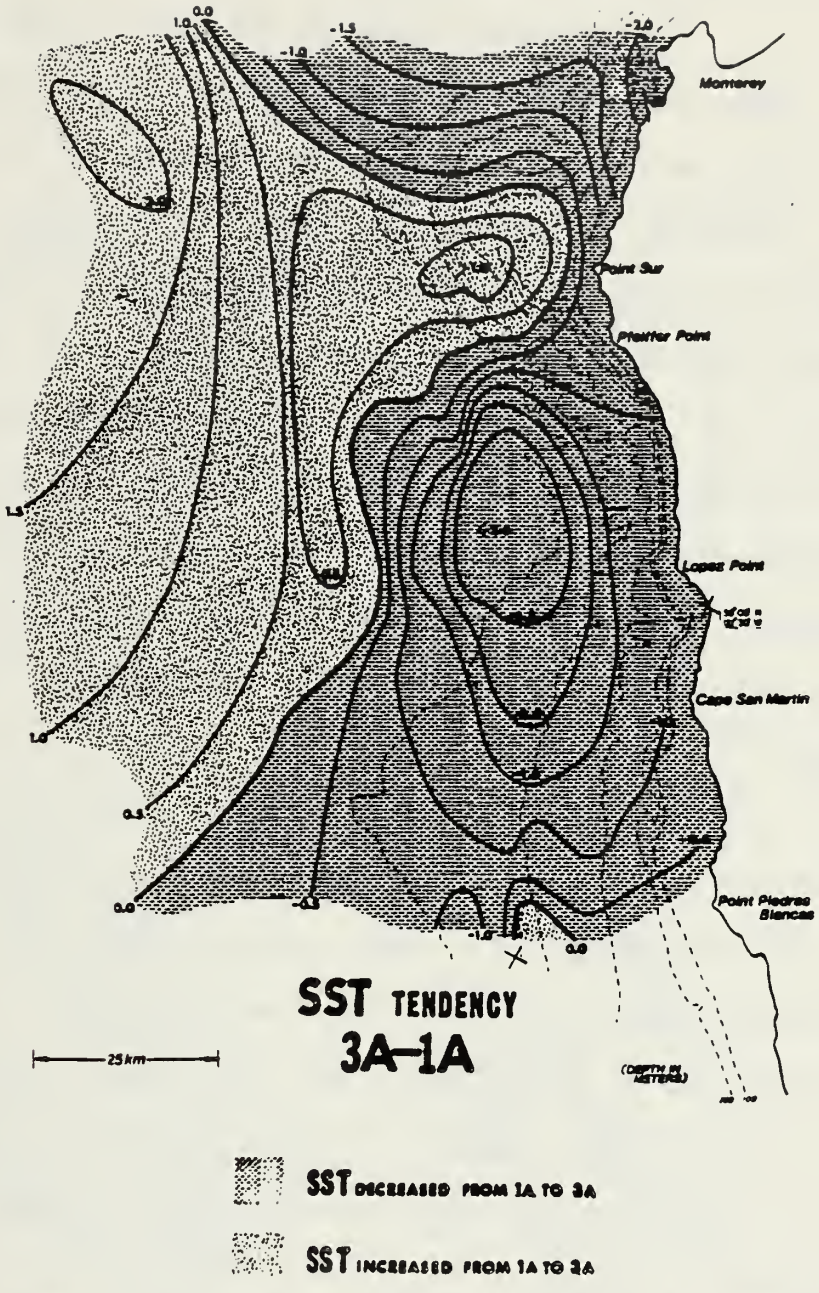

Figure 12. Map of sea-surface temperature tendency between Phases 1A and 3A. Random stippling indicates areas of increased SST; horizontal stippling indicates areas of decreased SST. The contour interval is 0.5C.

or less are required to estimate the high frequency variations in SST anomaly.

Tendencies between 1A and 3A for depths of 10, 50, 100, and 200m have also been constructed (Fig. 13). The 10m tendency is generally similar to the tendency at the surface. However at 50m the warming off Pt. Sur appears to be more local than advective in origin. South of Pt. Sur cooling now appears to be more advective than local. At 100m the tendency pattern changes again. At this level, warming is seen in the center of the area and cooling in the SW corner. At 200m some cooling is still observed toward the SW corner. The tendency patterns show the greatest change across the thermocline, between 50 and 100m.

The tendency in mixed layer depth (MLD) between 1A and 3A shows dramatic deepening in the area just south of Pt. Sur (Fig. 14). The area of maximum MLD deepening corresponds closely to the area where sea surface and 10m temperatures experience their maximum decrease (Figs. 12 and 13). Apparently the local decreases in temperature were caused by the entrainment of cold water from levels initially below the depth of the mixed layer. The question arises, however, as to why the area of MLD deepening was restricted to only part of the area. Two possible explanations arise. First, although such an effect is not indicated by the shipboard winds, the winds around Pt. Sur,

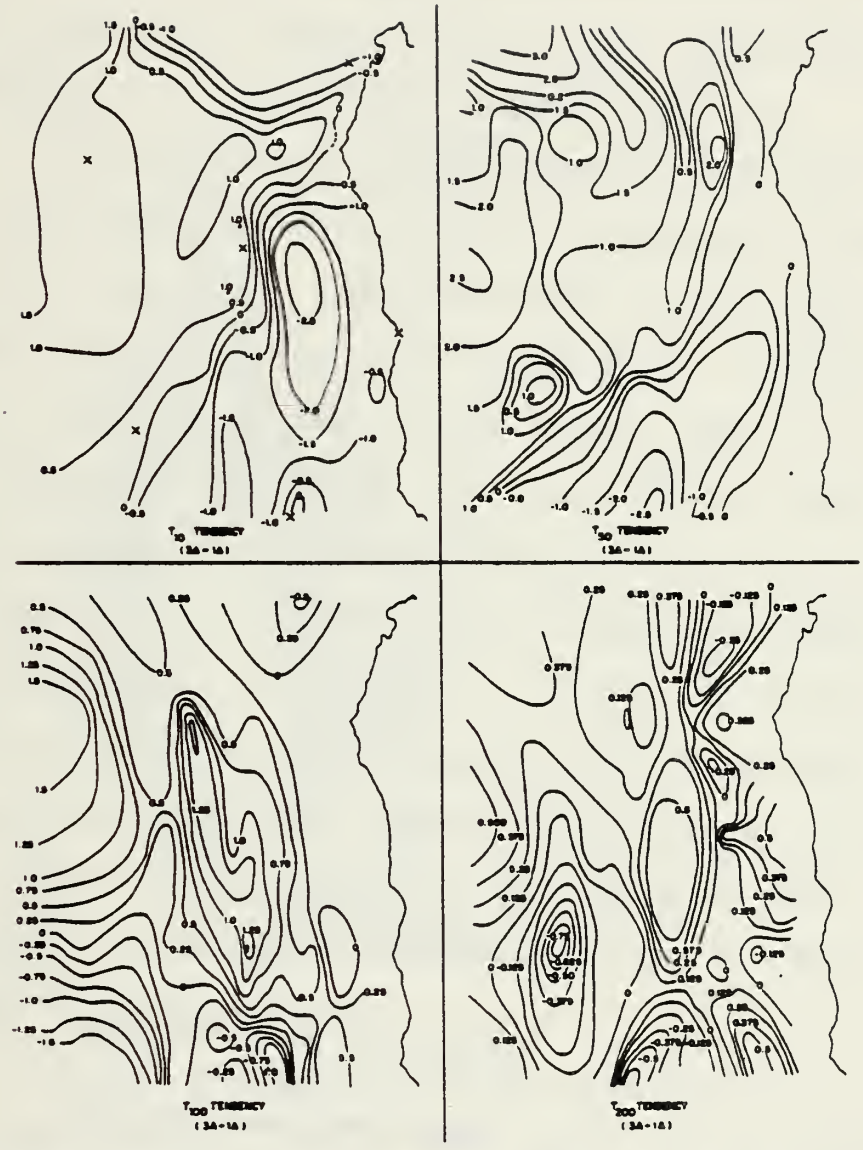

Figure 13. Maps of temperature tendency between Phases 1A and 3A at four depths. Upper left panel: 10m upper right panel: 50m, lower left panel: 100m, and lower right panel: 200m.

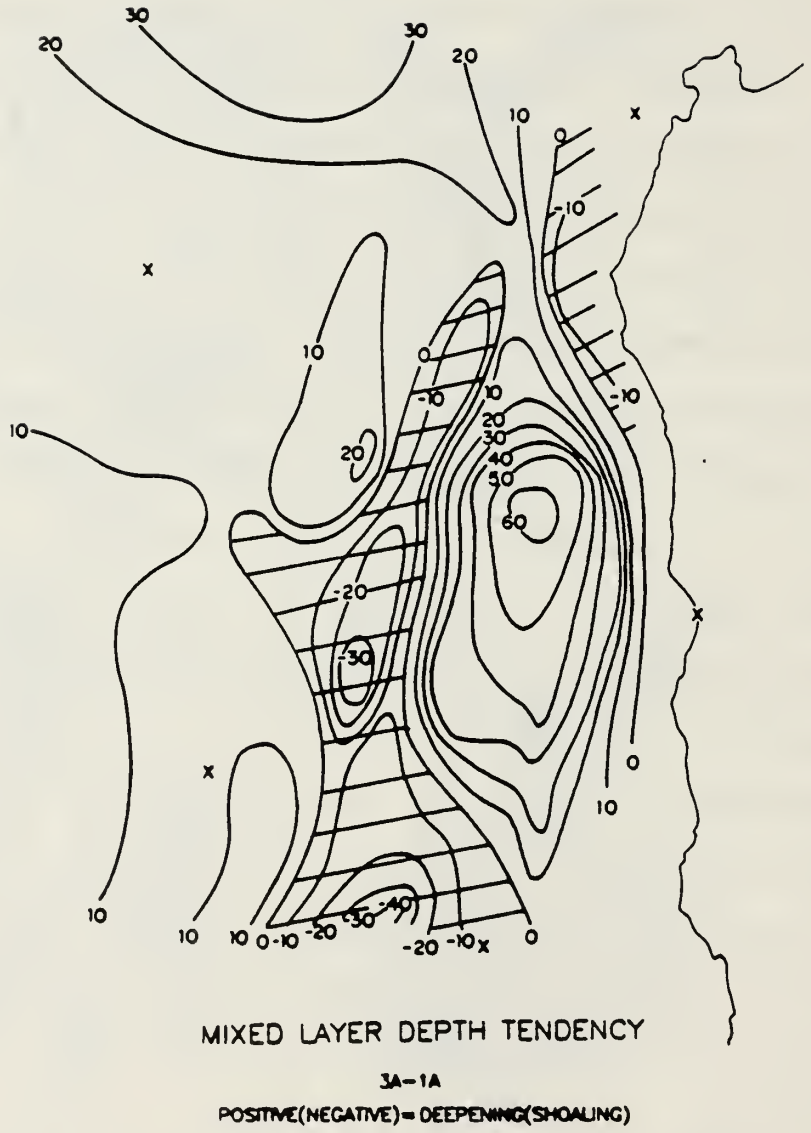

Figure 14. Map of mixed layer depth tendency between Phases 1A and 3A. Contours are in meters and cross-hatching represents shoaling areas.

and to the south, may be intensified due to local orographic effects. Secondly, because the stratification is generally weaker near the coast, less work is required by the wind to generate vertical mixing at deeper levels. Either, or both, of these effects could contribute to enhanced mixing in the area just south of Pt. Sur.

A mean transect tendency has been constructed from the individual mean transects for Phases 1A and 3A (i.e., 3A-1A) (Fig. 15). Cooling occurs in the upper 40m out to 40km offshore. However beyond 60km, significant warming took place from the surface down to 100m. Also an isolated region of warming is seen centered at a depth of 100m approximately 30 km offshore. This warming is similar in some respects to the warm anomaly frequently observed off the Oregon coast (Mooers et al., 1976). It is located at the base of the pycnocline, almost precisely where the warm anomaly off Oregon was located. The warm anomaly off Oregon is persistent during the upwelling season; the persistence of the localized subsurface warming observed here has yet to be established.

Because vertical property gradients are large below the mixed surface layer, this region is particularly sensitive to various types of internal and external forcing, including surface wind stress and coastal-trapped waves. Hence, it is of interest to examine the thermocline

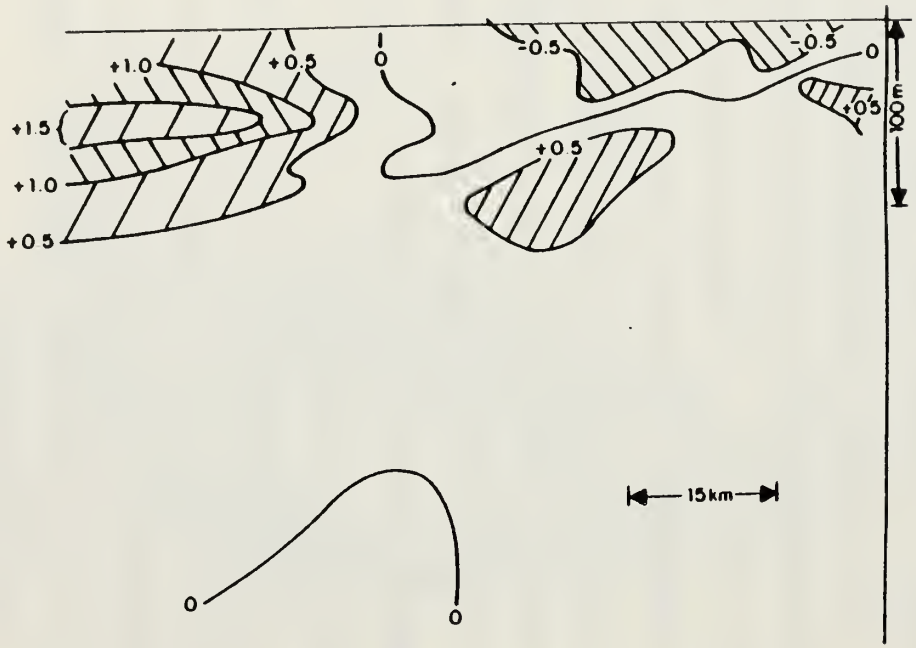

Figure 15. Tendency for mean vertical sections of temperature for Phases 1A and 3A. Cross-hatching represents areas of significant temperature change. Positive values indicate warming.

and its space-time variability during the period of the present study. Mean depth and thickness are used to characterize the thermocline. The mean thermocline depth is defined as the mean depth of the 9 and 11C isotherms (i.e., $(Z_9 + Z_{11})/2.0$). The mean depth of the thermocline (not shown) shoaled rapidly within the first 40km offshore (i.e., $O(1R_{bc})$)for each phase, consistent with active coastal upwelling and a nearsurface, equatorward jet. Between 1A and 3A (i.e., 3A-1A), there was a zone of negative mean thermocline depth tendency (ca. 20m) nearshore and a zone of positive tendency (ca. 40m) at a mean distance of order one baroclinic radius of deformation offshore (Fig. 16). The nearshore decrease in mean thermocline depth was probably due to increased upwelling. Based on the vertical displacement of the mean thermocline depth over the two weeks between 1A and 3A, maximum vertical velocities approached 3m/day. This velocity is compared with Yoshida's (1980) predicted vertical velocity, w, using a linear, two-layer, f-plane model,

$$w = \frac{\tau_w^{(y)}}{\sqrt{g h_1 \Delta\rho/\rho_2}} \sqrt{\frac{h_2}{h_1 + h_2}}$$

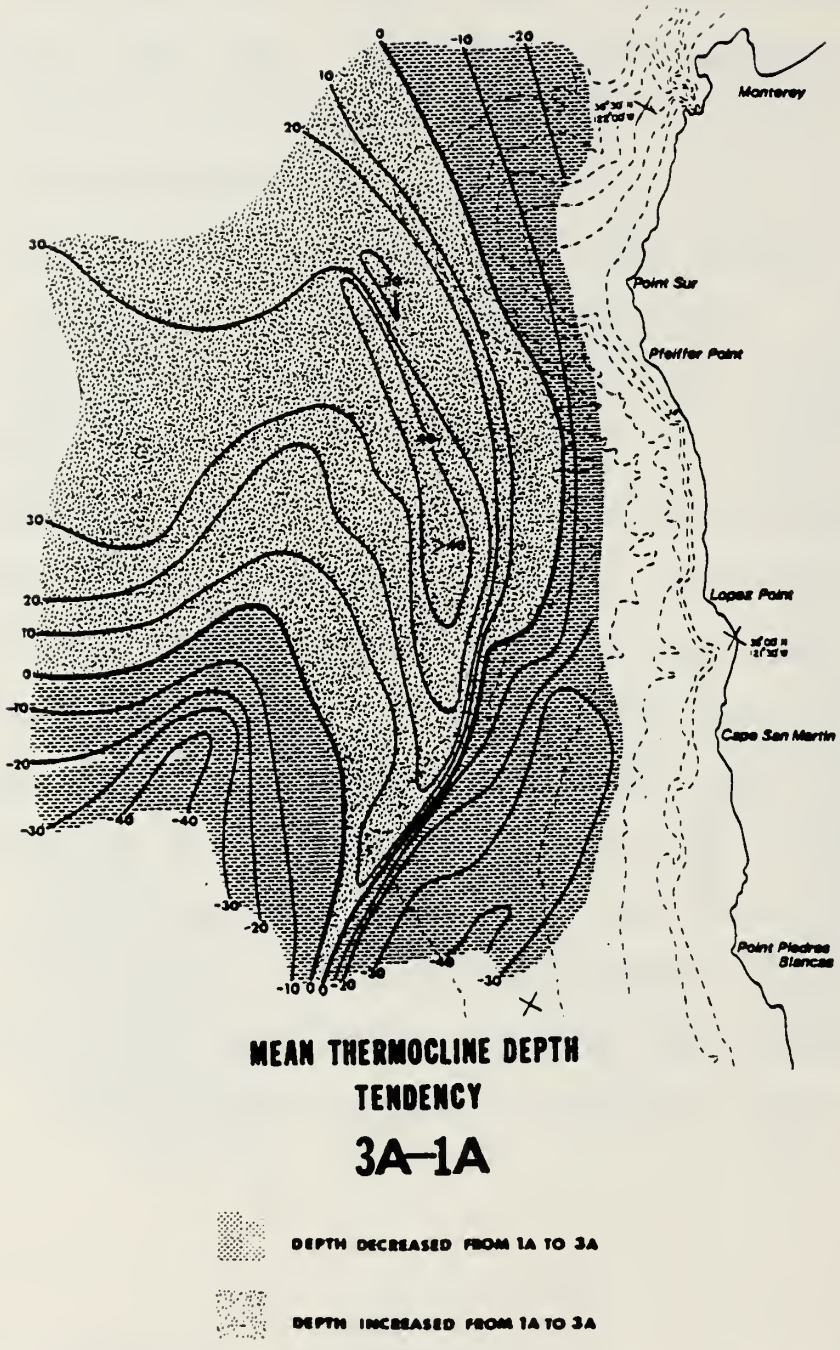

Figure 16. Map of mean thermocline depth (MTD) tendency between Phases 1A and 3A. Random stippling indicates areas of increased MTD; horizontal stippling indicates areas of decreased MTD. The contour interval is 10m.

where

$\tau_w^{(y)}$ = Alongshore component of the surface wind stress

$\Delta\rho$ = Density difference between upper (ρ_1) and lower (ρ_2) layers

g = Acceleration due to gravity

h_1 = Thickness of upper layer

h_2 = Thickness of lower layer

With $\tau_w^{(y)}$ = 1.Ø dyne/cm^2 and the other values taken from Mooers et al. (1983), w is predicted to be approximately 8.5m/day, a value slightly higher than that estimated from the change in thermocline depth.

The significant increase in mean thermocline depth farther offshore may be due in part to the accumulation of water which has been carried away from the coast through offshore Ekman transport. The mean thermocline depth (MTD) and 5Øm temperature ($T_{5Ø}$) tendencies are similar particularly on the coastal side of the zero contours that more-or-less parallel the coast. This result is not surprising since the $T_{5Ø}$ surface was usually contained within the thermocline. The integral effect of vertical averaging in the MTD tendency, relative to the $T_{5Ø}$ tendency, is indicated by the presence of less small-scale ($\sim$ 2Ø-25 km) structure in this analysis.

The thermocline thickness is defined as the difference in depth between the 9 and 11C isotherms. An increase in thermocline thickness implies an increase in cyclonic vorticity for flow within the thermocline. A thickness ridge extended onshore from the SSW in Phase 1A (Fig. 17). Beyond about 40km offshore, the thermocline thickness generally increased to the south for each phase. Also, there was a thickness maximum in a band parallel to the coast about 25 to 40 km offshore. The thickness field was organized on a scale approaching the size of the study area and had generally similar patterns for each phase. Between 1A and 3A, there was a major zone of positive thermocline thickness tendency centered near Sur Canyon (Fig. 18), suggesting locally intense upwelling or perhaps increased mixing (or both) in this area. This tendency is also consistent with enhanced alongshore flow in this region.

c. Geostrophy

Dynamic heights have been calculated from the temperature and salinity data acquired during this study for the surface relative to 50, 100, 200, and 300m. Geostrophic velocities have been calculated from the dynamic heights. Wide fluctuations in the geostrophic velocities were found near the coast where stations were often only a few kilometers apart and the location of the ship was not always precisely known.

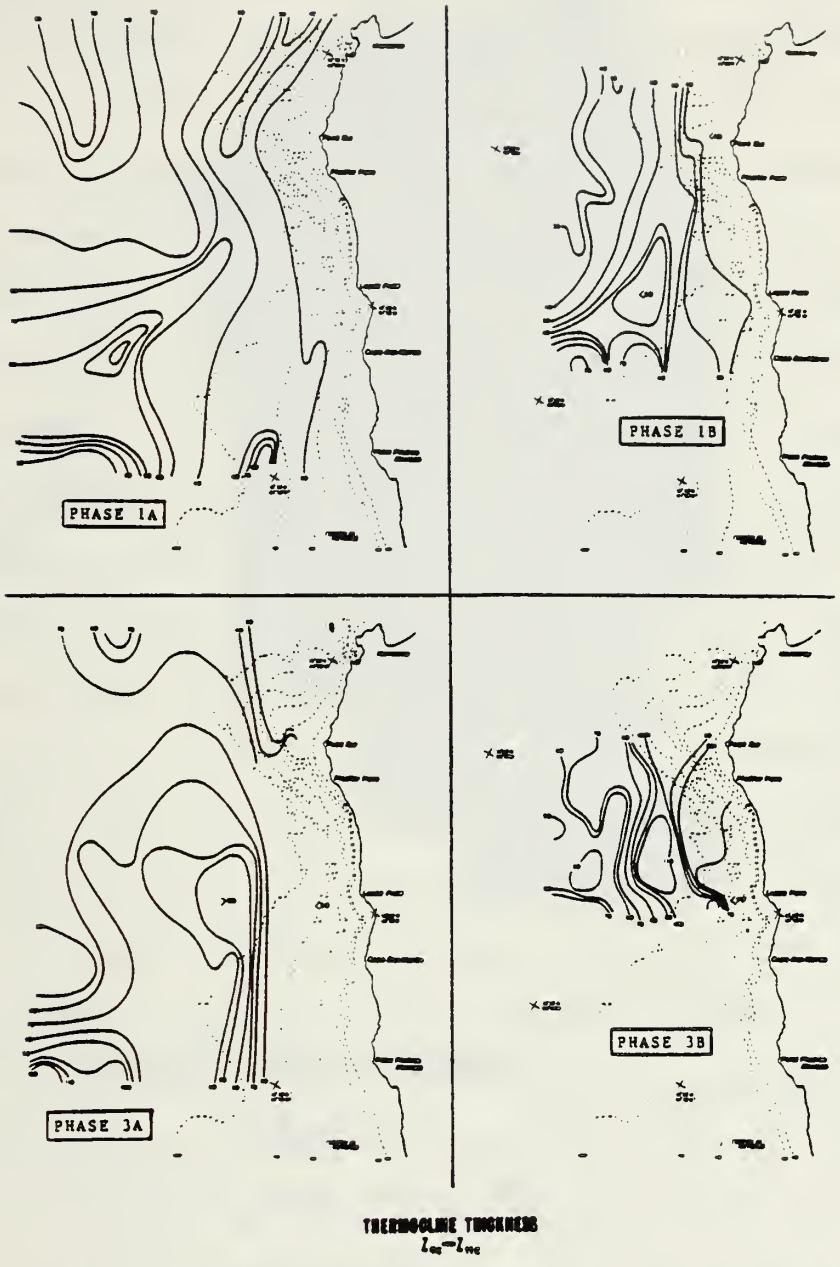

Figure 17. Maps of thermocline thickness (defined as the difference in depth between the 9 and 11C surfaces) for each phase. The contour interval is 10m.

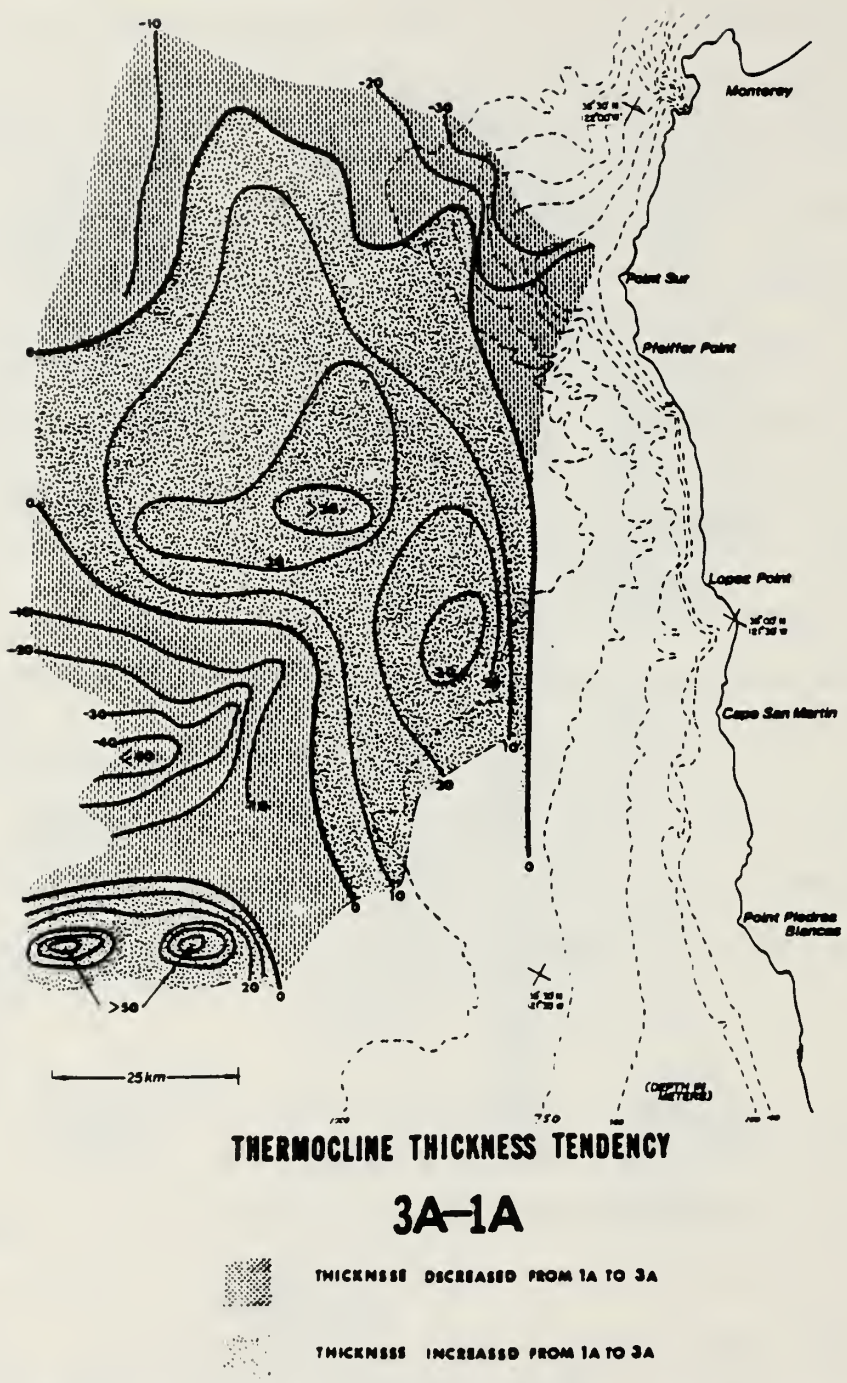

Figure 18. Map of thermocline thickness tendency between Phases 1A and 3A. Random stippling indicates areas of increased thickness; vertical stippling indicates areas of decreased thickness. The contour interval is 10m.

The dynamic height of the sea surface relative to 300m (0/300) for Phase 1A (Fig. 19) generally increased away from the coast, and, hence, the surface geostrophic flow relative to 300m was equatorward. The relatively high surface elevation in the SW corner was, again, suggestive of the presence of an anticyclonic eddy in this area. The 0/50m dynamic topography shown in Fig. 19 for Phase 1B clearly depicts the southward jet occurring within 10 to 15 km of the coast. The 0/100, 0/200, and 0/300 meter maps of dynamic height for this phase (not shown) indicated topographies similar to that for the 50m reference level. The coverage apparently did not extend far enough offshore during this phase to detect the anticyclonic eddy observed during the previous phase (or the eddy may have been displaced). The 0/200m dynamic topography for Phase 3A (Fig. 19) indicates that the equatorward jet intensified and moved slightly offshore over the two-week period between phases. At Cape San Martin for example, the 40 dyn. cm. height contour for the 0/200m topography moved seaward approximately 15 km between Phases 1B and 3A.

Finally, in the 0/300m topography for Phase 3B (Fig. 19) it is possible to observe greater detail in the alongshore flow because of the finer spatial sampling employed during this phase (5 vs. 10km sampling in the offshore direction and 7.5 vs. 30 km sampling alongshore),

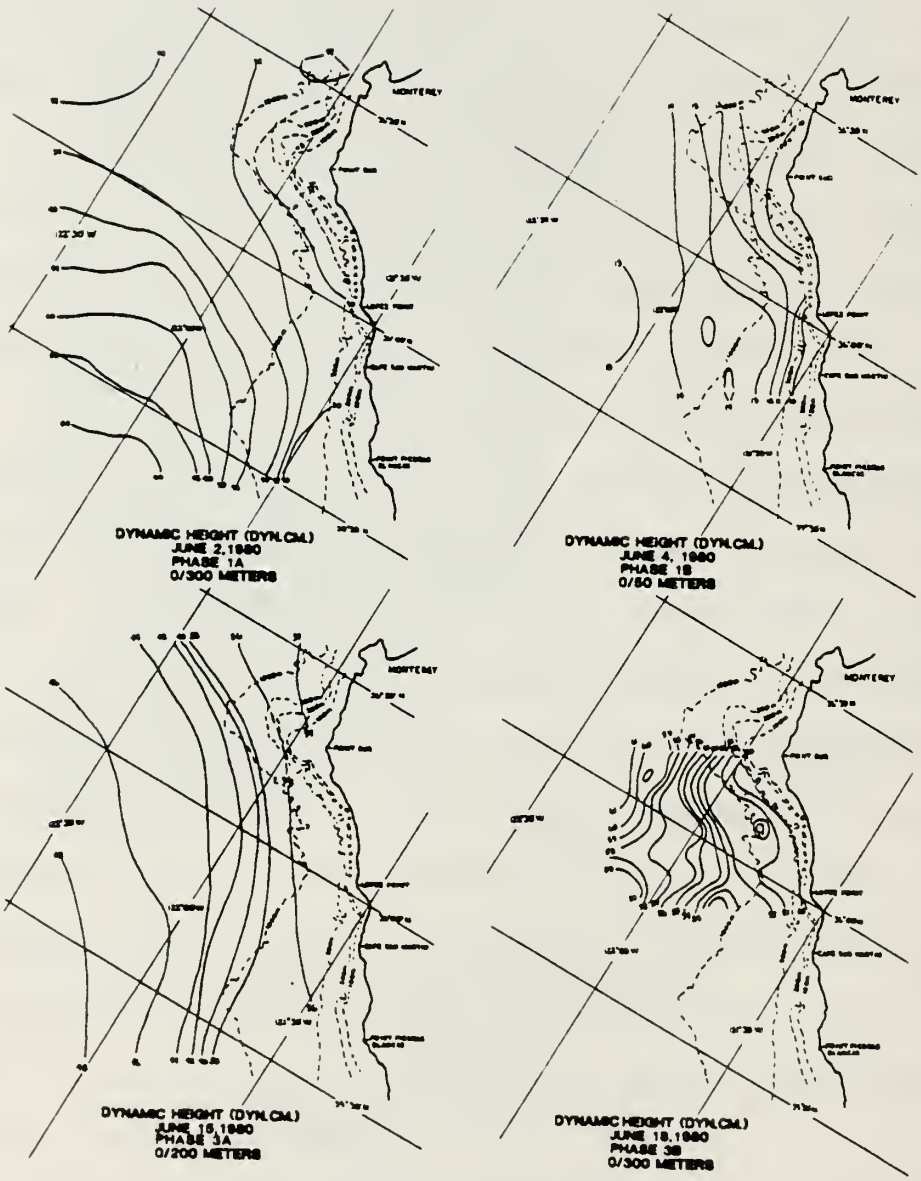

Figure 19. Maps of dynamic height in dynamic cm. for each phase. The different reference levels used in eah case are indicated.

plus the selection of a smaller contour interval (1 vs. 2.5 dyn. cm). A perturbation in the alongshore flow with an approximate wavelength of 40 km can be seen in the Phase 3B (0/300m) topography. Between 15 and 90 km off the coast, offshore profiles of dynamic height for Leg C (not shown) indicate that the mean elevation gradient (0/300m) increased by approximately 50% between phases 1A and 3A; thus if the gradient across this region were constant the geostrophic flow would be expected to increase by this amount.

Individual offshore profiles of dynamic height actually showed considerable variability from one section to the next. Slopes in some cases changed sign indicating reversals in flow direction. However some of this variability as mentioned is attributed to internal tides and navigational errors particularly for the inshore stations which were located sometimes less than 5 km apart.

Mean offshore geostrophic velocity profiles have been constructed for each phase by averaging individual profiles for each trackline over the alongshore domain (Fig. 20). Slight averaging in the offshore direction was also required since the station mid-points for each trackline were not perfectly aligned alongshore. Generally flow is equatorward with speeds of the order of 20cm/sec. The considerable variability in alongshore flow is apparent from the large standard deviations that are

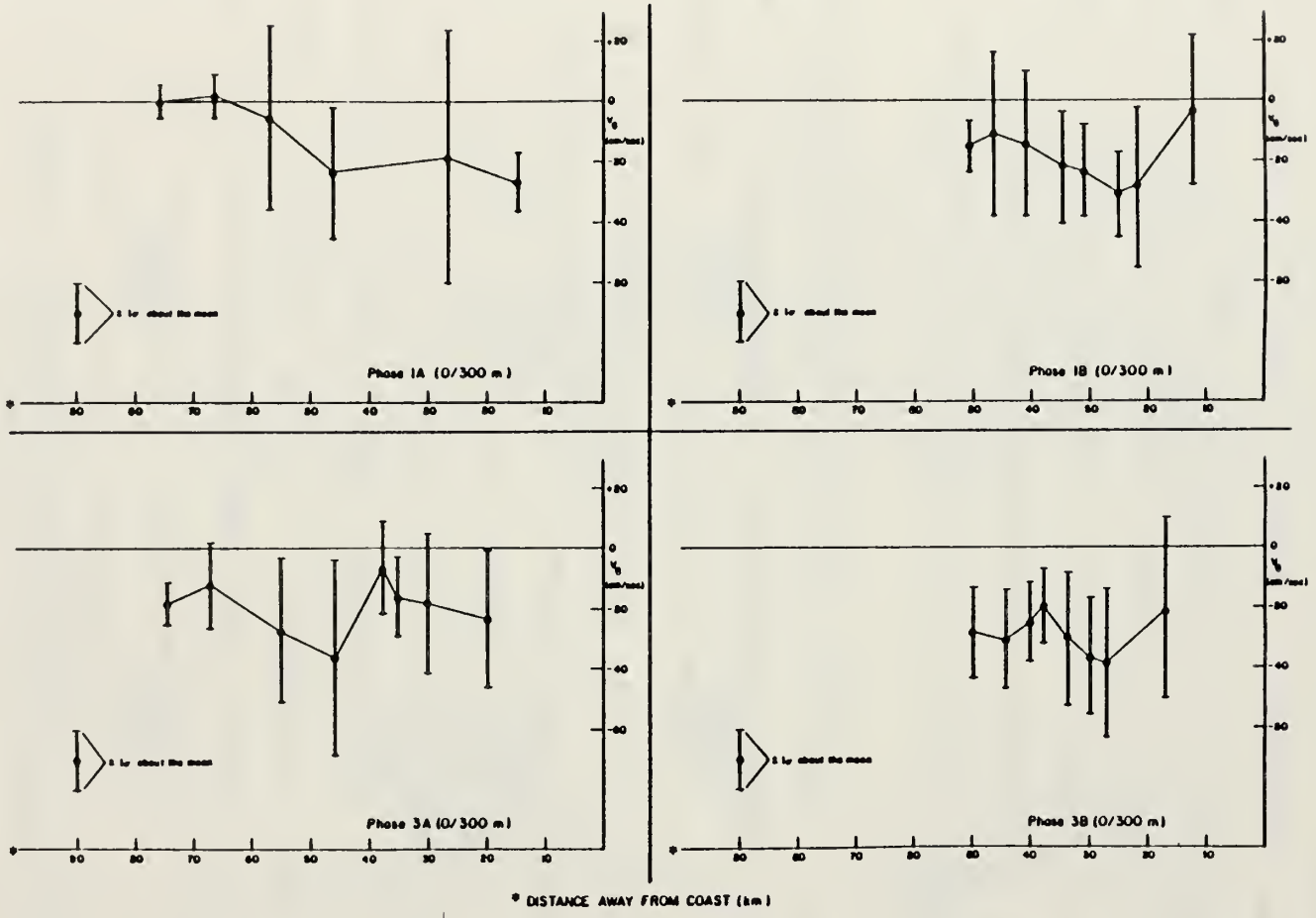

Figure 20. Mean offshore geostrophic velocity profiles in cm/sec for each phase for the surface relative to 300m. Individual profiles along each leg were averaged alongshore to obtain the mean profiles shown. Negative values indicate southward flow (assuming a negligible barotropic component). Horizontal bars indicate +1 standard deviation about the mean.

included for each point where the data were averaged; even occasional flow to the north is indicated. In addition to the spatial variability in alongshore flow, as indicated by these profiles, a slight tendency for increased flow to the south, accompanied by a slight offshore movement of the region of maximum flow can be seen during Phase 3. These trends may not be significant, however, in view of the relatively large standard deviations occurring at the offshore grid points.

Vertical sections of geostrophic velocity have been constructed with a vertical resolution of 25m for trackline C for each phase (Fig. 21). At least one equatorward jet can be identified in each case with maximum speeds approaching 50cm/sec (Phase 3A). However the offshore location of the jet maximum varies between 25 and 50 km offshore. The vertical extent of the jet varies between about 50 and 125m. Its width is of the order of 20km. Filaments of northward flow are also indicated occasionally, but whether or not the flow actually reverses direction will depend in part on the barotropic contribution. For each phase, northward flow is indicated near the coast at least for depths of 150m and greater. This component of the flow is interpreted to represent the California Undercurrent and corresponds approximately to the region associated with Equatorial Water previously

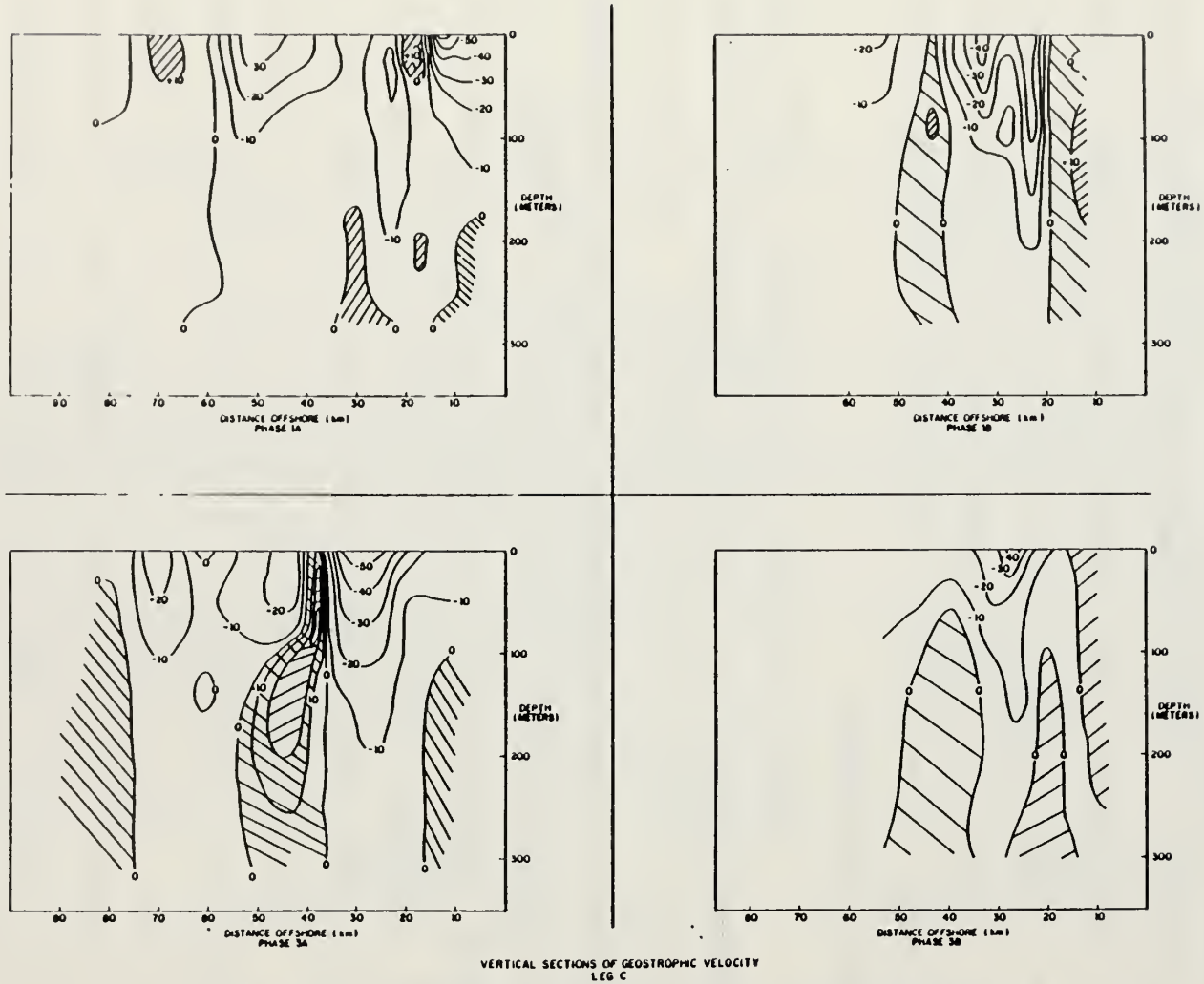

Figure 21. Vertical sections of geostrophic velocity (cm/sec) for Leg C of each phase. The vertical resolution is 25m, and areas of cross-hatching imply poleward geostrophic flow.

identified through T-S analysis. A similar section of geostrophic velocity at 36.3N, extending 50 km offshore for August 1972, showed a strong equatorward jet located approximately 30km offshore but with lesser horizontal extent (5 km) and greater vertical extent ($\sim$ 400m) (Wickham, 1975).

d. Frontal Analysis

During the spring and summer one of the primary characteristics of the coastal ocean along (central) California is the presence of cold, saline, dense upwelled water near the coast, and warmer, less saline, lighter water further offshore (Wooster and Reid, 1963). That these regions are usually separated by a major frontal boundary has been known for many years from direct observations of ocean color, turbidity, and marine life aboard ship. However the often convoluted patterns and general spatial complexity of this boundary region were not fully appreciated until the advent of IR remote sensing techniques from aircraft (Squires, 1971), and satellites (Stevenson and Miller, 1974; Bernstein et al., 1977). Since frontal regions are characterized by high property gradients, the variability associated with fronts is usually relatively easy to detect particularly in coastal upwelling areas where they frequently outcrop at the surface. Because of the relative importance of fronts in

coastal upwelling regions, a study of their occurrence and behavior is naturally motivated.

Fronts arise whenever two water masses with different physical properties come into immediate contact. Temperature and density fronts usually coincide in the atmosphere, but do not necessarily coincide in the ocean due to variations in salinity. If the gradients of temperature and salinity have the same sign in a frontal region then there may be little change in density. If the gradients of temperature and salinity are of opposite sign, then strong baroclinic flow may occur in the alongfront direction. Density fronts may become dynamically unstable due to the large shears associated with the alongfront flow and/or from a continual increase in the inclination of the pycnocline (Mooers et al., 1978).

A continuously recording surface thermalsalinograph was employed during the Pt. Sur study. The records from this instrument have been used to determine the location and intensity of frontal encounters during each phase. The thermalsalinograph sensor was located at a depth of approximately 2m below the surface and hence the values of temperature and salinity so obtained are taken to be representative of conditions in the mixed surface layer. Several problems arose during the analysis including (1) occasional data gaps, (2) the use of separate chart drives (with different speeds) for

temperature and salinity, (3) a lack of knowledge with regard to the angle- of-encounter between the ship and the frontal boundaries, and (4), the subjectivity involved in estimating the distances over which fronts persisted. Because of the data gaps, the overall coverage is fragmentary. With regard to the ship/front encounter angle, it has been assumed in each case that the ship crossed the front at right angles. Temperature was used initially to detect the presence of a front. Generally if the change in temperature (ΔT) was at least Ø.5C over a distance of approximately 1Økm or less, a frontal crossing was assumed.

The results of the frontal analysis are presented in Table 1. These results are presented again in the next chapter, in mapped form, where they are compared with the satellite data. Changes in temperature rarely exceeded 2C and frontal crossing distances were rarely less than 1km. Table 1 also shows that the larger gradients in density are usually associated with small values of ΔX rather than with large changes in property values. In other words, variations in frontal intensity appear to be associated primarily with changes in the width of the frontal zone. Cross-front scales were estimated by averaging the ΔX values presented in Table 1 for each phase.

Table 1

Frontal statistics for temperature, salinity, and density from the Pt. Sur upwelling center study

PHASE 1A

Location	Temperature Gradient					Salinity Gradient					Density Gradient[4]
	T_1	T_2	$\bar{T}$[3]	ΔX	$\Delta T/\Delta X$	S_1	S_2	$\bar{S}$[3]	ΔX	$\Delta S/\Delta X$	$\Delta\sigma_t/\Delta X$
36°15'N 122°42'W	12.75	11.51	12.13	2.4	0.52	DG[1]	DG	-	DG	-	-
36°12'N 122°45'W	11.96	12.62	12.29	4.0	-0.17	DG	DG	-	DG	-	-
36°12'N 122°39'W	DG[1]	DG	-	DG	-	33.78	33.59	33.69	7.7	0.25	-
36°11'N 122°07'W	12.81	10.45	11.63	15.0	-0.16	-	-	-	-	-	-
36°04'N 121°44'W	10.15	11.85	11.00	5.6	-0.31	33.80	33.65	33.72	5.6	-0.27	0.04
35°55'N 122°03'W	11.19	12.33	11.76	2.0	-0.58	DG	DG	-	DG	-	-
35°52'N 122°05'W	DG	DG	-	DG	-	33.90	33.75	33.82	1.4	0.11	-
35°40'N 122°20'W	DG	DG	-	DG	-	33.50	33.35	33.42	6.8	0.22	-
35°36'N 122°22'W	13.21	13.75	13.48	1.7	-0.32	DG	DG	-	DG	-	-
35°50'N 121°34'W	11.15	10.41	10.78	1.2	-0.63	33.75	34.12	33.94	1.2	0.31	0.35
35°37'N 121°20'W	9.80	11.40	10.60	11.0	-0.15	34.00	33.88	33.94	15.0	0.01	0.02
35°32'N 121°31'W	10.55	12.10	11.33	2.3	-0.67	33.96	33.72	33.84	3.3	0.07	0.14

Table 1 (Continued)

PHASE 1B

Location	Temperature Gradient					Salinity Gradient					Density Gradient[4]
	T_1	T_2	$\bar{T}$[3]	ΔX	$\Delta T/\Delta X$	S_1	S_2	$\bar{S}$[3]	ΔX	$\Delta S/\Delta X$	$\Delta\sigma_t/\Delta X$
35°37'N 122°01'W	13.73	12.99	13.36	1.7	-0.44	33.48	33.45	33.46	9.0	0.003	0.01
35°51'N 121°33'W	12.40	10.90	11.65	4.8	-0.31	33.50	33.95	33.72	6.0	0.08	0.11
35°59'N 121°34'W	9.70	11.80	10.75	1.3	-1.60	OS[5]	OS	-	OS	-	-
35°51'N 121°50'W	12.75	14.30	13.53	0.5	3.50	33.53	33.69	33.61	3.0	0.05	-0.06
36°06'N 121°40'W	12.80	10.76	11.78	2.2	0.93	33.68	33.30	33.49	7.5	0.05	0.01
36°08'N 121°37'W	11.00	9.55	10.28	6.7	-0.22	33.63	33.71	33.67	7.3	0.01	0.09
36°13'N 121°48'W	9.75	10.55	10.15	0.4	-2.00	OS	OS	-	OS	-	-
36°08'N 121°55'W	12.80	14.20	13.50	5.0	-0.28	DG	DG	-	DG	-	-
36°21'N 122°05'W	12.70	11.00	11.85	8.9	0.19	33.53	33.92	33.73	9.0	0.04	0.07
NA[2]	DG	DG	-	DG	-	33.23	33.52	33.38	5.0	0.06	-

Table 1 (Continued)

PHASE 3A

Location	Temperature Gradient					Salinity Gradient					Density Gradient[4]
	T_1	T_2	$\bar{T}^3$	ΔX	$\Delta T/\Delta X$	S_1	S_2	$\bar{S}^3$	ΔX	$\Delta S/\Delta X$	$\Delta\sigma_t/\Delta X$
36°33'N 122°00'W	9.16	11.10	10.13	OS	-	34.07	34.04	34.06	OS	-	-
36°31'N 122°07'W	11.00	11.88	11.44	1.2	-0.73	DG	DG	-	DG	-	-
36°22'N 122°19'W	11.36	10.61	10.98	3.3	0.23	33.85	34.00	33.92	4.5	0.03	0.06
36°20'N 122°22'W	10.39	11.41	10.90	5.7	-0.18	33.93	33.97	33.95	4.0	0.01	0.03
36°10'N 122°41'W	13.70	13.32	13.51	1.0	0.38	33.40	33.45	33.42	1.0	0.05	0.15
36°13'N 122°06'W	12.86	12.28	12.57	4.3	-0.14	33.57	33.59	33.58	4.3	0.005	0.03
36°1 'N 122°02'W	11.71	11.05	11.38	2.0	-0.33	33.66	33.83	33.75	2.7	0.06	0.13
36°08'N 121°37'W	9.49	10.35	9.92	1.86	-0.47	DG	DG	-	DG	-	-
36°07'N 121°36'W	10.06	11.07	10.56	OS	-	34.07	34.05	34.06	OS	-	-
36°05'N 121°40'W	10.71	9.02	9.86	1.6	1.05	DG	DG	-	DG	-	-
36°01'N 121°49'W	9.65	10.19	9.92	1.2	-0.46	DG	DG	-	DG	-	-
35°58'N 121°54'W	10.23	11.58	10.91	1.6	-0.83	DG	DG	-	DG	-	-
35°56'N 122°00'W	11.84	12.79	12.31	0.5	-1.83	DG	DG	-	DG	-	-
35°51'N 122°10'W	13.19	14.10	13.64	1.0	-0.91	DG	DG	-	DG	-	-
35°41'N 121°51'W	13.50	11.97	12.74	1.4	-1.11	33.55	33.60	33.57	1.4	0.08	0.22

Table 1 (Continued)

PHASE 3A (Continued)

Location	Temperature Gradient					Salinity Gradient					Density Gradient[4]
	T_1	T_2	$\bar{T}^3$	ΔX	$\Delta T/\Delta X$	S_1	S_2	$\bar{S}^3$	ΔX	$\Delta S/\Delta X$	$\Delta\sigma_t/\Delta X$
35°43'N 121°49'W	12.00	11.28	11.64	1.6	-0.46	DG	DG	-	DG	-	-
35°53'N 121°28'W	11.03	9.80	10.42	0.4	-3.08	DG	DG	-	DG	-	-
35°34'N 121°28'W	9.95	10.9	10.43	1.6	-0.59	DG	DG	-	DG	-	-
35°30'N 121°36'W	12.05	11.25	11.65	1.4	0.58	DG	DG	-	DG	-	-
35°27'N 121°41'W	13.00	10.90	11.95	5.2	-0.40	33.86	33.55	33.70	8.4	0.04	0.08
35°20'N 121°53'W	12.90	14.15	13.53	4.8	-0.26	33.56	33.52	33.54	8.5	0.05	-0.03

Table 1 (Continued)

PHASE 3[8]

Location	Temperature Gradient					Salinity Gradient					Density Gradient[4]
	T_1	T_2	$\bar{T}^3$	ΔX	$\Delta T/\Delta X$	S_1	S_2	$\bar{S}^3$	ΔX	$\Delta S/\Delta X$	$\Delta\sigma_t/\Delta X$
35°44'N 122°02'W	14.10	11.90	13.00	4.	-0.47	DG	DG	-	DG	-	-
35°51'N 121°51'W	12.23	10.96	7.59	5.4	-0.23	DG	DG	-	DG	-	-
35°57'N 121°38'W	11.45	10.31	.88	2.3	-0.49	DG	DG	-	DG	-	-
35°57'N 121°47'W	11.60	10.70	11.15	2.2	0.41	DG	DG	-	DG	-	-
35°56'N 121°50'W	10.70	11.70	11.20	3.2	-0.31	33.75	33.80	33.77	1.6	0.03	0.09
33°55'N 121°53'W	11.65	12.80	12.23	4.3	-0.27	33.80	33.59	33.70	6.5	0.03	0.06
35°47'N 122°47'W	12.80	14.00	13.	2.2	-0.56	33.56	33.28	33.57	2.2	0.01	0.10
35°50'N 122°08'W	13.80	12.96	13.38	0.7	-1.20	DG	DG	-	DG	-	-
36°17'N 121°39'W	11.45	10.00	12.73	2.3	-0.63	DG	DG	-	DG	-	-
36°08'N 121°45'W	9.92	11.09	10.51	1.4	-0.14	DG	DG	-	DG	-	-
36°52'N 121°59'W	11.50	12.90	12.20	5.2	-0.27	32.81	33.53	33.67	3.9	0.07	0.09
36°03'N 122°06'W	13.56	11.79	12.	5.6	-0.34	DG	DG	-	DG	-	-
36°06'N 122°02'W	11.65	10.40	7.	6.5	-0.20	DG	DG	-	DG	-	-

Table 1 (Continued)

PHASE 3B (Continued)

Location	Temperature Gradient					Salinity Gradient					Density Gradient[4]
	T_1	T_2	$\bar{T}$[3]	ΔX	$\Delta T/\Delta X$	S_1	S_2	$\bar{S}$[3]	ΔX	$\Delta S/\Delta X$	$\Delta\sigma_t/\Delta X$
36°07'N 121°53'W	10.49	9.32	9.71	7.1	-0.16	DG	DG	-	DG	-	-
36°08'N 122°05'W	9.74	12.10	12.90	1.3	-1.89	33.91	33.68	33.79	4.1	0.06	0.15
36°0 'N 122°13'W	11.98	13.20	2.	5.4	1.22	33.69	33.50	33.59	5.3	0.04	-0.07
36°07'N 122°15'W	13.79	12.28	13.04	9.2	-1.51	33.42	33.31	33.36	4.2	0.03	0.02
36°14'N 122°03'W	11.50	10.60	11.05	4.2	-0.90	DG	DG	-	DG	-	-

[1] DG = Data Gap

[2] NA = Not available

[3] $\bar{T}(\bar{S})$ represents median temperature (salinity)

[4] $\Delta\sigma_t/\Delta X$ calculated using the larger value of ΔX from the temperature and salinity gradients where they were different

[5] OS = On Station

These scales ranged from about 2 to 5 km for temperature, and from about 4 to 7 km for salinity.

From the table there is no obvious time dependence associated with the estimated frontal intensities. This is somewhat unexpected since the previous property maps indicated gross changes in the location and intensity of the surface baroclinic zone, particularly between Phases 1A and 3A. Because of the higher salinities and lower temperatures found near the coast it was expected that the fronts would not generally be density compensated. In approximately two-thirds of the cases the fronts were not density compensated. It is assumed that these cases include, at least in a few instances, the major frontal boundary that essentially separates the zone of coastal upwelling from oceanic waters, this region is not easy to identify from the gradients alone. Identification of this boundary requires a separate examination of the magnitudes of $\triangle T$ and/or $\triangle S$. It may be reasonable to expect $\triangle T$'s of at least 2C and S's of Ø.3 ‰ or greater across the major boundaries, based on the previous hydrographic data and on the values given in Table 1. The offshore position of the major frontal boundary is also expected to more-or-less coincide with the location where the shoaling pycnocline intersects the surface (Fig. 9).

As indicated above, changes in salinity usually occurred over greater distances than the corresponding changes in temperature for the density-enhanced fronts. In a few cases temperature and salinity both increased approaching the coast, contrary to the general pattern of increasing density in this direction. One obvious explanation for these apparent anomalies provided by the satellite imagery is that they arise from frontal meanders which have doubled back on themselves. Table 1 also reveals that the fronts generally lie between temperatures of 1Ø and 13.5C, and so are usually contained within the zone of upwelled water. That the fronts are generally weak and are found between certain temperatures results partly from the solar radiation available over the period taken by a freshly upwelled parcel of water near the coast to be transported offshore and into the frontal zone. For example, upwelled water off the coast of NW Africa (Cape Bojador) increased in temperature by Ø.25C per day for a MLD of 2Øm (Bowden, 1977). Using this value, an offshore speed of 1Øcm/sec, and an offshore frontal distance of 35km, water initially upwelled at the coast would increase in temperature by approximately 1C by the time it reached the front. Satellite data presented in Chapter III also indicate that much of the frontal activity identified through the thermalsalinograph data was confined to the region inside the major upwelling boundary.

D. SUMMARY OF RESULTS FROM THE PT. SUR UPWELLING CENTER STUDY

Surface winds during the Pt. Sur upwelling center study were continuously upwelling favorable. Winds increased significantly however between Phases 1 and 3. Wind stress curl, calculated from the shipboard winds, was usually positive out to 50 km and sometimes out to 70 km offshore. Because of the possible importance of positive wind stress curl with respect to upwelling away from the coastal boundary, a brief calculation of expected curl-forced upwelling is made. A value for wind stress curl taken from the shipboard winds observed during Phase 3A, is used (Fig. 4). The associated vertical velocity can be approximated as

$$w \simeq \frac{1}{\rho f} \{ \mathrm{Curl}_z \ \tau \}$$

and for a meridional wind component only,

$$w \simeq (\rho f)^{-1} \frac{\partial \tau_w^{(y)}}{\partial x}$$

where $\rho = 1.025$ gm/cm^3, $f = 8.57 \times 10^{-5}$ sec^{-1}, and $\frac{\partial \tau_w^{(y)}}{\partial x} = 1.5$ dynes/cm^2/70km. A value of 2.1m/day for w is obtained, or about 25% of the value estimated previously for coastal upwelling. Shipboard winds also revealed diurnal variations which did not appear to be sea-breeze related. These variations in the alongshore winds could, for example, be related to diurnal variations in the height of the marine

inversion and/or to nocturnal radiation from the marine boundary layer. It is also noted that synoptic-scale winds at Pt. Sur suggested a wind event time scale of approximately 8 days during the period of the Pt. Sur study.

Spatial distributions of temperature, salinity, and sigma-t indicate that coastal upwelling was active during the period of the study. During Phase 1A, SST's were 3C lower, sea-surface salinities Ø.3‰ higher, and density, Ø.6 sigma-t units higher within the first 25 km of the coast. Locally intense upwelling was suggested by cold water extending south of Pt. Sur towards Sur Canyon. An anticyclonic eddy was tentatively identified in the SW corner of the area near the Davidson Seamount through surface and subsurface property distributions. An IR satellite image from May 3Øth also showed that SST was clearly highest in the SW corner of the study area, although it was not possible to uniquely identify an eddy in this region. The anticyclonic eddy near Davidson Seamount could not be identified during the subsequent phases. Between Phases 1A and 3A (2 weeks), the surface baroclinic zone parallel to the coast, moved about 15 km further offshore and intensified. SSTs nearest the coast also decreased by about 1C. These changes reflect the intensified winds.

Individual offshore transects of temperature, salinity, and density showed considerable variability. Alongshore averaging of these transects reduced the variability significantly. The overall mean vertical transect clearly indicates the expected characteristics of a coastal upwelling regime.

A mean transect tendency between 1A and 3A showed near-surface cooling within the first 40 km offshore, and significant warming beyond 60 km. The tendency analysis also revealed an isolated pocket of warming at the base of the pycnocline, reminiscent of the warm anomaly frequently observed off the Oregon coast during the summer.

T-S diagrams, for stations within approximately 20km of the coast, indicate slightly higher temperatures and salinities at depths greater than 100m, consistent with the presence of poleward flowing Equatorial Water in this region. T-S profiles averaged alongshore indicate slightly higher concentrations of Subarctic Water moving toward the main body of the California Current.

Tendency analysis of surface and subsurface property maps often showed major changes over time periods as short as two days. Coherent spatial patterns generally resulted from the various tendency analyses suggesting scales ranging from 10, or a few 10's, of km, to scales approaching the size of the study area itself. Local decreases in SST south of Pt. Sur were spatially concurrent

with mixed layer deepening between 1A and 3A; thus mixing was apparently an important response mechanism to the intensified winds in at least one area.

The mean depth of the thermocline (MTD) decreased between 1A and 3A within about 20 km of the coast, which is consistent with active coastal upwelling. Offshore, the MTD increased, consistent with an accumulation of upwelled water carried offshore through Ekman transport. The mean transect tendency indicated that these offshore waters had increased in temperature, consistent with surface-heated water being transported offshore. A tendency toward onshore-offshore mass compensation was suggested by these results.

Maps of thermocline thickness generally show maxima in a band 25-40 km offshore paralleling the coast. The thermocline thickness tendency between 1A and 3A showed an increase in thickness, centered over Sur Canyon. Johnson (1980) found consistent increases in the thickness of the upper thermocline in the area of Sur Canyon from XBT data where upwelling features had been independently identified through satellite data. An increase in thickness of the thermocline implies an increase in cyclonic vorticity. Other factors also favor cyclonic development in the nearshore region. These factors include the development of positive shear on the coastal side of the surface jet, plus

the advection of water off the shelf, or slope, into areas where the bottom depth has increased significantly. These factors may be important in determining the subsequent circulation patterns that can be observed in satellite coverage of this area.

Geostrophic velocities computed from dynamic heights generally indicate predominant equatorward flow at the surface on the order of 20 cm/sec over most of the offshore domain. Large variations in geostrophic velocity were found, however, and surface flow over limited regions may actually be poleward upon occasion. Poleward flow was usually indicated at subsurface levels within 15 km of the coast; this flow corresponds to the region of higher temperatures and salinities identified previously and is associated with the California Undercurrent. High-resolution vertical sections of geostrophic velocity also showed marked variability, both spatially and temporally. Narrow, jet-like flows to the south with core speeds of up to 50 cm/sec are indicated. These jets can apparently change their position by as much as 10-20 km in just two days. They are usually 20 km or less in width and extend vertically to depths of 100 to 200m. Based on similar jet-like patterns, Wickham (1975) estimated that transverse mixing scales were of the order of 10-20 km, values in good agreement with those that can be inferred from the calculated vertical patterns presented here.

In most of the property maps, and in the derived distributions as well, the overriding influence of the bathymetry is unmistakable. The influence of local bathymetry is even more clearly revealed in the satellite data and will be considered in more detail in the next chapter.

Frontal intensities were estimated from thermalsalinograph data acquired during the Pt. Sur study. Temperature gradients rarely exceeded 3C per 10 km. Because of the major differences in property distributions observed between phases, it was somewhat surprising that frontal intensities did not show any obvious time dependence. However, the surface winds generally increased during the three-week period of the study, and according to Curtin (1979), surface fronts in the Oregon upwelling region are consistently weaker during periods of spin-up than during periods of spin-down. Increasing winds may lead to Ekman divergence in the mixed surface layer, a condition that certainly should not favor frontal intensification. In the majority of cases examined the fronts encountered during this study were density-enhanced. This result was expected since temperature generally increases and salinity decreases in moving offshore. Therefore, vigorous alongfront baroclinic flows are likewise to be expected. Cross-front scales were estimated

for each phase by averaging values of ΔX used in calculating the property gradients. These scales ranged from about 2 to 5km for temperature and from about 4 to 7km for salinity.

III. ANALYSIS OF THE SATELLITE DATA

A. INTRODUCTION

High-resolution IR satellite data have been acquired for the Central California coast region over a 15 month period starting in May of 1980. Coverage of the Pt. Sur upwelling center and the surrounding region from May to September of 1980 and from April to September of 1981 has been emphasized. The former period overlaps the period of the Pt. Sur upwelling center study.

Before the satellite data were used to examine the spatial and temporal variability of the SST field, it was compared with the *in situ* data in several cases where the satellite data and the shipboard data were acquired almost concurrently. The satellite data have been used mainly to establish the location, orientation, and shape of selected thermal boundaries, because quantitative SSTs have not been available from the images. Because of the large gradients in SST across the major boundaries separating the upwelling zone from oceanic waters further offshore, the frontal region is relatively easy to identify and monitor through a sequence of satellite images. The importance of this frontal region in upwelling areas was discussed earlier. The space-time variability of this frontal boundary is

examined together with the correlation between this boundary and the underlying bathymetry.

Three sequences of images between May and September from 1980 and 1981 are examined qualitatively to obtain preliminary estimates of space-time variability, first over the time period of the Pt. Sur upwelling center study, and second, over a period of several months, to study changes on seasonal time scales.

From dynamical considerations, a relationship between the position of the major upwelling frontal boundary and the local winds is expected, if local wind forcing is a major factor that contributes to the observed upwelling around Pt. Sur. As a result the surface area associated with the zone of active upwelling has been estimated from a sequence of satellite images for a selected period and then compared with integrated alongshore wind stress over the same period. These images are also used to obtain estimates of the offshore position of the major upwelling frontal boundary for comparison with offshore scales derived by Philander and Yoon (1983).

The satellite imagery were acquired by the Advanced Very High Resolution Radiometer (AVHRR) aboard the TIROS-N, NOAA-6, and NOAA-7 polar-orbiting satellites. The data used in producing these images were received and processed at the NESDIS Satellite Field Services Station in Redwood City, CA. The 8-bit data have a corresponding thermal

resolution of Ø.45C at 29ØK. The nominal spatial resolution of the AVHRR is 1.1km at the satellite subpoint. At angles off nadir, the cross-track spatial resolution decreases to values of several km or more due to the obliqueness of the viewing angle between the spacecraft and the surface of the earth. The images have been digitally enhanced using look-up tables that are approximately linear in temperature. However, the photographic contrast between adjacent gray-shades in the processed imagery is not constant from black to white, the greatest contrast occurring in the mid-range of photographic densities (i.e., the grays). Also the degree of enhancement is maintained at a low enough level so that each 1-step change in gray-shade corresponds to a least count change in temperature (i.e., Ø.45C). The images have a distance scale which is approximately constant over the area covered by a single frame since a geometric correction for earth curvature has been applied (Legeckis and Pritchard, 1977). However, the lesser geometric distortion due to earth rotation has not been taken into acount. Because of the earth's rotation and the time required to acquire enough data to produce a complete image (2ØØØ scanlines in 5.5 minutes), individual scanlines are systematically displaced either to the east or to the west depending on the direction in which the spacecraft is travelling.

As a rule, the major upwelling frontal boundary has been taken to coincide with the location where the gradient in SST is a maximum in the satellite imagery. In some cases visual pattern recognition, although subjective, helped in estimating the location of this boundary. Atmospheric moisture and gradients in atmospheric moisture may at least partially invalidate such a direct interpretation of the imagery. It is well-established that even uniform distributions of moisture in the atmosphere will reduce the magnitude of SST gradients observed at IR wavelengths (Maul and Sidran, 1974; Maul et al., 1980; Rouse, 1982). However, non-uniform moisture distributions, depending on their relative contribution to the observed satellite radiance field, could completely confound the actual location of the surface gradients of interest. However, at mid-latitudes along the Central California coast, atmospheric moisture levels are not expected to be high enough to invalidate a direct interpretation of the SST gradient locations (Hagan, 1983; Breaker et al., 1984). Previous surface-truth data off Pt. Sur also support this argument (Hanson, 1980; Silva, 1981). An inherent uncertainty in feature location also results from the quantization process that takes place aboard the spacecraft. For an SST gradient of 1C/km, for example, this uncertainty will be approximately 0.5km.

Another potential problem in the interpretation of satellite-derived temperature fields is that such an interpretation applies only to a surface layer of the order of 5 x 10^{-4}m in thickness. The thinness of this emitting surface layer is due to the very high absorption of IR radiation by water. Because heat flow near the ocean surface is normally upwards, the actual surface or "skin" temperature is usually several tenths of a degree (C) to one degree cooler than water only a few mm below the surface. A number of processes affect the temperature structure of this boundary layer, including turbulence due to wind mixing, wave breaking, and current shear (Katsaros, 1980). The limitations of IR satellite temperature fields will not be overlooked during the interpretations.

To earth locate the thermal boundaries identified in the satellite imagery, an optical device called a Zoom Transfer Scope (Bosch and Lomb trademark) has been used. This device employs a half-silvered mirror permiting the user to overlay an image and a base map in the same field-of-view. Once easily identified landmarks are properly aligned, it is a simple matter to earth locate the features of interest from the original image. Obviously the closer the feature is to a given reference, the greater the accuracy obtained in locating the feature. The accuracy of this technique can be readily estimated in the vicinity of islands.

B. COMPARISON OF THE SATELLITE AND *IN SITU* DATA

A comparison of selected satellite and shipboard data was considered necessary to establish the validity of the satellite data for subsequent use in locating thermal boundaries and in interpreting the space-time variability of the area. Because of persistent cloud cover during most of Phases 1 and 3, it was not possible to obtain concurrent satellite and shipboard coverage of the study area under cloud-free conditions. However, two images just prior to Phase 1 (May 29 to May 30, 1980), and seven images just following Phase 1 (June 4th to June 9th), were available and have been used as a basis for comparison with previous maps of SST. In particular, the major frontal boundary has been estimated using the nine satellite images bracketting Phase 1 by calculating a mean front location over the sequence.[4] The mean position for this boundary was estimated from the SST maps by locating the region where the SST gradient was a maximum (the range of SSTs associated with the maximum gradient in SST fell between about 11.0 and 12.5C). Maximum gradients in SST were initially estimated separately for Phases 1A and 1B; then a single boundary location was estimated by taking the median value for both phases (Fig. 22). The two boundaries diverge just north of Lopez Point. This discrepancy may be related to the difficulty in choosing the region of maximum

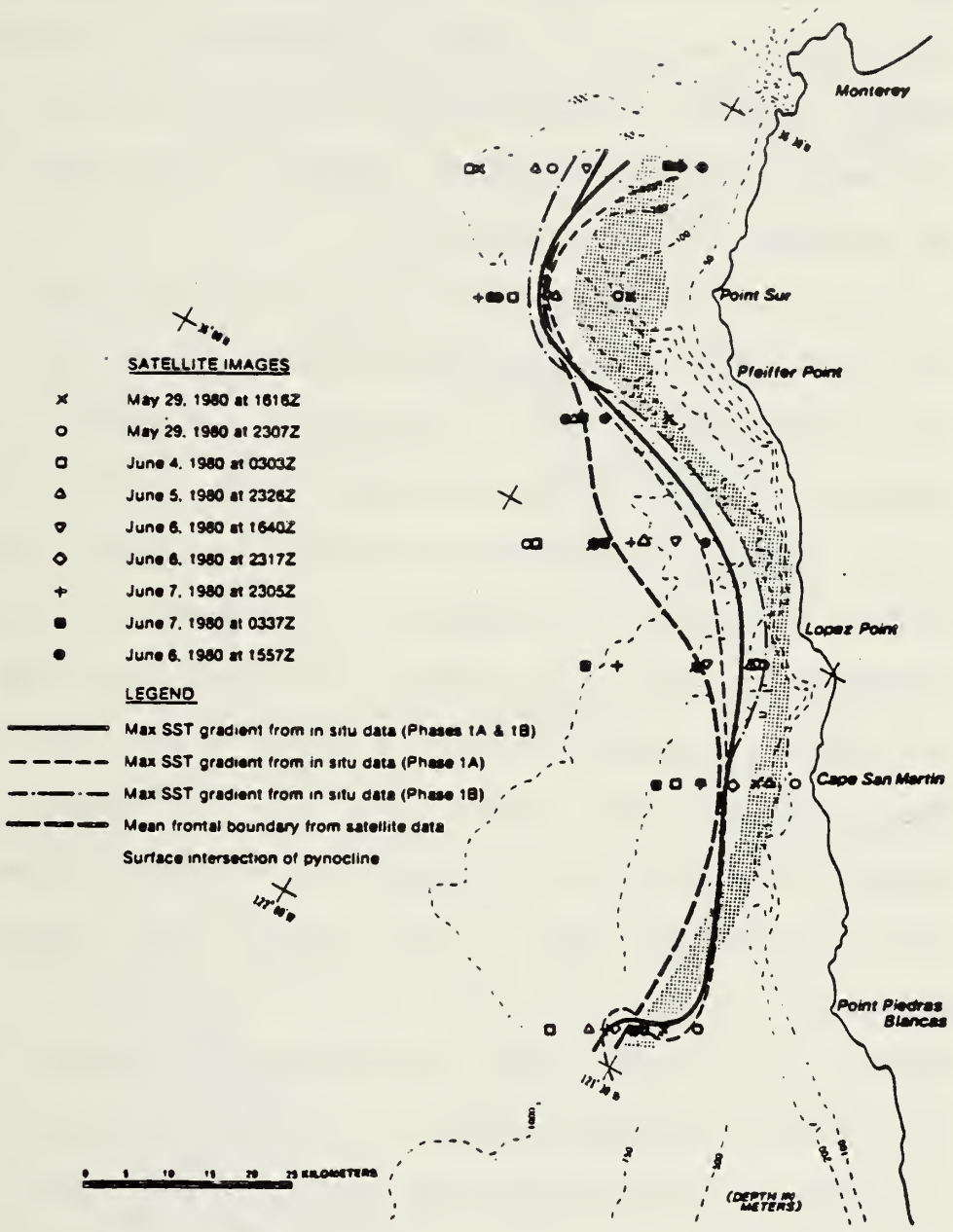

Figure 22. Location of the mean upwelling frontal boundary fom IR satellite imagery and from the in situ temperature data, for Phases 1A and 1B. Symbols associated with the satellite data represent the position of the frontal boundary taken from individual images. The solid line corresponds to the mean boundary position from the in situ data for both phases. The dotted region corresponds to the estimated region where the pycnocline broke the surface along each track leg.

gradient south of Pt. Sur during Phase 1A. The location of the satellite-derived mean frontal boundary lies essentially seaward of the mean position of the maximum gradient boundary derived from the STD/XBT data. The mean difference in their offshore location is about 4km; overall the agreement is considered good.

Next, frontal boundary locations taken from selected satellite images are compared with frontal SST and sea-surface salinity (SSS) boundaries extracted from the shipboard (2m) thermalsalinograph (T/S) records (Figs. 23, 24, and 25). For these comparisons an image acquired on June 6, 1980 is first compared with the T/S frontal data for Phase 1B (Fig. 23); second, an image acquired on June 14, 1980 is compared with T/S frontal data for Phase 3A (Fig. 24). In the first case the difference in time between the satellite coverage and the median phase time is approximately 40 hours; in the second case, approximately 50 hours (in this case the satellite image was received before the field data were acquired). The locus of maximum SST gradient estimated from the respective satellite images is superimposed on maps that show the mean locations and cross-frontal distances for selected temperature and/or salinity fronts previously identified in the T/S records (Figs. 23 and 24). Because the data from the T/S are not complete along each trackline, the lack of corresponding T/S frontal information at certain trackline/satellite

Figure 23. A comparison of frontal boundary locations obtained from an AVHRR IR satellite image acquired on June 6, 1980 and temperature/salinity frontal crossings obtained from the thermalsalinograph (T/S) data acquired during Phase 1B. Frontal crossings from the T/S data are labeled with the observed temperatures and salinities at the beginning and end of each encounter, along with the distance over which the front persisted.

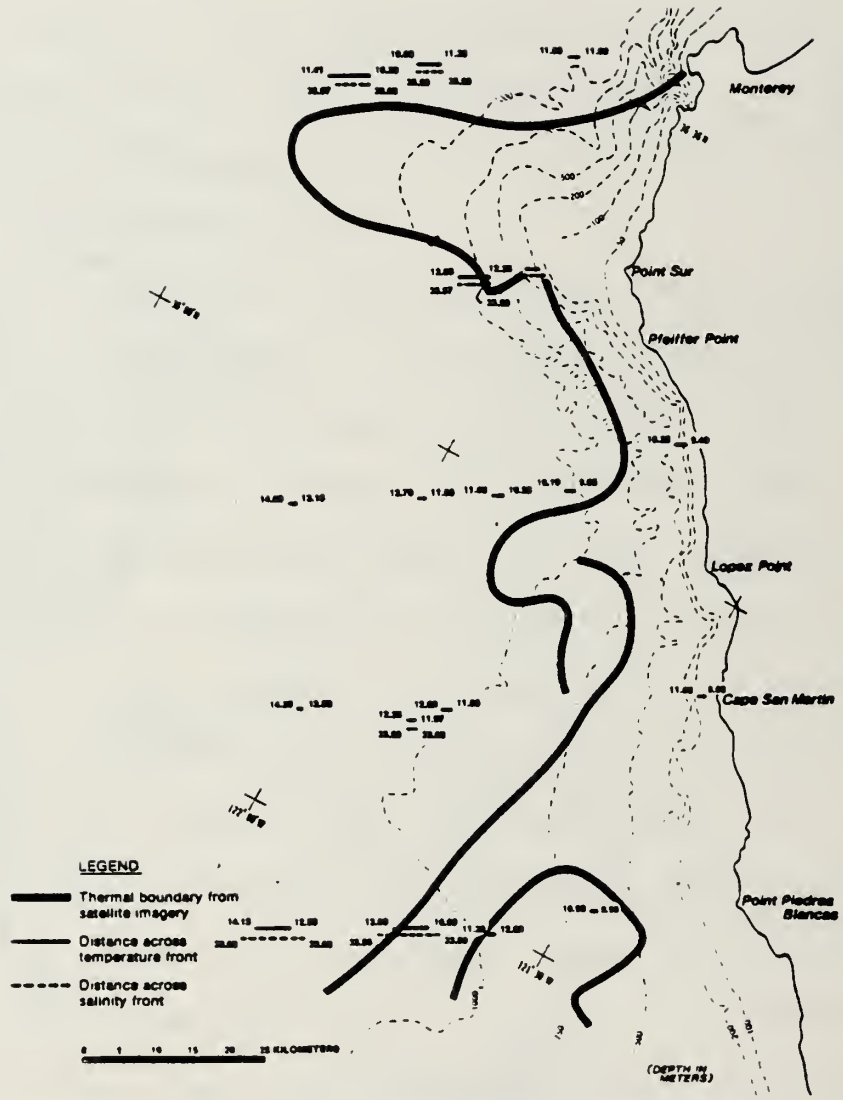

Figure 24. A comparison of frontal boundary locations obtained from an AVHRR IR satellite image acquired on June 14, 1980, and T/S frontal crossings obtained during Phase 3A.

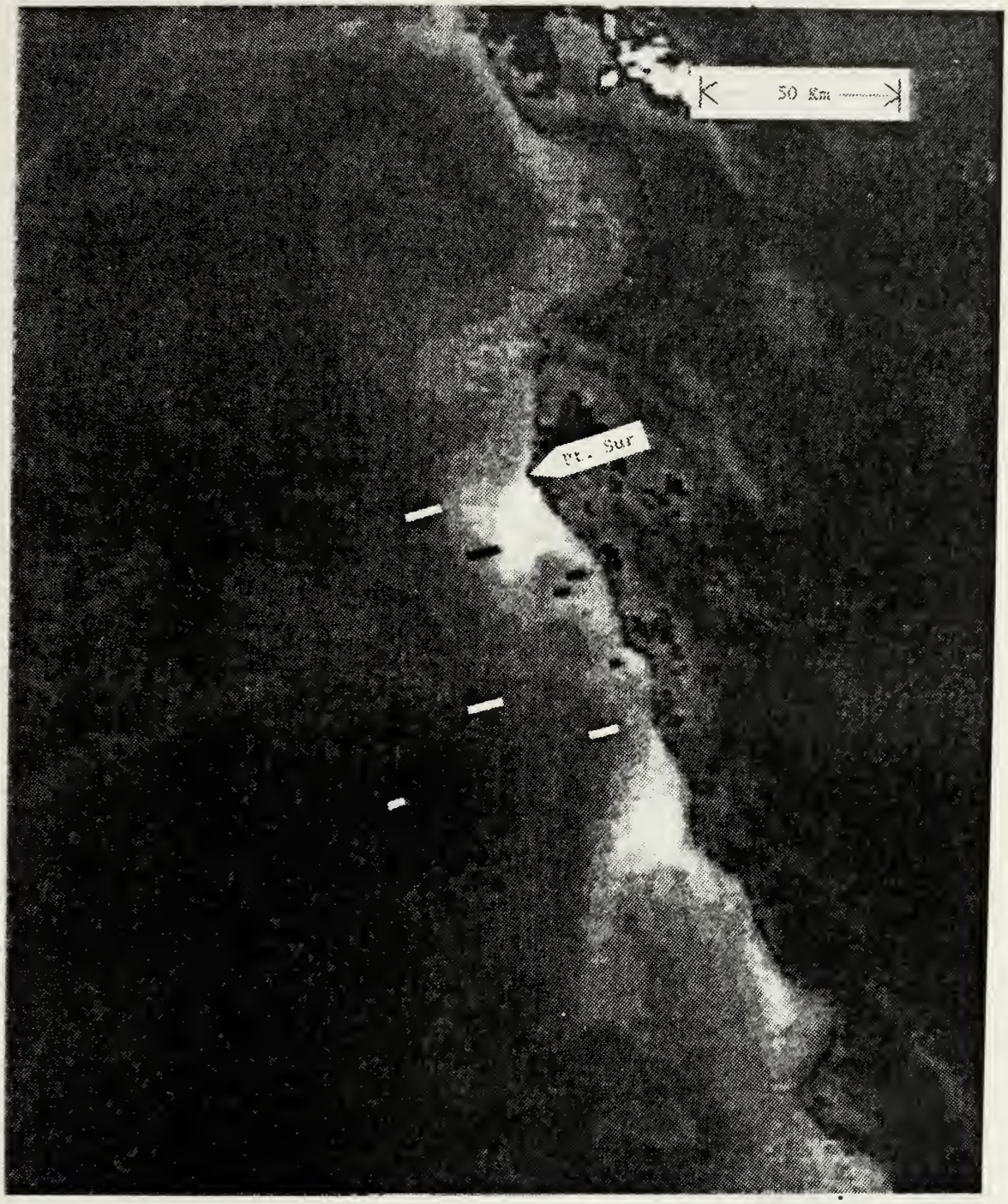

Figure 25. Temperature frontal crossing transects from the thermal salinograph data for Phase 1B superimposed on the June 6, 1980 AVHRR IR satellite image. Transect distances are only approximate (1 inch 30 Km), and lighter gray shades correspond to cooler temperatures.

front intersections should not necessarily be taken as a lack of agreement between the two sources of data, but rather that T/S data probably does not exist at that location. To provide additional insight into the frontal selection process (i.e., with respect to the satellite imagery), the T/S frontal crossing lines have, for the Phase 1B/June 6, 1980 case, been alternatively superimposed on the corresponding satellite image (Fig. 25). In this format it is possible to evaluate the adequacy of the previous frontal selections. Clearly, the selection of the major frontal boundary locus from satellite imagery may, upon occasion, be ambiguous. Examples of excellent, poor, and total lack of agreement can be found in these comparisons. Close to the coast (within the first 25km) where the gradients are stronger, the agreement is generally good. Better agreement between frontal loci from the imagery and from the thermalsalinograph could possibly be obtained by taking into account the additional offshore Ekman transport that occurred between the image and thermalsalinograph data acquisition times for Phase 3A. However this does not appear to be true in the previous case for Phase 1B.

The surface intercept of the permanent pycnocline for Phases 1A and 1B has also been superimposed on the satellite image acquired on June 6, 1980 (Fig. 22).

Offshore transects for each trackline were examined first to determine the density values associated with the permanent pycnocline, and second, to estimate the distance offshore where the pycnocline intersected the surface. Inspection of the individual density transects indicated that a value of 25.7 for sigma-t was a reasonable value to associate with the pycnocline. In each case a range about the median offshore distance was estimated from the transect and these values were then used to establish the range band indicated by the hash marks. The surface band associated with the surfacing pycnocline is seen to lie close to, but consistently just shoreward of the region of maximum temperature gradient indicated in the satellite imagery. The agreement overall is considered good.

To obtain some insight into the relationship between the surface temperature field depicted by the AVHRR, and a dynamically important variable such as geostrophic velocity, the Ø/2ØØm dynamic height field for Phase 1B has been superimposed on the same image used in the previous comparison (June 6, 198Ø) (Fig. 26). Because dynamic heights are obtained by a vertical integration of the mass field, the influence of the entire mass field down to the reference level chosen for the calculation, is taken into account. The contours in Figure 26 are plotted at 2 dynamic cm. intervals and show a general increase in elevation in the offshore direction of 1Ø-15 dyn.cm. over a

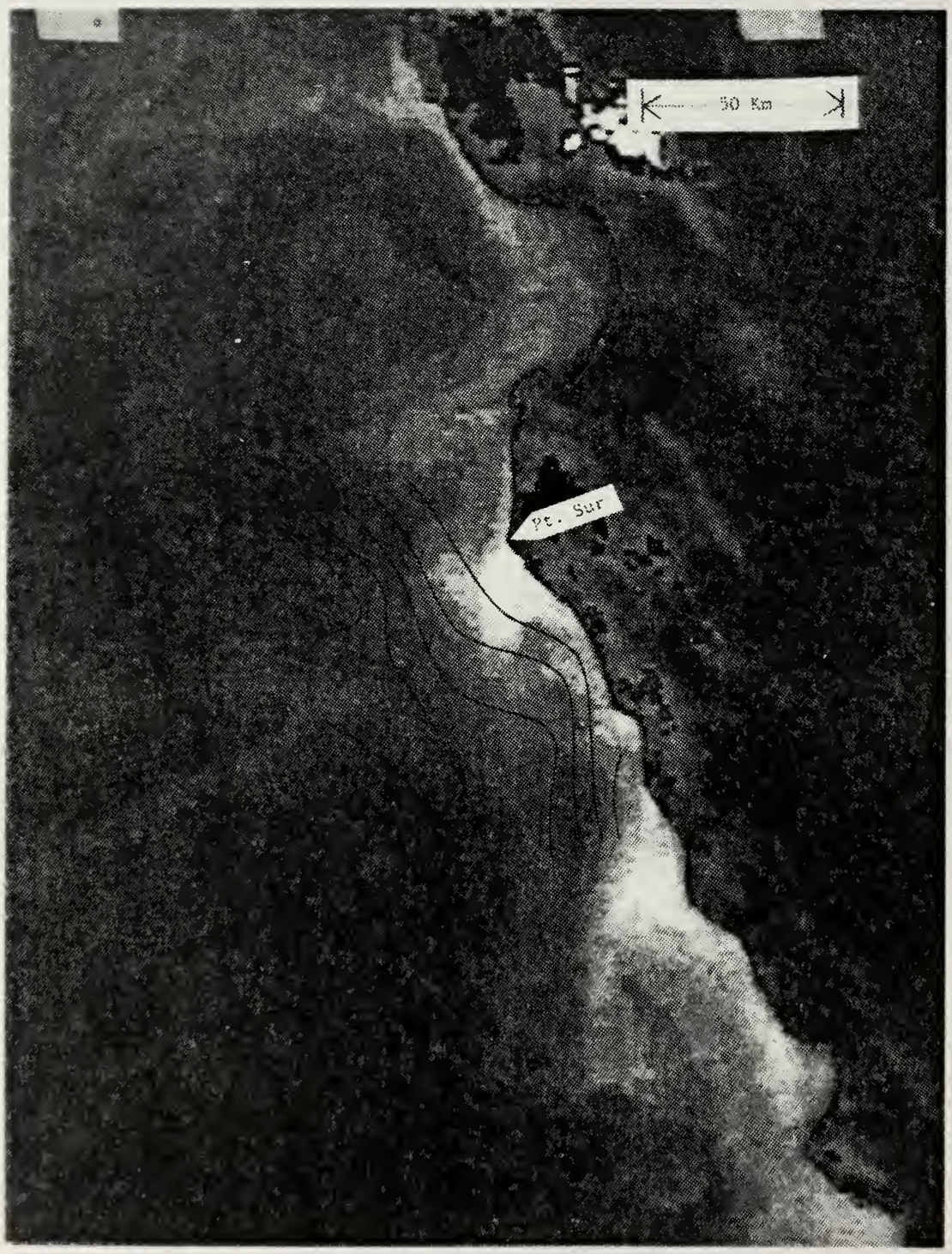

Figure 26. Superposition of the surface relative to 200m dynamic height field from Phase 1B, on the June 6, 1980 AVHRR IR satellite image. Dynamic height contours are in dynamic cm, with a contour interval of 2 dynamic cm.

distance of 60km. To a first approximation the region of maximum SST gradient corresponds to the region of maximum gradient in dynamic height, a region approximately 25km offshore and roughly parallel to the coast. The temperature field provides a clear indication of equatorward flow at the surface and of the confluences and diffluences associated with this geostrophic flow. This comparison suggests that the internal/surface changes occurring in this region over the 40 hours between the time of the image and the median data acquisition time were not great enough to destroy the obvious correlation that exists. It also implies that the surface temperature field was essentially conservative during this same period.

Saunders (1973) has shown, however, that it is not usually possible to infer the entire surface flow field from measurements of SST alone. Repeated measurements do provide estimates of the local time derivatives of temperature, and of the horizontal gradients of temperature, but do not provide an estimate of the flow parallel to the isotherms. However, a few direct surface current measurements, or geostrophic computations, can be used to remove this ambiguity, thus allowing the entire surface flow field to be mapped.

C. FRONTAL STATISTICS

In the following analyses, various aspects of the frontal region that separates the zone of coastal upwelling

off Pt. Sur from the warmer waters further offshore are considered. Such analyses imply that the frontal surface is a material boundary. As such, it is assumed that fluid particles do not cross this boundary but instead maintain their relative position with respect to this surface as the interface moves in toto.

The following analyses are based on a sequence of 31 images starting on 2 May and ending on 13 June, 1980. The distribution of images over this six-week period was not uniform due to frequent periods of low-cloud cover which often lasted for several days or more. It has been assumed that typical upwelling patterns is SST prevailed during the cloud-free periods. This assumption can be questioned since offshore (and thus not upwelling favorable) winds may have contributed to the cloud-free conditions. However, often the coastal winds change direction only slightly, from NNW to NNE. Upwelling usually continues in this situation but the slight offshore wind component often removes the coastal stratus. Also the upwelling patterns in SST are not expected to change as rapidly as the winds change.

The frontal boundary in each case was estimated by locating the region of maximum SST gradient and/or through visual pattern recognition. The boundary, once identified, was then digitized over a grid oriented with respect to

lines of latitude and longitude at a grid spacing of 2km. The grid extended from Cypress Point to the north, to Pt. Piedras Blancas to the south, i.e., over an alongshore distance of 100km.

The mean position of the major frontal boundary is shown in Fig. 27. Two contours have been used to depict the mean boundary *per se*. The need for two contours arose because of the basic limitations inherent in one-dimensional sampling. In many cases the major frontal boundary swung back on itself, particularly between Pt. Sur and Lopez Point, and thus became double-valued at certain locations. Rather than make an arbitrary choice as to which value to use in such cases, the boundary was digitized in one case always picking values closest to the coast, and in a second case always picking values furthest away from the coast. The two contours are usually within 5km of each other, the spread essentially representing a measure of the uncertainty in estimating the true position of this feature, presumably due to meanders. Standard deviations in frontal location have also been included for each of the mean boundaries. Standard deviations are greatest directly off Pt. Sur where the mean boundary is also located furthest offshore. Extreme values in frontal location are also shown. The discontinuities seen in the outer (dotted) contour arise because the measurements of

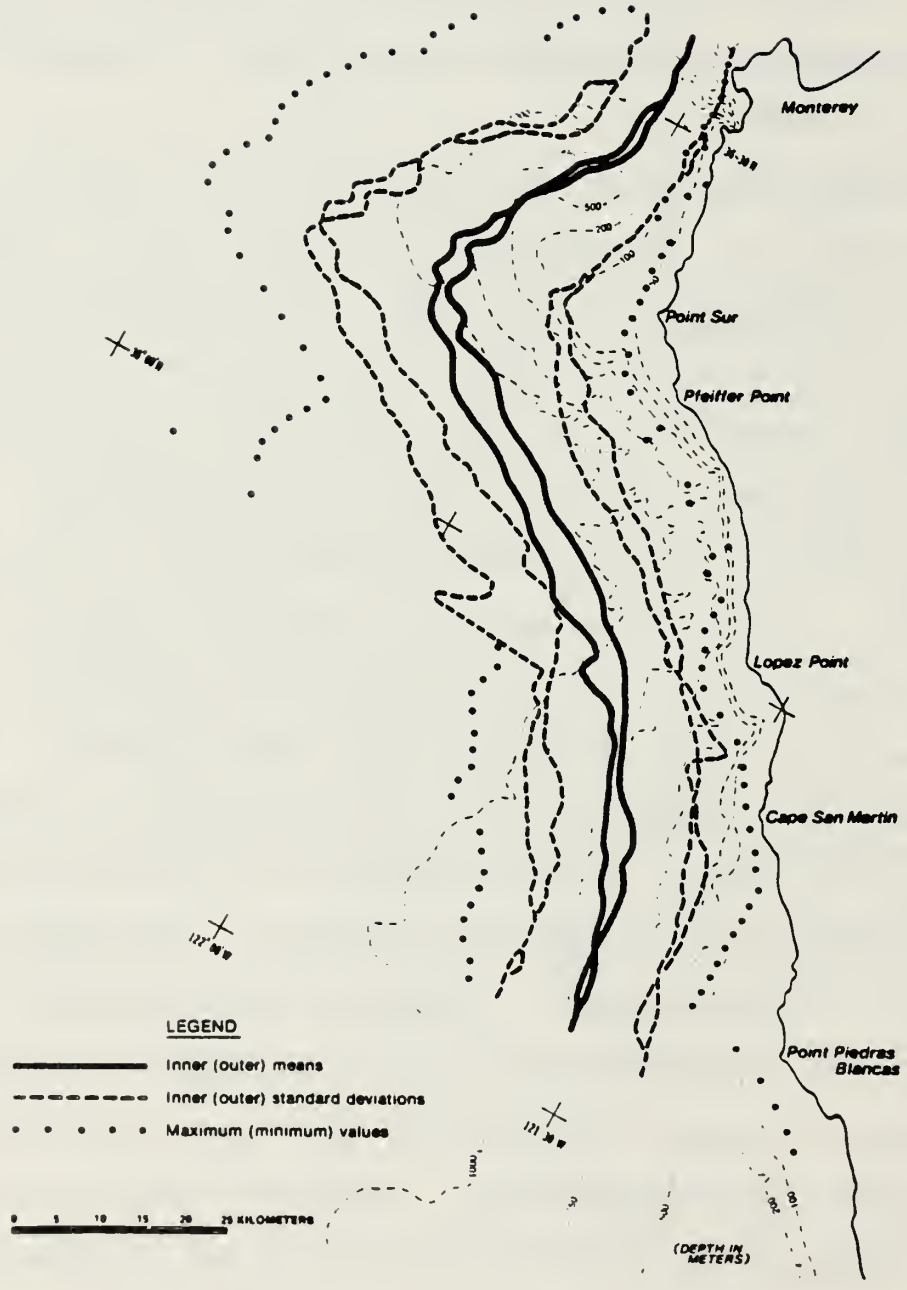

Figure 27. Mean position of the major upwelling frontal boundary obtained from a sequence of 31 AVHRR IR satellite images starting on May 2, 1980 and ending on June 13, 1980. Individual images were digitized at a grid spacing of 2km. Two boundaries representing the mean and standard deviations were required because of ambiguities that arose occasionally from double valued boundary locations.

offshore distance to the boundary were taken with respect to a coordinate frame that was not optimally aligned to resolve the reversals in frontal direction that often occurred, particularly between Pt. Sur and Lopez Point. The similarity between the mean boundaries and the underlying bathymetry is striking. The mean frontal boundaries roughly follow the 750m isobath except in the area of Sur and Lucia Canyons south of Pt. Sur. The mean surface pattern is phase shifted slightly to the south with respect to the isobaths around Pt. Sur, however. This offset may be due to southward advection by flow associated with the surface jet described in Chapter 2. After June 15th, the upwelling front near Pt. Sur moved rapidly offshore, apparently less influenced there by the local bathymetry.

In the next analysis a probability distribution, subsequently referred to as a number density contour plot, has been constructed which represents selected probabilities of encountering surface water within the boundaries of the Pt. Sur upwelling center (Fig. 28). The same individual mapped boundaries used in constructing the previous figure are used here. However, the images in this case were digitized in two dimensions with a corresponding cell resolution of 2 x 2km, or at a resolution just slightly less than the resolution of the satellite sensor itself (1.1km at nadir). The position of the upwelling

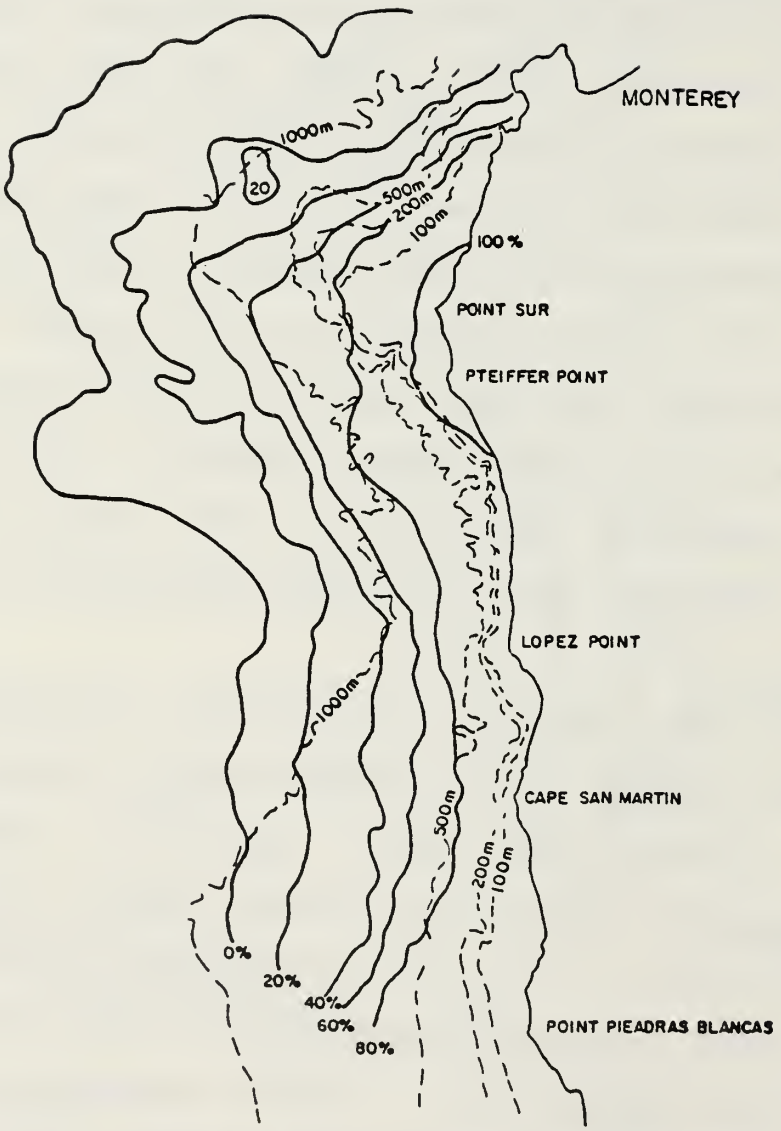

Figure 28. Normalized number density contour analysis. Images from the May 2, 1980, to June 13, 1980 sequence were composited to obtain probabilities of encountering water within the major upwelling frontal boundary.

boundary did not tend to fluctuate about a mean position but rather gradually expanded farther offshore during the 44-day period. In the figure, contours which tend to parallel one another are seen. One exception is the 0% contour in an area about 45km SW of Pt. Sur. This perturbation overlies Sur Canyon and may represent the influence of intensified upwelling and/or eddies at this location. Also the locus of major contour turning points just west of Pt. Sur are closely aligned, suggesting a preferred orientation for the surface distribution of cold water associated with the Pt. Sur upwelling center. Again there is a close similarity between the contours and the underlying bathymetry. Bathymetric influence is clearly observed out to the 1000m isobath.

Empirical orthogonal functions (EOFs) are calculated for the upwelling frontal boundary based on its position from two sequences of IR satellite images. The first sequence corresponds to a subset (24 vs. 31) of images that were used in previous sections but cover the same period: May 2 to June 13, 1980. The second sequence of images covers the period between April 4 and July 14, 1981. Forty-six images are included in the second sequence and their distribution in time is slightly more uniform than those included in the original sequence. Although the same grid spacing was used in digitizing the 1981 images (2km),

the grid for 1981 has been extended by 15km in both directions to an overall distance of 128km. EOFs computed from the satellite data partition the alongshore dependence of the offshore displacement of the frontal boundary into an ordered series of spatial functions or modes. Each EOF has associated with it a series of coefficients or principal components, which describe its behavior in time. EOFs are used to obtain estimates of (1) the alongfront spatial scales, (2) the time variation of the principal components, (3) interannual variability in frontal behavior, and (4) possible insight into the causes of the observed variability. The EOFs are calculated according to standard procedures (e.g., Morrison, 1976). The original data were transformed to standard values by removing the mean and dividing by the standard deviation.

The distribution of eigenvalues expressed in terms of percent of total variance for 1980 and 1981 are shown in Figures 29 and 30, respectively (upper panels). For the 1980 data about 82% of the total variance is contained in the first 4 EOFs while for 1981, about 85% of the total variance is contained in the first 4 EOFs. Alternately, the entropy associated with the eigenvalues (λ's) is considered. The concept of entropy is borrowed from information theory in electrical engineering and as used here provides a measure of concentration in the distribution of variance over a complete set of λ's. If

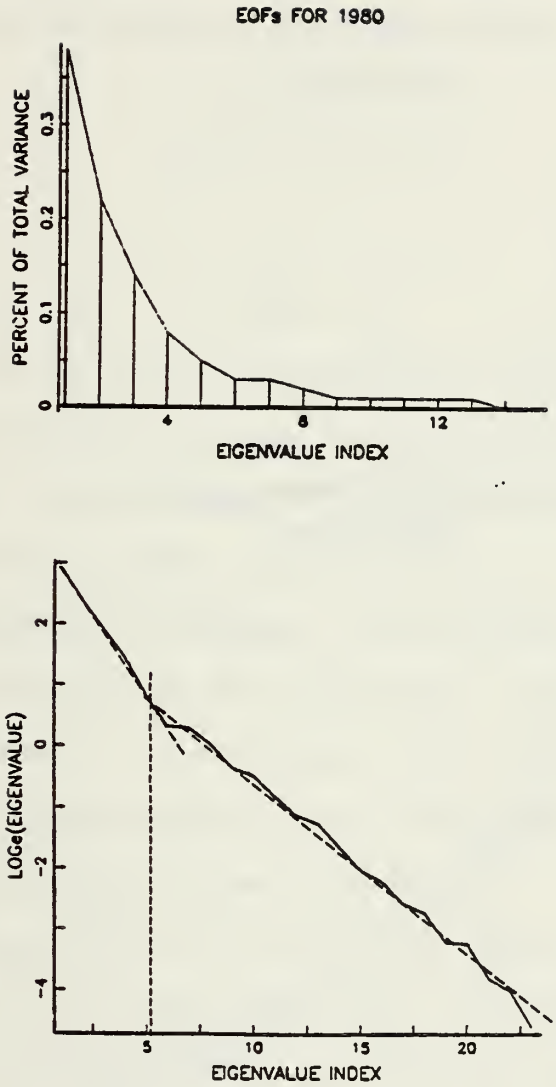

Figure 29. Distribution of eigenvalues for the EOFs calculated from the digitized frontal locations taken from the sequence of AVHRR IR satellite images starting on May 2, 1980 and ending on June 13, 1980. Upper panel is a linear plot of the variance associated with the first 14 eigenvalues versus eigenvalue index, and the lower panel is the corresponding plot with a natural log ordinate (over 23 eigenvalues). In the lower panel, the eigenvalue index corresponding to the intersection of eigenvalue slopes represents the approximate number of signal-like EOFs (Craddock, 1972).

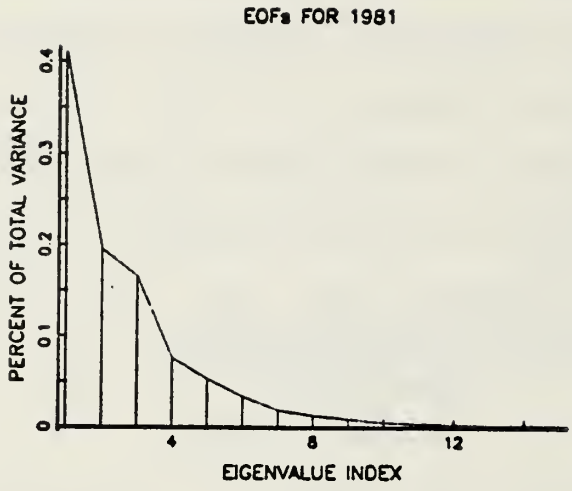

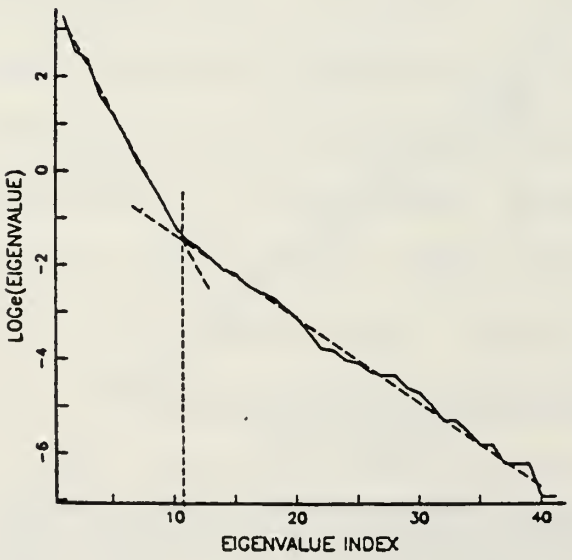

Figure 30. Same as preceeding figure except that these eigenvalues correspond to the 1981 image sequence from April 4, 1981 to July 14, 1981.

the fraction of total variance accounted for by each EOF is first calculated, then a normalized entropy can be expressed as (Halliwell and Mooers, 1979),

$$H = -(\ell nN)^{-1} \sum_{i=1}^{N} \gamma_i \ell n \gamma_i \qquad (3.1)$$

where

$$\gamma_i = \lambda_i \left(\sum_{i=1}^{N} \lambda_i \right)^{-1}$$

If all of the variance is concentrated in one mode then H = Ø. If the variance is equally distributed over all EOFs, then H = 1.Ø. The normalized entropy for the 198Ø data was Ø.61 while for the 1981 data it was Ø.5Ø. Therefore since H (1981) $<$ H(198Ø), a greater concentration of variance, or order, was present in the 1981 data. However, this rather small difference in entropies may not be particularly significant since part of this difference may arise from the different sample sizes involved.

To estimate how many of the EOFs contain useful information (i.e., are signal-like) an eigenvalue selection rule from Craddock (1972) is used. To use the rule, the natural logarithm of λ, the eigenvalue, is simply plotted versus index number. Typically the resulting slope is steeper for the low-order signal-like EOFs than it is for the higher-order noise-like EOFs. The range of signal-like EOFs then corresponds to the projection along the abscissa where the two slopes intersect. Although this technique

lacks the statistical elegance of the principal component selection rules presented more recently by Preisendorfer et al. (1981), it is far easier to implement. The lower panels in Figs. 29 and 30 show Craddock's so-called "LEV" plots for both data sets. Using this criterion the first 5 or 6 EOFs appear to be signal-like for the 1980 data, and perhaps the first 11 EOFs for the 1981 data.

The first six EOFs for 1980 have been plotted with respect to the coast, together with the mean frontal boundary (MFB) and the 100, 500, and 1000m isobaths in Figs. 31 to 36. The MFB and the EOFs have been rescaled, multiplying each by the original standard deviation. For comparison with the MFB, each EOF(e_i) has also been multiplied by $\lambda^{\frac{1}{2}}$. The first EOF has its maximum amplitude between Point Sur and Lopez Point (Fig. 31). The first mode has two zero-crossings with respect to the mean frontal boundary, one off Pt. Sur, and a second off Lopez Point. This principal mode of variation associated with the first eigenvector may represent a meander in the offshore location of the major upwelling frontal boundary. The distance between zero-crossings with respect to the mean for this mode is about 40km. The second EOF (Fig. 32) has three zero-crossings between Pt. Sur and Pt. Piedras Blancas. The distance between zero-crossings for the major antinode off Lopez Point is again about 40km.

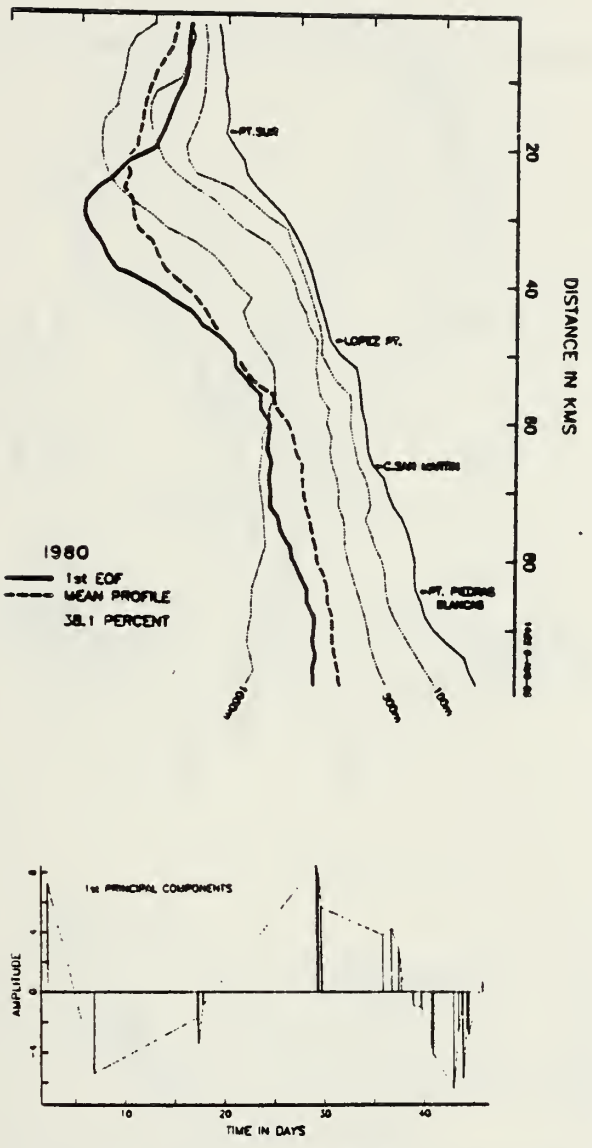

Figure 31. Upper panel represents the satellite - derived mean frontal boundary (MFB) and the first EOF, with respect to the 100, 500, and 1000m isobaths, and the coastline. MFB and first EOF have been rescaled by multiplying by standard deviation. First EOF has also been multiplied by $\lambda^{\frac{1}{2}}$. Value in percent indicates percent variance accounted for by the first EOF. Lower panel represents the distribution of principal components versus time (in days) associated with the first EOF.

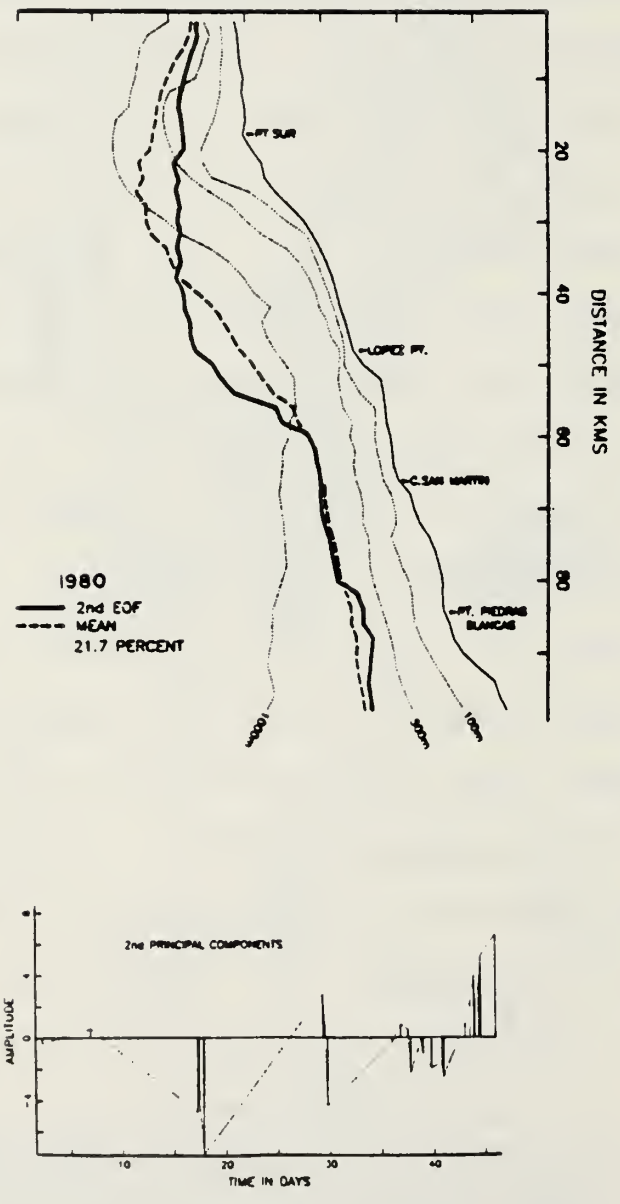

Figure 32. Same as Figure 31, except for second EOF.

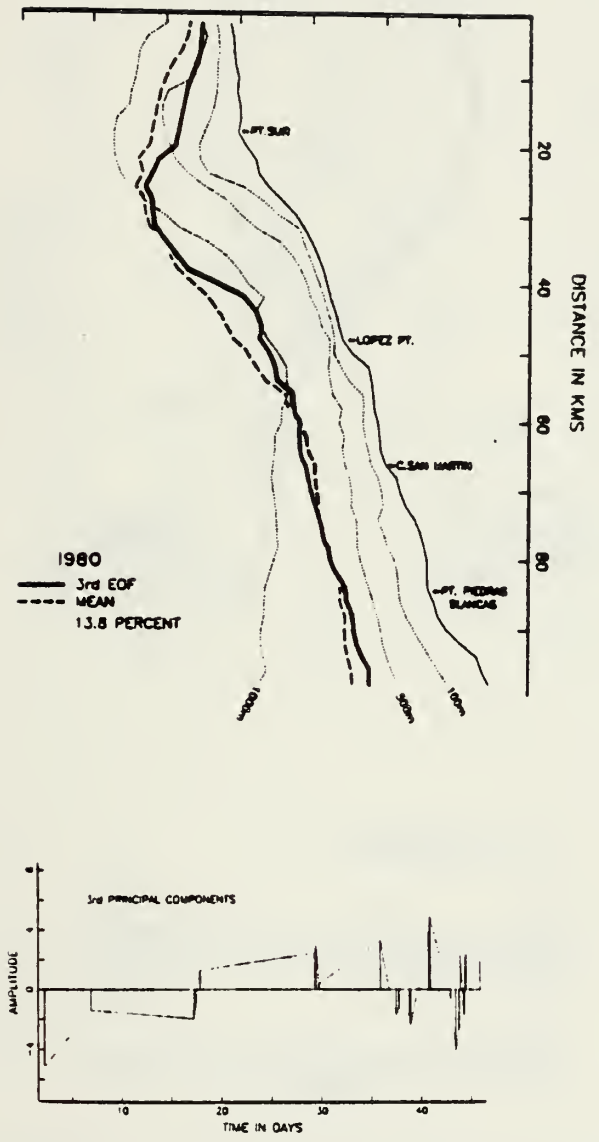

Figure 33. Same as Figure 31, except for third EOF.

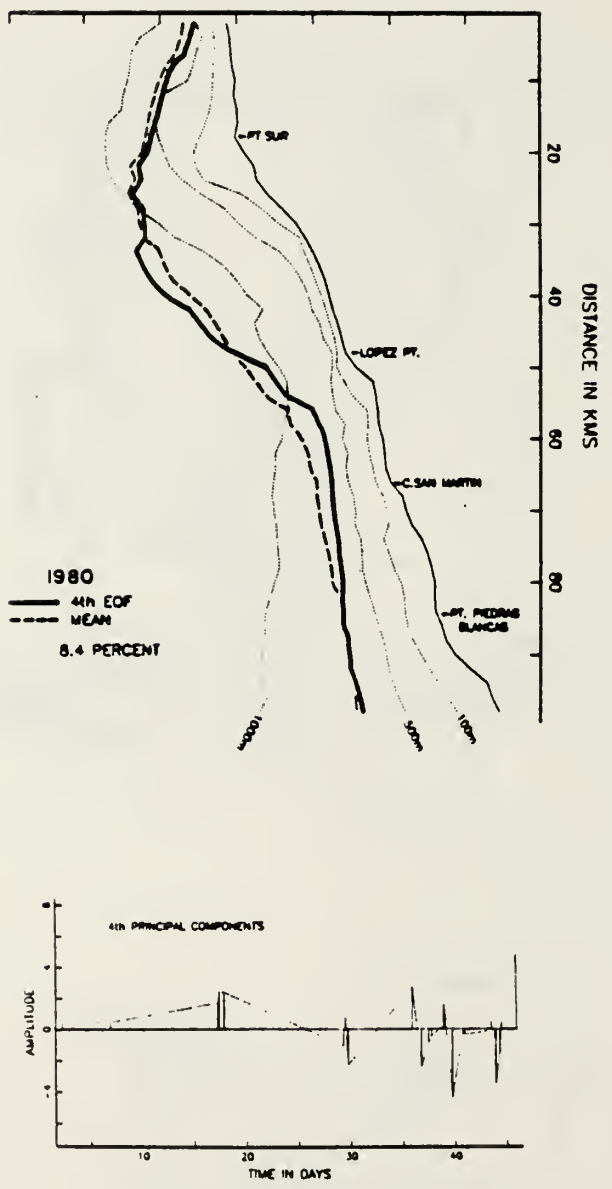

Figure 34. Same as Figure 31, except for fourth EOF.

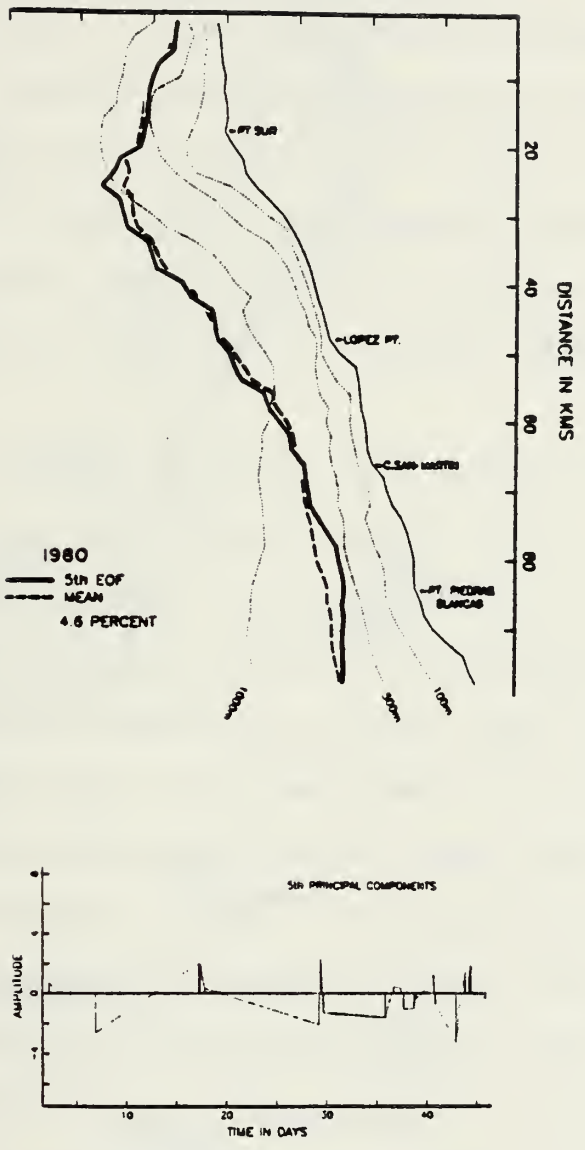

Figure 35. Same as Figure 31, except for fifth EOF.

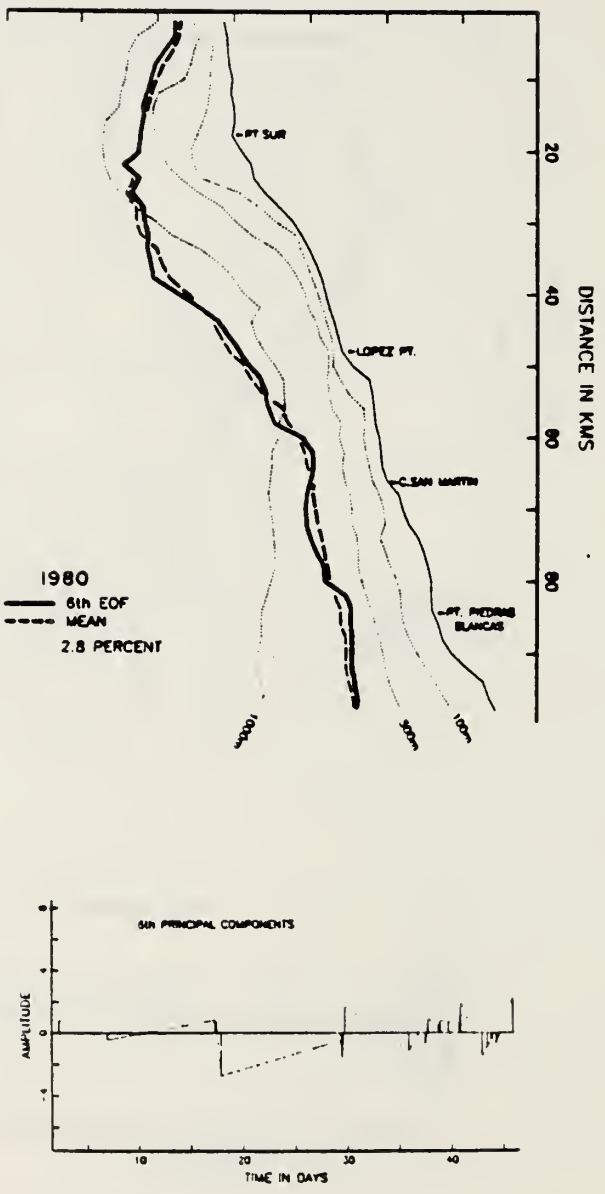

Figure 36. Same as Figure 31, except for sixth EOF.

The third EOF (Fig. 33) also has three zero-crossings between Pt. Sur and Pt. Piedras Blancas. The zero-crossing (ZC) distances for this EOF are 43 and 22km, respectively. The fourth EOF (Fig. 34) also has three ZCs between Pt. Sur and Pt. Piedras Blancas with corresponding ZC distances of 27 and 45km. ZCs become progressively more frequent and the ZC distances correspondingly shorter for the 5th and 6th modes. The ZC distances with respect to the mean frontal boundary for the first four modes range between 22 and 45km.

The first 6 EOFs for 1981 have also been plotted similarly to the previous data in Figs. 37 to 42. Compared to 1980, the mean frontal boundary extends considerably further offshore from just south of Point Sur northward. The spatial pattern associated with the first mode, unlike most others, shows that the primary mode of variability for 1981 is shoreward with respect to the mean frontal boundary over almost its entire length. The first EOF crosses the mean frontal boundary at essentially one location only, hence no ZC distance can be estimated in this case (Fig. 37). The second EOF (Fig. 38) has 4 ZCs, the first near Carmel Bay, the second and third just north of Pt. Sur, and the fourth off Lopez Point. The ZCs are 17, 4, and 45km apart, respectively. The major antinode pattern between Pt. Sur and Lopez Point is very similar to the EOF pattern for the first mode for 1980. The third EOF contour (Fig.

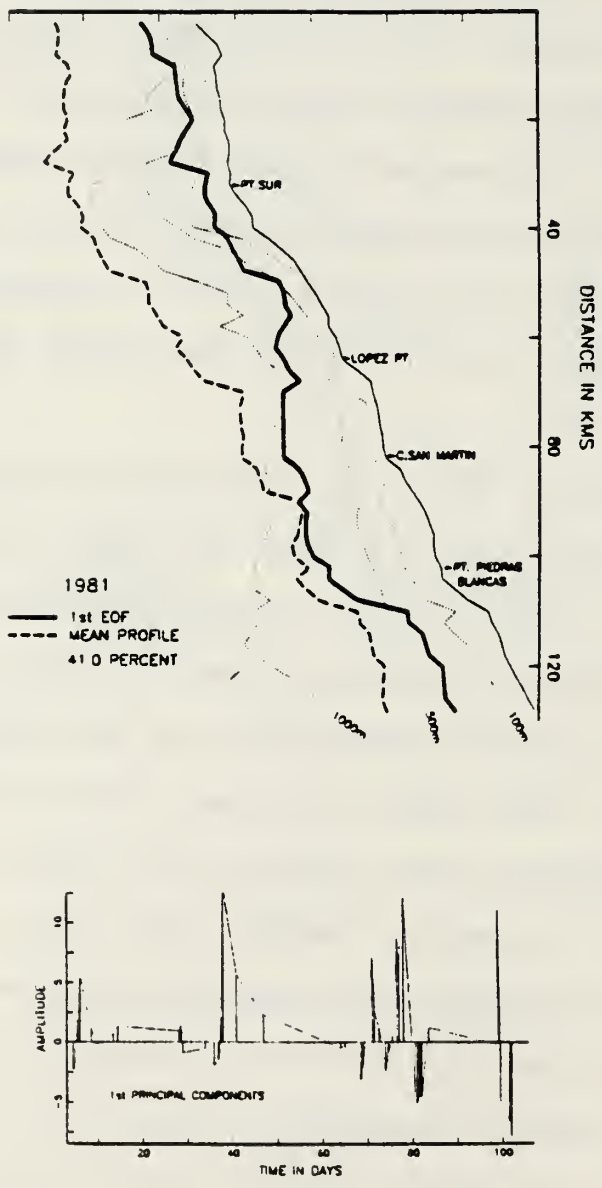

Figure 37. Same as Figure 31, except for 1981 data.

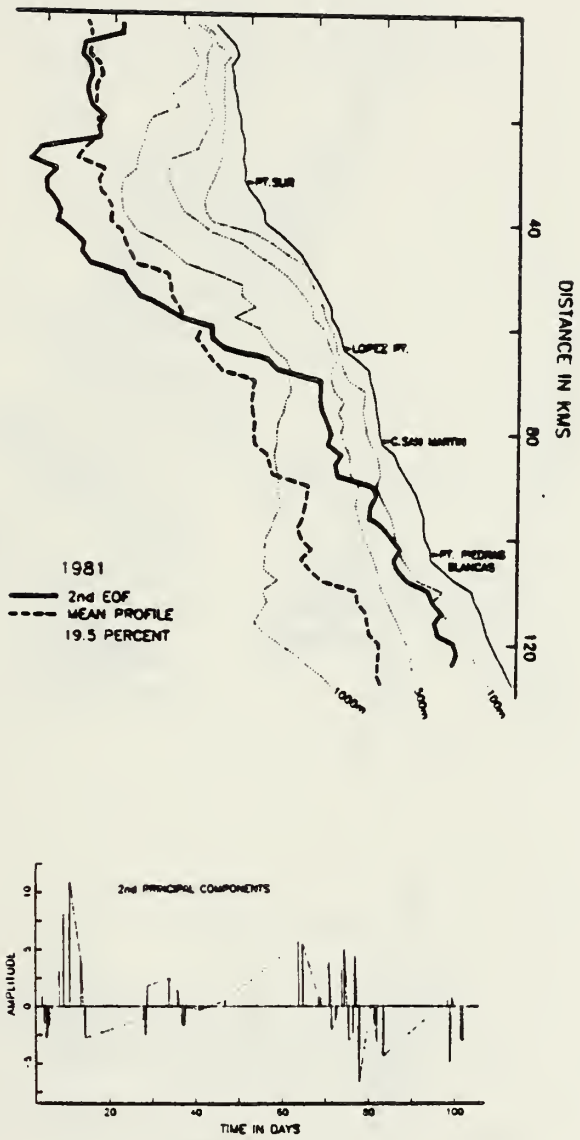

Figure 38. Same as Figure 37, except for second EOF.

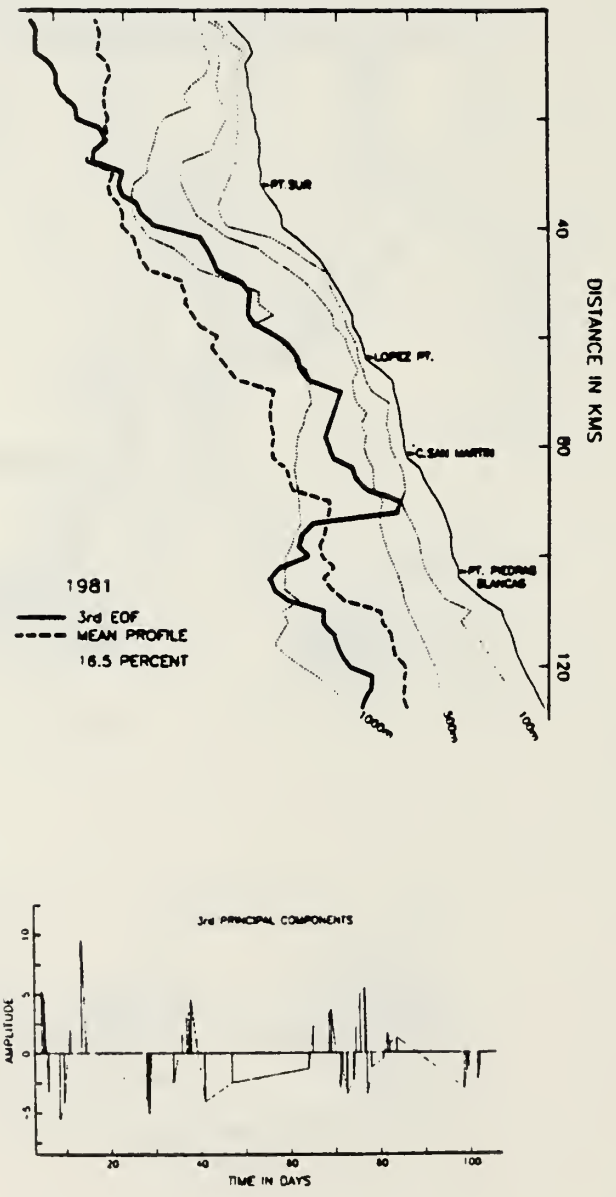

Figure 39. Same as Figure 37, except for third EOF.

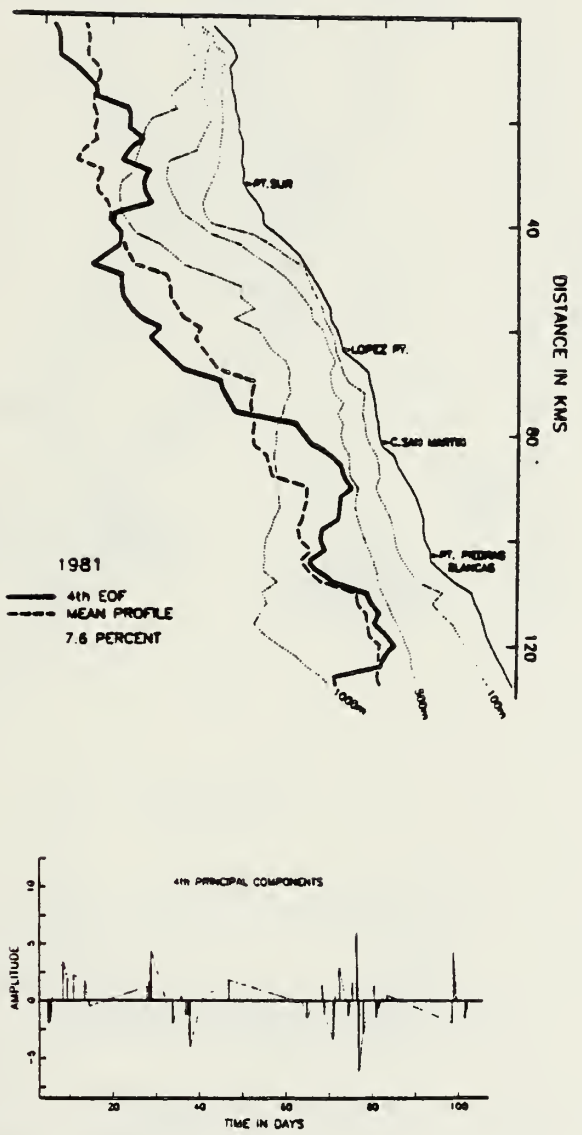

Figure 40. Same as Figure 37, except for fourth EOF.

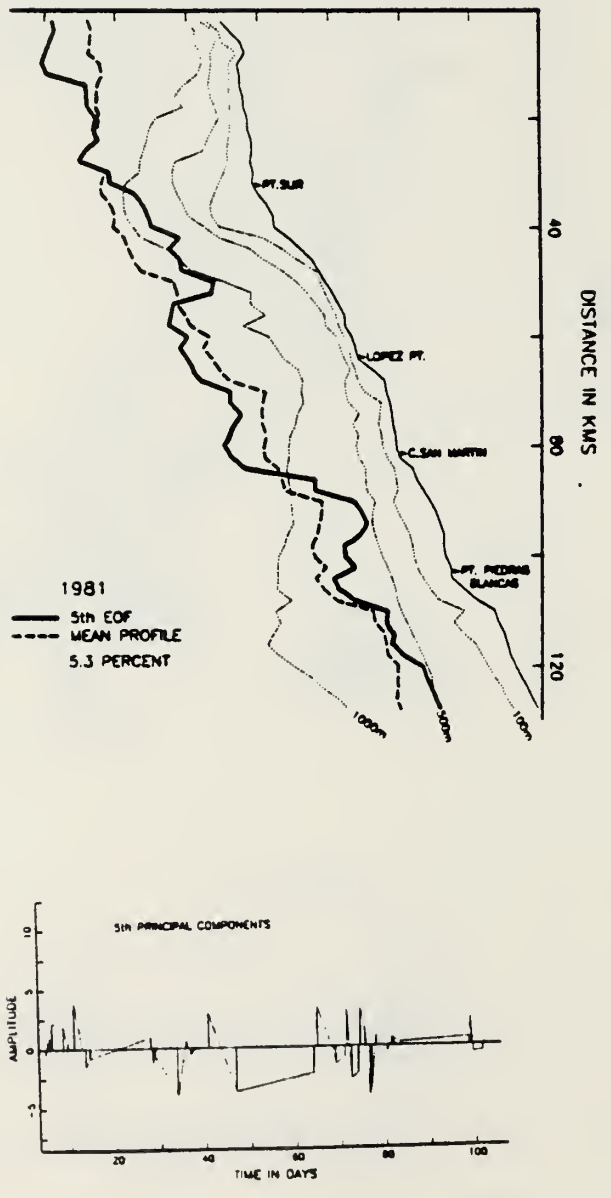

Figure 41. Same as Figure 37, except for fifth EOF.

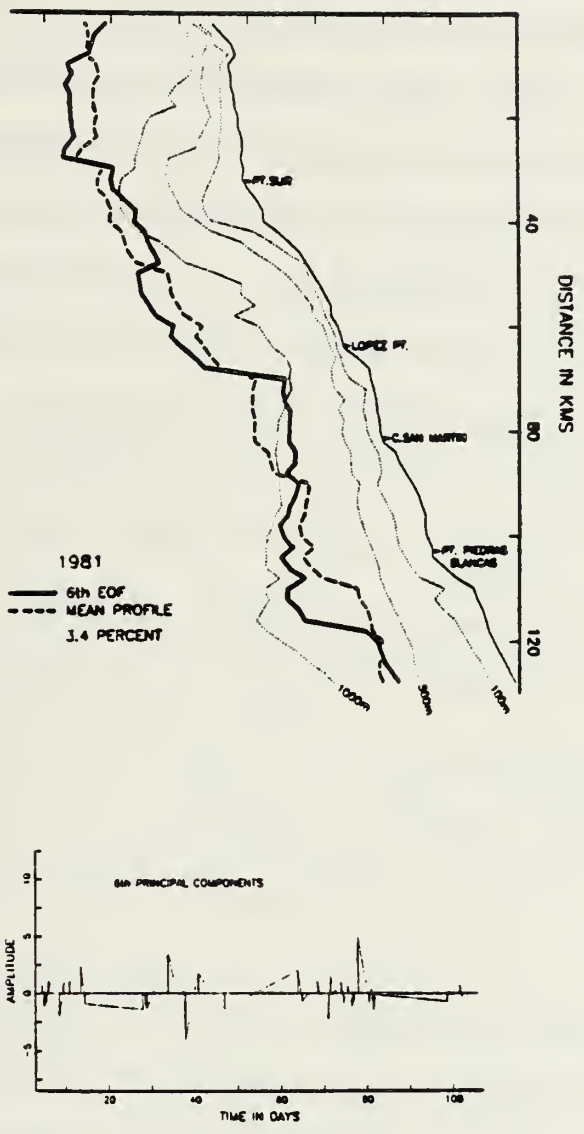

Figure 42. Same as Figure 37, except for sixth EOF.

39) is rather irregular south of Cape San Martin and appears to have only one ZC over the area. The fourth EOF has 3 ZCs, the first pair approximately 33km apart and the second about 48km apart (Fig. 40). The fifth EOF (Fig. 41) also has 3 ZCs, the first pair about 37km apart and the second pair about 42km apart. The pattern of the sixth EOF ZCs is quite similar to the fifth (Fig. 42). Although the individual EOF patterns for 1981 are considerably different than the corresponding patterns for 1980, particularly with respect to nodal locations, the range of ZC distances is roughly the same (with the exception of the second and third ZCs for the second mode). For the 1981 data the overall range extends from 4 to 48km. Inspection of the individual images for 1981 also indicates that the mean frontal boundary might be expected to occur further off the coast since upwelling appeared to be more extensive for certain periods during the first two months of this sequence.

In the foregoing it has been assumed that the zero-crossing distance with respect to the mean frontal boundary provides a direct measure of the appropriate spatial scale for variability in the alongfront direction. The actual scale is taken to be approximately twice the zero-crossing interval since it is assumed that this distance corresponds to a half wavelength of variation.[5] This interpretation

assumes a first-order stationary process. However, the mean frontal boundary was observed to move further offshore on a time scale of the order of the record (sequence) length (for both years). Consequently some of the variability contained in the various modes must be coupled to the gradual offshore movement of the boundary. A regression analysis between boundary location and time was undertaken for the 1980 data in an attempt to establish a basis for adjusting the mean frontal position for its offshore movement. However, the results of this analysis showed that only portions of the boundary moved offshore while other portions (particularly toward the south) actually moved slightly onshore. Because of this complication it was ultimately decided not to pursue an adjustment for mean boundary movement.

The first six principal components for 1980 are plotted as a function of time in the lower panels of Figs. 31 to 36, and show considerable variability over the sequence. Because of severe undersampling during the first 30 days, and nonuniform sampling over the entire period, it is difficult to resolve any definite cyclic trends in these results. However, an approximate 30 to 40 day cyclic variation is suggested by the principal component sequence associated with the first EOF (Fig. 31, lower panel). The principal components over the last 15 days where more samples were available (and for modes greater than the

first), also show persistence on the order of three days. The first six principal components for 1981 are shown in the lower panels of Figs. 37 to 42. Although the data density is higher for the 1981 sequence, it is still very difficult to discern any clearly identifiable patterns in these series. However, for the first three sets of principal components (i.e., those associated with the first three EOFs), a several-day persistence time scale is suggested.

The mean frontal boundary and the various EOFs were often closely aligned with the general orientation of the local bathymetry. Since the major frontal zone is not expected to be density compensated, relatively strong alongfront baroclinic flows are generally to be expected. The tendency for alongshore flow to be closely aligned with the bathymetry has frequently been observed in other coastal regions, most notably the Oregon continental shelf region (Allen, 1981). That the alongshore flow should be aligned along contours of constant depth is to be expected for the case of steady motion in a homogeneous fluid. This result is a consequence of the Taylor-Proudman Theorem for rotating fluids (Greenspan, 1968). Such a close alignment between a surface frontal boundary and the shelf margin might also be expected in regions where shelf-edge upwelling is important. Along the Central California

coast, however, the width of the continental shelf is so narrow that it is probably not possible to distinguish between coastal and shelf-edge upwelling.

To examine the degree of association between the orientation of the satellite derived frontal boundaries and the bathymetry, the mean frontal boundary (MFB) together with the first four EOFs for 1980, and the 100, 500, and 1000m isobaths have been lag (cross) correlated (Table 2).

The first and fourth EOFs are maximally correlated with the 1000m isobath whereas the mean and the second and third EOFs are maximally correlated with the 100m isobath. Based on the lag correlation analysis, the MFB is in-phase with the 100 and 500m isobaths but displaced 8km to the south of the 1000m isobath. Similarly, the patterns of the first four EOF's are either in phase or displaced to the south (by 0 to 14km) of the patterns of the 100, 500, and 1,000m isobaths. It is also obvious that if one of the EOFs or the mean frontal boundary are highly correlated with one of the selected isobaths it will be highly correlated with the others, since each of the isobaths is highly correlated with the other two. The maximum correlation between the 100m and 500m isobaths was 0.99 at zero lag, 0.95 between the 500m and 1000m isobaths at zero lag, and 0.91 between the 100m and 1000m isobaths, again at zero lag. That these correlations are maximum at zero lag is somewhat fortuitous since the actual lag will depend in part on the coordinate

Table 2

Lag-Correlation Analysis for the Mean Frontal Boundary (MFB) and the First 4 EOFs for 1980 vs Selected Isobaths

	Maximum Correlation (MC)	Lag (km)
MFB vs 100m isobath	0.93*	0
MFB vs 500m isobath	0.91	0
MFB vs 1000m isobath	0.90	+8
EOF-1 vs 100m isobath	0.83	+8
EOF-1 vs 500m isobath	0.87	+10
EOF-1 vs 1000m isobath	0.92*	+12
EOF-2 vs 100m isobath	0.87*	0
EOF-2 vs 500m isobath	0.82	0
EOF vs 1000m isobath	0.82	+14
EOF-3 vs 100m isobath	0.92*	0
EOF-3 vs 500m isobath	0.90	+2
EOF-3 vs 1000m isobath	0.89	+8
EOF-4 vs 100m isobath	0.89	0
EOF-4 vs 500m isobath	0.87	+4
EOF-4 vs 1000m isobath	0.91*	+10

*Maximum MC

NOTE: Maximum correlation at a positive lag means that the MFB or an EOF pattern is displaced southward relative to an isobath. The alongshore resolution of the frontal boundary and the bathymetric data is 2km.

frame used for the calculations (latitude and longitude in this case).

Overall it is seen that the MFB and the first four EOFs are all highly correlated with the local bathymetry. However, correlations between the various EOFs and the local bathymetry may be somewhat elevated from coupling between each mode and the gradual offshore movement of the MFB. There is also a tendency for the MFB and the EOFs to be displaced slightly to the south (0-14km) with respect to the local isobaths, particularly with respect to the 1000m isobath.

D. IMAGE SEQUENCES

In this section three sequences of IR satellite images are presented. The first sequence represents a burst sample of images acquired during the period between Phase 1 and 3 of the Pt. Sur study. Nine images acquired over a 9-day period provide an opportunity to examine daily changes in surface temperature that apparently took place along the Central California coast. The second sequence of images covers the period from 2 May to 10 July, 1980. Attention is focussed on the changes in upwelling patterns observed off Pt. Sur on a seasonal time scale. The third sequence covers the period from April 4 to September 19, 1981. This sequence is also used to observe seasonal changes in upwelling but it is also used to indicate the

interannual variability of the upwelling zone. Finally, an observational model of upwelling along the Central California coast is proposed.

1. Sequence from June 6 to June 14, 1980

The first sequence of images was acquired between June 6, 1980 and June 14, 1980 (Figs. 43 to 51). Time differences between images in this sequence range from about 4 hours to 49 hours over the 9-day period. This period is of particular interest with respect to the Pt. Sur upwelling center study since it corresponds to the period between Phases 1 and 3 when no shipboard data from the present study were available. As such, the images help to provide continuity between the phases and also to provide a basis for interpreting some of the changes that were observed between the phases in the in situ data. Since the winds were upwelling favorable during and between phases, coastal upwelling was expected to take place more-or-less continuously. The images (Figs. 43 through 51) indicate the presence of cooler SSTs particularly around Pt. Sur over the 9-day interval. That no major changes took place during this period is also supported by coastal observations of SST taken daily at Granite Canyon (10km north of Pt. Sur). Between June 5th and June 15th, SSTs ranged between 10 and 11C at Granite Canyon, values consistent with coastal upwelling at this location. Because these images have not been corrected for

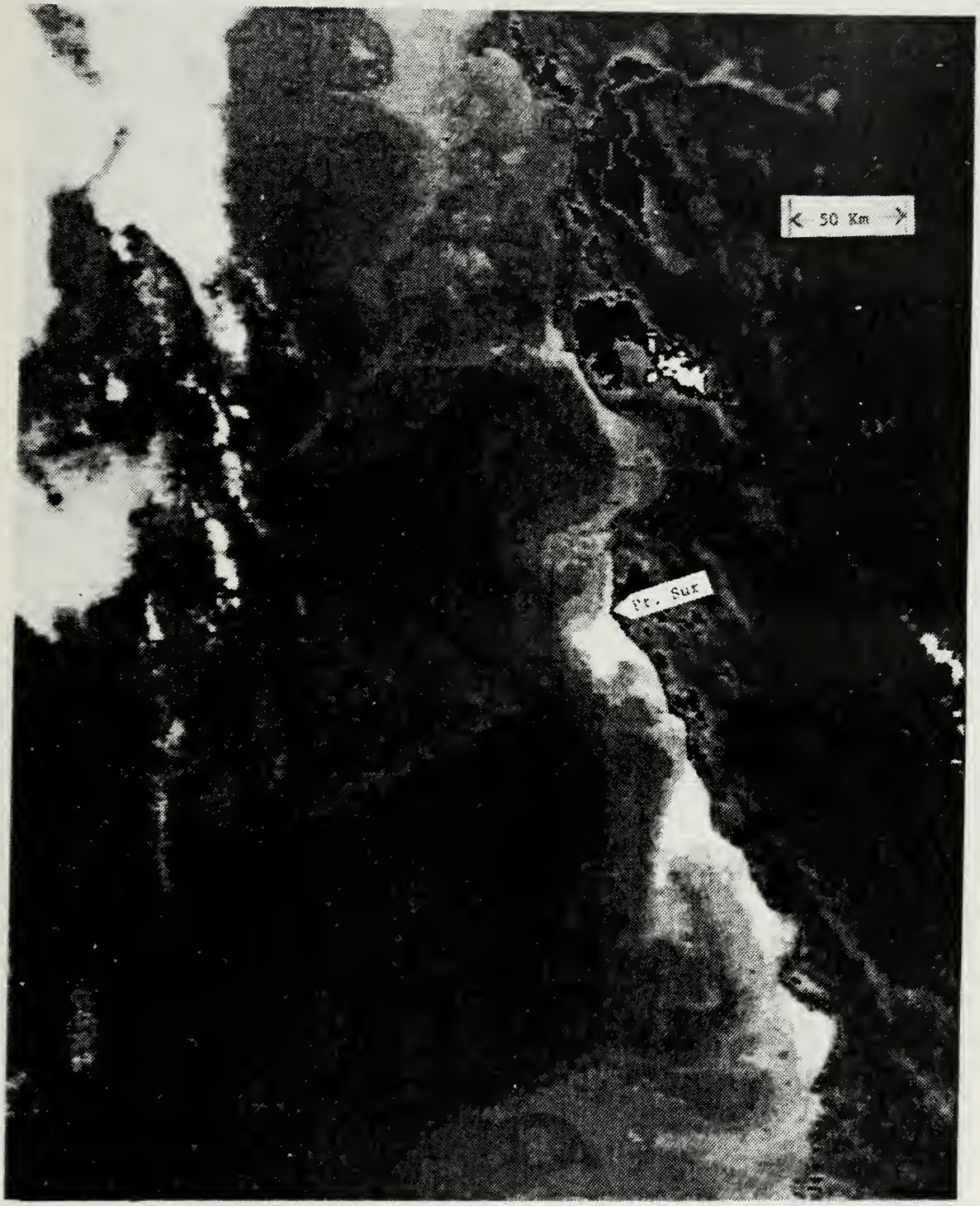

Figure 43. Advanced Very High Resolution Radiometer (AVHRR) infrared (IR) satellite image acquired on June 6, 1980 at 1517 Pacific Standard Time (PST).

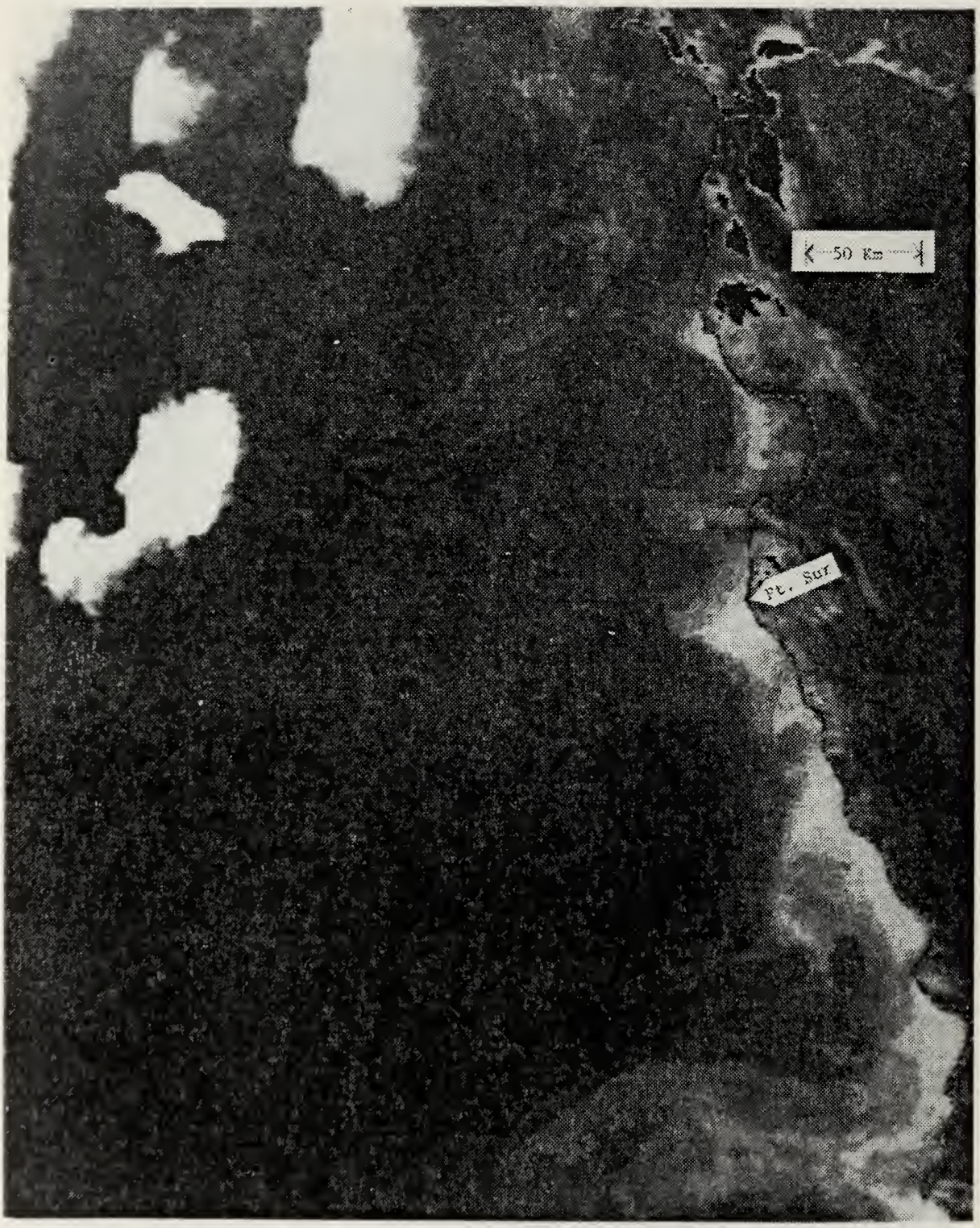

Figure 44. AVHRR IR satellite image acquired on June 7, 1980 at 1505 PST.

Figure 45. AVHRR IR satellite image acquired on June 7, 1980 at 1937 PST.

Figure 46. AVHRR IR satellite image acquired on June 9, 1980 at 1443 PST.

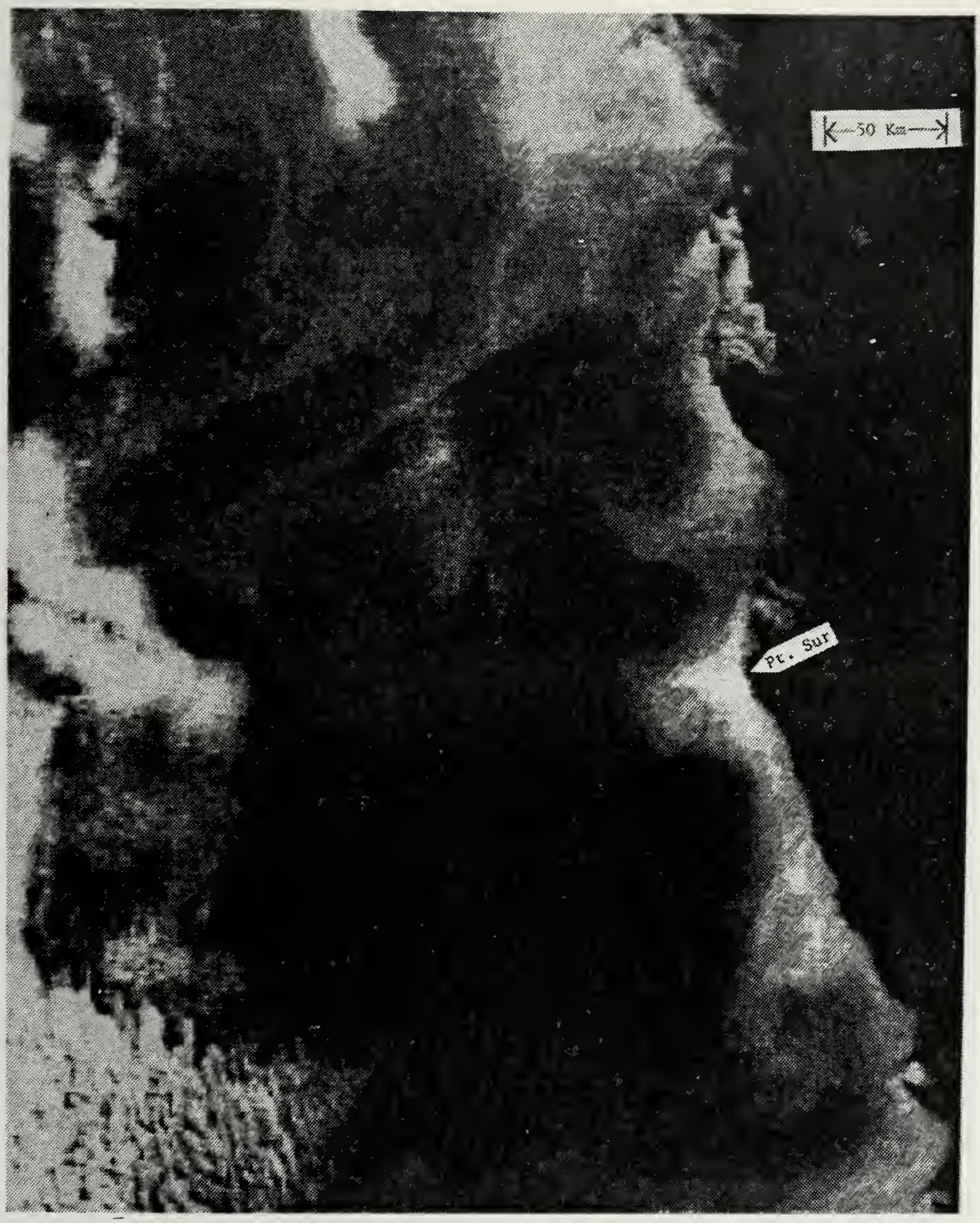

Figure 47. AVHRR IR satellite image acquired on June 9, 1980 at 1853 PST.

Figure 48. AVHRR IR satellite image acquired on June 11, 1980 at 1949 PST.

Figure 49. AVHRR IR satellite image acquired on June 12, 1980 at 1550 PST.

Figure 50. AVHRR IR satellite image acquired on June 12, 1980 at 1927 PST.

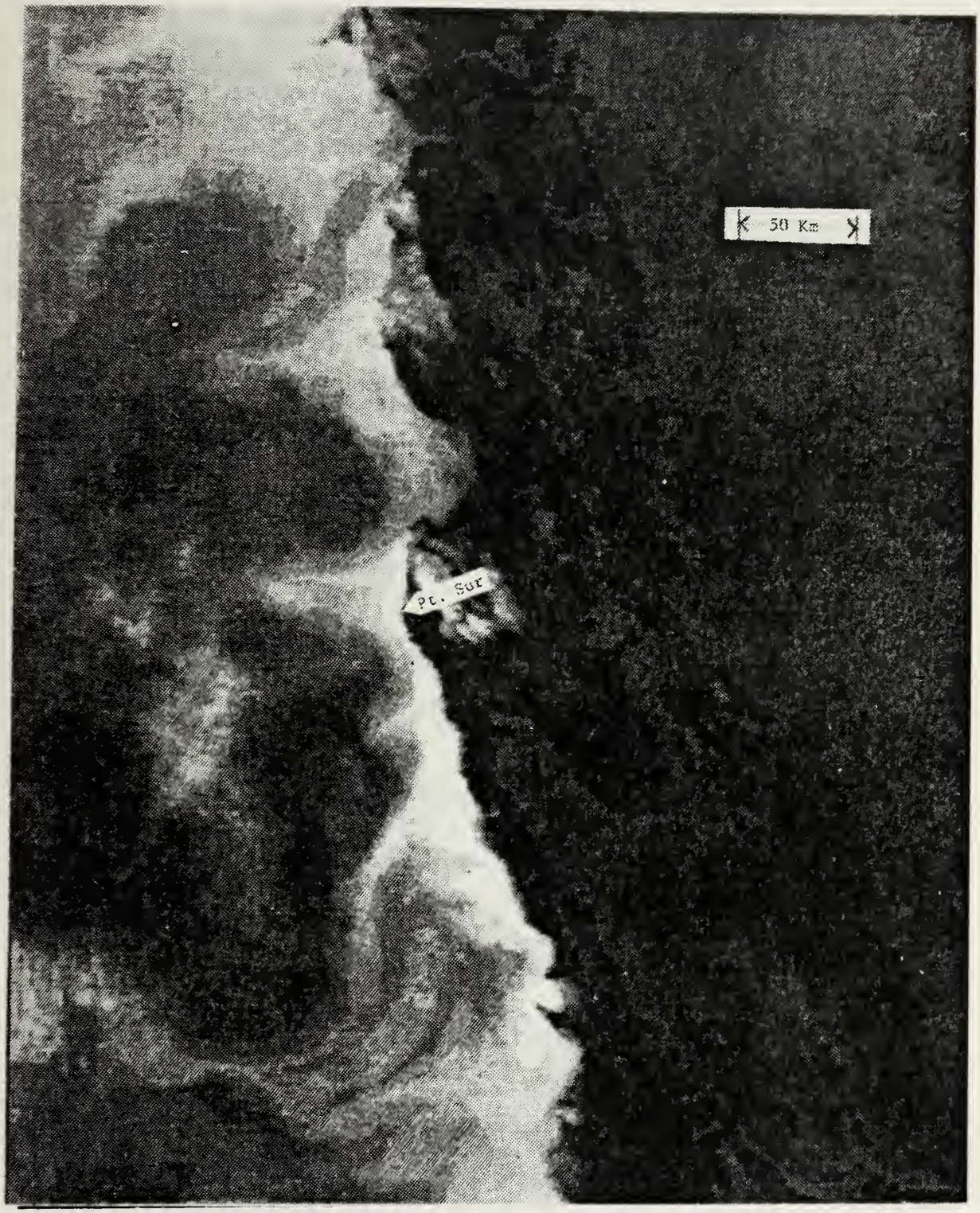

Figure 51. AVHRR IR satellite image acquired on June 14, 1980 at 1843 PST.

atmospheric moisture, only the gross changes in patterns are considered. First, the area of cooler water directly off Pt. Sur expanded further offshore ($\sim$ 25km) during the 9-day period. Also a protrusion of cooler water developed in the region between Lopez Point and Cape San Martin. This protrusion appeared to intensify on/or about June 11th. Between June 9th and June 11th, the cool center off Pt. Sur evolved in a cyclonic pattern. Limited XBT data acquired between these dates in this area support this interpretation (Traganza, 1983). Even the images taken only four hours apart on June 9th (Figs. 46 and 47), suggest subtle changes in the SST field around Pt. Sur. However these subtle differences could be due partly to variations in the image processing and consequently are not pursued.

Small, but possibly significant, changes in SST around Pt. Sur occur in this sequence over periods of two days or less. Changes in SST may not necessarily indicate changes in the subsurface temperature field, however. Based on extensive <u>in situ</u> data acquired in the upwelling region off the tip of South Africa, Andrews and Hutchings (1980) found that the surface temperature field was far more mobile than the associated subsurface temperature structure. Also they found that the surface layers responded rapidly ($<$24 hours) to changes in the local

winds whereas the subsurface structure changed more slowly (>24 hours).

2. Seasonal Sequences

In the second sequence of images, eight scenes are shown starting on May 2, 1980 and ending on September 20, 1980 (Figs. 52 to 59). These images were chosen to show the seasonal pattern of change in upwelling. Apparently, coastal upwelling generally intensified and expanded offshore. Much of this offshore movement appears to have occurred during a three-week period commencing about mid-June. By the 3rd week in September (Fig. 59) cool surface waters are seen extending several hundred Kms offshore along the Central California coast. Coastal upwelling per se may not be responsible for the cool SSTs observed further off the coast during the summer. Rossby wave dispersion, for example, may contribute to the observed seasonal changes in the cool region off the Central California coast. This topic is discussed in Section E.2.

The third sequence of IR satellite images provides coverage of the Central California coast for 1981 (Figs. 60-64). These images were acquired starting on April 4, 1981 and ending on September 19, 1981. This sequence also shows that the region influenced by coastal upwelling expands offshore during this six month period. Images from the 21st of June and the 7th of July also

Figure 52. AVHRR IR satellite image acquired on May 2, 1980 at 0344 PST.

Figure 53. AVHRR IR satellite image acquired on May 29, 1980 at 1507 PST.

Figure 54. AVHRR IR satellite image acquired on June 5, 1980 at 1528 PST.

Figure 55. AVHRR IR satellite image acquired on June 13, 1980 at 0414 PST.

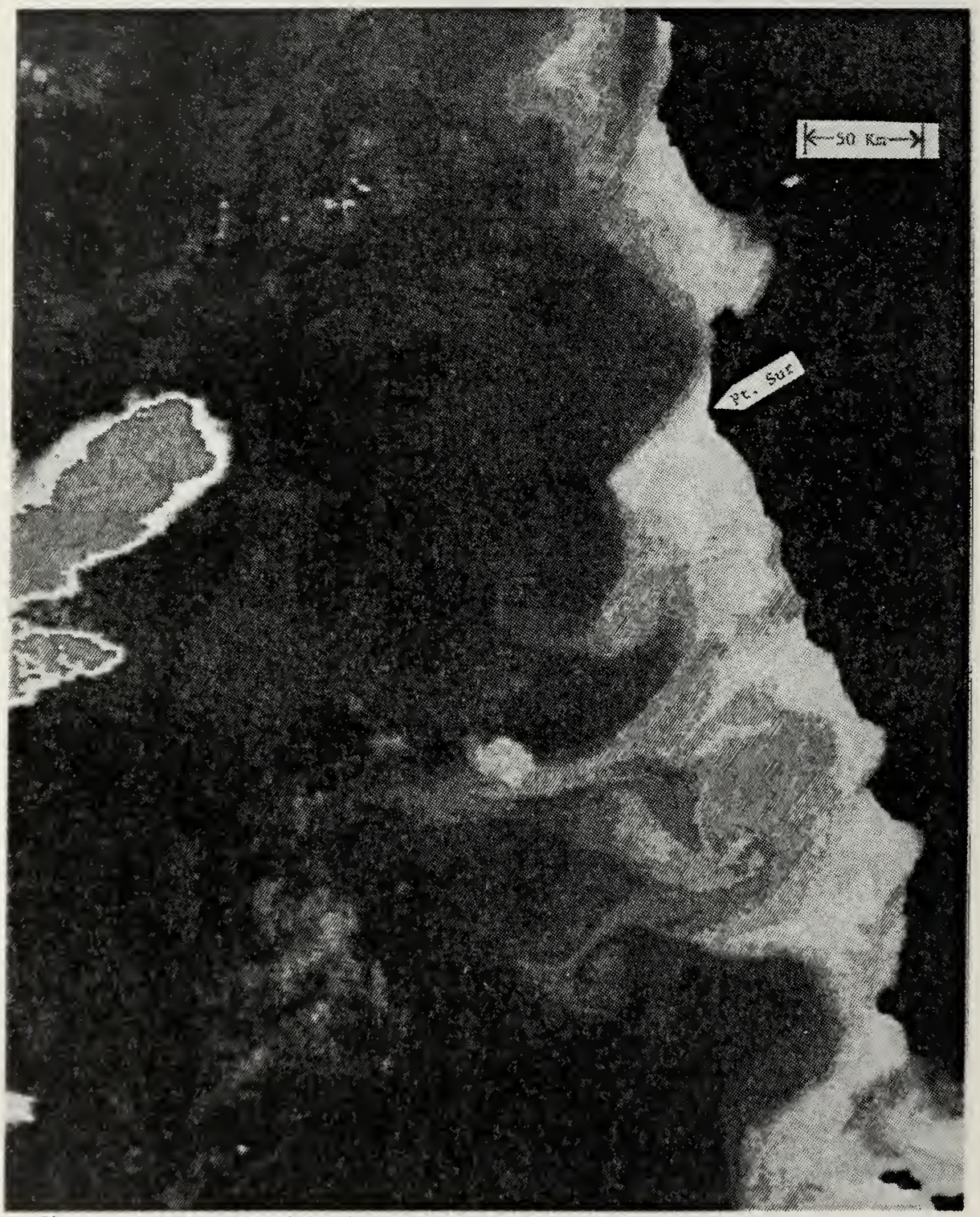

Figure 56. AVHRR IR satellite image acquired on June 25, 1980 at 1503 PST.

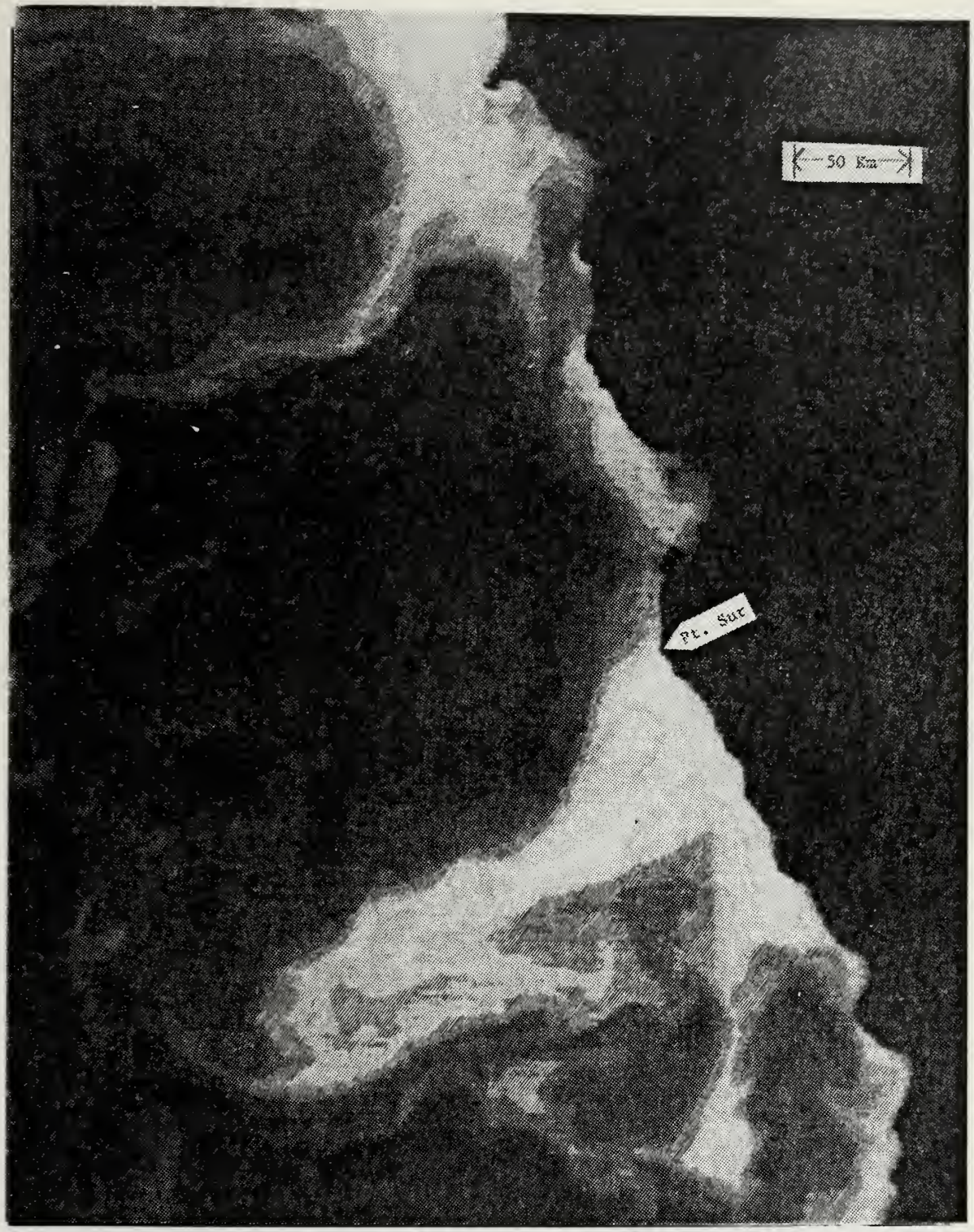

Figure 57.. AVHRR IR satellite image acquired on July 10, 1980 at 1535 PST.

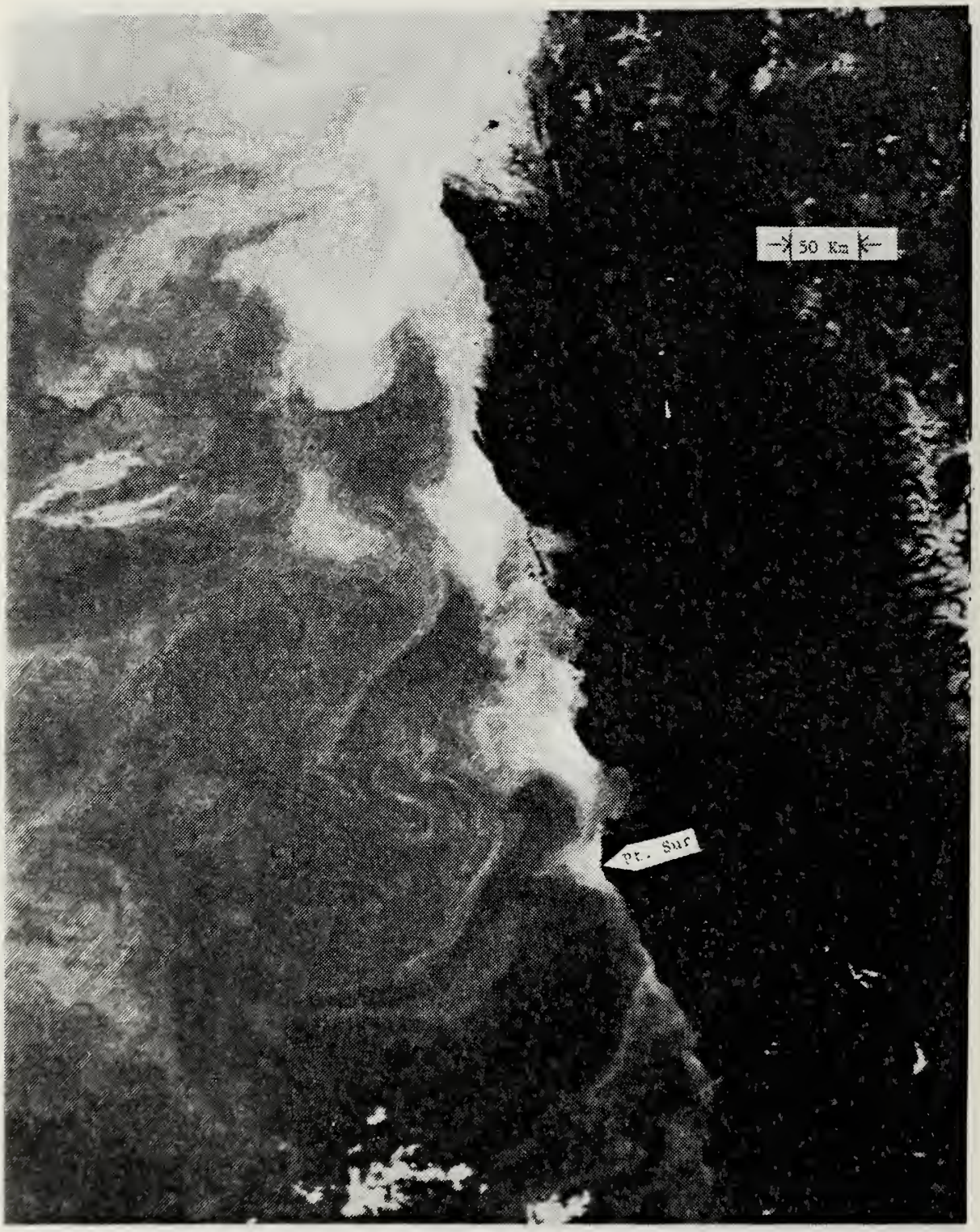

Figure 58. AVHRR IR satellite image acquired on August 1, 1980 at 1926 PST.

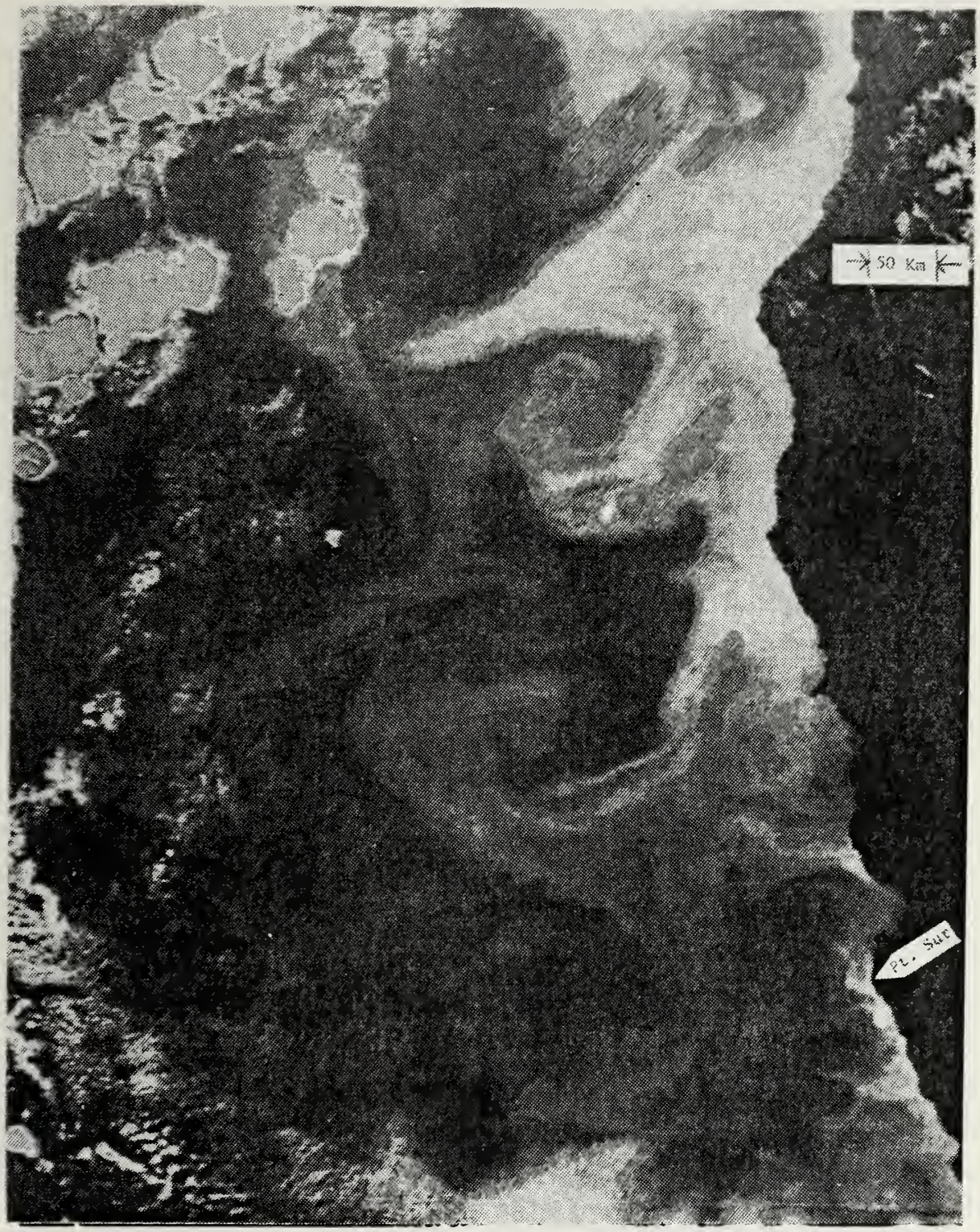

Figure 59. AVHRR IR satellite image acquired on September 20, 1980 at 1509 PST.

Figure 60. AVHRR IR satellite image acquired on April 4, 1981 at 0834 PST.

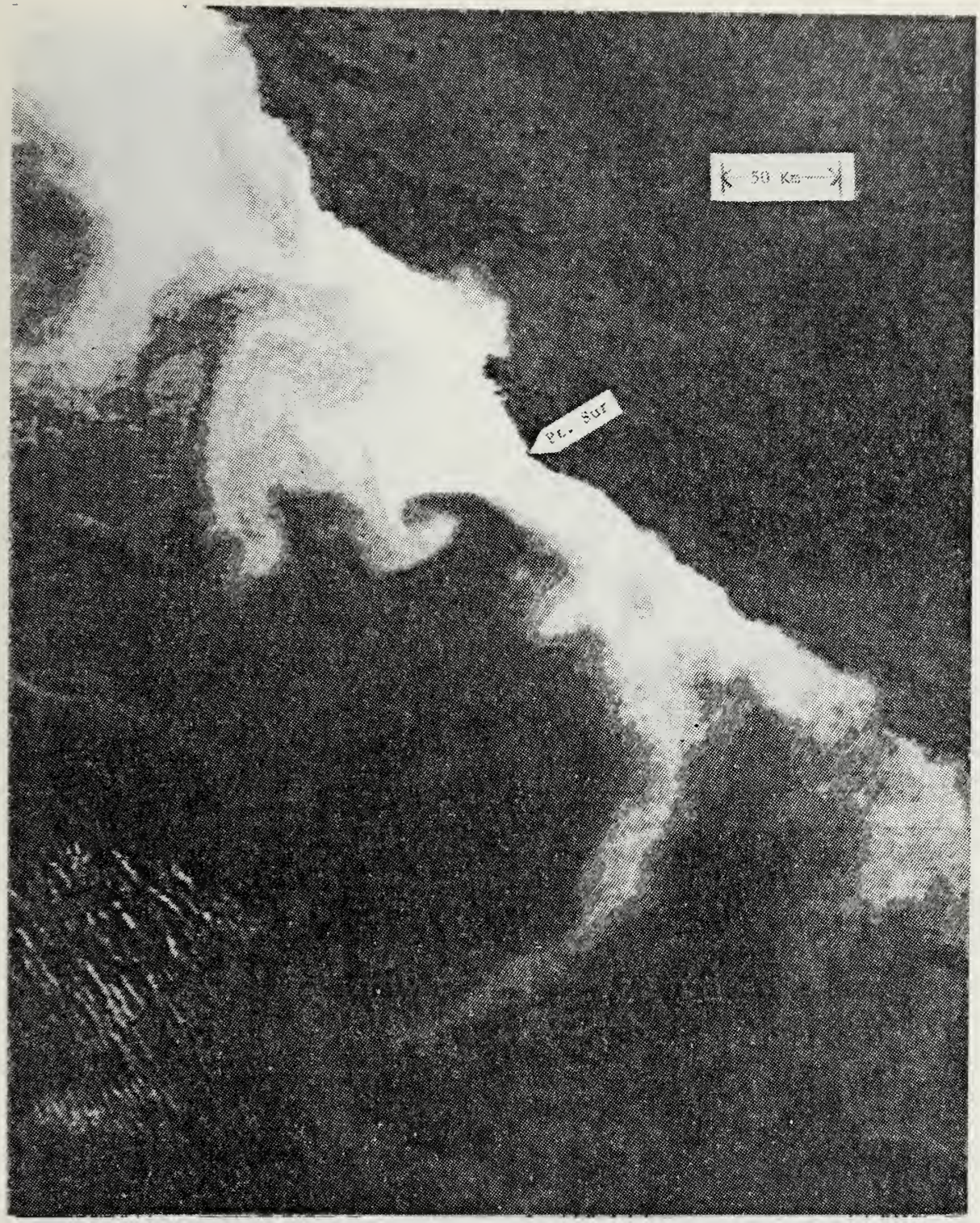

Figure 61. AVHRR IR satellite image acquired on June 10, 1981 at 0817 PST.

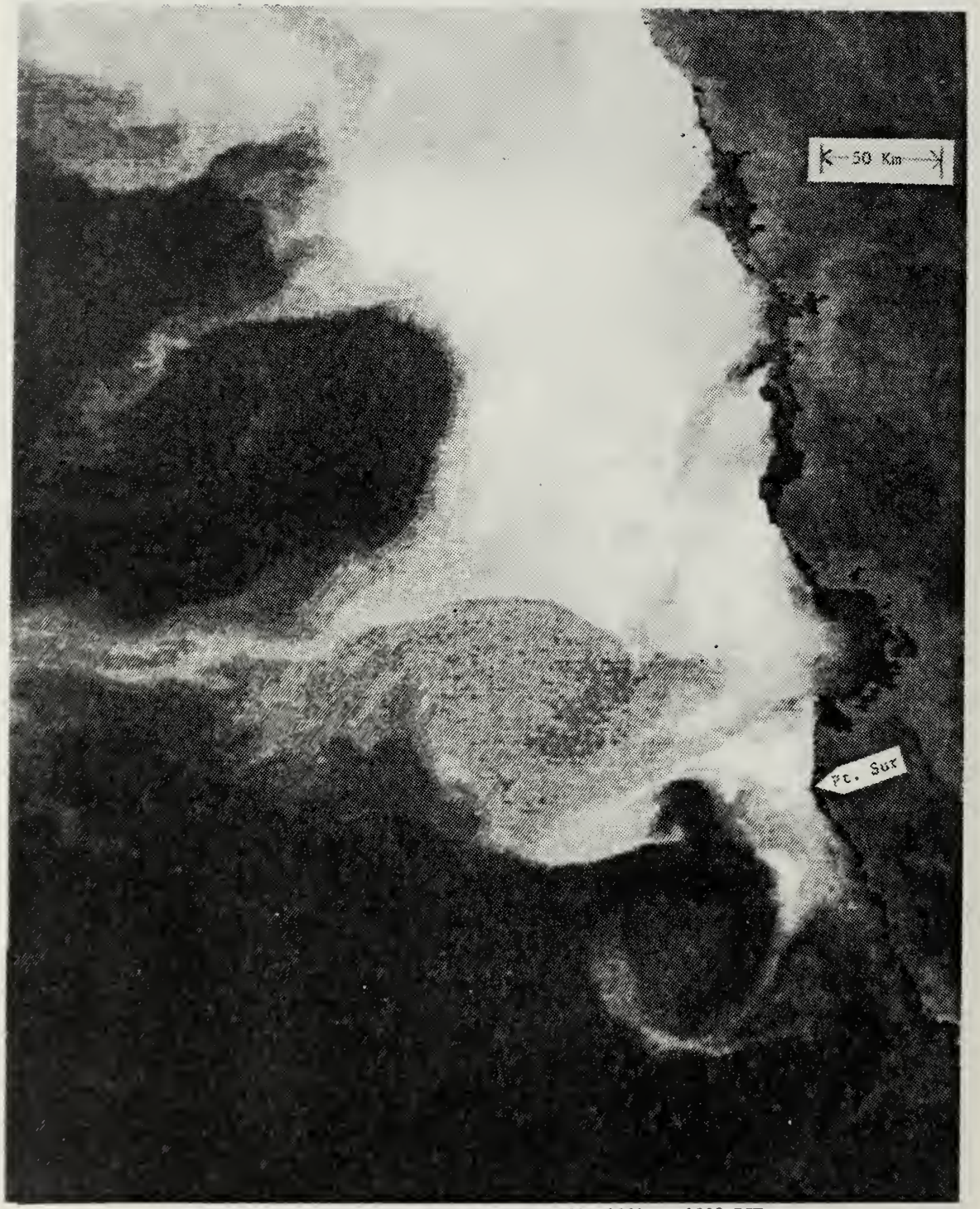

Figure 62. AVHRR IR satellite image acquired on June 21, 1981 at 1908 PST.

Figure 63. AVHRR IR satellite image acquired on July 7, 1981 at 1922 PST.

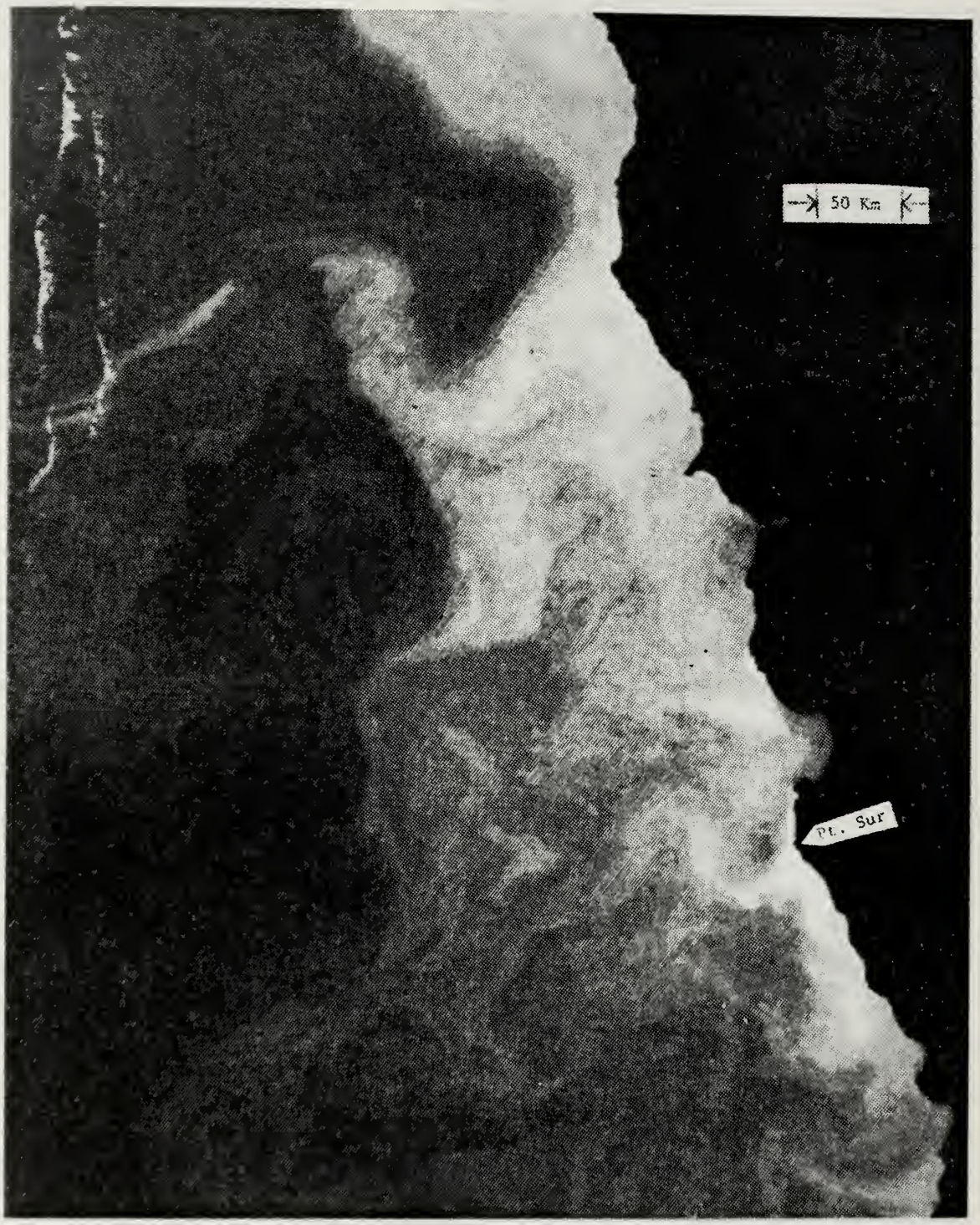

Figure 64. AVHRR IR satellite image acquired on September 19, 1981 at 1431 PST.

indicate that the area of most intense upwelling had moved north of Pt. Sur by this time. The image on June 21st clearly suggests the presence of an anticyclonic eddy southwest of Pt. Sur near the Davidson Seamount. The final image (Fig. 64) shows cool water extending hundreds of kms offshore between San Francisco and Pt. Conception, somewhat similar to conditions indicated at this time in 1980. By October, offshore waters may have cooled enough so that it is not possible to distinguish coastal waters from offshore waters on the basis of temperature.

IR satellite imagery suggests the same seasonal trend in upwelling zone expansion off the Central California coast in other years between April and September, but the details of this process vary considerably from year-to-year as seen by the comparison of the second and third sequences above. This seasonal expansion of the upwelling zone off Central California is to be contrasted with upwelling off the coast of Oregon (north of Cape Blanco), where the region of surface cool water is usually restricted to a narrow coastal band on the order of one R_{bc} throughout the summer. Thus off the Central California coast the R_{bc} may be an appropriate length scale for coastal upwelling, only during the early portion of the upwelling season.

In summarizing the changes that apparently take place with respect to upwelling along the Central California coast on seasonal time scales, usually in March or April, cool water first appears along the Central California coast around certain capes and/or in narrow bands along the coast. During this initial or restricted phase the offshore extent of coastal upwelling is on the order of the R_{bc}. Within a few weeks the upwelling has generally started to expand and intensify somewhat around capes and along the coast. During this intermediate phase the upwelling starts to spread offshore but is often contained within a coastal region where bathymetric control is apparently important. Bathymetric influence may be important out to depths of at least 1000m. By mid-June the upwelling has often expanded beyond the region of bathymetric influence. During the third extended phase, elongated filaments of cool water may extend 100's of kms offshore.[6] Typically these filaments trail off to the southwest away from the coast, and can consistently be traced back to a coastal source region from which they apparently originate. By September, the differences between the cool filaments and the surrounding waters become less distinct. Water from the coast out to 200-300km offshore appears more uniformly cool. This scenario on upwelling along the Central California coast represents a composite "typical" picture, based on about 5 years of

observation including the two earlier sequences. Perhaps even more characteristic of the upwelling in this region, based on satellite coverage, is its year-to-year variability. Because of the large year-to-year changes in upwelling, when it starts, and how it evolves, for example, a one-year sample could be very unrepresentative.

E. OFFSHORE MOVEMENT OF THE MAJOR UPWELLING FRONTAL BOUNDARY

Generally, during the 44-day period encompassing the shipboard measurements, IR satellite imagery showed that the surface area associated with upwelling off Pt. Sur gradually expanded in the offshore direction. One or several mechanisms may contribute to this offshore expansion of cool water whose origins may be, in part, coastal, and in part local. Two possible mechanisms, offshore Ekman transport and Rossby wave dispersion, are considered in the following sections.

1. Offshore Ekman Transport

In the first case, it is assumed that the observed upwelling is mainly in response to the local wind stress. An offshore Ekman mass transport balance is assumed to hold:

$$\rho H(x)\ f u_e = \tau_w^{(y)} \qquad (3.2)$$

where f is the Coriolis parameter, u_e is the offshore velocity component (taken positive onshore) in the upper surface Ekman layer, $\tau_w^{(y)}$ is the alongshore surface wind stress component (taken positive poleward), ρ is the mean density in the surface Ekman layer, and H is the mean depth of this surface layer, of O(20m). When integrated over time and alongshore distance, (3.2) can be expressed in terms of a surface area, A, as:

$$A(T) = K\int_0^T \tau_w^{(y)}(t)\, dt \qquad (3.3)$$

where K represents an appropriate alongshore distance divided by ρ fH, and T is the elapsed time (0 to 44 days). The offshore extent of upwelling at time T (as indicated by its associated surface area) is a function not only of the existing wind field but of previous wind conditions as well. To test this idea, the time dependences of the upwelling surface area, as depicted by the IR satellite imagery, and of the integrated alongshore wind stress are examined statistically. Finally, the relationship between the upwelling surface area and the integrated surface wind stress is considered.

The upwelling surface area was estimated using the 31 IR satellite images between 2 May to 13 June 1980. In 22 out of the 31 occasions, the study area was both completely cloud-free and entirely within the field-of-view

of the satellite. The surface areas associated with these 22 images are considered in the following discussion.

As before, the alongshore domain extends 100km, from Cypress Point in the north, to Pt. Piedras Blancas, in the south. From Fig. 65B, the following are observed, (1) the images were not uniformly spaced in time as mentioned earlier, (2) the surface area increased more rapidly after 9 June than previously, and (3) the change in surface area over the 44-day period was large, from about 500km^2 on 2 May to over 3400km^2 by 13 June. The linear regression of area on time is given by $A(t) = 49.3t + 734.2$, where $A(t)$ is in km^2 and t is in days. The linear correlation coefficient between $A(t)$ and t is 0.79 and is highly significant ($>99\%$). The expression for $A(t)$, when differentiated with respect to time yields a u_e of about -0.5 cm/sec, indicating a mean offshore movement of the upwelling boundary. However this net movement offshore of the upwelling front does not preclude the possibility that portions of the boundary may have remained stationary, or actually moved shoreward, during this period, as indicated previously in the EOF analysis.

Two sources of wind data have been used to examine the coastal surface wind field. These data include the six-hourly synoptic-scale winds computed by FNOC for Pt. Sur, and the three-hourly coastal wind observations at Pt.

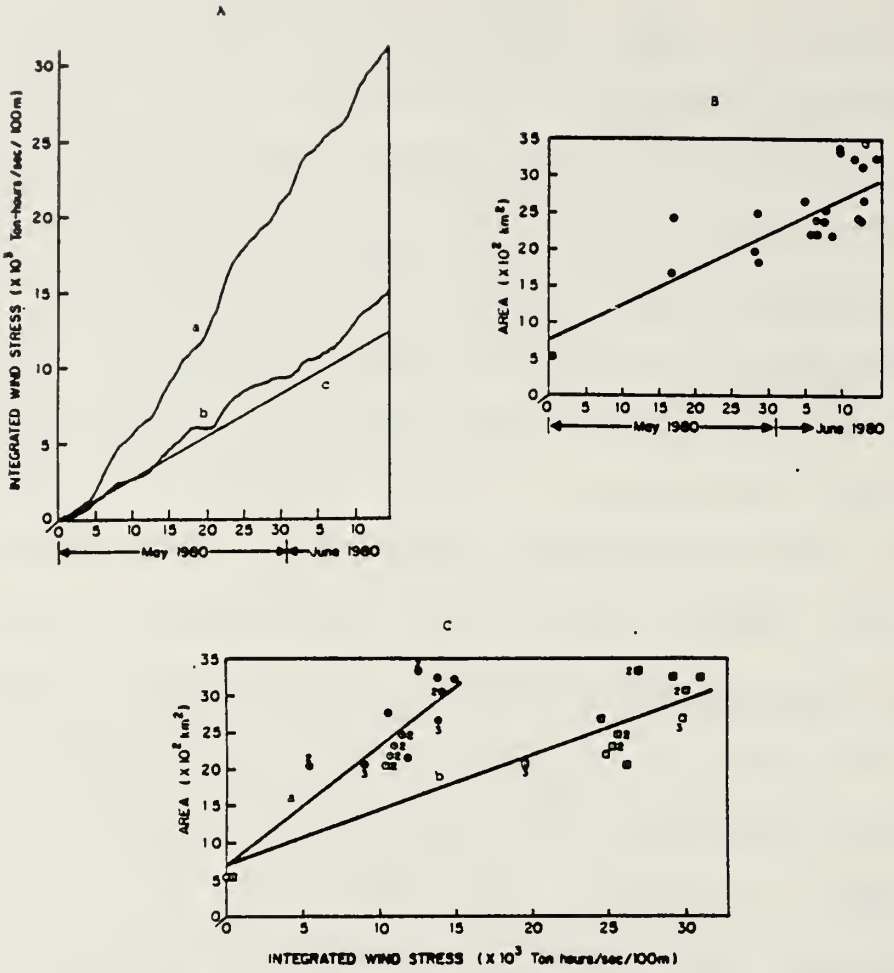

Figure 65. A comparison of coastal and geostrophic winds and surface upwelling areas obtained from IR Satellite Data for Pt. Sur. 65A: Integrated wind stress (i.e., the corresponding upwelling indices) versus time starting on 1 May 1980. The upper curve, b, corresponds to the time integral of the geostrophic wind stress and the middle curve, a, corresponds to the time integral of the coastal winds averaged between Pt. Sur and Pt. Piedras Blancas. t for each series is 6 hours. The line of constant slope labeled c, represents the time integral of u H. 65B: Linear regression between upwelling surface area obtained from the satellite data, and time starting 1 May 1980. This area is defined as the area separating the mean frontal boundary (MFB) offshore and the coast and bounded to the north and south by th approximate latitudes of Cypress Point and Pt. Piedras Blancas, respectively. 65C: Linear regression of Area vs Integrated Wind Stress (IWS) from the averaged coastal winds, a, and the geostrophic winds, b.

Sur and Pt. Piedras Blancas reported by the National Weather Service. The FNOC winds and the corresponding upwelling indices which represent the offshore component of the wind-driven Ekman transport, are calculated from the atmospheric pressure field using the geostrophic approximation plus an adjustment for Ekman veering and surface friction (Bakun, 1975). These indices as calculated represent a spatial average over about 3^{o} of latitude and longitude. The coastal wind observations have also been converted to upwelling indices using the same procedures. The upwelling indices at Pt. Sur and Pt. Piedras Blancas were first averaged between the two locations and then averaged over time to obtain six-hourly winds. Both sets of wind data were then integrated from Ø to 44 days and the results plotted as a function of elapsed time (Fig. 65A). The dependence of the integrated wind stress on time is approximately linear in both cases although the slope associated with the geostrophic winds is approximately twice that associated with the coastal winds. Since $\rho u_e H$ also represents the offshore Ekman transport, this quantity, when appropriately scaled, can be used as an independent estimate of $f^{-1}\int_0^T \tau_w^{(y)}(t)\,dt$, where u_e has been estimated previously from the satellite-derived surface areas, and H is of O(2Øm). A third line with constant slope is shown representing the time integral of $\rho u_e H$. The slope and position of this line is quite similar to

that for the time integral of the averaged coastal winds. H is often taken approximately as the MLD, which varies with location, particularly with offshore distance (Fig. 5). The time integral of the coastal winds has been taken over the entire 44-day period to obtain an estimate of H. This calculation yields a value for H of 26m, which compares favorably with the MLDs near the coast (Fig. 5). H is interpreted as an average value from the coast to the mean position of the upwelling front, taken over the period of integration. The time integral of the geostrophic winds over the same 44-day period yielded an equivalent MLD of slightly over 50m or almost twice the value obtained from the coastal winds.

Next, the relationship between the upwelling surface area and the Integrated Wind Stress (IWS) is considered, (Fig. 65C). The number of surface areas has been reduced from 22 to 13 by averaging areas estimated on the same day (local time). This procedure helped to reduce some of the random variability that arose in the measurement of surface area. The linear regression of surface area on IWS for the averaged coastal winds is; $A = 697.6 + 0.164$ (IWS), and for the geostrophic winds is; $A = 719.3 + 0.075$ (IWS), where A is in km^2 and IWS is in 10^{-3} ton-hours/sec/100m. The linear correlation coefficients associated with these regressions of surface area versus

integrated wind stress are Ø.9Ø and Ø.88 for the coastal winds and geostrophic winds, respectively. Both correlation coefficients are significant at a confidence level exceeding 99%. These results appear to support the original ideas expressed in equations (3.2) and (3.3). However, as is well known from statistics, because two variables are highly correlated does not necessarily indicate a direct cause and effect relationship between them. Other processes could also account for the observed offshore movement of the major upwelling boundary.

The time integral of the geostrophic winds reached a value almost twice that of the time integral of the coastal winds at the end of 44 days. An equivalent MLD of over 5Øm would have been obtained if this value had been used, a depth far greater than that observed. However, from the limited data used in this analysis, it is not possible to address this discrepancy between the two sources of wind data.

The apparent agreement between the time integrals of $\rho u_e H$ and $\tau_w^{(y)}/f$ could be fortuitous. For example, it has been assumed that the upwelling front which has been used to estimate offshore movement, moves as a material surface. This assumption implies that no mixing takes place across the front. However deSzoeke and Richman (1981) have shown that the momentum imparted by the alongshore wind stress undoubtedly causes mixing and

entrainment as well as upwelling at least within a baroclinic radius of deformation of the coast.

2. Rossby Wave Dispersion

An alternative to the previous explanation for the observed offshore movement of the major upwelling boundary is now considered. When the β effect is taken into account in eastern boundary current regions, it has been shown that over periods of several months, Rossby wave dynamics may be important (Ichiye, 1972; Anderson and Gill, 1975; McCreary, 1977; and Philander and Yoon, 1982). According to Philander and Yoon (P/Y) Rossby waves excited by time-dependent wind forcing along the coast may give rise to a complex system of equatorward and poleward flowing currents near the coast. They propose that Rossby waves may be responsible for the observed complexity of the system as described by Hickey (1979). From their analysis, P/Y derive a modified length scale for coastal upwelling expressed as

$$R_r = \beta T / (\ell^2 + \lambda^{-2}) \qquad (3.4)$$

where ℓ is a meridional wavenumber, $\lambda = R_{bc}$, $\beta = \partial f / \partial y$, and T is the time interval. Since $\beta / (\ell^2 + \lambda^{-2})$ represents the phase speed, s, of a non-dispersive Rossby wave, R_r then represents the distance travelled by a Rossby wave in time T. For non-dispersive waves, s also

represents the group velocity, while β/ℓ^2 represents the barotropic group velocity. The frequency equation for s arises from a vorticity equation previously derived by Anderson and Gill (1975) and given in the following form:

$$\frac{\partial^3 U}{\partial x^2 \partial t} + \beta \frac{\partial U}{\partial x} - (\ell^2 + \lambda^{-2}) \frac{\partial U}{\partial t} = (fH_o\lambda^2)^{-1} \frac{\partial \tau_w^{(y)}}{\partial t} \qquad (3.5)$$

where X is taken positive to the east,

U = Basic state zonal velocity

$\tau_w^{(y)}$ = Meridional wind stress

Ho = Total water depth for the barotropic mode or an "effective depth", Hn, for the baroclinic modes, where

$$Hn << Ho \text{ for } n \geq 1$$

In (3.5), the 3rd term on the L.H.S., and the R.H.S., represent the Ekman balance; this advective contribution is expected to be important on shorter time scales. On longer time scales, the β term becomes important, resulting in the wavelike contributions to the final solution. When the waves are long and non-dispersive, Lighthill (1969a) showed that the first term in the L.H.S. of (3.5) becomes small in comparison to the other terms, and thus to a first approximation can be neglected. Then (3.5) becomes a simple first-order differential equation whose solution P/Y have expressed as follows:

$$u = \frac{2\tau_w^{(y)}}{fH} \text{ Sin } (\frac{\pi x}{sp}) \text{ Sin } \{\frac{\pi}{sp} (x + 2st)\} \qquad (3.6)$$

where

P = the period of forcing associated with $\tau_w^{(y)}$

For (3.6) to be a solution to (3.5), the phase speed, s, must be given by $\beta / (\ell^2 + \lambda^{-2})$. According to (3.6) if the waves are long and non-dispersive, they propagate westward at a phase speed s only where forcing is not present; in regions of forcing the phase speed is 2s. In order to compare these scales with observed values, s is evaluated. An estimate for this quantity already exists from the previous regression analysis of upwelling surface area versus time in section E.1. A reasonable value for L ($\ell = 2\pi/L$) is taken as the distance between major capes along the Central California coast where upwelling is often observed to be more intense. These capes include Pt. Reyes, Pt. Sur, and Pt. Conception. Thus a value of 175km for L is assumed. A value of 18km is taken for R_{bc}. R_{bc} has been estimated from continuous Brunt-Vaisala frequency profiles calculated from density data acquired during the Pt. Sur upwelling center study at approximately 40km offshore. The details of this calculation are presented in Appendix A. β is taken as $2.0 \times 10^{-11} m^{-1} sec^{-1}$. A value of 0.25 cm/sec is obtained for s, using the values above. If 2s is taken as the phase speed then a value of 0.5 cm/sec results, which is consistent with the velocity obtained from the previous regression analysis of the satellite data (Fig. 65B). Whether s or 2s is used in this

case depends in part on the validity of the original assumptions in deriving (3.5), and on whether the regions of observation and forcing coincide. Equation (3.5) was derived assuming that the Rossby waves are non-dispersive; however at low wavenumbers this assumption breaks down. The assumption that the regions of observation and forcing coincide is reasonable. Overall, whether s or 2s is used for comparison, the agreement is close. However, this level of agreement may be somewhat fortuitous since the overall movement of upwelling away from the coast did not appear to be a linear function of time. The images shown in the second sequence of the previous section span a period of 70 days. For a period of 70 days (3.4) yields a spatial scale of approximately 30km. Because of the extreme longshore variability in upwelling depicted in the imagery, particularly towards the end of the sequence, it is difficult to establish the adequacy of this scale estimate. However, because this offshore scale is time-dependent, it appears to be more applicable, at least along the Central California coast, than R_{bc}.

Satellite observations on the type and distribution of low clouds are also consistent with the existence of an upwelling zone which tends to broaden considerably offshore along the Central California coast. Satellite observed low clouds, and separate observations of SST along the California coast have shown that stratiform clouds are

usually associated with cool water in this area (Gerst, 1969; Simon, 1976). Cold upwelled water cools the incoming moist marine air and as it cools it condenses forming stratus[7].

From visual satellite data acquired over several years, Simon (1976) analyzed imagery for cloud type and percent cloud cover along the California coast. Stratus was found to occur consistently from May to September between the coast and 125W. Fig. 66 shows his results for July (1975). His cloud contours tend to parallel the zone of upwelling observed independently in cloud-free IR imagery between about 35 and 40N.[8] Additionally however the cloud cover analysis acts to smooth out the boundary of cold water below and thus provides perhaps a more general indication of the offshore extent of cold water and of its latitudinal dependence. That this region of cold water tends to broaden between Cape Mendocino (40N) and Pt. Conception (35N) is also consistent with expected Rossby wave behavior. As shown by Lighthill (1969b), Rossby wave speeds increase approaching the equator because of the decrease in f with latitude.

The importance of westward propagating Rossby waves originating in the eastern Subtropical North Pacific has been discussed in detail by White and Saur (1981), and White (1982). White and Saur used the depth of the 9C

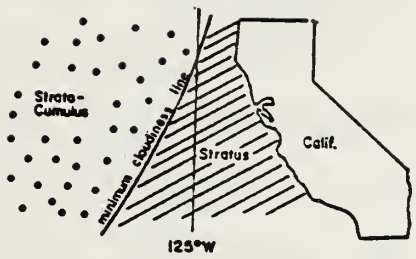

Predominant Cloud Types during Summer

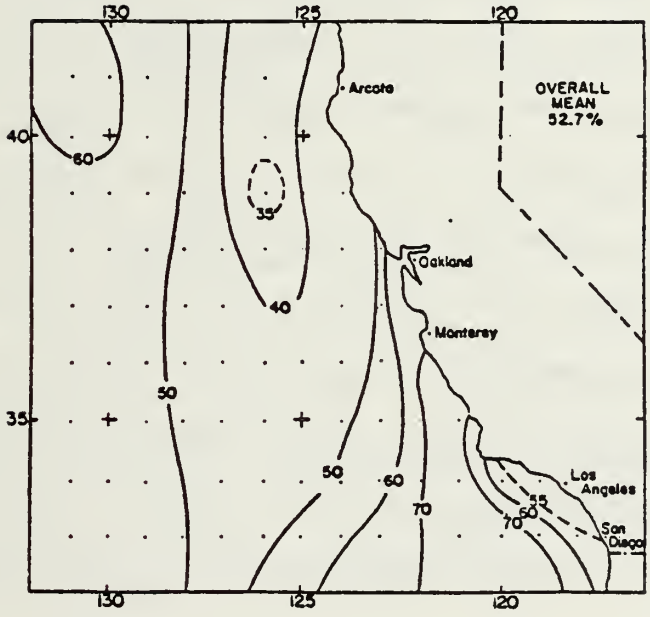

Mean Low Cloudiness, Percent. July, 1975

Figure 66. Distribution of mean low cloudiness along coast of California. Upper panel shows the location of the boundary that separates stratus and strato-cumulus cloud types. Lower panel shows percentile distributions of mean low cloudiness obtained from satellite imagery for July 1975 (Simon, 1976).

isotherm and surface salinity to identify westward propagating annual baroclinic long waves along a line from San Francisco to Honolulu. They concluded that large amplitude values of wind stress curl near the eastern boundary could act as a generating mechanism for baroclinic long waves observed further west. White (1982) found evidence for westward propagating wavelike perturbations emanating from the eastern boundary between 35 and 45N, using XBT data. These waves had wavelengths of 500 to 1000km and periods of one to two years. Further analysis yielded phase speeds of 1.4cm/sec at 45N, increasing to 2.7 cm/sec at 35N. This reduction in phase speed with increasing latitude is consistent with previous observations on the variable width of the upwelling zone based on cloud cover statistics. The actual values are somewhat higher than the previous value of 0.25-0.50 cm/sec determined from an analysis of the satellite data. However, White used data extending from the U.S. West Coast out to 180W, a region over which global and local estimates of phase speed would not be expected to agree because of the significant changes that occur in the internal density field.

In summary, the model presented by Philander and Yoon contains certain results which are consistent with the variability observed from satellite data along the Central California coast. The concept of a coastal jet gradually

dispersing into westward propagating Rossby waves on a several month time scale is consistent with the SST patterns indicated by the satellite data between about April and September. However, carefully planned *in situ* measurements taken over the appropriate space-time scales will be required to firmly establish the importance of Rossby waves in this region. The above model also provides an offshore scale which appears to be more representative along the Central California coast than the Rossby radius of deformation.

3. Comparison of Results

Two possible explanations have been given for the observed offshore movement of the major upwelling frontal boundary. Either, neither, or both explanations could apply. However, based on the limited information available, it is considered likely that both mechanisms are important. A scale analysis of equation 3.5 which includes both the Ekman balance and the β term, shows that on time scales of days-to-weeks, offshore Ekman transport is likely to be important whereas on time scales of several months, Rossby wave dispersion dominates.

F. SUMMARY OF RESULTS

To justify the application of IR satellite data to the present study, several preliminary comparisons with the *in situ* data were undertaken. The locations of corresponding

boundaries and patterns were compared rather than absolute temperature values. In the first comparison, the location of the satellite-derived mean frontal boundary was found to lie about 4km seaward of the high-gradient zone in SST estimated from the in situ data. Also a surface band indicating the region where the pycnocline appeared to intersect the surface was shown. This band was found just shoreward of the satellite-derived thermal boundary. In a second comparison, thermal boundaries obtained from near-surface thermalsalinograph data were compared with the satellite data. Agreement varied between the two sources of data. However, near the coast, where the gradients were generally more intense, the correspondence was good. Finally, a map of dynamic height from Phase 1B (Ø/2ØØm) was compared with an IR satellite image taken approximately 4Ø hours later; the patterns were generally similar. Overall, these comparisons were favorable in view of (1) the inherent differences in the types of data being compared and (2) the lack of synopticity between the data sets.

The mean position, the standard deviation, and the extremes of the major frontal boundary were calculated from a sequence of 31 images between May 2 and June 13, 198Ø, between Cypress Pt. and Pt. Piedras Blancas. The similarity between the mean frontal boundary and the underlying bathymetry was strong. The mean frontal boundary was shifted slightly to the south, however, with

respect to the isobaths directly off Pt. Sur. This offset may be related to southward advection associated with the equatorward surface jet.

A number density plot was constructed from the imagery showing the probability of encountering surface water within the zone of coastal upwelling around Pt. Sur. Again, the influence of bathymetry on the shape and orientation of the contours of probability was obvious. Bathymetric influence was apparent at least out to the 1000m isobath.

EOFs for the major upwelling boundary were calculated from several-month sequences of satellite images for 1980 and 1981. The purposes of these calculations were to estimate (1) the spatial scales for alongfront variations, and (2) the time scales from the time series of principal components. The first EOF for the 1980 sequence indicated a frontal meander with a spatial scale of about 80km over a period of 30 to 40 days. Zero-crossing distances with respect to the mean frontal boundary yielded scales ranging from 44 to 90km for the first four modes for 1980, and from 8 to 96km for the first four modes for 1981. Although the zero-crossing distances were generally similar over the first 5 modes for both 1980 and 1981, the nodal locations were usually different for corresponding modes. Due to the shortage and non-uniform distributions of samples, the

principal component sequences were generally difficult to interpret.

To help quantify the relationship between the local bathymetry and the surface temperature field, the mean frontal boundary and the first four EOFs from the 1980 sequence were lag-correlated with the 100, 500, and 1000m isobaths. The mean frontal boundary and the first four EOFs were each correlated with the 100, 500, and 1000m isobaths, at values of 0.82 or greater. Also there was a tendency for the mean frontal boundary and the EOFs to be displaced slightly to the south with respect to the local isobaths, consistent with the previous observations based on Figs. 28 and 29.

In Section D, three sequences of IR satellite images were presented. The first sequence helped provide continuity between Phases 1 and 3. The sequence indicated that upwelling was continuous between phases, although certain small-scale changes in the surface temperature field were observed. In particular, the region of cool water off Pt. Sur expanded offshore ($\sim$ 25km) and a protrusion of cool water developed further south. These changes are consistent with the offshore movement of the surface baroclinic zone observed from the <u>in situ</u> data over the period between phases. These satellite data also indicated that small changes in surface temperature could take place within two days. This time scale is also

consistent with the observed changes in the in situ data between Phases 1A and 1B and/or between 3A and 3B.

The second sequence of images was presented spanning a period of almost 5 months, starting on May 2, 1980. This sequence demonstrated the gradual offshore seasonal expansion of the coastal upwelling zone. The third sequence of IR satellite images provides additional coverage of the Central California coast for 1981. This sequence, covering the period of April 4th to September 19th, 1981, also indicated a seasonal expansion of upwelling along the Central California coast during approximately the same period. This sequence also emphasized the interannual variability in coastal upwelling that characterizes this region.

These results suggest that the Rossby radius of deformation is not a representative offshore scale for the region apparently influenced by coastal upwelling, except perhaps in the early stages during April and/or May.

In Section G, two possible explanations for the gradual offshore movement of the major upwelling frontal boundary, as observed through two sequences of satellite images, are presented.

First, a simple model based on an assumed Ekman balance between the Coriolis force and the alongshore wind stress is proposed. This balance indicates that the upwelling

surface area should be directly proportional to the time integrated local wind stress. To test this relationship using existing data, the upwelling surface area out to the major frontal boundary between Cypress Pt. and Pt. Piedras Blancas, was estimated from the previous sequence of satellite images. The integrated wind stress came from two sources, the coastal winds at Pt. Sur and Pt. Piedras Blancas, and the synoptic-scale winds from FNOC. The winds at Pt. Sur and Pt. Piedras Blancas were then averaged. The integrated wind stress (from both sources) and the upwelling surface areas were both linearly correlated with elapsed time. Also the correlation between upwelling surface area and integrated wind stress was high (>0.90 for both sources of wind data). Although these high correlations tend to support the original balance of forces, other possible explanations for the observed offshore movement of the major upwelling boundary exist. Also the integrated geostrophic wind stress yielded an exceedingly high equivalent mixed layer depth, almost twice that obtained from the integrated coastal wind stress. This discrepancy between the geostrophic and coastal winds should be investigated.

A second possible explanation for the offshore movement of the major upwelling frontal boundary due to Rossby wave dispersion was proposed. By taking into account Rossby wave dynamics, Philander and Yoon derived a modified length

scale for the offshore width of the upwelling zone. This scale corresponds to the distance travelled by a Rossby wave in a given time and thus depends on phase speed. This scale has immediate appeal by virtue of its time dependence. The predicted Rossby wave phase speed compares closely with a previous estimate obtained from the sequence of satellite images using regression analysis. Over a period of 100 days, for example, the predicted phase speed yields an offshore scale of almost 50km.

Cloud types and distributions were also drawn upon to provide additional evidence for the offshore extent of cool water along the Central California coast during the height of the upwelling season. Stratus and hence cold surface water may extend as far west as 125W ($\sim$250km) off the Central California coast.

It was concluded that both offshore Ekman transport over periods of days-to-weeks, and Rossby wave dispersion over periods of several months probably contribute to the offshore movement of the major upwelling frontal boundary.

In summary, the satellite data not only complement the *in situ* data where they coexist, but they also extend the synoptic coverage and help to identify the important space-time scales of variability that are inaccessible from the standpoint of shipboard observations alone.

IV. TIME-SCALE ANALYSIS OF OCEAN TEMPERATURES OFF THE CENTRAL CALIFORNIA COAST

A. INTRODUCTION

In this chapter several time series of surface and subsurface temperature are analyzed. The time-scales of variability associated with temperature at several locations are estimated. First, time-scales for SST at Granite Canyon, Pacific Grove, and the Farallon Islands are estimated (Fig. 1). In addition, a time-scale analysis of subsurface temperature at a moored array on the continental slope off Cape San Martin is undertaken (Fig. 1). In estimating these time-scales, opportunities arose to examine the data from both statistical and oceanographic viewpoints at various stages in the analysis. Not only the results, but also the techniques used to obtain those results are emphasized. The techniques used in analyzing the various time-series generally follow Box and Jenkins (1976) under the heading of stochastic model building.

An important aspect of stochastic model building involves the partitioning of a time-series into its deterministic and random components. Once the deterministic components are identified, they are removed from the original series, after appropriate fitting with analytic functions. The deterministic components

themselves of course are of considerable importance since they must likewise be taken into account in establishing an overall sampling strategy. Deterministic components in fact frequently constitute the major source of variability that can be identified in the data. Time scales associated with the deterministic components are obtained from the fitting process. The residuals are then modeled in accordance with their random structure. The random residuals are also used to estimate the time-scales of variability, since they often determine an upper limit in establishing an adequate sampling plan. If deterministic components in the data are not first removed from the original series, the resulting scale estimates associated with the random residuals are often excessive. This point has not received the attention it deserves in most previous scale analyses of oceanic data.

In the following analyses, the major focus is on the time-series data acquired at Granite Canyon. However similar analyses have been conducted for SST at Pacific Grove and the Farallons. In sections 4.9, 4.10, and 4.11, the results from all three coastal locations are considered.

SSTs are collected regularly along the California coast at approximately 25 locations (SIO Reference 81-30, 1981). In view of the increasing interest in coastal circulation

with respect to the dispersal of pollutants and a continuing interest in fisheries, it is surprising that few systematic studies have been conducted to examine these records, particularly within the past 15 years. The coastal observations often extend over many years providing a unique opportunity to examine coastal variability over relatively long periods. Where measuring sites have a good exposure to the continental shelf and slope, SST may reveal physical processes that occur regionally as well as locally. In this regard, 12-year records of SST off the Central California coast at Granite Canyon, 15km south of Monterey, Pacific Grove, in Monterey Bay, and the Farallon Islands off San Francisco have been chosen for study. These data span a 12-year period starting in March of 1971 and ending in February of 1983. Granite Canyon has an excellent exposure to the deep ocean with the continental shelf extending less than 10km offshore. Pacific Grove lies inside Monterey Bay, and hence the data from this location are not necessarily representative of data acquired along the open coast. The Farallons are located about 40km off San Francisco and have a good exposure to the deep ocean.

Prior to the mid-1960's, SSTs along the U.S. West Coast were frequently examined and the results reported in the oceanographic literature. Usually the SSTs were monthly averaged. Based on surface and subsurface temperatures

along the California coast, Reid et al. (1958) suggested two different causes of seasonal variability in SSTs. The first is coastal upwelling; north of Pt. Conception the upwelling process decreases the seasonal range in temperature and increases the duration of cooler temperatures. The second cause stems from the importance of the coastal countercurrent; this flow to the northwest transports warm water from the south along the California coast, increasing surface temperatures during the fall. They also found that variations in temperature along the U.S. West Coast show considerable coherence over great distances and that major anomalies in temperature persist for several months.

Coastal SSTs and air temperatures are highly correlated and SST anomalies identified at coastal locations are often correlated with SST anomalies up to 250km offshore (Robinson, 1957). Roden (1963) found that non-annual extreme temperature fluctuations were coherent and in phase over distances of 200-300km. SST spectra along the California coast over several years exhibited strong peaks at 14.7 days; these peaks were probably the result of tidal aliasing and/or the spring and neap tides (List and Koh, 1976). They also found that a well-defined seasonal variation in SST was essentially absent between Pt. Conception and Monterey Bay. Surface and subsurface

temperatures across Monterey Bay were used to define three separate oceanic seasons for the Monterey Bay area (Skogsberg, 1936).

B. THE SOURCES OF DATA

SSTs at Granite Canyon, Pacific Grove, and the Farallons, are measured daily at approximately 0800 local time (Fig. 67). Because the data are sampled only once every 24 hours, the possibility of aliasing by the predominant semidiurnal tide exists. This problem is addressed later in the analysis. Temperatures are read to the nearest 0.1C using a calibrated VWR thermometer, and are considered accurate to about $\pm$ 0.2C (SIO Reference 81-30, 1981). As mentioned, the observations at all three locations span 12 years, starting on March 1, 1971 and ending on February 28, 1983. A one-year record of temperature sampled 5m below the surface on the continental shelf off Diablo Canyon is also included for comparison with the Granite Canyon data (Fig. 68). A 52-day record of temperature (November 25, 1978 to January 15, 1979), acquired from a moored array at a depth of 175m approximately 8km off Cape San Martin is also included (Fig. 94). These data were recorded to the nearest 0.01C.

Since the data from Granite Canyon (GC) have only been available since 1971 and since they have not been compared with other coastal temperatures, their representativeness must be determined. Consequently the Granite Canyon data

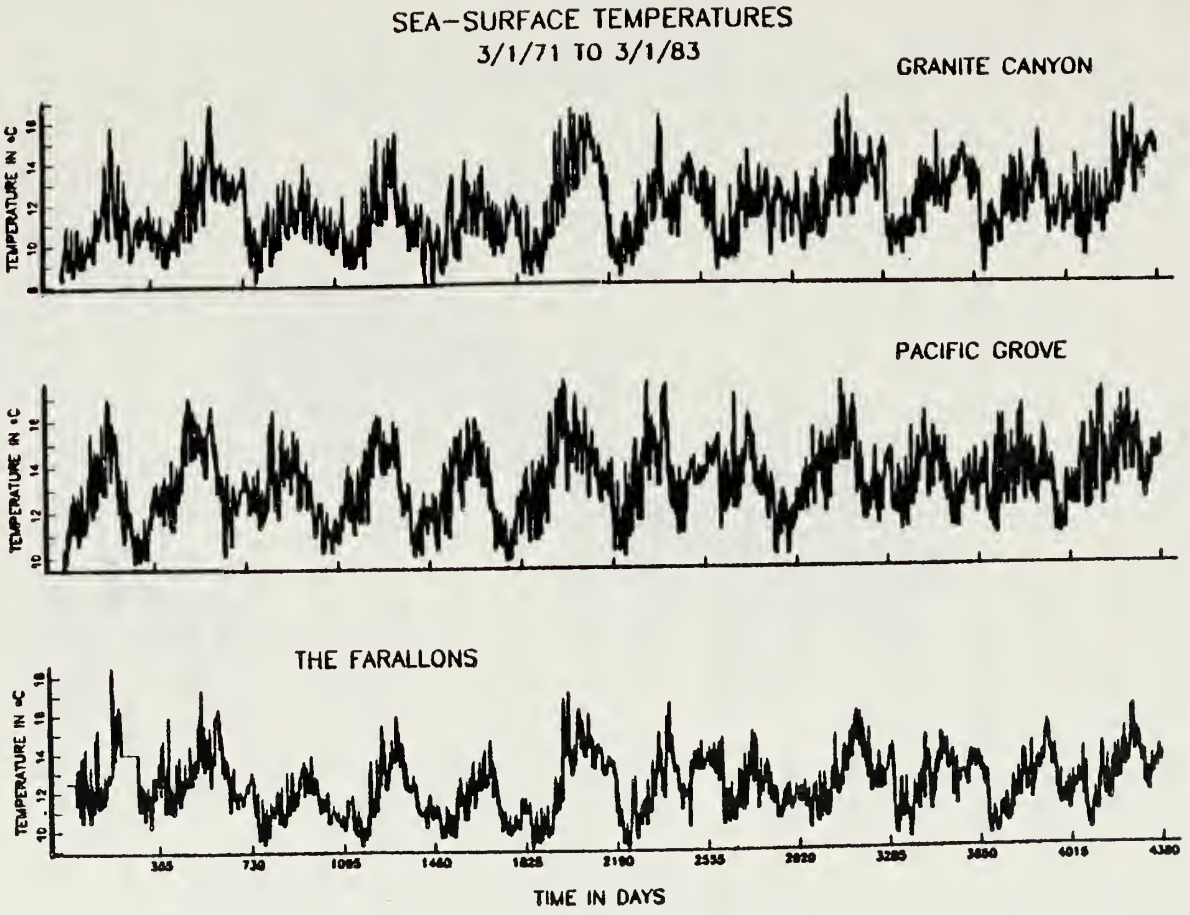

Figure 67. Sea-surface temperatures at Granite Canyon, Pacific Grove, and the Farallons. Observations acquired with immersion thermometers (+0.2C) daily at approximately 0800 local time. These 12-year records start on March 1, 1971 and end on February 28, 1983.

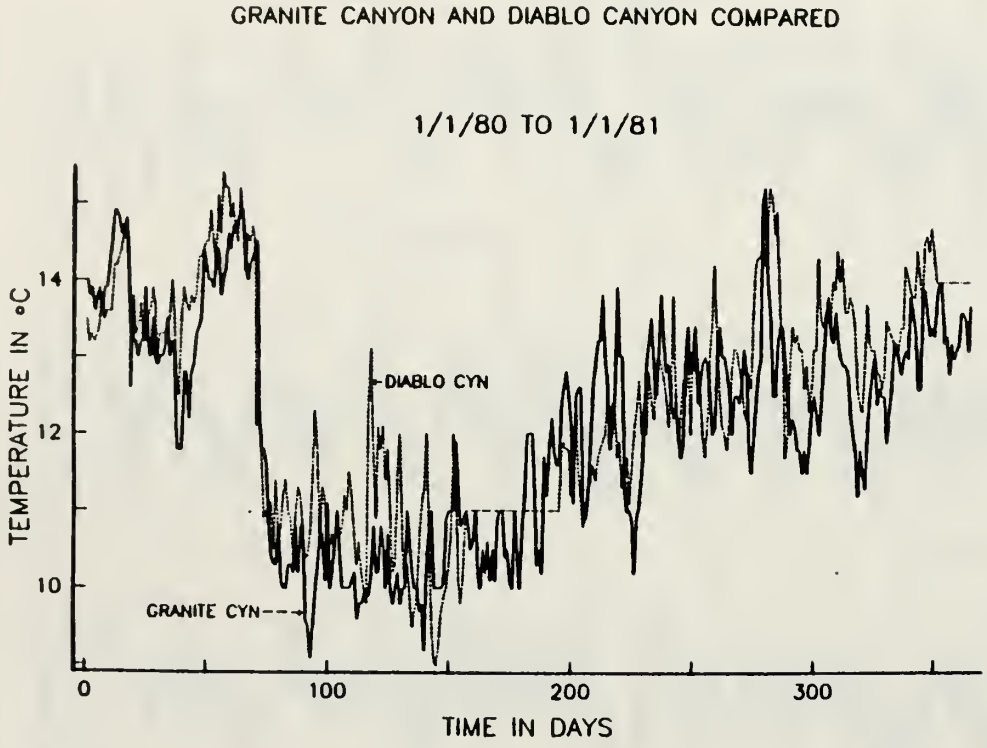

Figure 68. Sea-surface temperatures at Diablo Canyon (dashed) and Granite Canyon (solid) for the year 1980.

have been compared with several other data sets for periods where comparisons could be made. The annual variations in SST are generally similar at Granite Canyon, Diablo Canyon and the Farallons, but temperatures were consistently higher at Pacific Grove during the spring and summer months than they were at the other three locations. The annual cycles in SST for 1980 at Diablo Canyon, Pacific Grove, and the Farallons are compared with Granite Canyon in Figs. 68, 69, and 70. The annual cycles are generally similar but a major event identified as the spring transition to coastal upwelling is clearly observed in each of these figures. This phenomenon was identified for the first time just a few years ago off the coast of Oregon (Huyer et al. 1979).

Temperature data at four depths between 113 and 510m acquired from the moored array described above but for a shorter period (March 5, 1980 to April 7, 1980) are also compared with the SST data at Granite Canyon (Fig. 71). This period was chosen because it also includes the 1980 spring transition. This event can be identified from the raw data in a number of the annual cycles (Fig. 67 and Table 11). The drop in temperature associated with this event during March of 1980 can also be seen at each depth in Fig. 71, down to 510m.

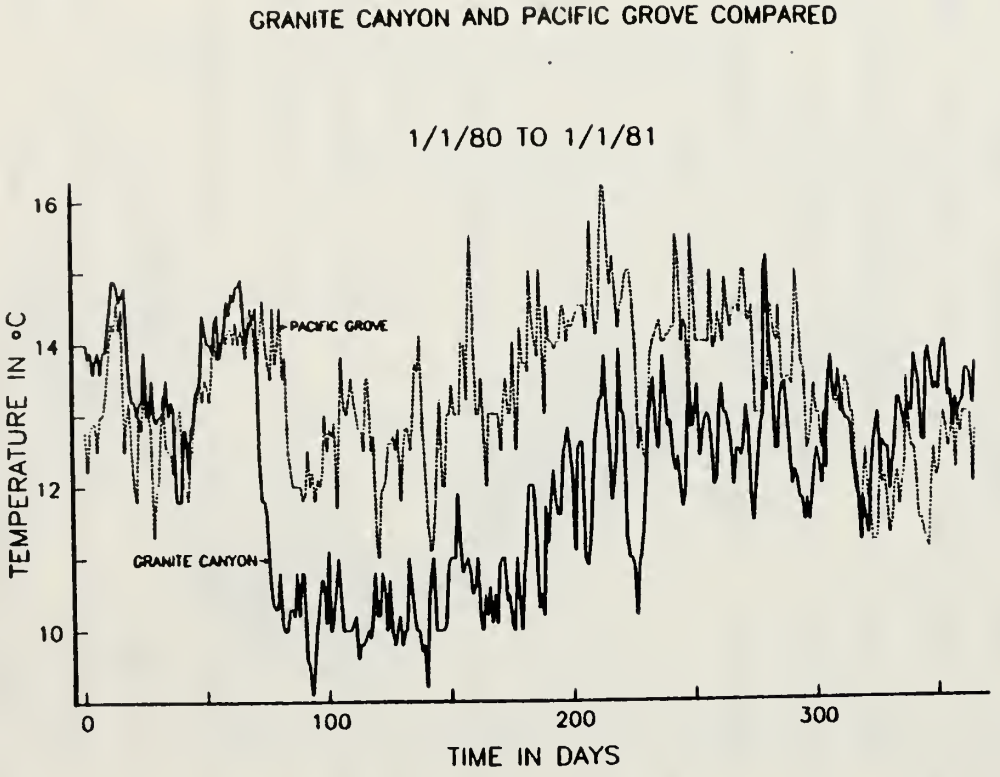

Figure 69. Sea-surface temperatures at Pacific Grove (dashed) and Granite Canyon (solid) for 1980.

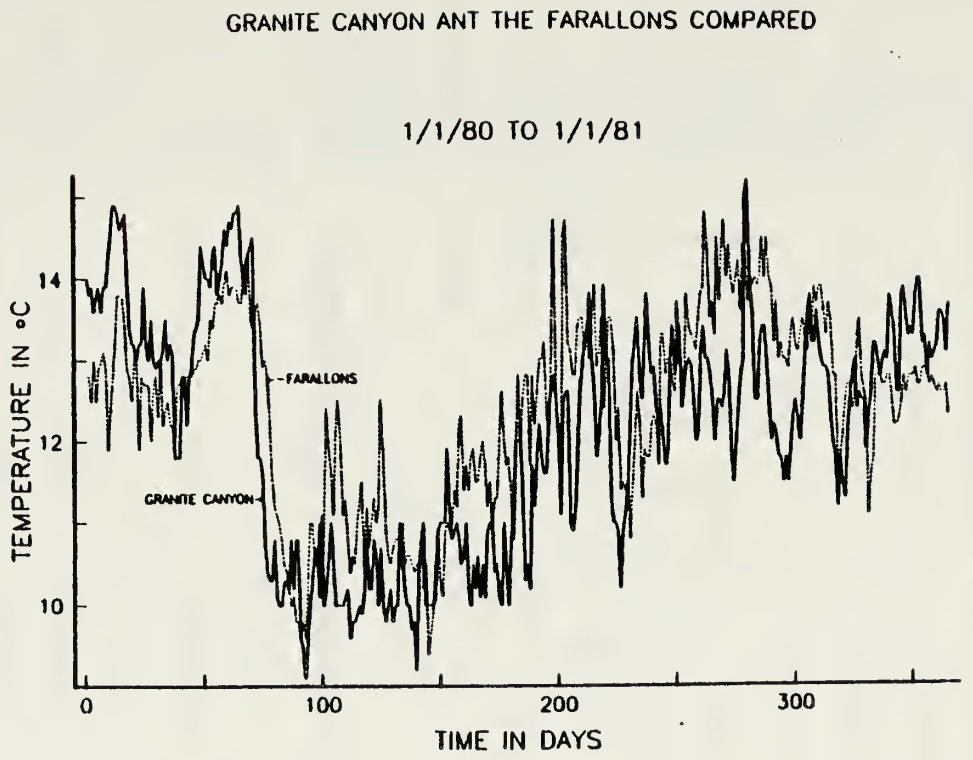

Figure 70. Sea-surface temperatures at the Farallons (dashed) and Granite Canyon (solid) for 1980.

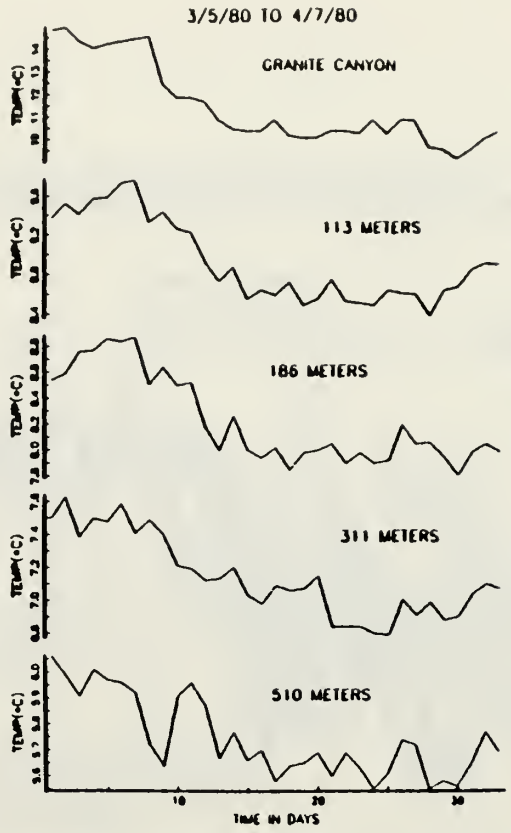

Figure 71. Sea-surface temperature at Granite Canyon, and subsurface temperatures approximately 8km off Cape San Martin (see Fig. 1). Subsurface temperatures acquired at 113, 186, 311, and 510m. Sample period extends from March 5, 1980 to April 7, 1980.

C. TRENDS IN THE DATA

Because details of the analyses at all three coastal locations (i.e., Granite Canyon, Pacific Grove, and the Farallons) are generally similar, the following discussion is devoted to the Granite Canyon data except for occasional comments on significant differences. Starting in Section J., results from all three locations are considered.

Fig. 72 shows a scatter plot of the temperature data versus day number. In most years fewer than three observations were missing from the raw data.[9] Linearly interpolated values were substituted for missing values. Since the individual observations in Fig. 72 are not connected, quantization of the data (Ø.1C) can be seen.

A significant feature in Fig. 72 is the positive slope that extends over the entire record. A least-squares fit was applied to the data assuming a linear trend yielding $y(t)=1Ø.9 + Ø.ØØØ37(t)$, where t is in days, and y(t) is temperature in ^{o}C. This relationship indicates temperature increasing from 1Ø.9 to 12.5C over the twelve-year period (t_{max} = 438Ø days). Higher-order polynomial fits to the data provide only slight improvement. However, this record may constitute only a part of a much longer cycle of fixed or variable period. The statistical significance of the trend parameter $\hat{\delta} = 3.7 \times 1Ø^{-4}$ is confounded by the presence

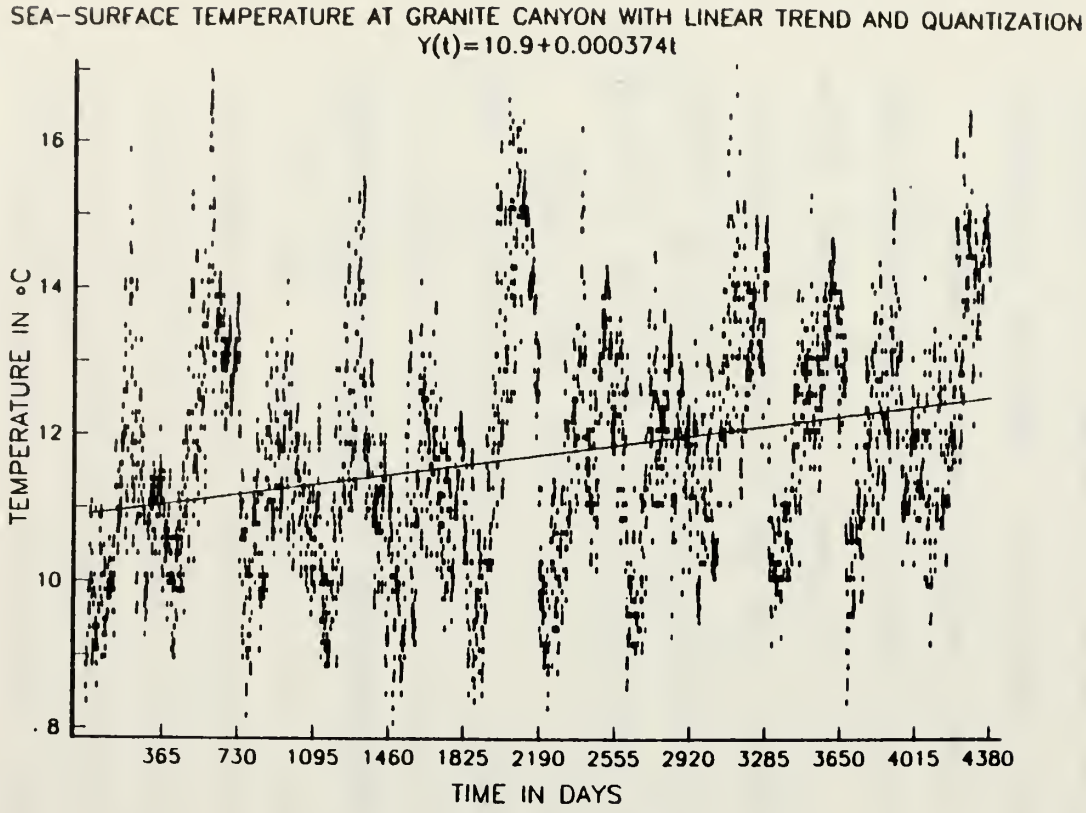

Figure 72. Scatter plot of sea-surface temperature versus day number at Granite Canyon. A least squares linear trend is superimposed.

of cycles and possible short term correlation in the data. Thus standard tests that $\delta = 0$ based on independent data are invalid. However, using simulation techniques to be described later, the standard deviation of δ was found to be 1.1×10^{-5} and hence the hypothesis that $\delta = 0$ is rejected at the 95% level of confidence. Increases in SST over the 12 year period were also found at Pacific Grove and the Farallons, but the slopes were somewhat less.

The gross features of the Granite Canyon SST's clearly include annual cycles, and inter-annual variability is apparent as well (Figs. 67 and 72). In particular, the El Nino events of 1972-73, 1976-77, 1979, and 1983 are readily apparent. Although the effects of El Nino events are sometimes restricted to equatorial regions and to regions along the South American coast, their influence often extends as far north as Central California (Bretschneider and McLain, 1983).

D. CYCLIC FIT AND DECOMPOSITION OF THE DATA

The Granite Canyon time series is next decomposed into an additive model of the form

$$y(t) = m(t) + s(t) + \varepsilon(t) \qquad (4.1)$$

where the trend m(t) is defined as a long-term change in the mean (Chatfield, 1980), s(t) consists of seasonal and cyclic changes, and $\varepsilon(t)$ is a stationary random sequence which describes the irregular fluctuations. The $\varepsilon(t)$

sequence is assumed to have mean zero, (i.e., $E(\mathcal{E}(t))=0$), constant variance, and possibly some serial dependence. That m(t), s(t) and $\mathcal{E}$(t) are treated as additive implies the gross assumption that the $\mathcal{E}$(t), as well as the variance, is not affected by m(t), or s(t).

The model (4.1) provides a conceptual framework; its usefulness and approximate validity must be established from the data. Thus, to estimate scales from the data, the different components must be identified.

Next let

$$y_1(t) = y(t) - m(t) = s(t) + \mathcal{E}(t) \qquad (4.2)$$

insofar as it can be observed. With the estimate $\hat{m}(t)$ = 10.9 + 0.000374(t) removed from y(t), the resultant is denoted as the first residual, $r_1(t)$, ignoring possible interaction between m(t), s(t), and $\mathcal{E}$(t).

Next the structures of s(t) and $\mathcal{E}$(t) are estimated by analyzing $r_1(t)$. The component s(t) includes seasonal terms such as the annual cycle and its harmonics, and terms with periods longer than a year which might be interpreted as global fits to the obvious long-term modulation of the annual cycle seen in Figs. 67 and 71. There may be cycles at shorter periods associated with the tides and the winds for example; these effects may be difficult to distinguish from other apparent cycles caused by high correlations in $\mathcal{E}$(t). Thus it is assumed that s(t) can be represented by a set of orthogonal basis

functions and associated coefficients in the following way

$$s(t) = \sum_{j=1}^{J} \{\gamma_j \cos(\omega_j t) + \beta_j \sin(\omega_j t)\} \qquad (4.3)$$

$$= \sum_{j=1}^{J} A_j \cos(\omega_j t + \theta_j) , \qquad (4.4)$$

where $\omega_j = 2\pi f_j = 2\pi / T_j$ are (unknown) frequencies corresponding to periods T_j, and $A_j = (\gamma_j^2 + \beta_j^2)^{1/2}$ is the amplitude at frequency ω_j . $\theta_j = \tan^{-1}(-\beta_j / \gamma_j)$ is the phase, and J is the number of cycles which comprise s(t). The γ's and the β's are estimated by the method of least squares.

Again it is noted that cycles with periods longer than one year may represent long-term random fluctuations and it may be unrealistic to predict long-term behavior on the basis of the model given in 4.3 for s(t) and m(t). Also, while the model includes cycles with periods shorter than a year, such cycles may not represent real cyclic behavior, but rather only the non-sinusoidal nature of the annual cycle and the abrupt change in that cycle which occurs during the spring transition (Table 11).

Positive identification of periodicities in s(t) may be non-trivial, even if the spectrum of the random component $\varepsilon(t)$

$$f(\omega) = \frac{1}{\pi}\left\{1 + 2\sum_{k=1}^{\infty} \rho(k)\cos(k\omega)\right\}, \qquad 0 \leq \omega \leq \pi, \tag{4.5}$$

where $\rho(j) = E(\mathcal{E}(t+j)\mathcal{E}(t))$, is constant (white). To find these periodicities in the presence of a non-white spectrum for the $\mathcal{E}(t)$'s, the following steps were followed:

1. Examine the periodogram of the first residuals, $r_1(t)$, to find possibly significant periodicities. Estimate s(t) as s(t). Given the chosen frequencies ω_j, this involves obtaining least squares estimates of the γ_j's and β_j's in the linear model (4.3). The least squares estimates of the amplitudes A_j are directly proportional to the periodogram values at the given frequencies (Bloomfield, 1976).

2. Examine the second residuals $r_2(t)=y(t)-\hat{s}(t)-\hat{m}(t)=r_1(t)-\hat{s}(t)$ to determine the properties of $\mathcal{E}(t)$. Determine if $\mathcal{E}(t)$ can be represented, as a pth-order autoregressive (AR) process,

$$\varepsilon(t) = a_1\varepsilon(t-1) + \ldots + a_p\varepsilon(t-p) + n(t), \tag{4.6}$$

where the n(t) are uncorrelated. Many geophysical processes in practice can be satisfactorily modeled as autoregressive; this representation implies persistence in the data over time, plus an autocorrelation function that ultimately decays exponentially (Bendat, 1958). Then estimate a_1 through a_p by least squares to be a_1 through a_p and then remove from the first residuals, $r_1(t)$, as

$$r_3(t) = r_1(t) - \hat{a}_1 r_1(t-1) \ldots - \hat{a}_p r_1(t-p). \quad (4.7)$$

Next examine the periodogram of these third residuals, $r_3(t)$, to ascertain whether the $\hat{s}(t)$ chosen in step (1) is still a "reasonable" representation of the seasonal and cyclic changes (global fit) for the data. The AR removal is performed because highly autocorrelated data will elevate spectral values near zero frequency, making it difficult to decide whether a given spectral peak is due to correlation or due to a periodicity in the data. Once the AR component is removed, a clearer picture obtains of which cycles should be included in s(t). Obviously some subjectivity is involved during these stages of the analysis.

3. Next use $r_3(t)$ to obtain a possibly refined $\hat{s}(t)$, then re-examine the structure of $\mathcal{E}(t)$ via a refined set of second residuals, $r_2(t)=y(t)-\hat{m}(t)-\hat{s}(t)$. Knowledge of the structure of $\mathcal{E}(t)$ may be important for determining the time scales of interest and for obtaining the final residuals, $r_4(t)$. Thus, if it is determined that $\mathcal{E}(t)$ has pth order autoregressive structure, possibly different from that in 2. above, the fourth residuals are computed as

$$r_4(t) = r_2(t) - \hat{a}_1 r_2(t-1) \ldots - \hat{a}_p r_2(t-p) \quad (4.8)$$

These residuals are used primarily to establish the overall goodness-of-fit of the estimated model, since the $r_4(t)$ process should have a white spectrum and a correlogram approximating a delta function if the model is reasonable. Secondly, they can be used in cross-correlation analyses with other data sets. Thirdly, they provide a basis for checking the assumptions made during previous stages of the analysis.

E. GLOBAL FIT AND CYCLIC COMPONENTS

Figure 73 (top panel) shows a cyclic fit s(t) with J = 13 terms to the first residuals (original data minus long term linear trend). The data consist of N = 4380 daily observations of temperature.[10] Thus if angular frequency is re-expressed at the discrete frequencies $\omega_p = 2\pi p/N$, where p is the "number of cycles per period of 4380 days", then the cycles removed from the data as components of s(t) have frequencies p = 12,24,94, corresponding to periods of one year, six months, and approximately 1.5 months, respectively. The remaining p = 2, 3, 4, 5, 6, 7, 8, 9, 11, and 18.

The determination of these frequencies follows Section D. First, Fig. 74 shows the estimated serial correlations of the first residuals

$$\hat{\rho}(k) = \sum_{t=1}^{N-k} (y(t) - \hat{m}(t))\,(y(t+k)-\hat{m}(t))/\{(N)S^2\}$$

$$= \sum_{t=1}^{N-k} r_1(t)r_1(t+k)\Big/\{(N)S^2\} \qquad (4.9)$$

13-TERM CYCLIC FIT OF LINEARLY DETRENDED DATA
(FIRST RESIDUALS)

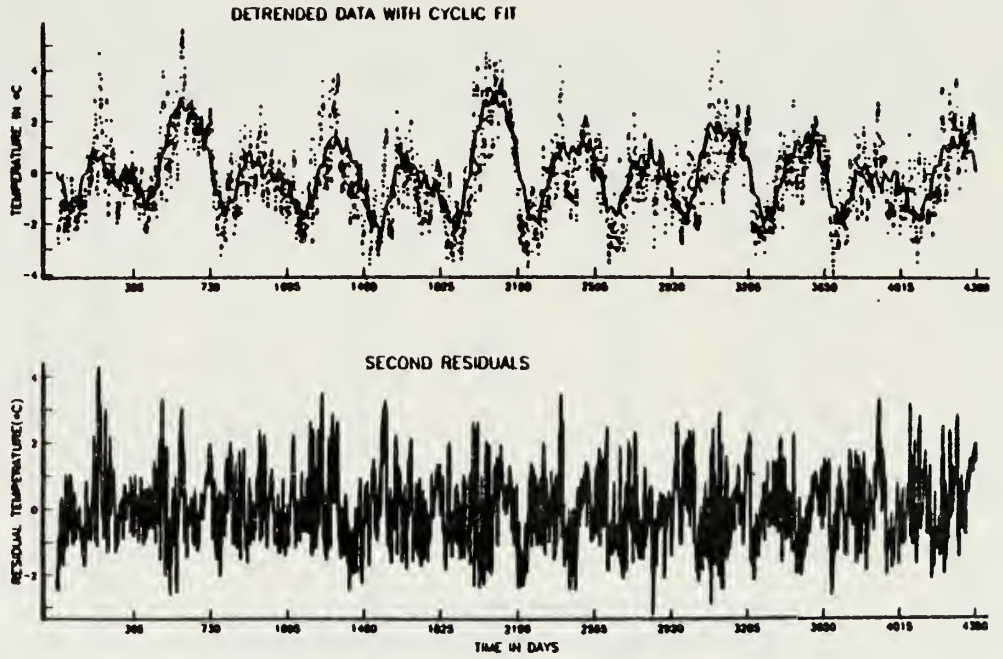

Figure 73. Upper panel shows a 13-term cyclic fit to the linearly detrended data at Granite Canyon. Lower panel shows the second residuals created by subtracting the detrended data with cyclic fit, from the original data.

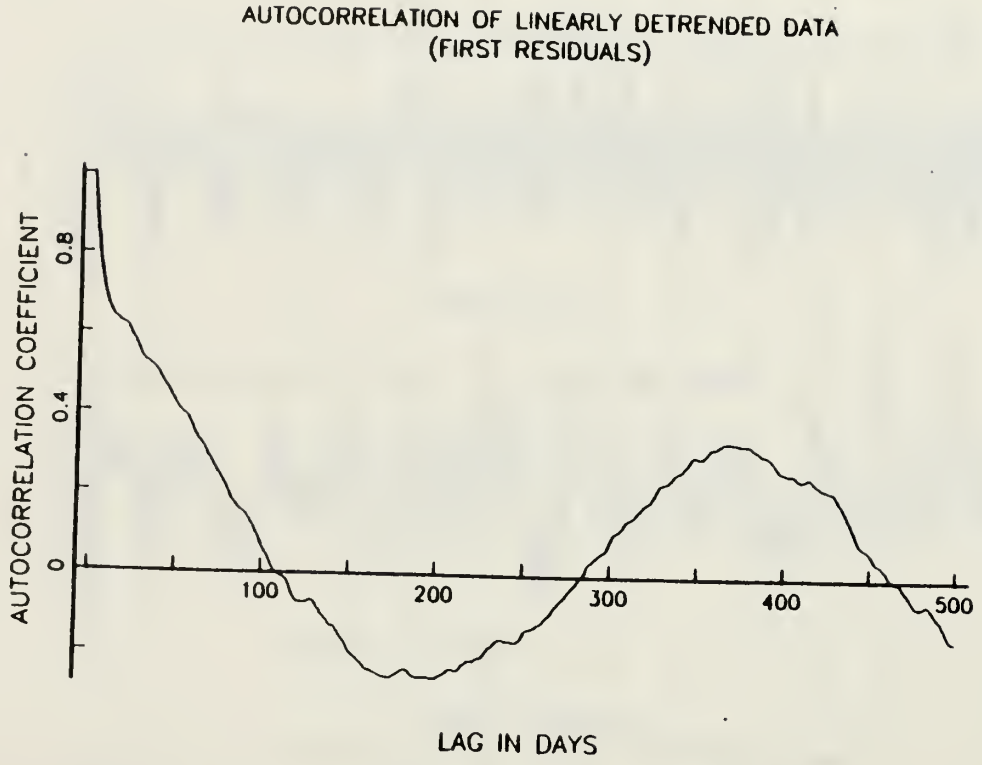

Figure 74. Autocorrelogram of linearly detrended data (first residuals).

where S^2 is the sample variance of the $r_1(t)$'s and 1 / N (vs. 1 / (N-k)) has been used as a normalizing factor. Thus $\hat{\rho}(k)$ is a biased estimator of the true autocorrelation function but as shown by Jenkins and Watts (1968), $\hat{\rho}(k)$ has a smaller mean square error than its unbiased counterpart and is thus to be preferred. The correlogram is dominated by the yearly cycle and therefore cannot be used to model the $\mathcal{E}(t)$, or to identify more than the yearly cycle itself.

A harmonic spectral analysis of the $\hat{\rho}(k)$'s is given by the periodogram of the first residuals, defined as

$$I_n(\omega_p) = \{A_n^2(\omega_p) + B_n^2(\omega_p)\} / (2\pi N), \quad p = 1,..,N/2 , \quad (4.10)$$

where

$$A_N(\omega_p) = \sum_{t=1}^{N} r_1(t) \cos(t\omega_p), \text{ and } B_N(\omega_p) = \sum_{t=1}^{N} r_1(t) \sin(t\omega_p),$$

are the real and complex parts of the discrete Fourier transform of $r_1(t)$, t=1,.., N. Here $\omega_p = \frac{2\pi p}{N}$ for p = 1,...,N/2 . Since the expected value of the periodogram for uncorrelated data is $\sigma^2/2\pi$, a normalized periodogram is used. The normalized periodogram is defined to be the result (4.10) multiplied by $2\pi/S^2$, where S^2 is the sample variance of the data being considered, namely $r_1(t)$. Periodogram analysis is one method of estimating the variance spectrum of a given time series. The periodogram and the spectrum are equivalent if the

appropriate degree of smoothing has been applied to the periodogram. Although periodogram spectral estimates are unbiased, they are not consistent (Chatfield, 1980). In most of the subsequent spectral computations, periodogram analysis has been used to achieve maximum spectral resolution.

The logarithm of the normalized periodogram of the first residuals from the Granite Canyon data, with confidence bands for individual components and for the maximum value of the periodogram components, is displayed (Fig. 75). These confidence limits are based on the approximation that each value in the normalized periodogram is independent with a chi-square distribution with two degrees of freedom. A major spectral peak occurs at p = 12, i.e., a period of one year. Also in the expanded periodogram (top panel) significant harmonics occur at p = 24 and 94. The latter frequency is surprising, since it is not an exact harmonic of p = 12. The full periodogram, because of its gradual decrease in amplitude with increasing frequency, suggests an autoregressive type spectrum for the $\mathcal{E}(t)$. Thus the distinction between true periodicities and autoregression at frequencies below 12 is difficult. Based on the considerations above, frequencies corresponding to p=2,3,4,5,6,7,8,9,11 and 18 are selected for removal, in addition to p = 12, 24 and 94.

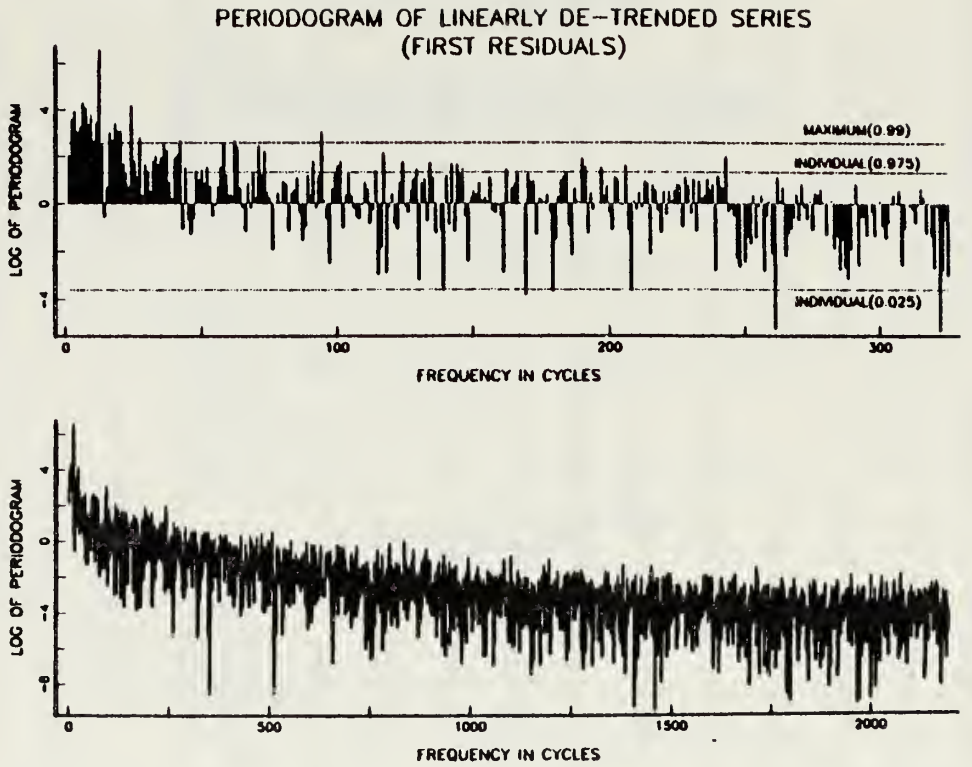

Figure 75. Upper panel shows a Log_e periodogram of the first residuals out to 325 cycles per 4380 days. Maximum (0.99) and individual (0.025, 0.975) confidence limits have been included. Lower panel shows the entire periodogram out to 2190 cycles per 4380 days.

The periodogram for the Farallon Island data was generally similar to the periodogram for the Granite Canyon data. However, the periodogram for the Pacific Grove data indicated strong peaks at 626 and 1251 cycles. These components were due to the data being acquired several hours later in the morning on weekends than during the week. This suggests that diurnal heating may be an important contributor to variability in SST at Pacific Grove and perhaps at the other coastal locations as well.

Smoothed versions of the periodogram of first residuals for Granite Canyon have also been calculated (Fig. 76, middle and lower panels). Periodogram smoothing can be accomplished in several ways. For example, raw spectral estimates within overlapping segments, with various degrees of overlap, can be averaged. In the present case, adjacent, smoothed estimates have been calculated with no overlap, as recommended by Tukey (1967). Also the weights used in averaging need not be uniform, although uniform weights have been used here. The smoothed version shown in the middle panel was obtained by averaging adjacent spectral estimates in groups of 5 (10 degrees of freedom) whereas the version shown in the lower panel was obtained by averaging in groups of 15 (30 degrees of freedom). Naturally as the degrees of freedom increase, spectral resolution decreases. As a case in point, note the

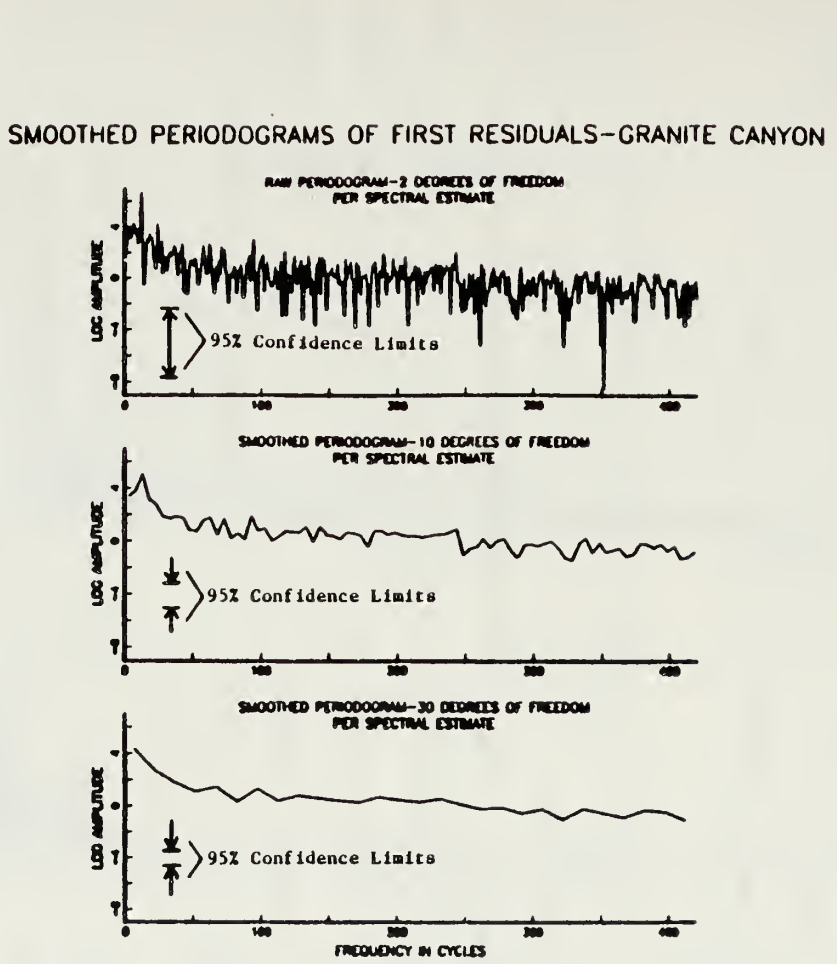

Figure 76. Smoothed periodograms of first residuals at Granite Canyon. Middle and lower panels show smoothed versions of the raw periodogram (upper panel). Middle panel shows periodogram smoothed by non-overlapping groups of five (10 DOFs) and lower panel shows smoothing by groups of 15 (30 DOFs). 95%

disappearance of the spectral peak at 24 cycles (6 months) in both of the smoothed periodograms.

Removal of the aformentioned frequencies yields a set of second residuals whose periodogram is shown in Fig. 77. In the expanded version, zeros are seen where cycles have been removed because, as mentioned, the least squares estimates of the amplitudes in (4.4) are exactly proportional to the corresponding periodogram values. Again, in the lower panel of Fig. 77, the autoregressive-like spectrum is noted. A theoretical spectrum for an AR(2) process using parameters computed below is shown for comparison.

Figure 78 shows the calculated autocorrelations for the second residuals as well as the first 50 correlations for four theoretical AR(p) models computed from the first four estimated correlations using the Yule-Walker equations (Chatfield 1980). From Fig. 78 it is seen that the AR(p) models of order greater than 2 do not give a much better fit than the AR(2) model to the estimated autocorrelations; hence following the principle of parsimony, an AR(2) model is subsequently used. A 95% confidence limit has been included in this figure and the next. Thus correlations less than about 0.03 (or greater than -0.03) are not considered statistically significant on this basis. However, these limits assumed N = 4380 independent observations where in reality, the

PERIODOGRAM FOR SECOND RESIDUALS

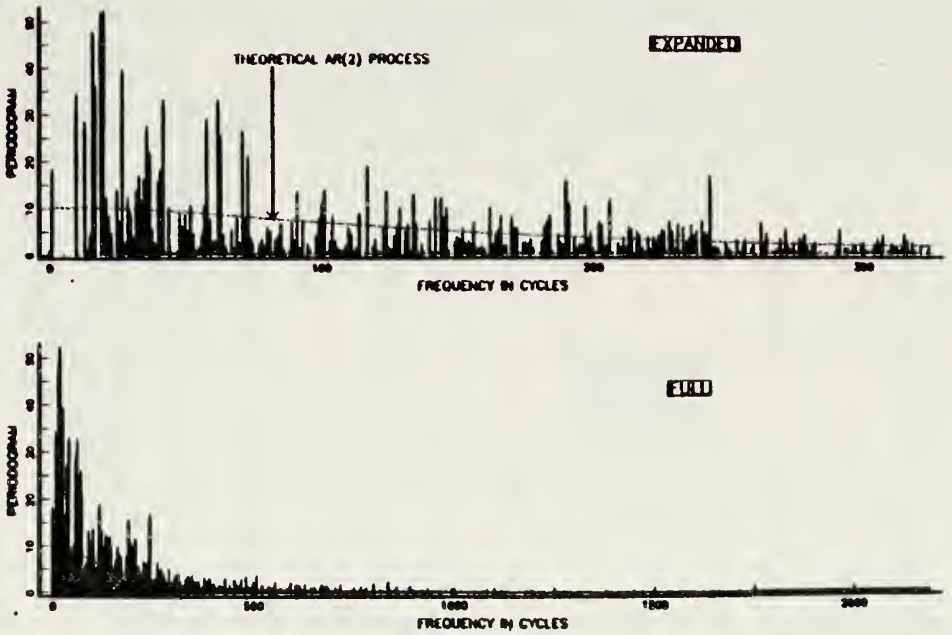

Figure 77. Upper panel shows an expanded periodgram (325 cycles) for second residuals with a theoretical spectrum for an AR(2) process superimposed. The lower panel shows the corresponding full spectrum out to 2190 cycles.

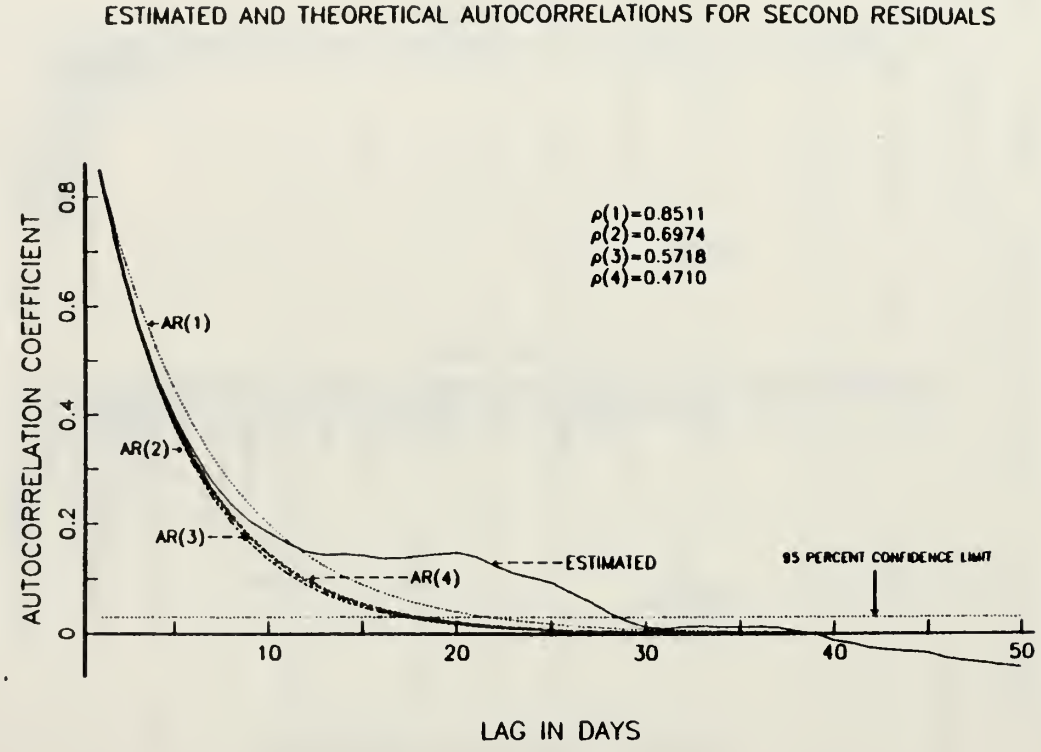

Figure 78. Estimated and theoretical autocorrelations for second residuals out to 50 lags. The theoretical autocorrelations were calculated using the Yule-Walker equations (Chatfield, 1980).

autocorrelogram shows that approximately N/6 would provide a better indication of the actual number of independent observations. On this basis, confidence limits of $\pm$Ø.Ø74 would be more appropriate. Table 3 gives the estimated correlation coefficients and the estimated coefficients of autoregression for the second residuals for p = 1, 2, 3 and 4.

A persistent hump occurs at a lag of about 21 days in the autocorrelogram. The autocorrelations in Fig. 78 were extended to lags beyond 5Ø (not shown), but there was no indication of a cycle of period 21. Similar humps show up in the autocorrelograms for Pacific Grove and the Farallons. At Pacific Grove it occurs at about 14 days and at the Farallons at approximately 22 days. No clear explanation for this effect has yet emerged; however preliminary fitting with a higher-order (but non-sequential) AR model that includes lags of 14 and 15 days improves the fit to the calculated correlations considerably for Granite Canyon (not shown). Consequently, aliasing by the predominant semidiurnal tide at 14.8 days may contribute to this effect at least at one location.

The third residuals are calculated according to (4.7) with p = 2 and $\hat{a}_1$ = Ø.9343 and $\hat{a}_2$ = -Ø.Ø975 derived from the values $\hat{\rho}(1)$ = Ø.8511 and $\hat{\rho}(2)$ = Ø.6973. The residual process $r_3(t)$ and its autocorrelogram are shown in Fig. 79 with the logarithm of the normalized periodogram in Fig.

Table 3

Estimated correlation coefficients for second residuals and estimated autoregressive coefficients for p=1, 2, 3, and 4

Correlations	Estimated coefficients	p
$\beta(1) = \emptyset.8511$	$\hat{a}_1 = \underline{\emptyset.8511}$	1
$\beta(2) = \emptyset.6973$	$\hat{a}_1 = \emptyset.9343$; $\hat{a}_2 = \underline{-\emptyset.\emptyset975}$	2
$\beta(3) = \emptyset.5718$	$\hat{a}_1 = \emptyset.9355$; $\hat{a}_2 = \emptyset.1\emptyset98$; $\hat{a}_3 = \underline{\emptyset.\emptyset129}$	3
$\beta(4) = \emptyset.471\emptyset$	$\hat{a}_1 = \emptyset.955$; $\hat{a}_2 = \emptyset.1\emptyset9$; $\hat{a}_3 = \emptyset.\emptyset\emptyset7$; $\hat{a}_4 = \underline{\emptyset.\emptyset\emptyset\emptyset6}$	4

Table 4

Partitioned sample variances for Granite Canyon sea-surface temperature data

	Sample Variance	Sample Standard Deviation	% Variance Removed
Original data	2.624	1.62	8.4%
$r_1(t)$	2.4Ø3	1.55	51.9%
$r_2(t)$	1.Ø4Ø	1.Ø2	28.7%
$r_4(t)$	Ø.288	Ø.537	1Ø.9%

THIRD RESIDUALS

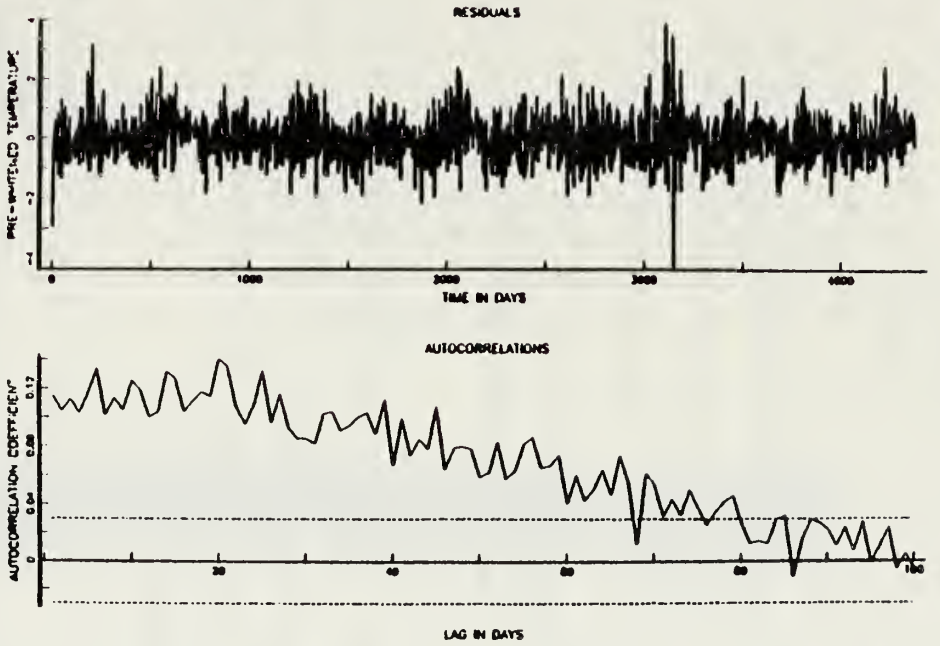

Figure 79. Upper panel shows third residuals (first residuals less an AR (2) process). Lower panel shows the autocorrelogram of third residuals with 95% confidence limits superimposed.

80. The choice of frequencies removed, on the basis of the first residuals, is confirmed.

The sample variance of the original data (raw data minus grand mean), the first residuals (linear trend removed), the second residuals (removal of linear trend and s(t)), and the fourth residuals are shown below (Table 4).

About half of the variance is accounted for by the cyclic component s(t). A summary for the J = 13 cyclic components is given below in Table 5. Components are listed in descending order based on their amplitudes, A_j. The variance after removal of each of these (orthogonal) components is given in the last column. The annual cycle accounts for almost 60% of the total variance in the cyclic components. These estimated coefficients will be used in a simulation of the data.

F. EXAMINATION OF THE RANDOM COMPONENT, $\mathcal{E}(t)$

To estimate the fourth residuals the autoregressive component, modeled as an AR(2) process, is removed from the second residuals, yielding

$$r_4(t) = r_2(t) - \hat{a}_1 r_2(t-1) - \hat{a}_2 r_2(t-2). \qquad (4.11)$$

These residuals are first tested for adequacy with respect to the modeling which has been done up to this point. Two questions arise, (1) the physical adequacy of the model, and (2) the statistical adequacy. Any given model may

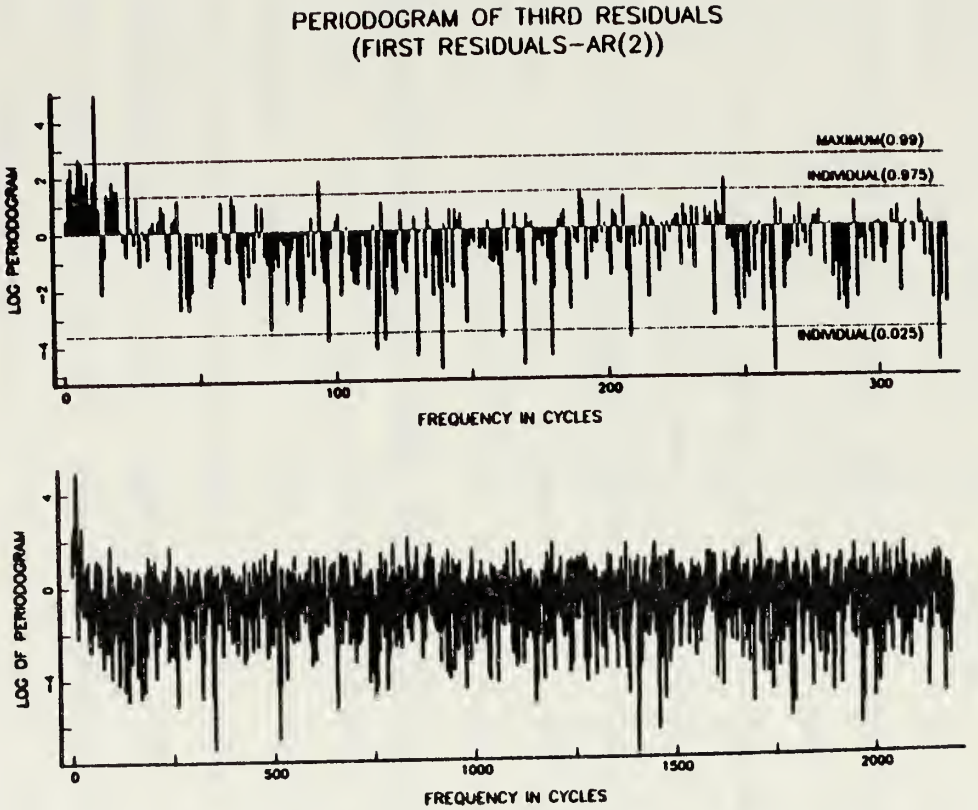

Figure 80. Periodogram of third residuals. Upper panel shows an expanded version with maximum and individual confidence limits superimposed. Lower panel shows full periodogram.

Table 5

Summary of parameters associated with cyclic components

j	P_j	T_j (years)	γ_j	β_j	A_j	θ_j	Variance $2.4\emptyset^1$
1	12	1.00	-Ø.465	-1.187	1.275	111.4°	1.59
2	6	2.00	Ø.273	-Ø.295	Ø.402	47.2°	1.51
3	24	Ø.50	Ø.342	-Ø.162	Ø.378	25.4°	1.44
4	7	1.71	Ø.345	Ø.112	Ø.363	342.Ø°	1.37
5	3	4.00	-Ø.266	Ø.211	Ø.340	218.4°	1.32
6	9	1.33	-Ø.101	Ø.302	Ø.318	251.6°	1.28
7	2	6.00	Ø.074	Ø.275	Ø.285	285.1°	1.23
8	11	1.09	Ø.097	Ø.250	Ø.268	291.2°	1.19
9	18	Ø.67	-Ø.187	-Ø.180	Ø.260	136.1°	1.15
10	8	1.50	Ø.079	-Ø.243	Ø.256	72.Ø°	1.12
11	5	2.40	-Ø.176	-Ø.174	Ø.247	135.3°	1.08
12	94	Ø.13	-Ø.155	-Ø.152	Ø.218	135.6°	1.06
13	4	3.00	Ø.194	-Ø.097	Ø.217	26.6°	1.04

[1] Initial variance before removal of the individual cyclic components

satisfy either, neither, or both of these requirements. For physical adequacy the model should describe a substantial amount of the variation in the data with as few terms as possible, i.e., the principle of parsimony, with the prospect that at least the dominant terms may provide a basis for interpretation. For statistical adequacy, the assumption has been made that the fourth residuals are estimates of n(t) and, as such, should be approximately uncorrelated.

The fourth residuals are plotted in the top panel of Figure 81. There is an anomaly at about 3100 days associated with isolated extrema in SST encountered during the fall of 1979. It emphasizes the fact that the model is global, and therefore cannot account for transient events in the data. Except for the anomaly at 3100 days, the fourth residuals generally fall in the range of $\pm$2.0, a considerably smaller range than that of the original data (8.0 to 17.0). Table 4 shows that the fourth residuals, which represent the purely random, or unpredictable, part of the data, account for only 10.9% of the total variation. Bands corresponding to the approximate 95% confidence limits are included with the autocorrelation function for the fourth residuals (Fig. 81, lower panel). Again there may be an anomaly at lag 20, but since the correlation at this lag barely exceeds the confidence limit, it may not be

FOURTH RESIDUALS

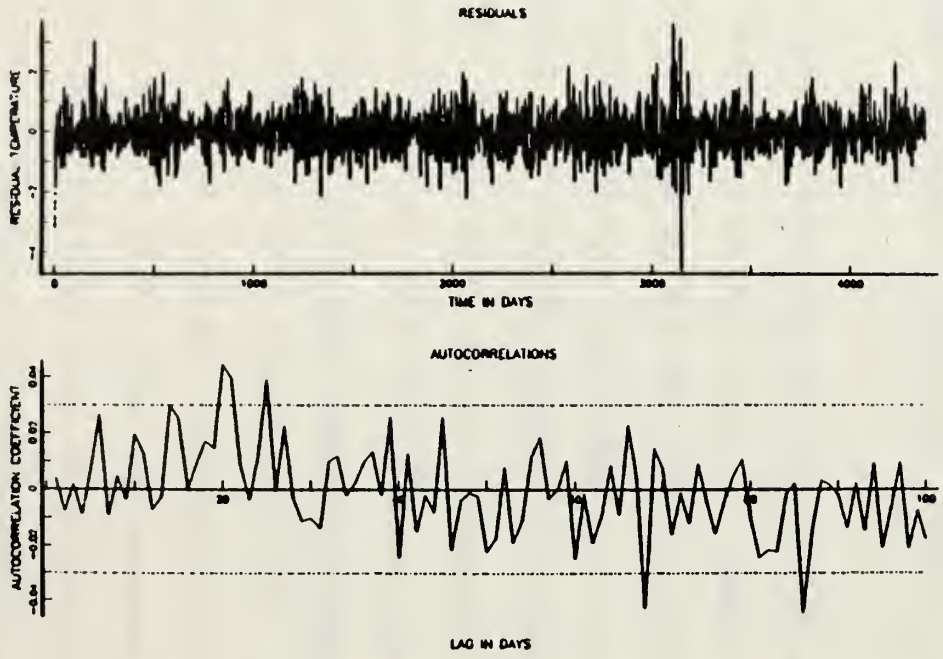

Figure 81. Fourth residuals (upper panel) and autocorrelogram of fourth residuals (lower panel). Autocorrelogram of fourth residuals has 95% confidence limits included.

significant. A more rigorous test for uncorrelatedness in the $r_4(t)$'s is given in the next figure.

The top panel in Fig. 82 contains the unsmoothed, normalized periodogram and the bottom panel, the cumulative periodogram. Barely distinguishable upper and lower 95% and 99% confidence intervals for a flat spectrum based on Kolmogorov-Smirnov (KS) statistics are shown. Since the cumulative periodogram lies within these bands, the Durbin test for a flat spectrum accepts the hypothesis of a flat spectrum (Jenkins and Watts, 1968; Cox and Lewis, 1966) . The value of the KS statistic is given as Ø.5136 and compares to the upper 5% point of the statistic which has value 1.355. In addition, the Anderson-Darling test statistic (value Ø.9139) is given; this test statistic is more sensitive to departures at low or high frequencies, and in this case also accepts the hypothesis of no correlation (Cox and Lewis, 1966).

Thus, the adequacy of the model has been established. Also if the $\mathcal{E}(t)$ are normally distributed, then a flat spectrum implies independence, but not otherwise. For this reason an examination of the distribution of fourth residuals is motivated.

In the top panel of Fig. 83 a histogram of the fourth residuals is shown together with sample statistics. The estimated kurtosis (3.61) is significantly different from zero and thus indicates that the residuals are not normally

FOURTH RESIDUALS

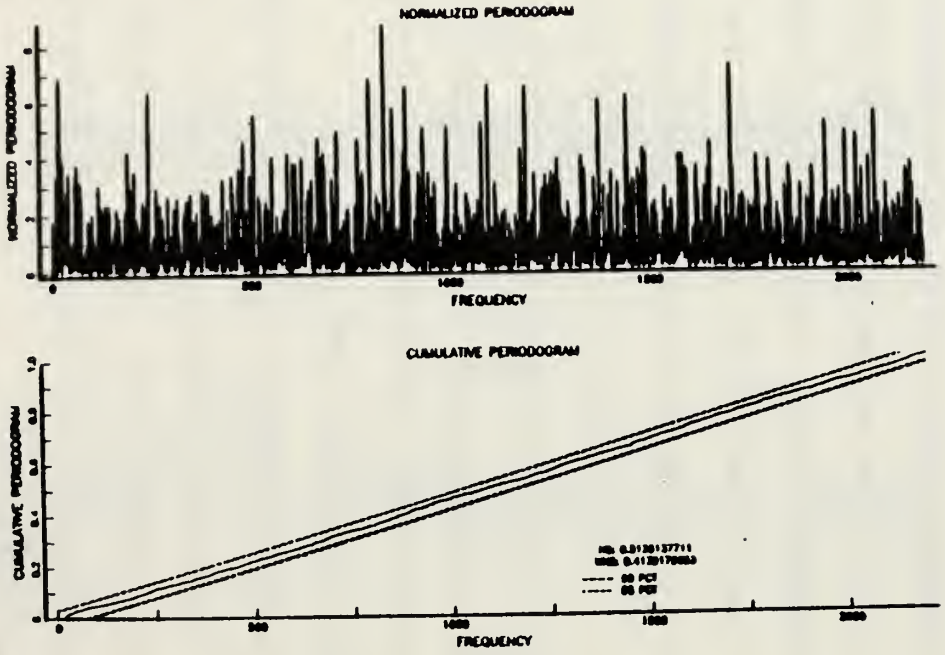

Figure 82. Periodograms of fourth residuals. Upper panel shows full periodogram of fourth residuals and lower panel shows a cumulative periodogram of fourth residuals with confidence limits included. Cumulative periodogram lying completely within confidence bands indicates that fourth residuals possess a white (noise-like) spectrum.

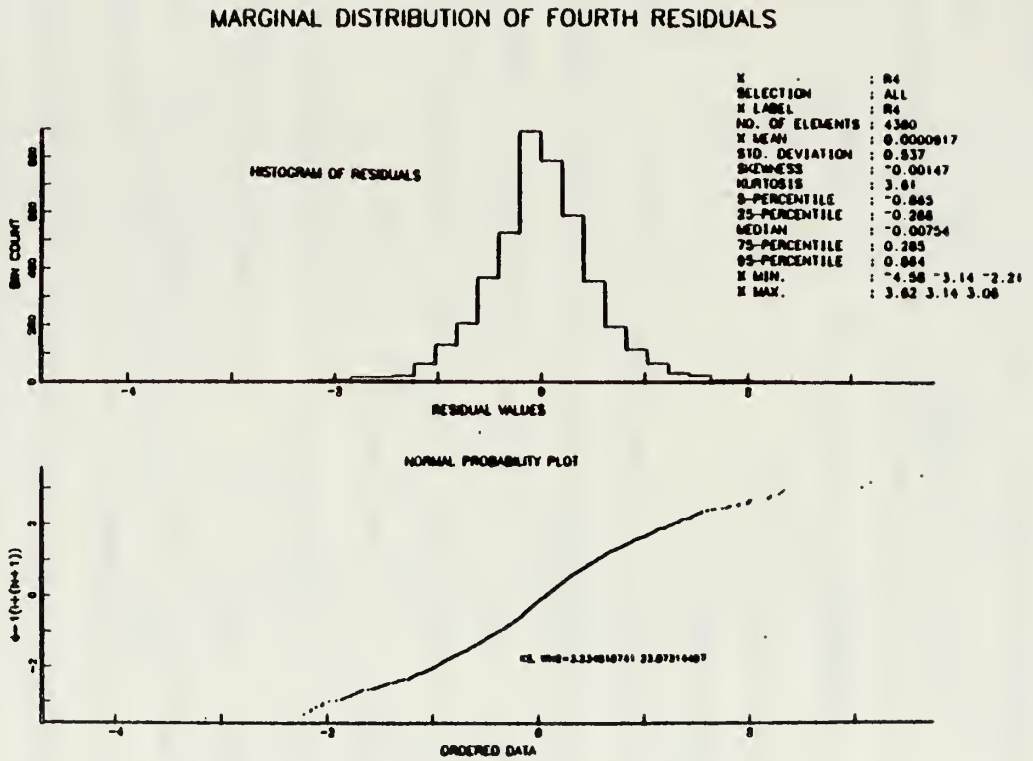

Figure 83. Distribution of fourth residuals. Upper panel shows a histogram of fourth residuals with slight skewness and significant kurtosis. Lower panel shows a cumulative probability plot of the fourth residuals with the ordinate scaled such that normally-distributed data produce a straight line.

distributed. This is confirmed in the probability plot in the lower panel. This is a plot of the ordered residuals against their approximate expected value $\phi^{-1}(i / N+1)$ where $\phi^{-1}(.)$ represents the inverse normal probability function. The curvature in this plot and the outliers indicate that the distribution of the $\mathcal{E}(t)$'s is somewhat non-normal, in fact drawn up in the middle and long in the tails. The distribution appears symmetric; this is reflected in an estimated coefficient of skewness of -Ø.ØØ147. The standard deviation for the $\mathcal{E}(t)$'s is, from Table 4, estimated to be Ø.537.

G. THE COMPLETED MODEL

The complete model is summarized in Table 6. The first 28 terms are contributions which have been represented deterministically and constitute approximately 60% of the total variance in SST, while the last 3 terms represent the random contribution to the overall variance.

The validity and accuracy of the model depend on many factors. These include (1) the choice of model type (additive or multiplicative, for example) and the basis functions used to represent the data, (2) the number of terms used to represent the various contributions, (3) non-linear interactions between various terms in the model, (4) the statistical properties and accuracy of the original data used to derive the model, (5) the likelihood

Table 6

Completed model including coefficients associated with linear trend, the cyclic components, and autoregression

$$\hat{X}_n = \hat{\gamma} + \hat{\beta}_n + a_1 \text{Sin}[\tfrac{4\pi n}{438\emptyset}] + b_1 \text{Coe}[\tfrac{4\pi n}{438\emptyset}] + a_2 \text{Sin}[\tfrac{6\pi n}{438\emptyset}] + b_2 \text{Cos}[\tfrac{6\pi n}{438\emptyset}] + \ldots\ldots$$

$$a_{13} \text{Sin}[\tfrac{188\pi n}{438\emptyset}] + b_{13} \text{Cos}[\tfrac{188\pi n}{438\emptyset}] + \hat{\alpha}_1 X_{n-1} + \hat{\alpha}_2 X_{n-2} + \varepsilon_t^*$$

Component	Coefficients	
Linear trend,	$\hat{\gamma}$ = 1Ø.9	
	$\hat{\beta}$ = Ø.ØØØ374	
Cyclic fit,	a_1 = Ø.2756	b_1 = Ø.Ø738
	a_2 = Ø.2116	b_2 =-Ø.2659
	a_3 =-Ø.Ø971	b_3 = Ø.1947
	a_4 =-Ø.1737	b_4 =-Ø.1762
	a_5 =-Ø.2951	b_5 = Ø.2734
	a_6 = Ø.1123	b_6 = Ø.3453
	a_7 =-Ø.2433	b_7 = Ø.Ø794
	a_8 = Ø.3Ø21	b_8 =-Ø.1ØØ7
	a_9 = Ø.25Ø1	b_9 = Ø.Ø97Ø
	a_{10} =-1.1871	b_{10} =-Ø.4653
	a_{11} =-Ø.1796	b_{11} =-Ø.1874
	a_{12} =-Ø.1622	b_{12} = Ø.3418
	a_{13} =-Ø.1523	b_{13} =-Ø.1554
Coefficients of autoregression,	$\hat{\alpha}_1$ = Ø.9343	
	$\hat{\alpha}_2$ =-Ø.Ø978	

*ε_t assumed to be Geuseien - generated by a random number generator

of unexpected transient events, (6) how the model is to be used, and (7) the criteria used to measure model performance.

Treating the model as a forecast function, future values can be predicted by simply "stepping" the model forward in time one data interval at a time. Forecast accuracy naturally deteriorates as values further into the future are predicted. This model has been used to predict SSTs up to 30 days in advance at Granite Canyon with reasonable success (Breaker et al., 1983).

This type of model can also be used to fill in missing data. Various possibilities exist for implementing the model in this fashion. The most appropriate method of implementation may depend on the particular characteristics of the series in question including the nature of the gap(s) involved. How well the model can be expected to perform in this case will depend in part on how long the gap(s) is(are) with respect to the overall record length. This application of the model is particularly appropriate for oceanographic time series where gaps are frequently encountered.

In the present study, this model is used to examine the adequacy of various sampling rates. This aspect is explored in the next section.

H. THE SAMPLING PROBLEM

The model is now used to generate independent realizations of the Granite Canyon time series. These realizations are taken as members of an ensemble from an underlying stochastic process, with the requirement that the model and the model parameters used to generate the time series are those estimated from the original Granite Canyon series.

One such realization is shown in Fig. 84. The top panel is the original series and the bottom panel is the model generated (the simulated series). The simulated series has been generated for one year beyond March 1, 1983 and this projection is shown in Fig. 85. That the one year simulation (1983-84) contains an apparent spring transition is noted (as is the rather unrealistic abrupt increase in temperature between days 100 and 120).

Ten independent realizations of the Granite Canyon SSTs were generated and used to compute estimated parameter values. In these simulations, the "white noise" sequence n(t) was taken to be an independently and identically distributed (i.i.d.) normal random variable, despite the slight departures from normality indicated previously. It is important to recognize that all of the variability between realizations is introduced through n(t), whereas in

ONE-YEAR MODEL EXTRAPOLATION AT GRANITE CANYON

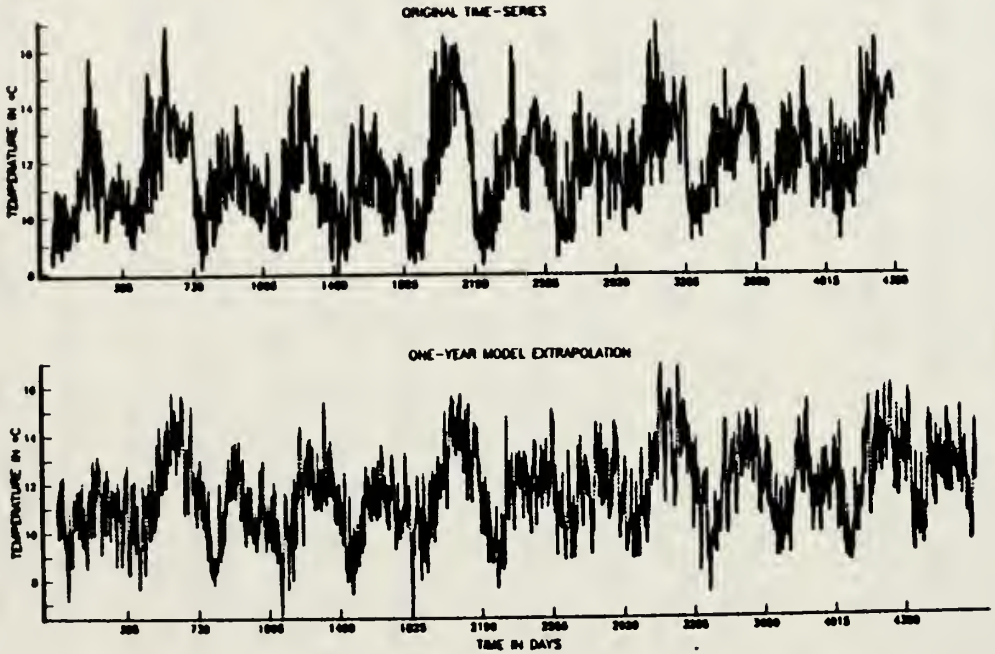

Figure 84. One year extrapolation of SST at Granite Canyon from model simulation. Upper panel shows original 12-year series, and the lower panel shows the 13-year simulation (original 12 years plus one additional year).

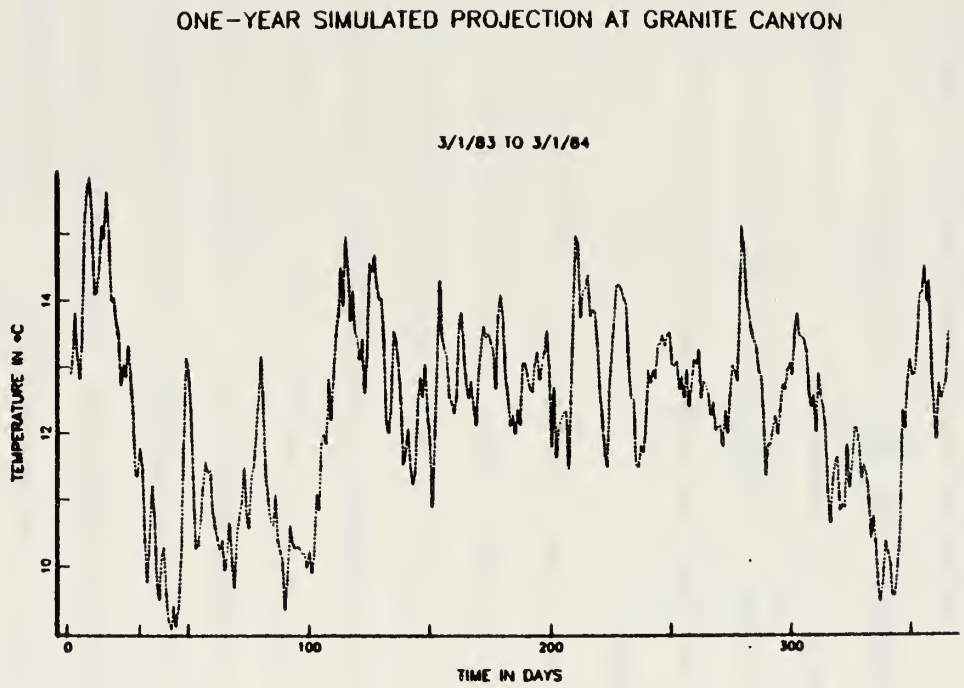

Figure 85. One year simulated projection at Granite Canyon (expanded from previous figure).

reality many of the parameters which are assumed known and are fixed in the model, are actually random variables themselves and thus should also contribute to the overall variability between realizations.

Table 7 summarizes the results of the simulation for the parameters α and δ in the long term trend, for the serial correlations at lags one and two in the second residuals $r_2(t)$, for the associated coefficients a_1 and a_2 in the AR(2) model, and for the amplitudes A_1 and A_2 for the two dominant frequencies in s(t) with periods of one year and two years. These are also denoted as A'_1 and A'_2 in Table 5. The nominal values are those estimated from the original data.

Since the estimated standard deviation (s.d.) of the slope of the (linear) long term trend $m(t) = \alpha + \delta t$ is Ø.ØØØØ11, the slope in the data is statistically significant, based on the model simulations. The gross approximations give the s.d.'s of the estimates of $\rho(1)$ and $\rho(2)$ in a sample of size 4380 as $1 / (4380)^{1/2} = Ø.Ø15$ which, given statistical fluctuations, are in reasonable agreement with the estimated s.d.'s of the serial correlations of Ø.ØØ74 and Ø.Ø141. Note, however, the estimates of $\rho(1)$ and $\rho(2)$ have averages below the nominal values. This reflects the fact that estimates of serial correlations with high values are biased; this kind of bias can be

Table 7

Simulation results for sampling every point

Parameter	Nominal value	Minimum	Maximum	Average	Standard Deviation
α	10.9	10.78	10.95	10.91	0.045
δ	0.000374	0.000350	0.000391	0.000360	0.000011
$\rho(1)$	0.8511	0.8251	0.8543	0.8403	0.0074
$\rho(2)$	0.6973	0.6559	0.7067	0.6752	0.0141
a_1	0.9343	0.890	0.961	0.929	0.0187
a_2	-0.0975	-0.136	-0.078	-0.106	0.0191
A_1 (1yr)	1.275	1.217	1.334	1.278	0.036
A_2 (2yr)	0.402	0.360	0.429	0.401	0.023

reduced by using a technique known as jackknifing (Miller, 1974).[11] Again, the estimated precision of the estimate of A_1 is 0.036/1.275 x 100% = 2.8%, which is acceptably small.

To investigate the problem of sampling rate, the simulations in Table 7 were run to produce estimates of α, δ, A_1 and A_2 based on every 2nd and every third point in the generated series (Table 8).

First it is noted that the estimated s.d.'s in the last columns in Tables 7 and 8 are almost identical. For independent data the s.d.'s in Table 8A would be approximately $\sqrt{2}$ times those in Table 7. The results therefore indicate that the day-to-day correlation in the data is so high that sampling every day does not provide any improvement in sampling the longer scale phenomena. Such phenomena are thus effectively accounted for in the model by s(t) and m(t), exclusive of $\varepsilon(t)$. Table 8B gives the results for sampling every third day. The s.d.'s increase only slightly in this case.

The calculations summarized in Table 8 have been extended in an attempt to obtain more insight into the sampling problem. Little if any change in the s.d.'s of the selected parameters was observed in going from every other point to every third point in the series. However, the simulated series can be continuously subsampled and the results plotted as a function of sample interval. This procedure has been followed, again using ten realizations

Table 8

Simulation results for sampling every second and every third observation

A
(every 2nd point)

Parameter	Nominal Value	Minimum	Maximum	Average	Standard Deviation
α	10.9	10.79	10.95	10.91	0.042
δ	0.000374	0.000352	0.000387	0.000360	0.000010
A_1	1.275	1.215	1.330	1.277	0.035
A_2	0.402	0.362	0.429	0.400	0.023

B
(every 3rd point)

α	10.9	10.78	10.95	10.91	0.049
δ	0.000374	0.000348	0.000393	0.000362	0.000012
A_1	1.275	1.213	1.342	1.279	0.037
A_2	0.402	0.369	0.429	0.403	0.022

in each case, taking every 4th, 5th, 6th, 7th, 8th, 9th, 10th, 15th, 20th, 25th, 30th, and 35th point for the three harmonic amplitudes, A_6, A_{12}, and A_{94}. The results indicate very little change up to intervals of 4 days, (Fig. 86). Beyond about 7 days the s.d.'s begin to fluctuate and generally to increase gradually with further increases in sample interval. No clearly defined break point arises from these calculations, but it is apparent that the series could probably be sampled once every 4 to 7 days with little loss of information.

I. TIME SCALES

In this section the time-series from all three locations are considered. As mentioned, the data from Pacific Grove and the Farallons were analyzed using the same approach used for the Granite Canyon data. Slight differences were found in the composition of each series, some of which were mentioned previously. The long-term trends at Pacific Grove and the Farallons for example were not as pronounced as the trend at Granite Canyon. Also the number of cycles selected for the harmonic fitting of the first residuals differed slightly. While 13 terms were found to be satisfactory for Granite Canyon, 17 terms were needed for Pacific Grove (2 terms were needed to remove the weekend time-of-day sampling problem), and 15 terms for the Farallons. In each case the annual cycle and its first

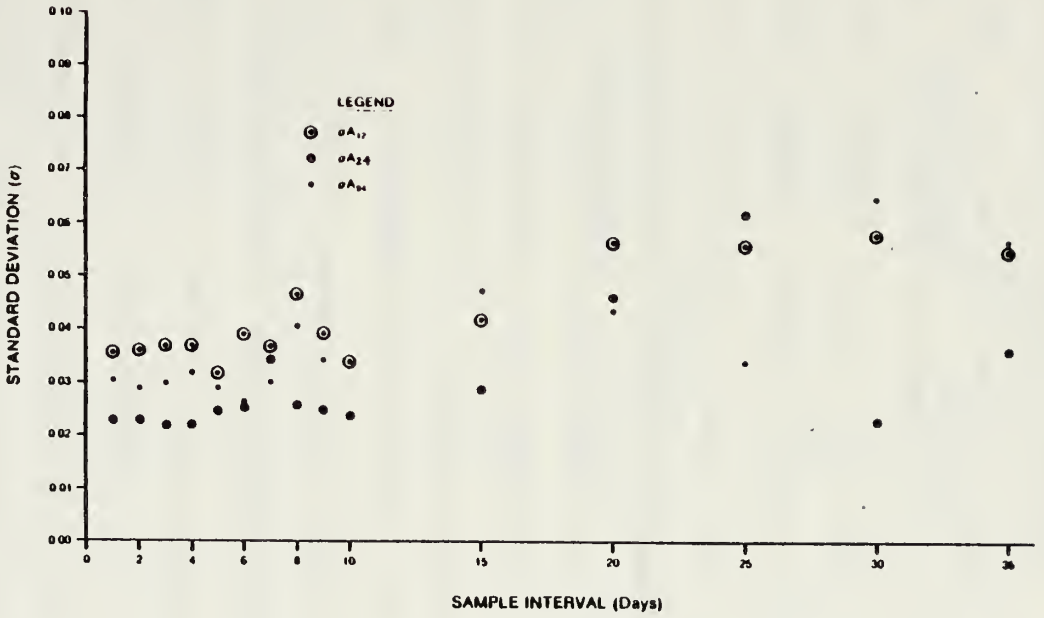

Figure 86. Standard deviations of selected harmonic amplitudes from simulated series versus sample interval in days for Granite Canyon. The one year fundamental (A_{12}), and the 6 month (A_{24}) and 46 day (A_{94}) harmonics are included.

harmonic were dominant. For the Pacific Grove and Farallon data, an AR(3) model provided a much better fit to the second residuals than did the AR(2) model used previously for the Granite Canyon data. Similar humps were found in the autocorrelograms for the second residuals for Pacific Grove and the Farallons, but at Pacific Grove the hump occurred at 14 days and at the Farallons it occurred at about 22 days. The partitioned variances from the three analyses are listed below (Table 9). The values for Granite Canyon are the same as those given previously in Table 6. In each case after linear detrending and appropriate cycle fitting either a second order or a third order AR model was found to yield fourth residuals whose statistical properties agreed reasonably well with those associated with an i.i.d. normal random variable.

Because the techniques for estimating time scales from time-series data are not well-established, several approaches to the problem are considered. The results from one approach using the previous statistical model have already been discussed. Now the correlation structure of the second residuals is examined in order to estimate these scales. The time constant for a linear system is often defined as the time required for the system response to decrease to e^{-1} of its initial value after the input has been terminated. In some engineering applications the time to the first zero-crossing is taken as a measure of the

Table 9

Partitioned variances for Granite Canyon, Pacific Grove, and the Farallons

GRANITE CANYON

Stage	Sample Variance	Sample s.d.	% Variance Removed
Raw data	2.624	1.62	
			8.4
$r_1(t)$	2.403	1.55	
			51.9
$r_2(t)$	1.040	1.02	
			28.7
$r_4(t)$	0.288	0.537	
			11.0 remainder

THE FARALLONS

Stage	Sample Variance	Sample s.d.	% Variance Removed
Raw data	2.10	1.45	
			0
$r_1(t)$	2.10	1.45	
			68.4
$r_2(t)$	0.664	0.815	
			20.8
$r_4(t)$	0.228	0.478	
			10.8 remainder

PACIFIC GROVE

Stage	Sample Variance	Sample s.d.	% Variance Removed
Raw data	2.132	1.46	
			2.7
$r_1(t)$	2.074	1.44	
			61.5
$r_2(t)$	0.763	0.874	
			21.8
$r_4(t)$	0.298	0.546	
			14.0 remainder

time constant of the system. In turbulence studies, an integral time scale is often used (Panchev, 1971) and is defined as

$$\tau_0 = 1/R(0)\int_0^\infty R(\tau)d\tau \qquad (4.12)$$

where $R(\tau)$ is the autocorrelation function and τ_0 is called the time scale of correlation and indicates that for separations greater than τ_0, the observations are essentially independent. As pointed out by Richman et al. (1977), (4.12) provides a reasonable measure for essentially positive correlation functions. However, in some cases where the correlation functions tend to oscillate, (4.12) may provide poor results. In such cases Richman et al. used an alternative definition of correlation time as

$$\tau = 1/R^2(0)\int_0^\infty R^2(\tau)d\tau$$

which in certain cases should provide more consistent results.

In the present study the first three scale criteria were used initially to estimate time scales. These criteria were applied to the second residuals in each case. Significantly different scales would have been obtained if correlation functions from the original data or the first

residuals had been used. Here the scale criteria are applied to the data after the important deterministic components have first been removed. Thus these estimates represent the coherence associated with the random components in the data. Once the appropriate time scales have been estimated, then a rationale exists for determining an adequate sample spacing. This assumes that the shortest or limiting time scales are associated with random components in the data. If even shorter time scales arise from periodicities in the data, it is assumed that these components have already been identified through spectral (periodogram) analyses of the first and second residuals. As indicated by Box and Jenkins (1976), the sampling interval will often be chosen to be proportional to the time constant (time scale) of the system (process) involved. In the present case the constant of proportionality is expected to be 0(1).

For the autocorrelations of the second residuals for Granite Canyon, e-folding (1/e), first zero-crossing, and integral time-scale criteria have been applied (Fig. 87). The results shown in the upper panel indicate time scales of 6.Ø, 39.Ø, and 4.Ø days, respectively. By comparing upper and lower panels it becomes immediately apparent that the integral time-scale depends on the number of lags used in calculating the correlation function, a rather undesirable property. However on closer inspection, if

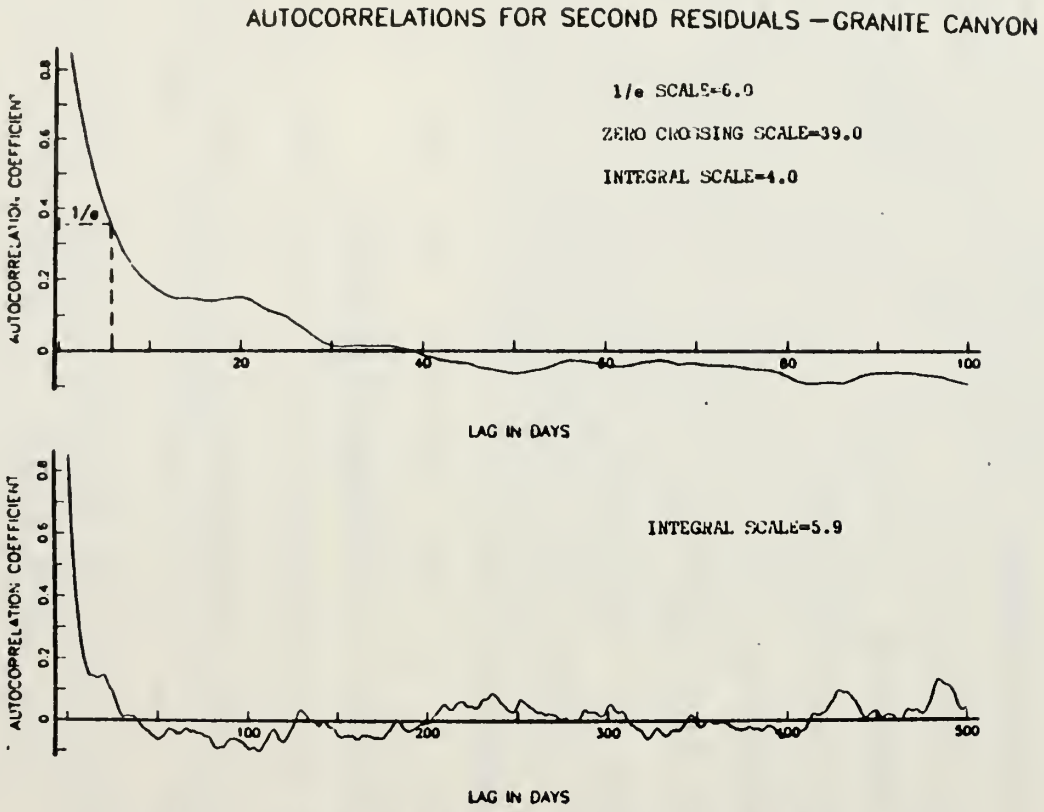

Figure 87. Time scale analysis of autocorrelograms for second residuals for Granite Canyon. Upper panel shows autocorrelogram out to 100 lags with e-folding, first zero-crossing, and integral scales included. Lower panel shows autocorrelogram out to 500 lags with corresponding integral scale included.

integral time scales are calculated over the entire range of lags and these results plotted against lag, this estimate will generally converge to a single value for series which have been adequately detrended and for correlation functions which tend to oscillate slightly around zero beyond the first zero-crossing. The calculations required to fully implement the integral scale criterion are nontrivial, particularly for long time-series. However, it is also possible to redefine this time scale as the integral between zero lag and the lag at which the autocorrelation function first becomes zero, as Enfield and Allen (1980) have done. For well-behaved autocorrelation functions that may simply oscillate slightly about zero beyond the first zero-crossing, this definition, although somewhat arbitrary, appears to be reasonable, and certainly much easier to implement.

It is obvious that the first zero-crossing scale estimate does not even remotely agree with the other two scale estimates. Consequently further results using this criterion are omitted.

Cumulative periodograms of the second residuals have also been calculated. The cumulative periodogram was calculated previously to test the spectrum of the 4th residuals for flatness. Since the cumulative periodogram is directly proportional to the integrated variance, this

analysis technique can be used to estimate how much of the total variance will be captured when a particular sample spacing is specified. Because most of the variance is contained in the lower frequencies, this method of presentation emphasizes that even relatively long sample intervals will capture most of the variability. The cumulative periodogram for the second residuals at Granite Canyon is shown in Figure 88. Sample intervals corresponding to the 90 and 95% values of cumulative variance have been identified in each case. At Granite Canyon, for example, by sampling once every 6.5 days approximately 90% of the variance in the second residuals will be captured. By sampling once every 4.5 days approximately 95% of the variance in the second residuals will be captured. However, if higher frequency periodic effects had been previously modeled and removed, the final sampling rate would have been determined by cyclic components in the data. The correlation time scale plots and the cumulative periodograms for Pacific Grove and the Farallons are shown in Figures 89 through 92. The results are summarized in Table 10.

Table 10 indicates time scales for the three locations ranging from 5.3 days at Pacific Grove to 8.4 days at the Farallons, using the 1/e scale criterion.

Because of the dependence of the integral time scale on the number of lags, these results are incomplete and should

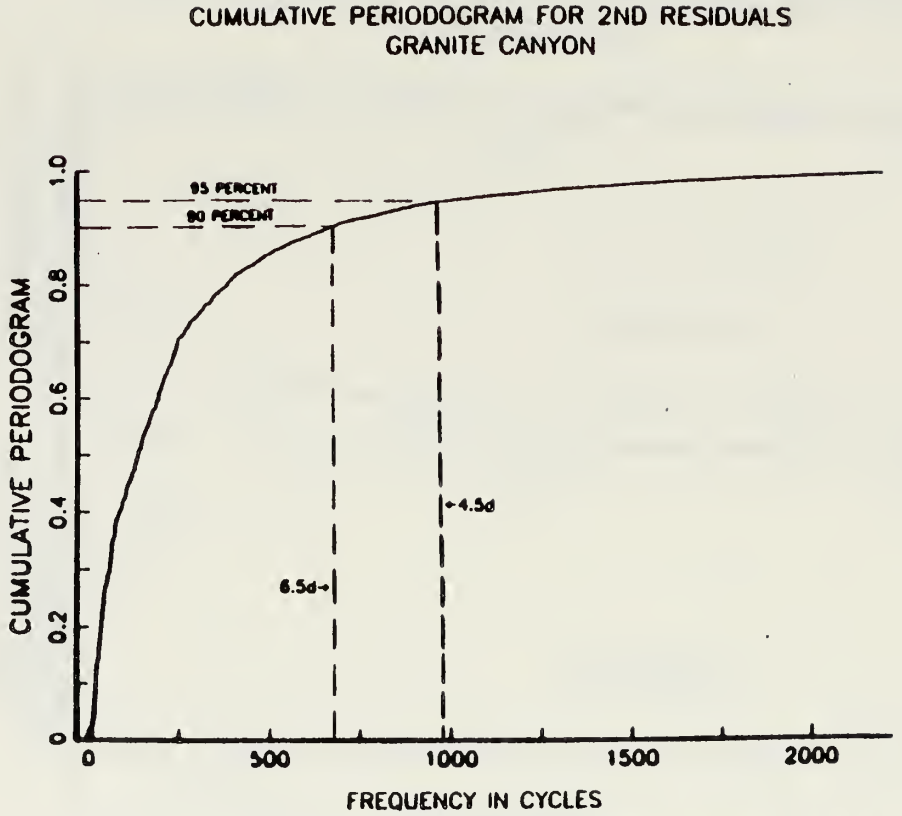

Figure 88. Cumulative periodogram of second residuals for Granite Canyon. Samples taken every 6.5 and 4.5 days capture 90 and 95% of the cumulative variance, respectively.

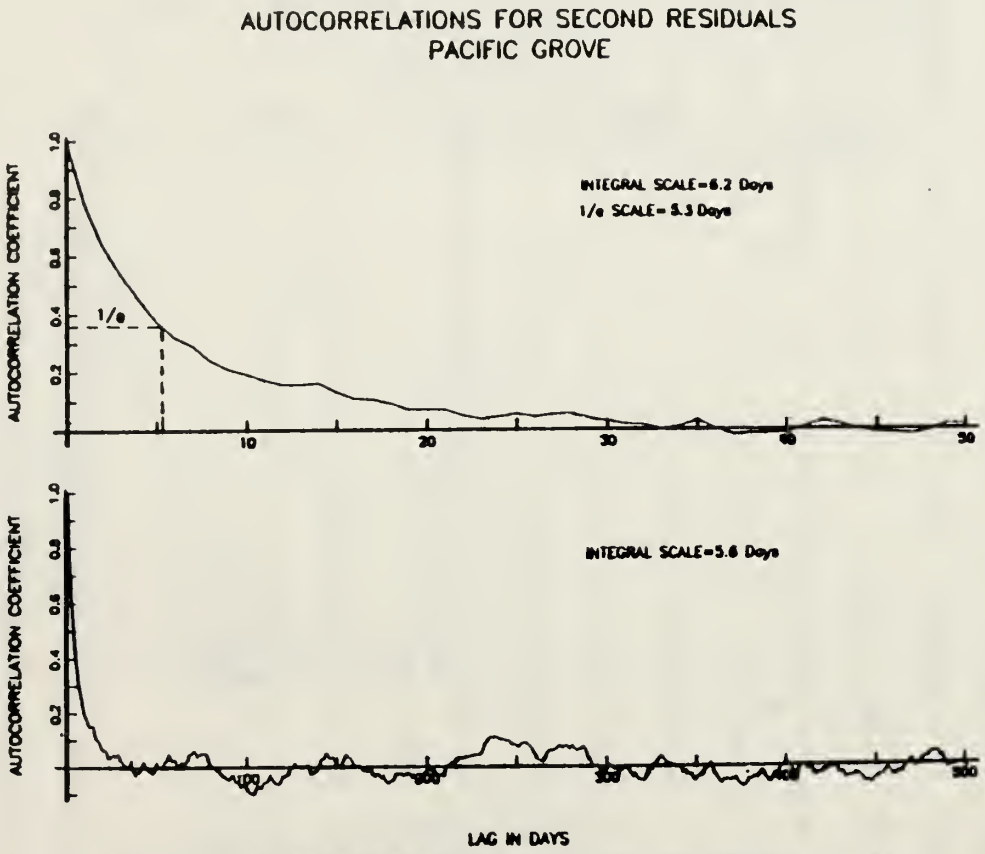

Figure 89. Time scale analysis of autocorrelograms for second residuals for Pacific Grove. Upper panel shows autocorrelogram out to 50 lags with e-folding and integral scales included. Lower panel shows autocorrelogram out to 500 lags with corresponding integral scale included.

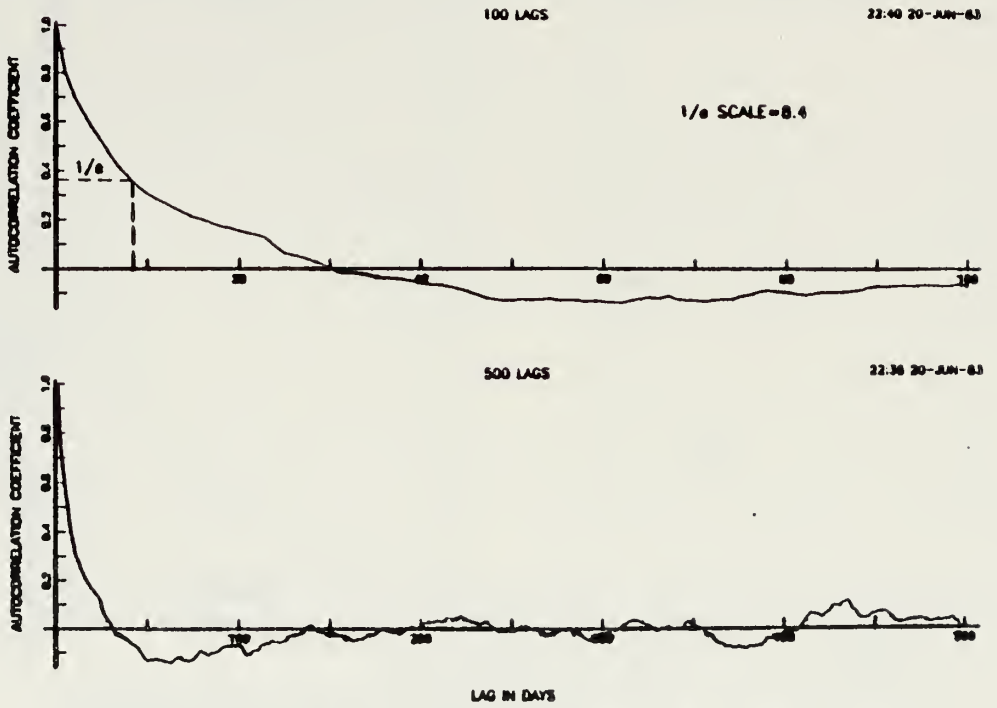

Figure 90. Time scale analysis of autocorrelograms for second residuals for the Farallons. Upper panel shows autocorrelogram out to 100 lags with e-folding scale included. Lower panel shows autocorrelogram out to 500 lags.

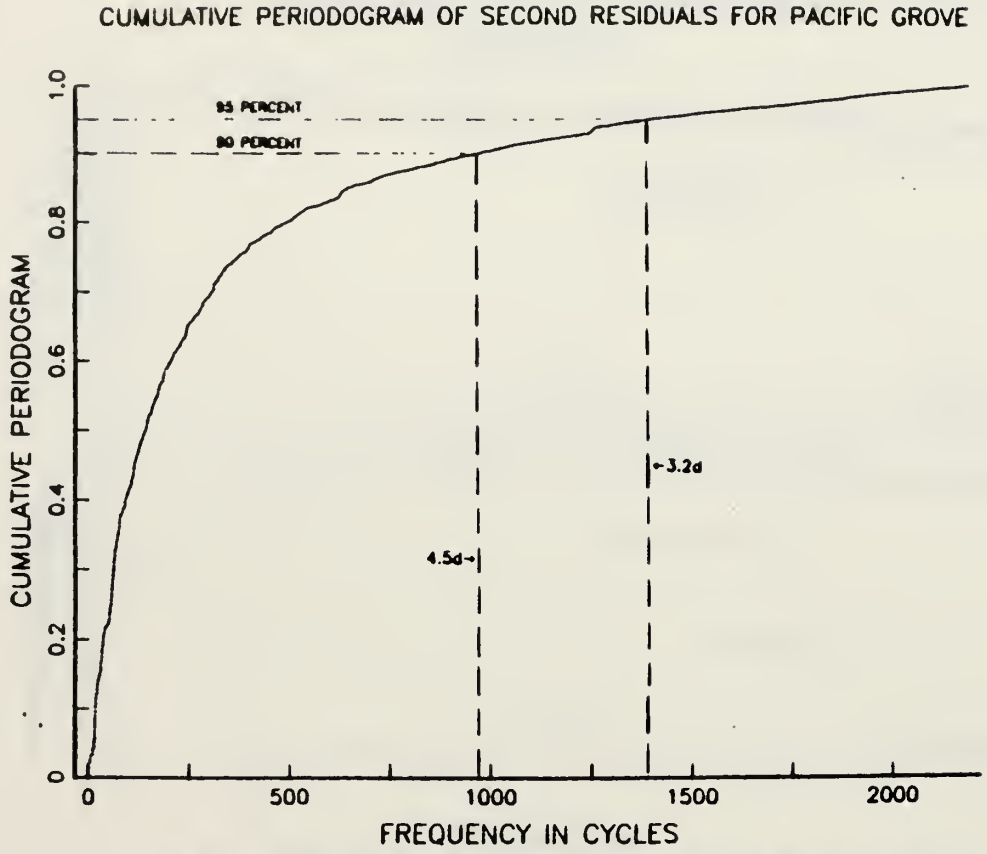

Figure 91. Cumulative periodogram of second residuals for Pacific Grove. Samples taken every 4.5 and 3.2 days capture 90 and 95% of the cumulative variance, respectively.

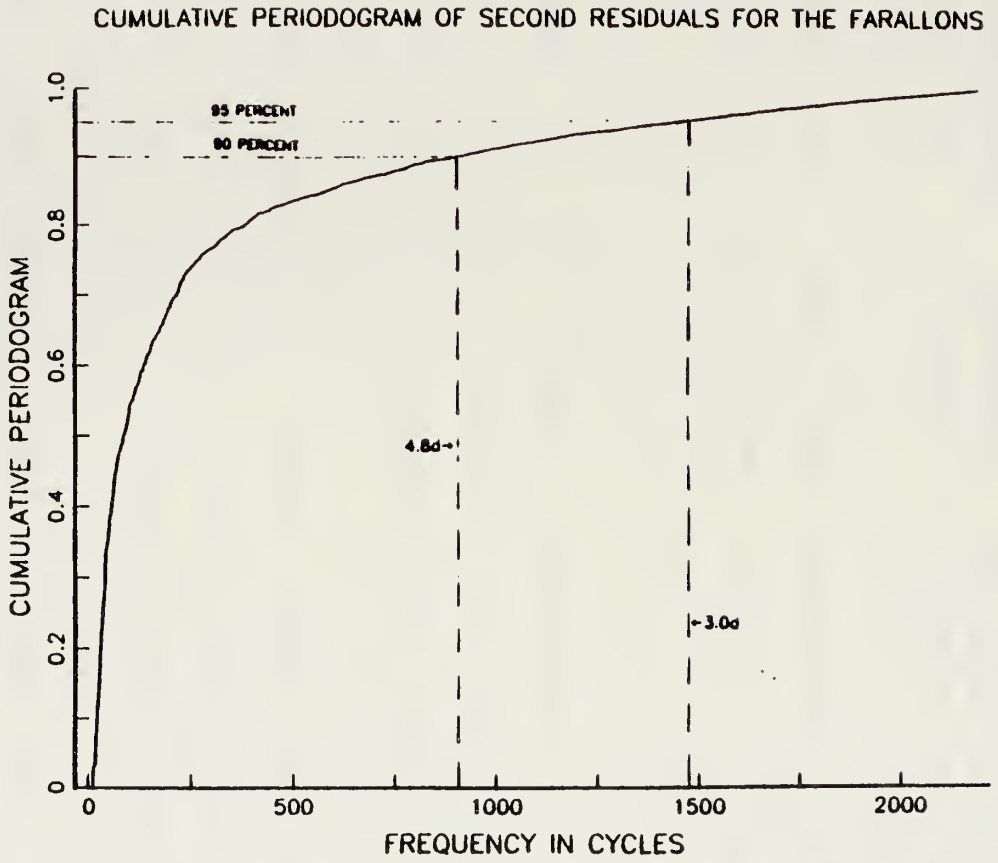

Figure 92. Cumulative periodogram of second residuals for the Farallons. Samples taken every 4.8 and 3.0 days capture 90 and 95% of the cumulative variance, respectively.

Table 10

Estimated time scales for Granite Canyon, Pacific Grove, and the Farallons

Scale Criterion	Granite Canyon	Pacific Grove	The Farallons
1/e	6.0	5.3	8.4
First Zero-Crossing	39.0	-	-
Integral			
50 Lags	-	6.2	-
100 Lags	4.0	-	-
500 Lags	5.9	5.6	-

not be directly compared with the other scale criteria. The e-folding criterion provided consistent estimates throughout the analyses. Its consistency is partially due to the fact that the estimate is selected at a point on the correlation curve where the rate of decay is well-defined and distinct, and not influenced by other effects that typically begin to appear as the function approaches zero. Results from the cumulative periodogram analysis indicate time scales ranging from 3.Ø days at the Farallons to 6.5 days at Granite Canyon. These scales should not be directly compared with those obtained from the correlation analysis since no clearly established basis for such a comparison exists. Of course the correlation time scales can be used together with the cumulative periodograms to estimate what percent of the total variance in the second residuals would be captured by using those particular sampling intervals.

Additional calculations, using correlation analysis of the second residuals at Granite Canyon, were performed to examine the robustness of the previous calculations. The original time series was broken in half yielding two 6-year time series; these series were then analyzed independently. Linear 6-year trends and the same cycles were removed as in the previous 12-year analysis.The results from both 6-year sequences indicate e-folding time scales of 5.6 days, as compared with 6.Ø days obtained previously (Fig. 93).

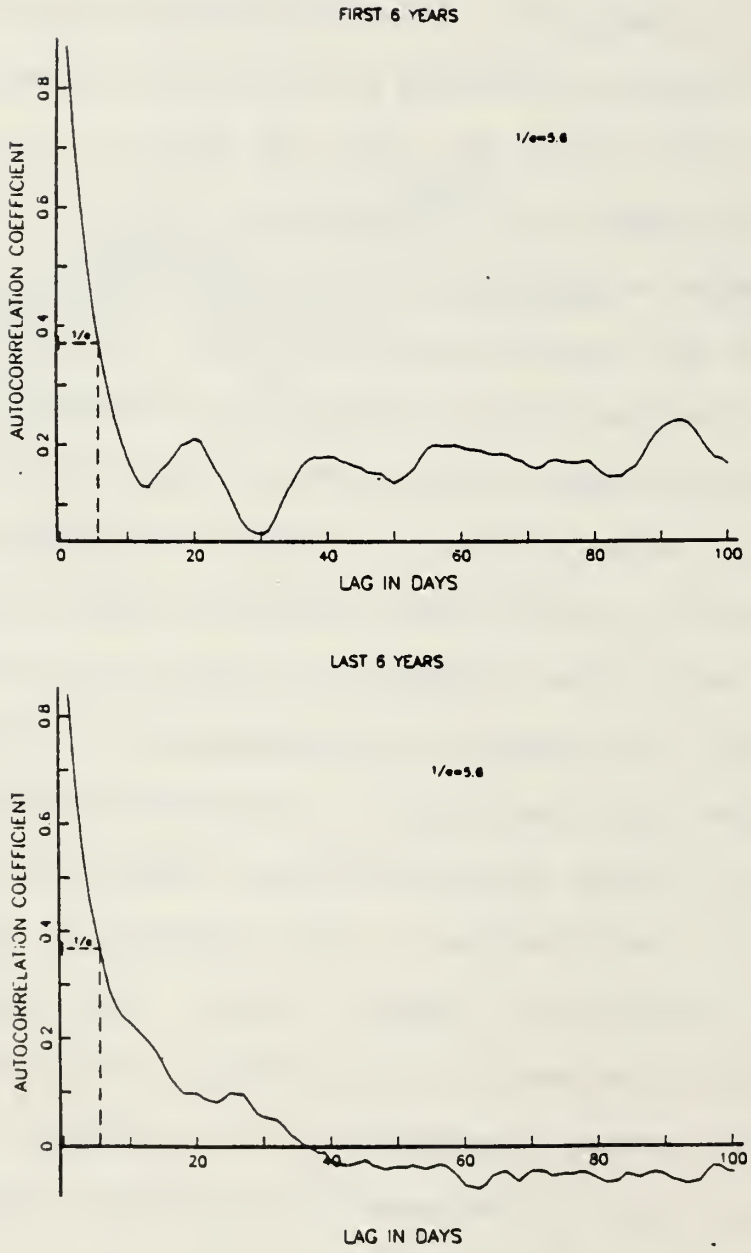

Figure 93. Autocorrelograms for second residuals at Granite Canyon. Upper panel shows autocorrelogram for first six years of the 12-year record and lower panel shows autocorrelogram for second six-year period. E-folding time scales are almost identical even though autocorrelograms differ markedly beyond lags of about 10 days.

These results are remarkably consistent in view of the differences seen in the individual correlation plots beyond lags of about 10 days. These results again emphasize the consistency obtained from using the e-folding scale criterion.

All of the scale analyses so far have dealt with SST. It is also of interest, where possible,to compare scale estimates obtained at the surface with those that can be estimated at subsurface levels, particularly in the vacinity of the Point Sur study area. In this regard, a 52-day record of subsurface temperature, recorded at a moored array located 8 km off Cape San Martin in a water depth of about 350m, has been selected (Fig. 94). These data were acquired at a depth of 175m between November 25,1978 and January 15,1979. A corresponding segment of SST from Granite Canyon has been extracted for comparison. At 175m the density gradient is sufficient to support vigorous internal wave activity in this region. As a result, the predominant semidiurnal (M_2) internal tide shows up clearly in the lower trace (Fig. 94). Consequently observations in this depth range will have to be acquired at least once every six hours to resolve this component of variability in the internal temperature field.

Unlike the SSTs which were sampled once per day, the subsurface temperatures were available once per hour. Both the daily observations of SST and the hourly values of

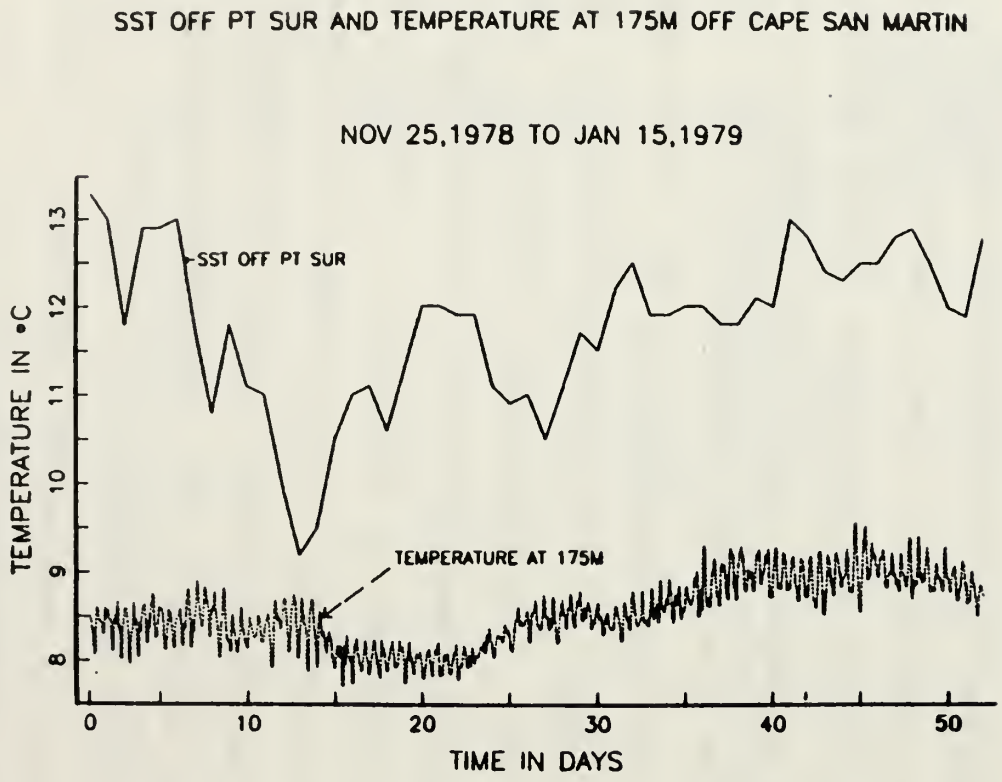

Figure 94. Sea-surface temperature (SST) at Granite Canyon and temperature at 175m off Cape San Martin. Observation period starts on November 25, 1978 and ends on January 15, 1979. Subsurface temperatures were acquired once per hour.

temperature at 175m show somewhat similar patterns with time but the amplitude of the pattern at 175m is reduced considerably (Fig. 94). Both time series were detrended using a 3rd-order polynomial least-squares approximation (Fig. 95). First residuals were calculated by subtracting the polynomial approximation from the original data in each case. Periodograms were calculated for the first residuals and the results examined for prominent spectral peaks. For the SST data, three major components were identified and then removed from the first residuals. Because of the strong tidal influences at 175m, seven cycles around the semidiurnal tidal frequency band were removed to reduce this influence to an acceptable level. It was also necessary to remove five additional cycles at the lower frequencies to produce a well-conditioned autocorrelogram. For present purposes, a well-conditioned autocorrelogram is obtained when the estimated correlation function ceases to change significantly as additional cycles are removed. The approach, as before, is essentially iterative. The results of the autocorrelation calculations are shown in Figs. 96 and 97. The e-folding time scale for the Granite Canyon SST data is approximately 30 hours. This time scale is considerably shorter than the original 6.0 day time scale estimated from the entire 12 years of data. This result is not necessarily surprising since the record length in the

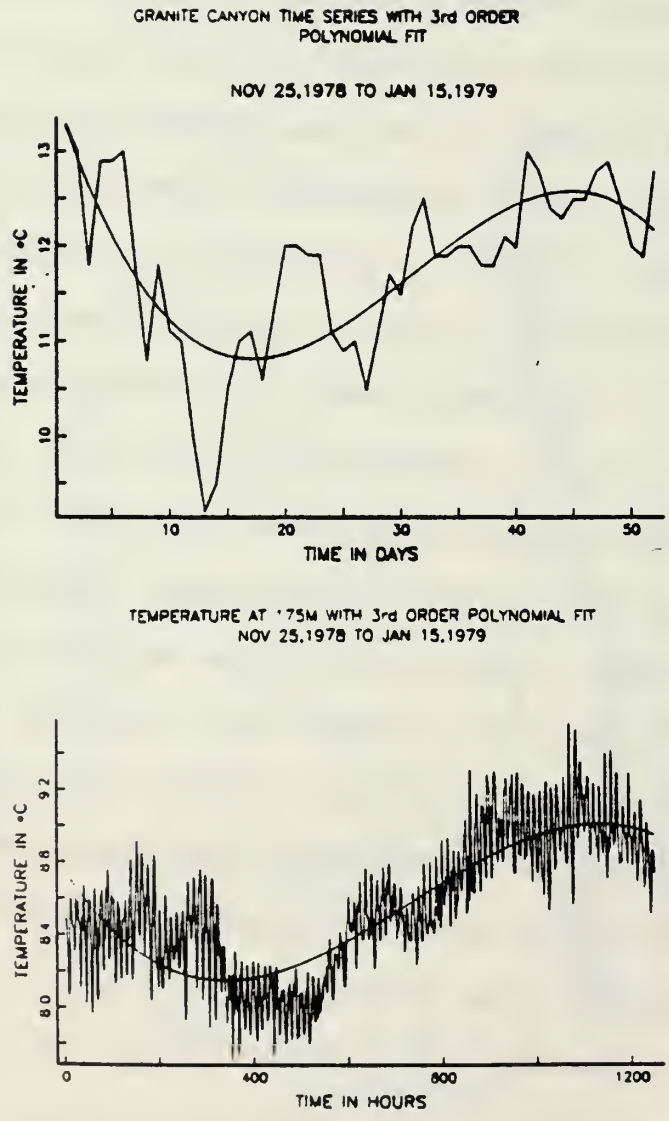

Figure 95. Third-order polynomial least squares fits to the Granite Canyon SST data (upper panel), and to the 175m temperature data (lower panel).

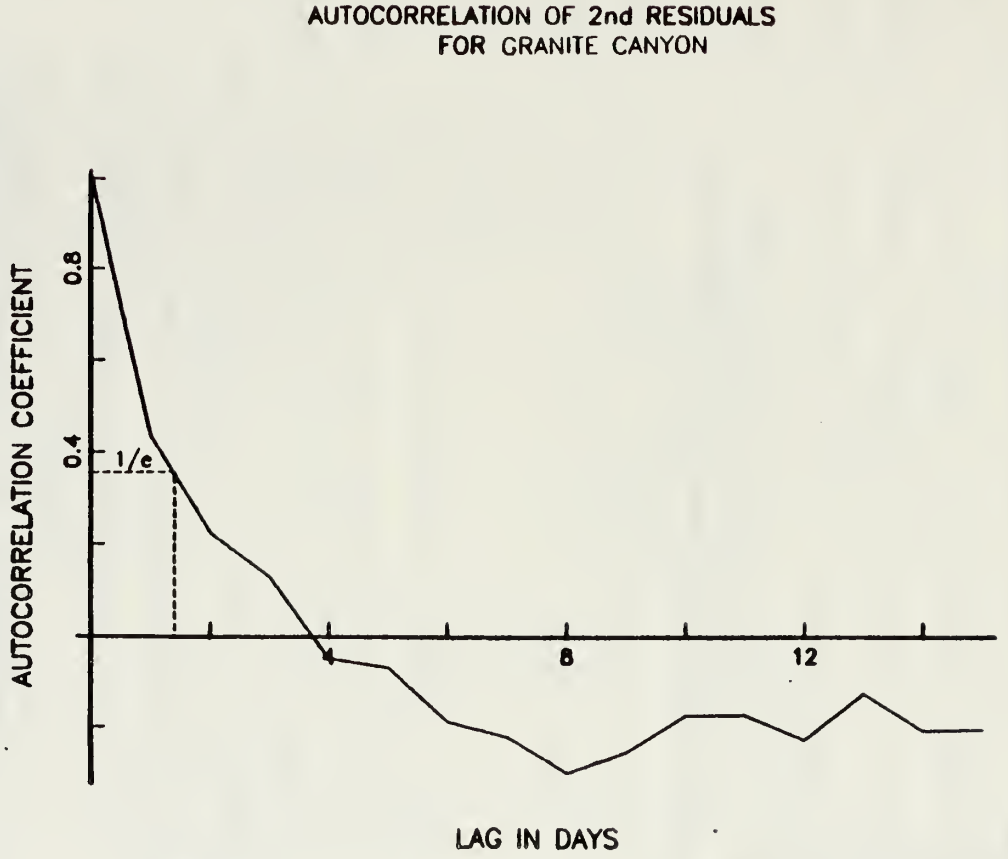

Figure 96. Autocorrelogram for the second residuals at Granite Canyon for the period between November 25, 1978 and January 15, 1979. E-folding time scale is about 30 hours.

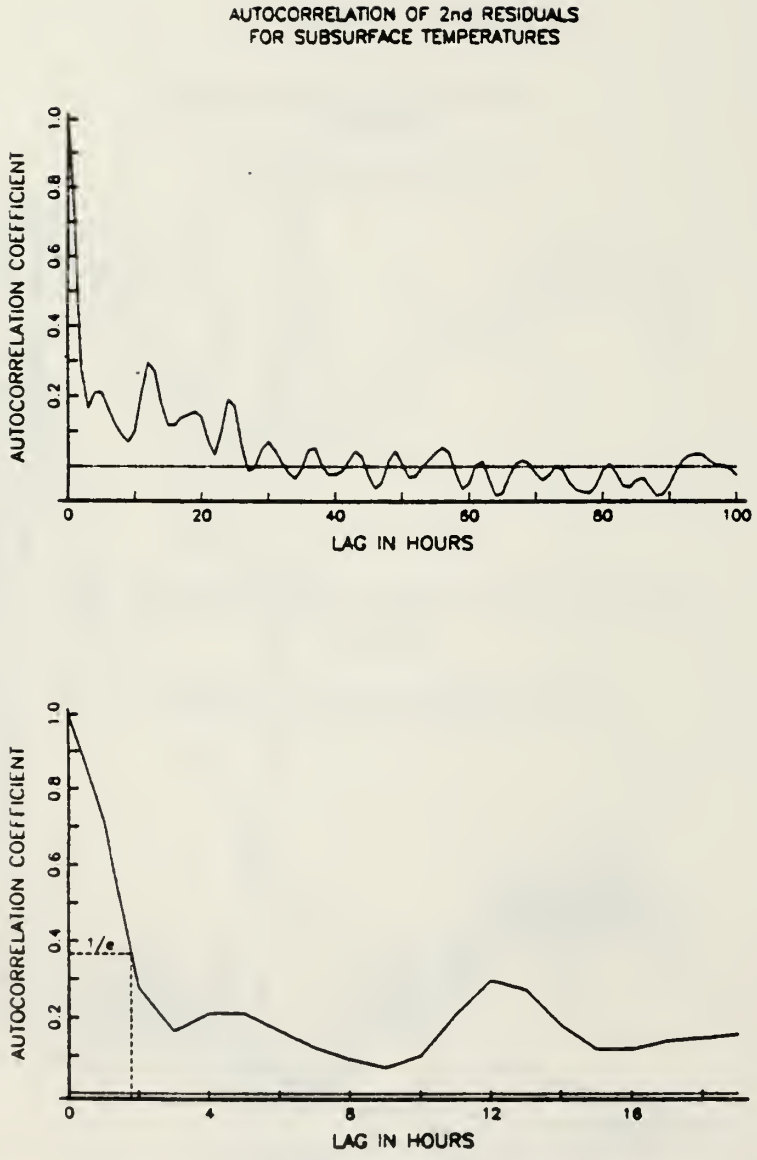

Figure 97. Autocorrelograms for second residuals for 175m temperature data. Upper panel shows autocorrelogram out to a maximum lag of 100 hours. Lower panel shows an expanded version out to 20 lags. E-folding time scale from the autocorrelogram in the lower panel is about 2 hours.

present case is only 52 days, or approximately 15% of the length of the annual cycle. However, the e-folding time for the temperature data at 175m is only about 2 hours, or less than 10% of the surface value estimated over the same time period.

J. OCEANOGRAPHIC ASPECTS OF THE DATA

1. Spring Transitions

Abrupt decreases in SST have been observed in the annual temperature cycle at Granite Canyon during the spring and appear to signal the onset of upwelling along the Central California coast. These dramatic changes in temperature occur in at least 6 out of the 12 years considered and have been individually identified and tabulated with respect to their dates of occurrence and associated changes in temperature. These results are shown in Table 11 below.

These transitions typically occur in March and last for about a week. Also the associated temperature drop is from about 13 to about 10C. The spring transition in 1980 which started on March 11th is examined in detail in Fig. 98. During this transition, temperatures dropped about 4C over a period of 7 days. As indicated in Fig. 71, the entire water column experienced this transition down to at least 500m. Alongshore currents measured at this location reversed from poleward to equatorward at the same depths and times as the decreases in temperature. The synoptic-

Table 11

Spring transitions at Granite Canyon between March 1, 1971 and March 1, 1983

YEAR	STARTING DATE	DURATION	DELTA T	dT/dt
1973	March 9	7 days	13.Ø - 1Ø.ØC	Ø.43C/Day
1974	March 31	5 days	12.3 - 1Ø.Ø	Ø.46
1977	Feb. 22	1Ø days	13.1 - 9.3	Ø.38
1978	April 25	9 days	13.Ø - 8.5	Ø.5Ø
198Ø	March 11	7 days	14.5 - 1Ø.4	Ø.59
1981	March 23	8 days	13.1 - 1Ø.Ø	Ø.39

*A lesser transition was observed on December 19, of 1981. Whether or not this event corresponds to a "spring" transition is not known.

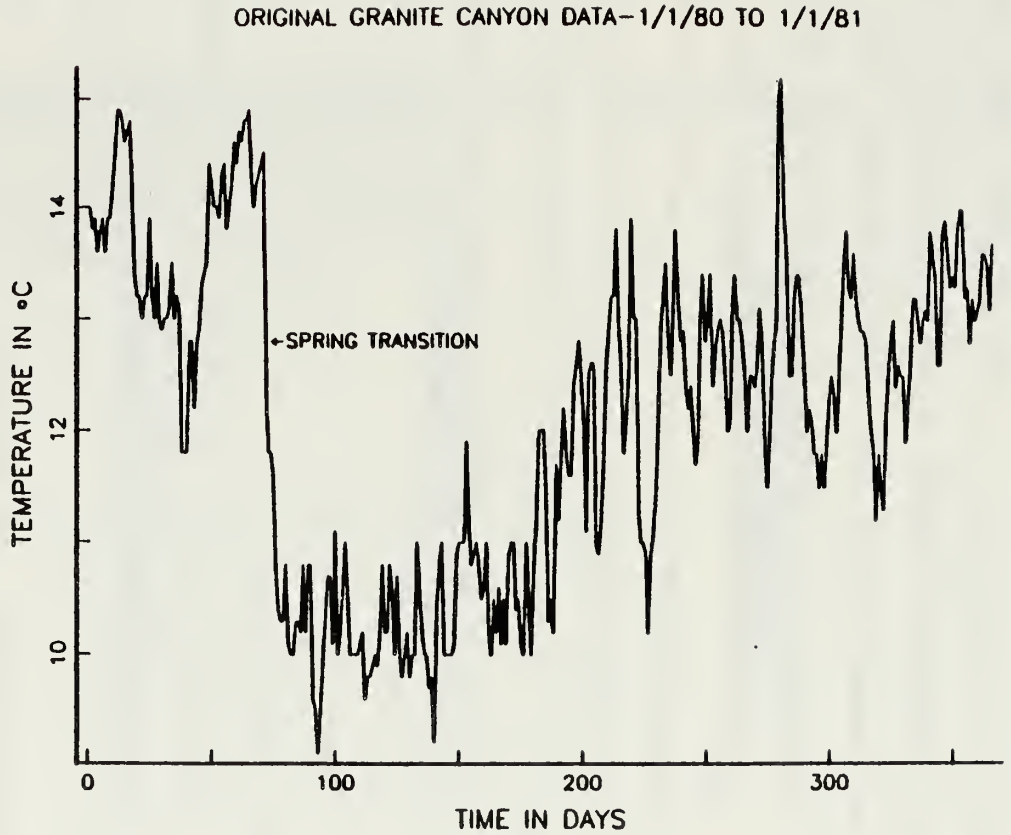

Figure 98. One-year time series at Granite Canyon from January 1, 1980 to January 1, 1981. Major decrease in SST around day number 70 corresponds to the spring transition to coastal upwelling.

scale winds at this location however did not become upwelling favorable until just after this event occurred (Fig. 99). Offshore Ekman transport, a quantity directly proportional to the local alongshore wind stress, is shown at four locations along the west coast starting at Point Sur and proceeding south to 27N along the Baja Peninsula (Bakun, 1980). It is quite evident at 30N, 33N, and 36N that the major seasonal change to upwelling favorable winds did not occur until about the 15th of March, about four days after the spring transition was observed at Point Sur. However a significant change to upwelling favorable winds may have occurred at 27N several weeks before it occurred at points further north. Thus it is possible that disturbances in the form of coastally-trapped waves initiated along the Baja Peninsula may have propagated poleward producing upwelling further north along the coast in the manner described by Gill and Clarke (1974). Unpublished analyses of sea level and coastal wind data indicate that the area off Northern Baja may indeed be a source region for poleward propagating disturbances (Halliwell, 1982). During a similar spring transition in 1981, Brink, Stuart, and Van Leer (1983) also concluded that local wind forcing was not responsible for the transition they observed off Point Conception during that year. IR satellite imagery acquired just prior to, and

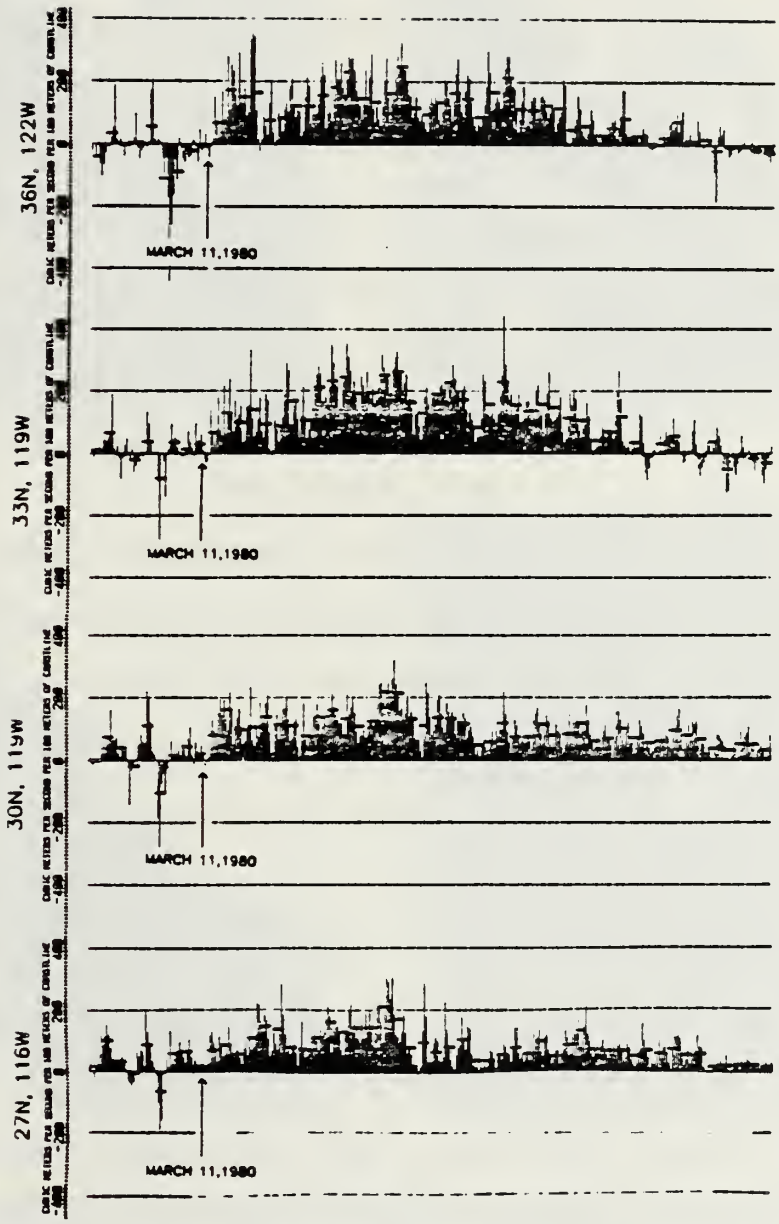

Figure 99. Upwelling index time-series for 1980 at 27, 30, 33, and 36N. Index values are directly proportional to alongshore wind stress, and are obtained from 6-hourly synoptic-scale winds calculated from sea level pressure (Bakun, 1980). March 11, 1980 corresponds to the date when the 1980 spring transition was first detected at Pt. Sur.

during this event (clearly) indicate a change from isothermal surface conditions to conditions suggestive of intense upwelling in the vicinity of Pt. Sur (Fig. 100). The last two images, on the 12th and 16th of March, 1980 coincide with the observed transition period per se, and show the development of upwelling as far north as the Monterey Peninsula.

The relative times at which the 1980 spring temperature transition occurred at four locations along the California coast are seen in Figs. 68, 69, and 70. This event arrived first at Diablo Canyon, second at Granite Canyon, third at the Farallons, and finally at Pacific Grove. To obtain an estimate of alongshore phase speed for the 1980 spring transition, eight arrival time differences (with respect to Granite Canyon) from Diablo Canyon ($\sim$35N) to the Oregon border ($\sim$42N) are plotted, as a function of alongshore distance (not including Pacific Grove) in Fig. 101. A phase speed of about 75cm/sec is obtained from a linear least squares fit to the data. Phase speeds of this order are consistent with those expected for coastally-trapped waves (Allen and Romea, 1980).[12]

Spring transitions off Oregon were observed from time series of currents and sea level in 1973 and in 1975 (Huyer et al., 1979). The spring transitions off Oregon also took place within about one week. However, these transitions were attributed to the cumulative wind stress

MARCH 3,1980

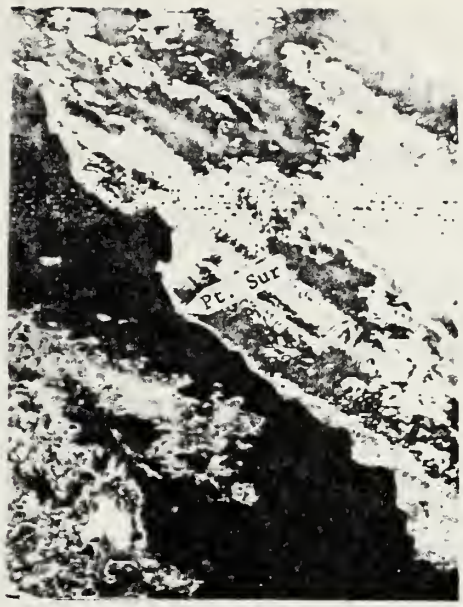

MARCH 8,1980

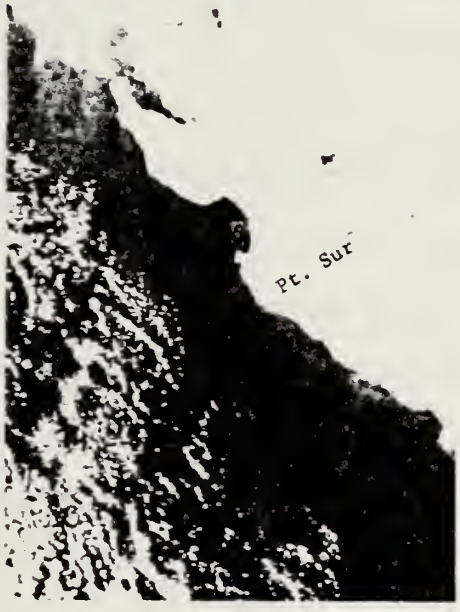

MARCH 12,1980

MARCH 16,1980

Figure 100. AVHRR IR satellite images showing coastal region off Pt. Sur just before, and during, the 1980 spring transition. Upper left panel shows an image from March 3, 1980. Upper right panel shows an image from March 8, 1980. Lower left panel shows an image from March 12, 1980, and lower right hand panel shows an image from March 16, 1980.

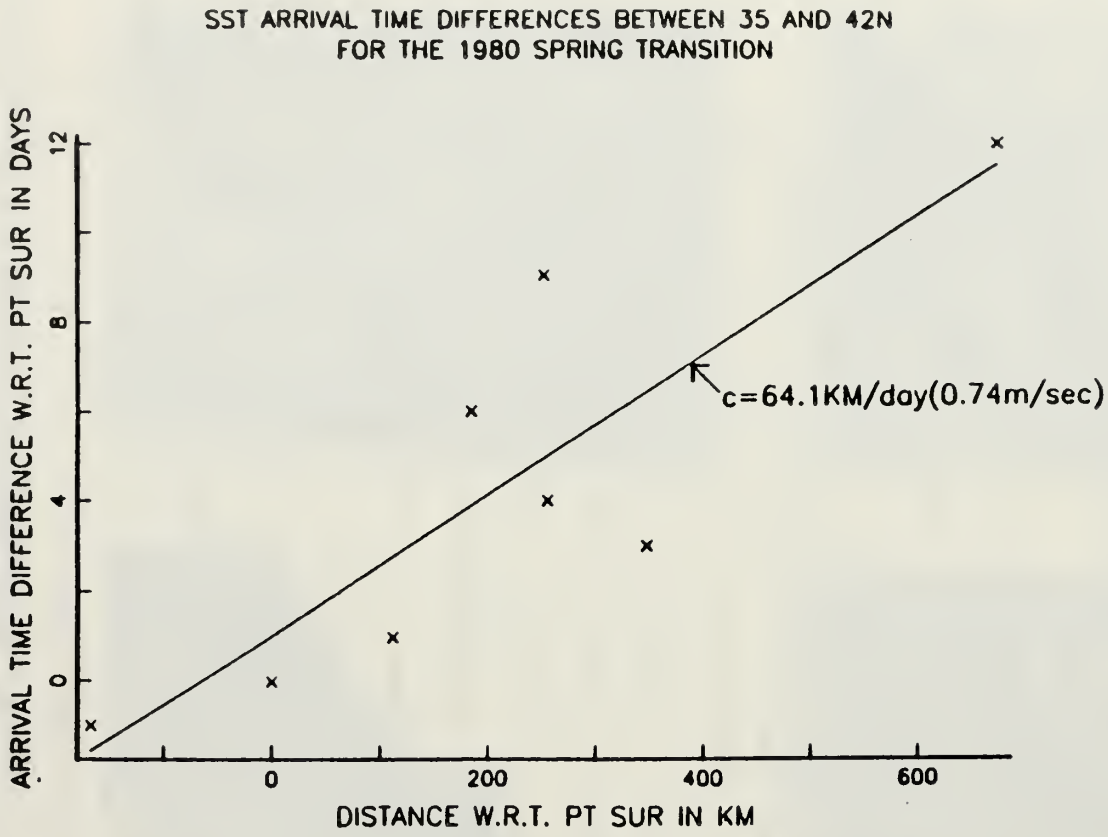

Figure 101. Sea surface temperature arrival time differences with respect to Granite Canyon at eight locations along the California coast between 35 and 42N. Along the abscissa, to the left is southward, and to the right, northward. A linear least squares fit to the data yields a poleward speed of 64.1km/day.

locally. According to the Coastal Ocean Dynamics Group (1983), the 1981 spring transition observed off Pt. Arena was the result of the onset of upwelling favorable winds associated with the establishment of the North Pacific high pressure system. It is certainly possible that different mechanisms may be responsible for initiating the spring transition in different years along the U.S. West Coast.

2. The Annual and Other Cycles

A mean annual temperature cycle has been calculated for the Granite Canyon data, realizing that from the previous statistical calculations a mean value may not be a truly representative measure of central tendency in the data. Points corresponding to the average temperatures and a smoothed version of that average (with a window of 25 points) are both presented in Fig. 1Ø2. According to List and Koh (1976), and to Reid, Roden and Wyllie (1958), a well-defined annual cycle in SST might not be expected near Pt. Sur, due to warming during the winter from the Davidson Current and cooling during the spring and summer from coastal upwelling. To the contrary, Fig. 1Ø2 shows a well-defined annual cycle at Granite Canyon, with a range of about 3C. However, in Fig. 1Ø2 the annual range of variability in temperature is reduced at Granite Canyon compared to the range of variation usually found at this latitude (Robinson, 1976). The effect of averaging the

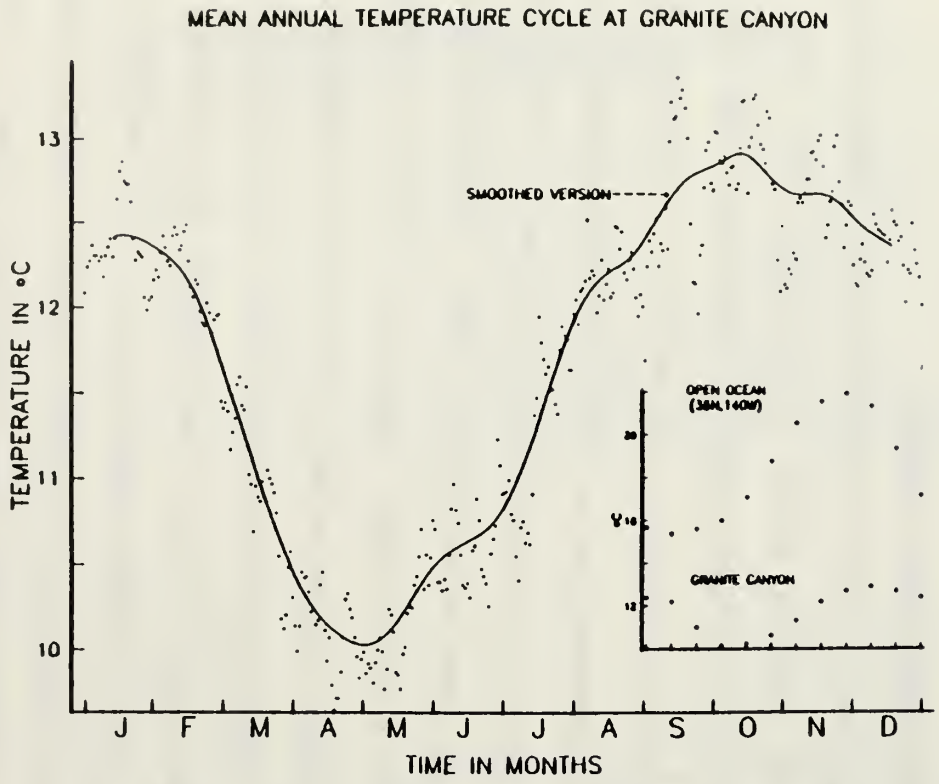

Figure 102. Mean annual temperature cycles at Granite Canyon and at an open ocean location (36N, 140W). The 12-year record at Granite Canyon was averaged to obtain the mean (dotted) annual cycle. The smoothed version was obtained by using a low-pass filter with a cosine taper and 49 weights. The open ocean data were obtained from Robinson, 1977.

data has been in part to "smear" the occurrence of the spring transition over a two-month period from about mid-February to mid-April. Maximum temperatures are seen to occur during mid-October, about a month later in the year than might be expected at this latitude. Obviously the phase relationships between such factors as the onset and cessation of the Davidson Current, and the onset and cessation of coastal upwelling determine in part the detailed structure of the annual temperature cycle off Pt. Sur in any given year. Skogsberg (1936) originally specified three oceanic seasons for Monterey Bay, an upwelling season from about February to July, an oceanic season from about July to November, and a Davidson Current season from about November to February. According to the smoothed average annual cycle presented in Fig. 102, at least two "seasons" can be identified, an upwelling season and a non-upwelling season. Based on the data presented here the distinction between an oceanic season and a Davidson Current season is not clear. However Skogsberg used spatially distributed temperature data as well as chemical and biological observations to construct his seasonal description. Also his seasonal model was derived for Monterey Bay and as a result it may not be valid to extrapolate his model to regions outside the Bay.

Since the annual cycle can be considered at least to a first approximation as consisting of two seasons, an

upwelling season and a non-upwelling season, it was of interest to examine these seasons separately for possible differences that would be unresolved in the global analyses. Consequently the original data have been partitioned into two segments, one 3 1/2 month segment from 15 March to 30 June, during the height of upwelling, and a second from 1 September to 16 December, a time clearly separate from the upwelling period. This partitioning was done for each of the 12 years. Periodograms were calculated for each of the segments for both seasons, and the resulting spectra for each season averaged over the 12 years. The results are shown in Fig. 103 for both periods and are similar over the limited range of frequencies available ($\sim$ 4 to 50 days). The differences between the two times of year are not statistically significant over any part of the spectrum as indicated by the 95% confidence limits.

3. El Nino Events

In addition to the seasonal variation in temperature at Granite Canyon, inter-annual variability is also evident, as mentioned previously in Section D. The significant increases in temperature during the winters of 1972, 1976, 1979, and 1983 correspond to El Nino episodes. These events have also been observed off Central California through biological measurements and measurements of sea level (Chelton, Bernal and McGowan, 1982).

COMPARISON OF PERIODOGRAMS FOR UPWELLING AND NON-UPWELLING PORTIONS OF THE YEAR AT GRANITE CANYON

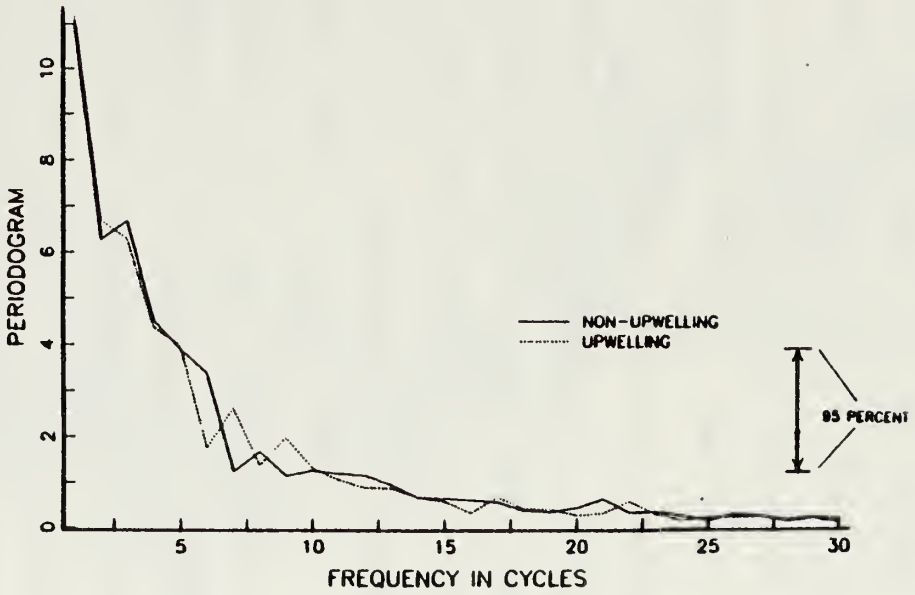

Figure 103. Comparison of spectra for upwelling and non-upwelling portions of the year at Granite Canyon. Upwelling period is defined from 15 March to 30 June, and non-upwelling period from 1 September to 16 December. Individual spectra for each period were averaged over the entire 12 years to obtain the plots shown.

Of particular interest is the major El Nino warming event of 1982-83. This warming was shown to extend at least 5ØØ Km off the coast of Central California during February 1983 (Linder and Breaker, 1983). The effects of the present warm anomaly are clearly evident in Fig. 1Ø4, which compares the 3/1/82 to 3/1/83 time period (the dashed curve) to the smoothed 12-year average (the solid curve). Early in 1982, warming off Granite Canyon appeared to be intermittent. However, by late 1982 warming at this location had become well-established. As of February 1983, the warm anomaly at Granite Canyon had reached almost 3C.

A closer inspection of Fig. 67 indicates that the most pronounced spring transitions usually occur in the springs following El Nino episodes. The spring transitions in 1973, 1977, and 198Ø provide the best examples. First, the SST time series show that the warmer temperatures associated with El Nino episodes occur mainly during the fall and winter, or non-upwelling, seasons. This pattern, which increases the overall temperature difference between winter and spring, amplifies the effect of the spring transitions when they occur. However, it is possible that the El Nino events additionally provide a mechanism by which the spring transitions are triggered.

SST COMPARISON BETWEEN 3/1/82 TO 3/1/83, AND
SMOOTHED 12-YEAR MEAN AT GRANITE CANYON

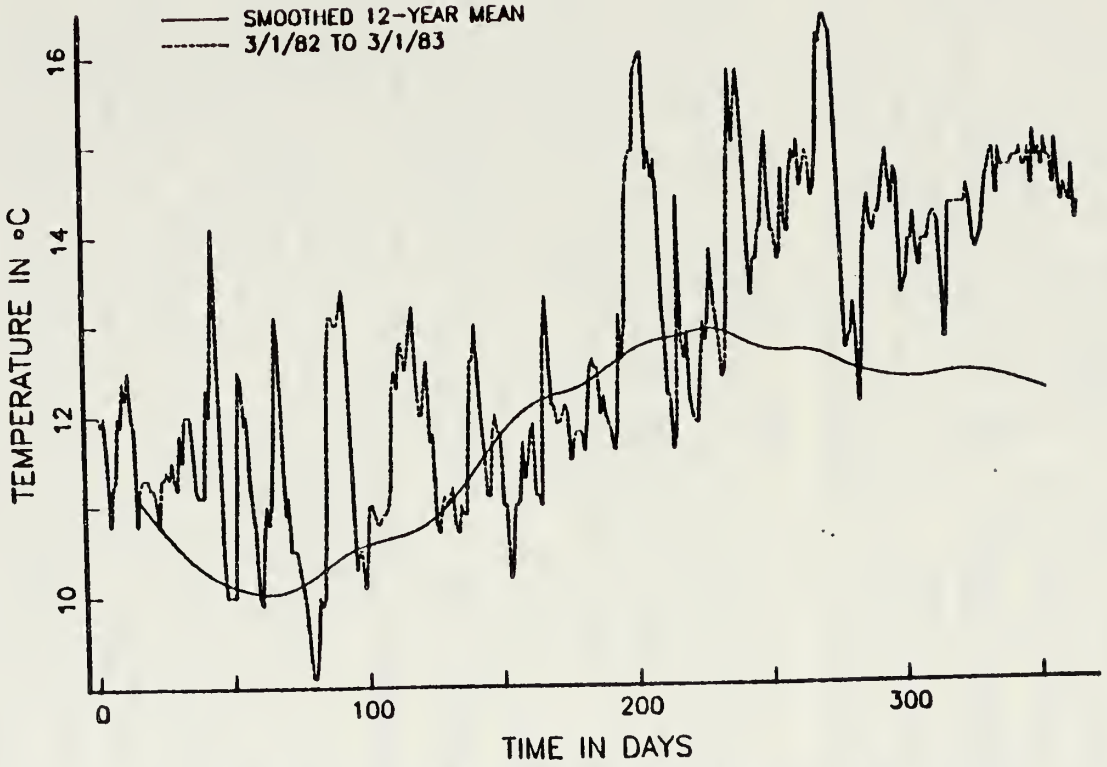

Figure 104.. Comparison of sea-surface temperatures at Granite Canyon for period of March 1, 1982 to March 1, 1983 with a smoothed 12-year mean (the dashed curve represents the actual observations).

4. Additional Periodic and Non-periodic Effects

From an oceanographic viewpoint, the periodogram shown previously in Fig. 75 is somewhat surprising for its lack of any major spectral components beyond 100 cycles. For example, spectra of winds along the California coast often show higher amplitudes at periods between 3 and 10 days (Van Patten, 1981). Continual stirring of the near-surface environment and the associated lack of stratification however may tend to inhibit these periodic influences on SST. It is also possible that periodic forcing by the wind is not important at this particular location.

Originally the possibility of aliasing by the semidiurnal and/or diurnal tides was a concern. Analysis of similar observations at other locations along the California coast by List and Koh (1976) indicated that tidal aliasing (or a natural periodicity corresponding to the spring/neap tides) by the semidiurnal (M_2) tide at 14.78 days or 14.19 days for the diurnal ($\emptyset_1$) tide could be important. Although peaks in the periodogram at 14.19 days (309 cycles) or 14.78 days (296 cycles) are not obvious, it was mentioned in Section 4.4 that the persistent hump in the autocorrelation plot of second residuals at Granite Canyon may be due in part to tidal aliases in the 14 to 15 day range. Additional work is needed to clearly identify tidal influences in these data.

In examining the periodogram of second residuals, particularly at higher frequencies, it is also of interest to consider the likely influence of turbulence on these results. Turbulence production undoubtedly occurs from the breaking of incoming surface waves and perhaps from local drift currents as well. In this regard a portion of the periodogram of second residuals has been smoothed and replotted on log coordinates in Fig. 105. The uniform decrease in spectral amplitude with increasing frequency is reminiscent of the spectral decay often associated with the inertial subrange from homogeneous turbulence theory (Batchelor, 1953). Between 200 ($\sim$ 22 days) and 2000 cycles ($\sim$ 2.2 days), the spectral slope is essentially constant at -1.8, close to the value of -5/3 predicted by classical turbulence theory (Phillips, 1977). Acording to this theory temperature is assumed to be a conservative quantity, an assumption which could be quite unrealistic at the sea-surface. In the present case, time replaces distance, where distance (i.e., wavenumber) is normally taken as the independent variable in representing turbulence spectra. However, if it is assumed that these coordinate frames are linearly related, then the spectral slopes observed here are directly comparable with those usually derived in oceanic turbulence calculations as a function of wavenumber. According to Taylor (1938), space and time spectra and correlation functions are equivalent

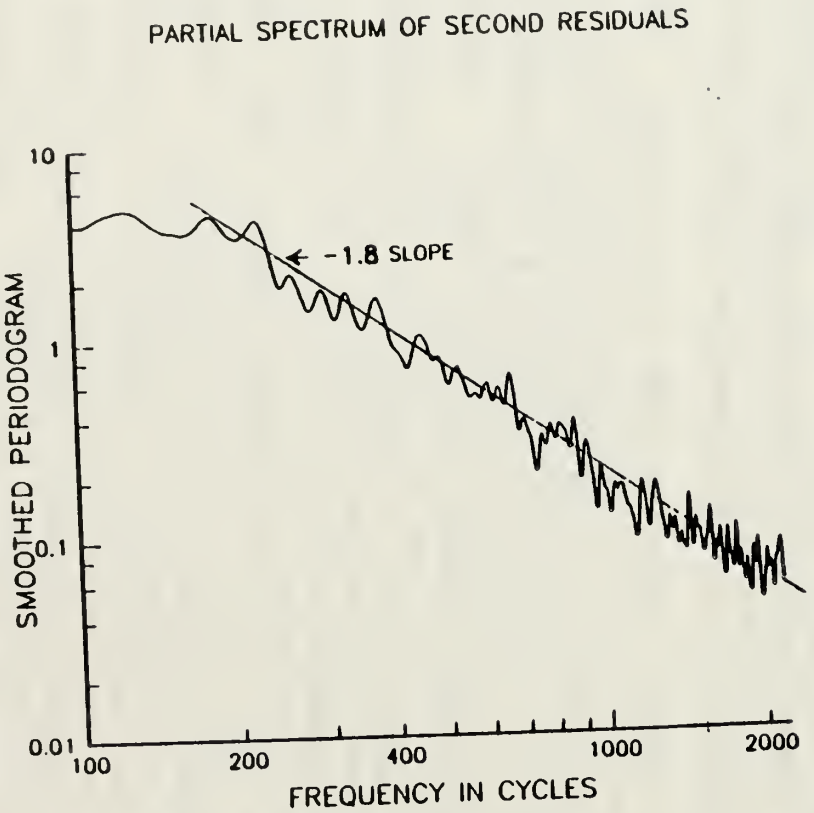

Figure 105. Partial spectrum of second residuals for temperature at Granite Canyon. Periodogram from 100 to 2000 cycles has been smoothed to show the constant slope that occurs over this range of frequencies. An estimated slope of -1.8 was obtained, and is similar to the -5/3 slope predicted by classical homogeneous turbulence theory.

provided that the relative intensity of turbulence is sufficiently low. In turbulence models where temperature is not assumed to be conservative, spectral slopes considerably greater than -5/3 are predicted (Panchev, 1980). Measurements of the spatial surface temperature spectrum by Saunders (1972) and Holladay and O'Brien (1975) yielded spectral slopes of -2.2 and -3.0 respectively, suggesting that temperature should not be treated as a conservative quantity at least under certain conditions.

K. SUMMARY AND DISCUSSION OF RESULTS

The major objective of this chapter has been to estimate the time scales of variability for ocean temperature in the area of the present study. Techniques as well as results are emphasized because the techniques used in time scale analysis are not well-established. Time series at four locations were examined. First, 12-year records of SST at three coastal locations were analyzed, and second, a 52-day record of temperature at 175m off Cape San Martin and a record of SST of the same length at Granite Canyon were analyzed and compared. As part of the analysis, a stochastic model was developed. The model provided a useful framework for analyzing the data. From the model, considerable insight was gained with respect to the types and causes of variability associated with the data. The model is based on a statistical decomposition of

the data into deterministic and random components. The deterministic components were first modeled using linear or polynomial trends. The periodic components were modeled using a least squares fit to selected harmonics which were identified through periodogram analysis. Random components were taken into account using an autoregressive model. Although it was not shown that an autoregressive model was in some sense the best model that could be used, it was shown that by using an autoregressive model, the final results agreed with certain theoretical expectations within acceptable limits.

In analyzing the SSTs at Granite Canyon, Pacific Grove, and the Farallons, long-term increases in temperature were observed at each location. At each location the annual cycle and its first harmonic were the most important periodic components. A hump in the autocorrelation plots in the range of 14 to 22 days occurred for all 3 data sets. The source of this anomaly is unknown but it may be related to the alias of the semidiurnal tide. Several uses for the model were discussed, in addition to using the model to estimate time scales. In particular, it was shown how the model could be used to produce simulations that could in turn provide a basis for estimating adequate sampling rates.

Time scales were estimated from the data after deterministic components were first removed. The

autocorrelation function provided the basis for estimating these scales, although cumulative periodograms were also calculated and examined in this regard. Several criteria were initially applied to the calculated correlation functions in order to obtain estimates of the desired time scales. E-folding, first zero-crossing, and integral time scale criteria were considered. The e-folding criterion was easy to implement and provided consistent results; therefore it was used almost exclusively in obtaining subsequent scale estimates. For SST, time scales were 5.3 days at Pacific Grove, 6.Ø days at Granite Canyon, and 8.4 days at the Farallons. Additional calculations were performed for the data at Granite Canyon to check the repeatibility of the previous results by breaking the 12-year record into two 6-year segments. Each segment was then analyzed separately. The results for each segment were similar, and similar to the overall 12-year scale estimate.

As indicated in Chapter I, the time scale associated with a given realization (τ_o), and the number of statistically independent observations contained in that realization (n^*) are intimately related. One of the primary reasons for wanting to know n^* is to specify confidence limits for the calculated correlation functions. Since n^* is not known a priori, the total number of data points, N, is often used to estimate confidence limits for correlation

functions. For highly autocorrelated time series the use of N vice n^* can lead to large errors in estimating the confidence limits. As indicated in Chapter I. the number of statistically independent observations and the associated time scale are related by

$$n^* = N \cdot \Delta t / \tau_o \qquad (4.13)$$

If confidence limits had been estimated for the first residuals in Section 4.3,for example,the value for τ_o would be approximately one year (the annual cycle) and n^* from (4.13) would be approximately 12. Thus, the confidence limits in this case would have become much wider. The e-folding scale criterion was found suitable for estimating τ_o but its use may not necessarily yield the same results as the integral scale criterion. Davis (1976, 1977) and Sciremammano (1979) used integral time scales in estimating τ_o. However as discussed previously, to fully implement the integral scale criterion requires considerable computational effort. Although the integral scale criterion is not fully implemented, another approach very similar to the integral scale method for estimating the number of statistically independent observations in a time series, and thus the corresponding time scale, is shown. It is applied to the Granite Canyon data (i.e., the second residuals). By using certain approximations, the number of statistically independent observations in a given time series can alternately be estimated from (Bartlett, 1946):

$$n^* = N \Big/ \sum_{j=0}^{N-1} \rho_j(\tau) \qquad (4.14)$$

where r_j represents the jth correlation. The denominator in (4.14) is obviously directly proportional to the previous integral defined in (4.12), the integral time scale. The autocorrelation function itself, calculated out to 1000 lags, shows slight oscillatory behaviour about zero beyond the first zero-crossing (Fig. 106, upper panel). The denominator in (4.14) has also been calculated for selected lags out to 1000 (Fig. 106, lower panel). Beyond about 450 lags, the sum of the autocorrelations tends to converge to a value of 5.0. This value corresponds to earlier estimates of obtained using the other criteria and agrees favorably with the previous value of 6.0 days. However, Fig. 106 (lower panel) also provides an indication of the spread in scale estimates that might be expected in using the integral scale criterion for similar autocorrelation functions.

One record of subsurface temperature was also subjected to time scale analysis. A 52 day record of temperature at 175m off Cape San Martin was chosen. A coincident segment of SST from Granite Canyon was also analyzed for comparison. The estimated time scale for the SST segment was about 30 hours, whereas the time scale for the corresponding subsurface segment was only about 2 hours. The difference in time scales was attributed in

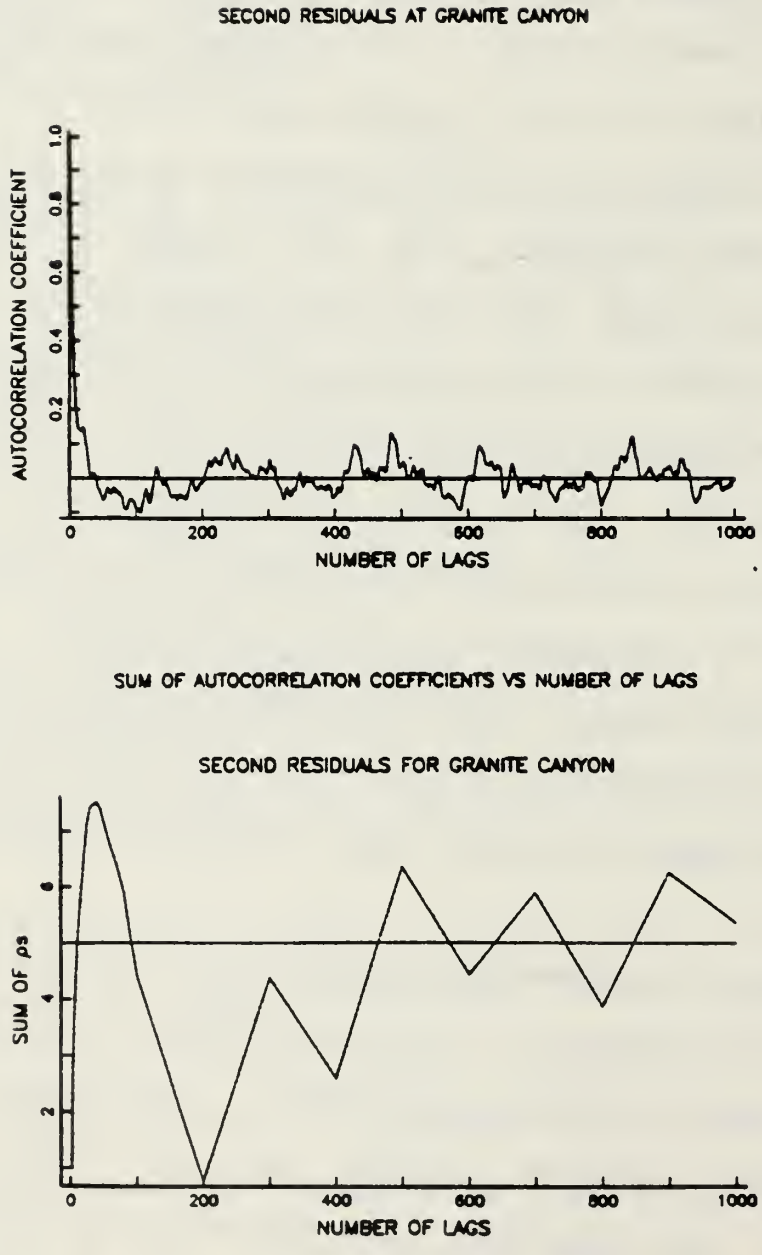

Figure 106. Autocorrelogram of second residuals for SST at Granite Canyon out to 1000 lags is shown in the upper panel. Lower panel shows the sum of autocorrelation coefficients versus selected lag numbers out to 1000 lags. The sum of the autocorrelation coefficients tends to converge to a value of about 5.0. This value agrees favorably with the previous time-scale estimate of 6.0 days obtained by using the e-folding criterion.

part to the difference in sampling rates (i.e., daily vs. hourly) Correlation time scales have been found to be strongly depth dependent in other areas also (Freeland et al., 1976). However more data at different depths will have to be analyzed to adequately define the vertical dependence of these time scales.

The SST data have also been examined from a purely oceanographic viewpoint. Major, abrupt decreases in temperature (Ø(3C)) were found during the spring in 6 out of the 12 years. These transitions are associated with the seasonal change to coastal upwelling although the overall duration of these events is only about 1 week. These dramatic changes in SST have not been identified previously because the data were usually presented as monthly averages. These transitions may not be due to local changes in the wind field, but could be the result of remote forcing by the wind at points further south along the West Coast.

A clearly defined annual cycle in SST was observed at Granite Canyon, although its range is only about 3C. Maximum temperatures occur at this coastal location in mid-October, about a month later than expected further off the coast at this latitude. However, cross-correlation of the Granite Canyon and Pacific Grove data (not shown) indicate that maximum values in SST in Monterey Bay at Pacific Grove preceed the seasonal maximum at Granite Canyon by almost

two months. This is mainly attributed to local heating in the Bay. Seasonal temperature maxima at Granite Canyon and the Farallons are approximately in phase. Four distinct El Nino warming events were observed in the records of SST over the 12 year period: 1972-73, 1976-77, 1979, and 1982-83. The temperature anomalies associated with these events along Central California can persist for many months and their magnitudes may reach several degrees C. The most pronounced spring transitions followed El Nino events. SSTs during El Ninos were noticeably higher during the fall and winter, a pattern which intensifies the spring transitions when they occur. The magnitude of the 1982-83 El Nino may ultimately be as great as the major warming event observed off the California coast during 1957-58. The influence of these events along the U.S. West Coast has received little attention, yet their effect on fisheries and local climate have been, in some cases, significant.

Periodogram analysis did not reveal obvious periodicities at the higher frequencies. Neither wind nor tide-related components could be identified. However, tidal influence may have contributed to the hump found consistently in the auto-correlation of the second residuals. Over time intervals of about 2 days to 3 weeks the slope of the spectrum of second residuals remained rather constant, suggestive of the likely influence of

turbulence on the data. An estimated spectral slope of about -1.8 agrees well with the -5/3 slope predicted by classical turbulence theory. However it was noted that due to non-conservative effects on temperature at the surface, a slope different from that predicted by classical homogeneous turbulence theory might be expected.

V. SPATIAL ANALYSIS OF THE IN SITU TEMPERATURE DATA

A. INTRODUCTION

In the present chapter the spatial scales of variability are considered. The techniques used in the previous time scale analysis are often similar to the techniques used in analyzing the spatial data. The differences arise mainly from the way in which the data used in the spatial analyses were acquired. In situ XBT and STD temperature profiles acquired aboard ship during the June 1980 Pt. Sur upwelling center study form the data base used in the spatial analyses.

The four-dimensional space-time correlation field can be expressed (for second-order statistics) as:

$$\rho_{ij}(h_1, h_2, h_3, \tau) = E\{A_i(x,y,z,t)A_j(x+h_1, y+h_2, z+h_3, t+\tau)\} \quad (5.1)$$

where

ρ = Auto(cross) correlation coefficient

$E\{\}$ = Expected value operator

A = Selected property

h_i, τ = Lags with respect to Cartesian coordinates, time

$i = j \Longrightarrow$ 4-D Autocorrelation structure

$i \neq j \Longrightarrow$ 4-D Cross-correlation structure

Because the number of observations is always limited, it is only possible to estimate certain subsets of (5.1). However (5.1) provides a useful conceptual framework within which certain correlations of lower dimension are considered and subsequently calculated. The problem is to select those combinations which are meaningful from a physical standpoint, and feasible from a computational standpoint. Such calculations would, for example, provide information on (1) the differences between the alongshore scales and the offshore scales (i.e., degree of anisotropy), (2) the location and extent of inhomogeneous regions, (3) the vertical coherence of horizontal temperature patterns, (4) degree of stationarity estimated from measurements repeated over the same volume, and (5) the separate contributions of space and time to the observed field of variability.

Because the data were acquired from a moving ship, observed property changes are both space and time dependent. One of the major problems in analyzing and interpreting these data arises because of the space-time ambiguity. Unlike the coastal time series data, where sufficient degrees-of-freedom (DOFs) were always available to obtain statistically significant results; the number of observations available for analysis with respect to the *in situ* data are often marginal, and in some cases are clearly insufficient to admit statistically significant

calculations. Because of these difficulties several approaches have been taken in attempting to obtain meaningful estimates of the spatial scales. Although all of the calculations are influenced by the amount of data available, the different approaches provide alternate ways of evaluating the significance of the results obtained.

Correlation analysis techniques were used initially. Vertical temperature profiles were cross-correlated in an attempt to ascertain the space-time changes in vertical temperature structure over the area. Interprofile cross-correlations were plotted in space-time coordinates in an effort to separate the effects of space and time. However, because of (1) the limited number of DOFs per profile, (2) the dominance of the mean profile shape, and (3) the ever present space-time ambiguity, the results of these analyses were difficult to interpret, and generally inconclusive. However, these analyses do provide a useful background for the calculations which were undertaken subsequently in this chapter, and demonstrate techniques which may be far more revealing with data sets that are more extensive. Consequently these analyses are included as APPENDIX B. Two types of spatial correlations were calculated that provided particularly useful results; spatial autocorrelations in the horizontal plane, and vertical

pattern correlations. The results of these analyses are included in this chapter.

EOFs were also calculated to obtain estimates of the spatial scales. EOFs are also a type of correlation function in that a given eigenvector characterizes the spatial pattern of variability associated with a particular mode. The isopleths associated with a given eigenvector then represent regions of similarity, directly analogous to the information obtained from spatial correlation functions. The final three sections of this chapter utilize EOF analysis techniques to examine spatial variability and to estimate the associated scales.

B. SPATIAL AUTOCORRELATIONS AND PATTERN CORRELATION ANALYSIS

Spatial autocorrelations have been calculated for selected temperature data from Phase 1A at Ø, 5Ø, and 1ØØ meters. The general calculation can be expressed as

$$R_{ij}(\Delta r,\Delta\theta) = E\{T_i(r,\theta,t) \cdot T_j(r+\Delta r,\theta+\Delta\theta)\}$$

In the following computational algorithm, Cartesian instead of polar coordinates have been used:

$$R_{ij}(\Delta x,\Delta y) = \sum_x \sum_y (T_i'(x,y)\cdot T_j'(x+\Delta x, y+\Delta y))/NF$$

where,

$$T'(x,y) = T(x,y) - \hat{T}(x,y)$$

$$\hat{T}(x,y) = Ax + By + C$$

and,

$$NF = N(\sigma_{T_i}^2 \cdot \sigma_{T_j}^2)^{1/2}$$

This technique follows that given by Davis (1975) and Bretherton et al. (1976). Also, in working with the actual data, no time dependence was assumed. The input data consist of a T(x,y), an x, and a y, for each observation. The algorithm calculates a covariance matrix from the available (de-meaned) data for specified ranges of Δx and Δy. As shown above, a bi-linear trend was removed from the data before calculating the autocorrelations. This bilinear trend was estimated from a least-squares fit to the data. After initial experimentation, values of 15 and 30km were chosen for Δx and Δy, respectively. The calculated correlations for each $\Delta x/\ \Delta y$ combination have been plotted at the mid-point of each interval (Phase 1A at 0, 50, and 100m) (Figs. 107-109). The number of pairs that enter into each calculation are shown in parentheses next to the plotted correlations. Table 12 shows the first zero-crossing distances for Δx and Δy for each depth. With one exception (Δy at 50m) the values group well showing slightly greater values for Δy than for Δx, and also that both Δx and Δy increase slightly with depth. The mean alongshore-to-offshore ($\Delta y/\ \Delta x$) aspect ratio for these scale estimates is about 2:1, indicating that the observed degree of anisotropy was less than that expected (O(3:1) based on the original station spacings. Also, these scale

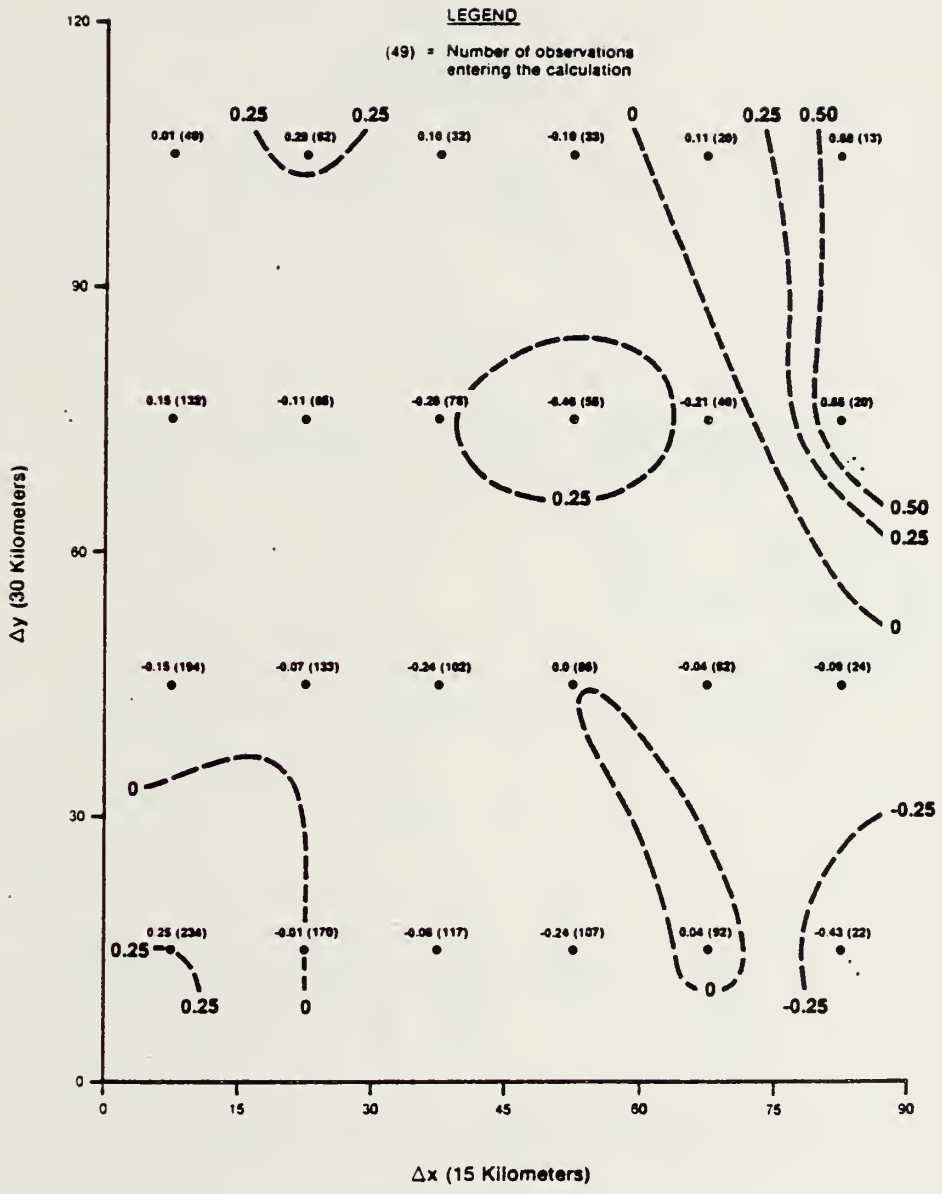

Figure 107. Spatial autocorrelation contours at the surface for Phase 1A. Values have been plotted at the midpoints of corresponding $\Delta x/\Delta y$ range increments.

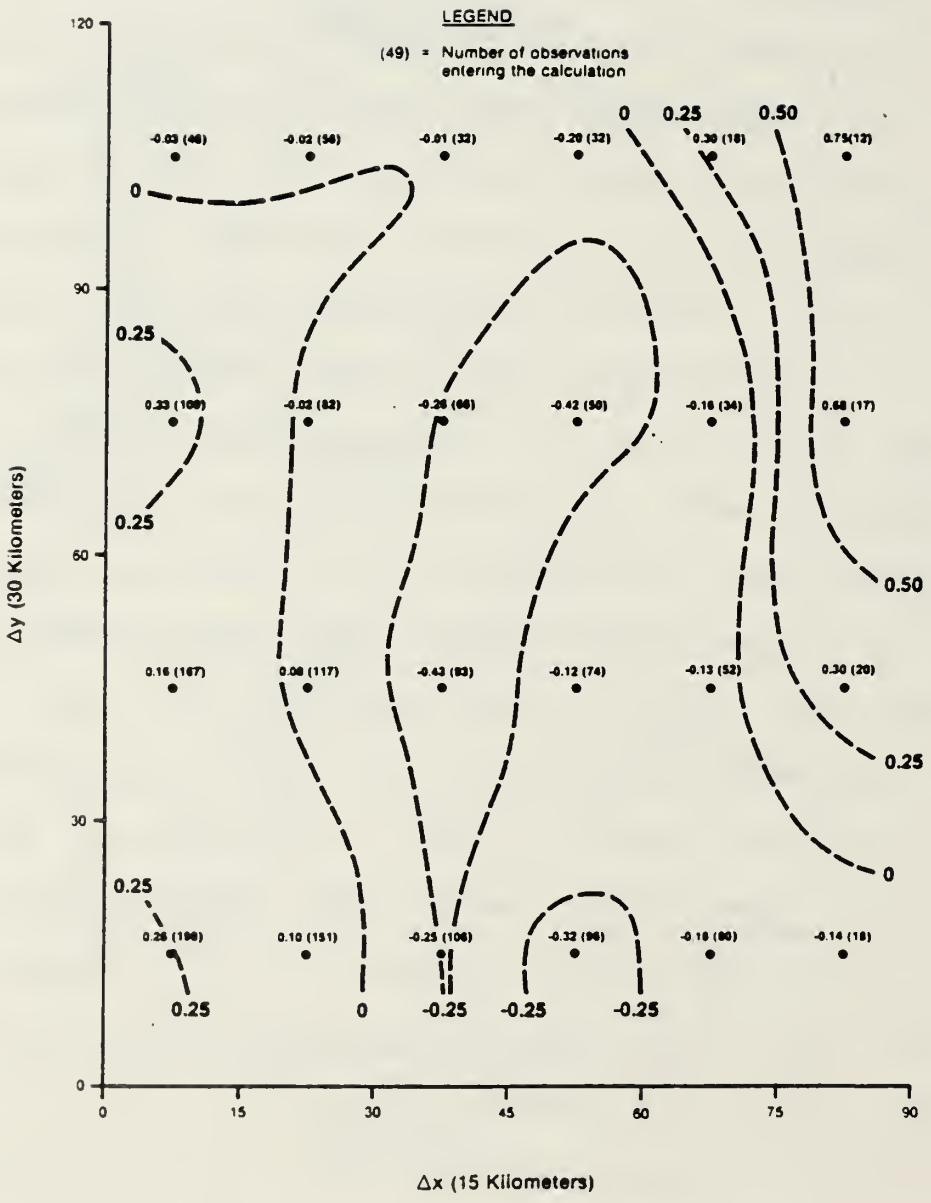

Figure 108. Spatial autocorrelations for Phase 1A at 50 meters.

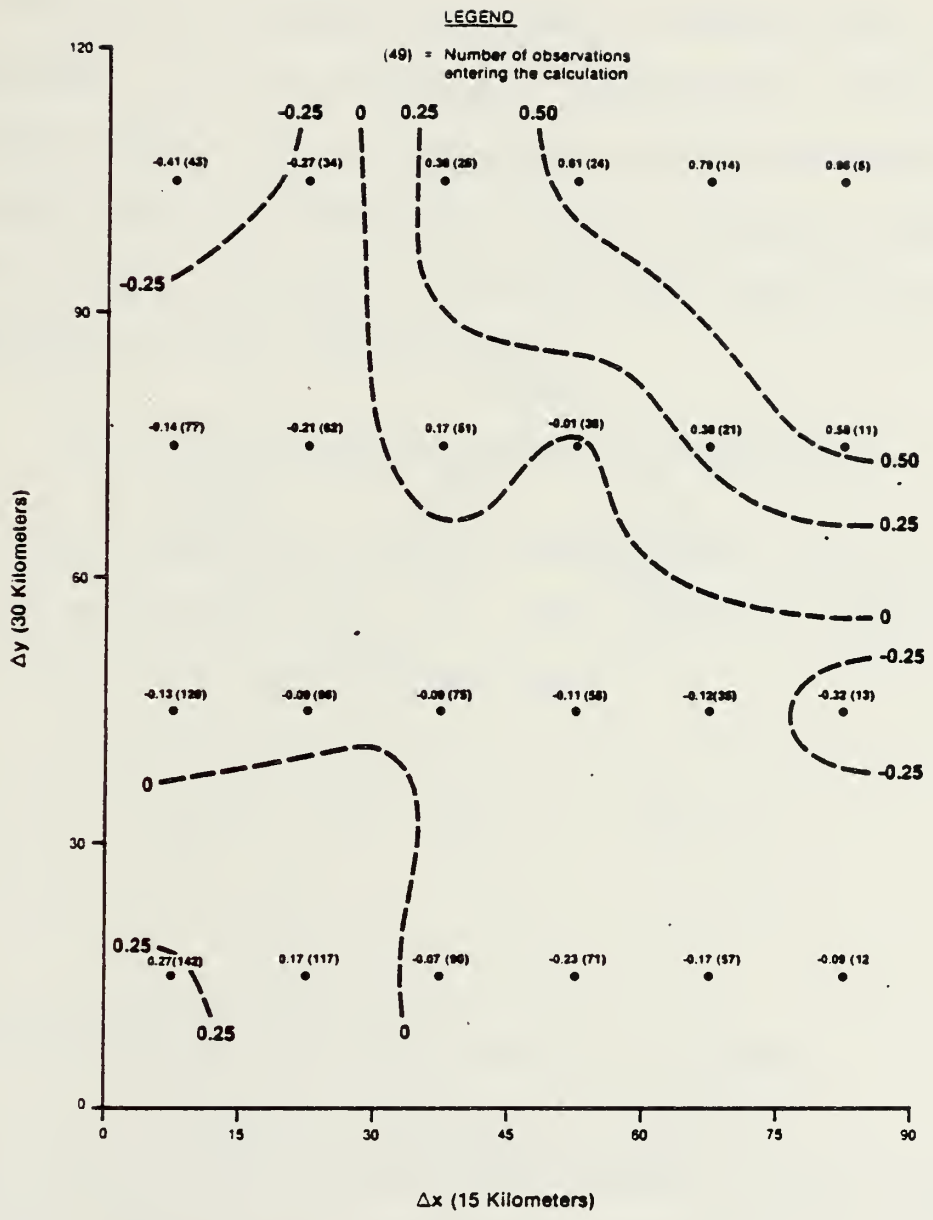

Figure 109. Spatial autocorrelations for Phase 1A at 100 meters.

Table 12

Spatial correlation scales for Phase 1A temperature data at 0, 50, and 100m

	0m	50m	100m
Δx(km)	22.5	29.0	33.0
Δy(km)	33.0	100.0	37.0

estimates are generally within the range of the alongfront scale estimates obtained from the previous EOF analysis of the satellite data.

C. PATTERN CORRELATIONS

Correlation analysis was used to examine the vertical dependence of the horizontal temperature field. The vertical correlation of temperature relates directly to the possible use of IR satellite data in predicting subsurface temperature patterns. The desired vertical pattern correlation can be expressed as:

$$R_{z_i,z_j} = E\{T_{z_i}(x,y) \cdot T_{z_j}(x,y)\} \qquad (5.3)$$

and if the temperature field is homogeneous, then R_{z_i,z_j} can be replaced by $R_{\Delta z_{i,j}}$. The computational form of (5.3) used in the calculations was:

$$R_{z_i,z_j} = \sum_x \sum_y (T'_{z_i}(x,y) \cdot T'_{z_j}(x,y))/NF$$

where

$$\hat{T}_{z_i}(x,y) = Ax + By + C$$

is the bilinear trend surface at $z = z_i$ and,

$$T'_{z_i}(x,y) = T_{z_i}(x,y) - \hat{T}_{z_i}(x,y)$$

To calculate pattern correlations between various levels it was first necessary to interpolate the <u>in situ</u> temperature data to a standard two-dimensional grid. The grid coverage for each phase is shown in Fig. 11Ø and corresponds

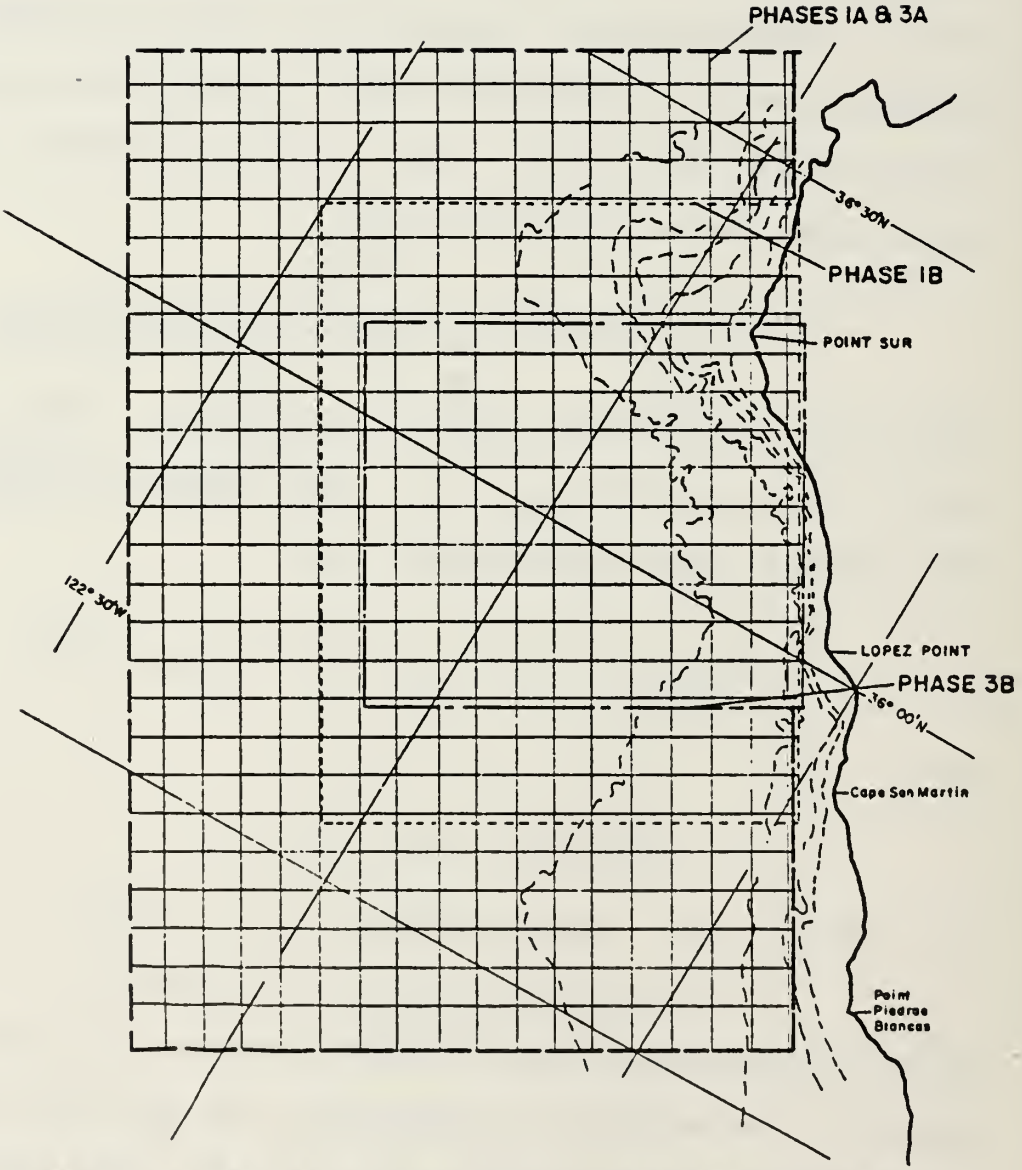

Figure 110. Spatial grid used to interpolate temperature data for each phase. Grid spacing is 5km (alongshore) x 5km (offshore).

approximately to the perimeter of the areas over which the field measurements were acquired. The grid spacing was chosen to be 5km in both the alongshore(y) and offshore(x) directions. A grid spacing of 5km was considered reasonable in view of the actual distances between stations which varied between 30km in the alongshore direction for phase 1A and 3A, to 1 or 2km, in the offshore direction, for stations near the coast, for phases 1B and 3B. Also the locations of grid intersections was kept the same for each phase thus facilitating interphase comparisons. This grid spacing resulted in array dimensions of 18 x 27 (85 x 130km) for phases 1A and 3A (i.e., 486 grid points). Nine grid points extend over land near Pt. Sur (Fig. 110), and corresponds to less than 2% of the entire interpolated data field for Phase 1A and 3A, and consequently has not been taken into account. Based on a comprehensive comparison of existing algorithms for two-dimensional (2-D) interpolation of scattered data by Franke (1979), the choice of suitable interpolation schemes for use with the present data was reduced to two. From a comparison of these algorithms, the so-called Modified Quadratic Method of Shepard (MQS) was adopted. A comparison between MQS and a previous hand-drawn analysis for SST is shown for Phase 1B (Fig. 111). These patterns are quite similar over the area. In a few cases, particularly at the surface, agreement was not as favorable. However, differences could usually be

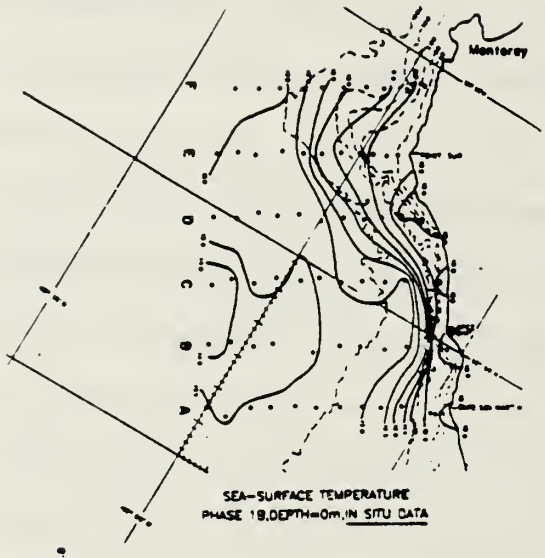

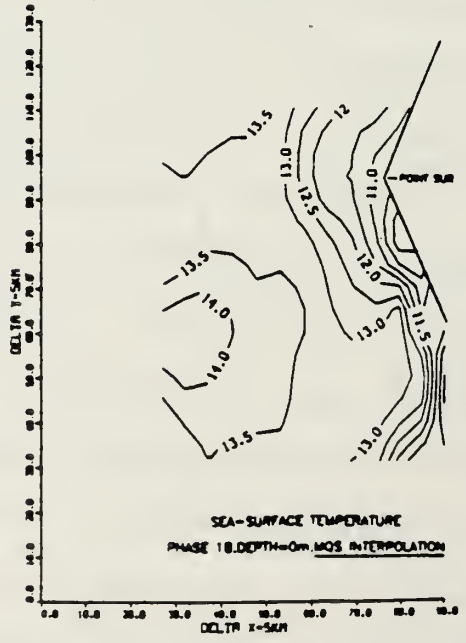

Figure 111. Comparison of contour maps for sea-surface temperature for Phase 1B. Lower panel shows machine-produced map using the MOS algorithm; upper panel shows hand-drawn version.

attributed to errors in the hand-drawn analyses. Subsurface property maps were generally less complicated and as a result, comparisons between MQS and the hand drawn analyses in these cases were almost always favorable. Details of the comparison between the two computational algorithms and explanations of how they are implemented, are given in Appendix C.

Ten levels were initially selected for interpolation: 0, 10, 25, 50, 75, 100, 150, 200, 250, and 300m. In principle, the selection of these levels should have been based on a vertical scale analysis of the temperature profiles. Such an analysis was attempted but because of (1) a lack of DOFs, (2) a lack of fine-scale structure (because of previous smoothing), and (3) the overriding influence of the mean profile shape, correlation techniques in this case proved to be unsatisfactory. However the results of separate EOF analyses using temperature profiles from all phases, generally support the original choice of depths.

A separate examination of the two-dimensional bilinear trend surfaces used to detrend the data is motivated since the slopes of these surfaces help to define physical characteristics of the local temperature field. A surface with an offshore linear trend has a physical basis in this case, since the dynamic height field generally increased

more-or-less monotonically in the offshore direction. Although a higher-order polynomial trend surface could have been removed, as much as 60% of the total variance in temperature is explained by a simple linear trend surface. A sequence of seven maps for Phase 3A, from the surface to 200m, that includes the original temperature field, the associated least squares bilinear trend surface, and the resulting residual surface, is shown in Figs. 112 through 118. First, the strongest gradients associated with the bilinear trend surface occur at 25 and 50m, in the upper thermocline. Secondly, a gradual counter-clockwise rotation of the axis of maximum gradient with depth occurs from the surface to 200m. Near the surface the axis of maximum gradient is oriented offshore while at 150m the axis has rotated by almost 20 degrees. This rotation with depth suggests that alongshore flow predominates in the upper 50m or so, while at deeper levels the influence of onshore flow may also be important, since the distribution of temperature and density are generally similar (Fig. 119). This general pattern of cyclonic rotation with depth occurs for each phase.

In Fig. 120A, the amount of variance explained by a bilinear trend is shown as a function of depth for Phases 1A and 3A. Over 60% of the total variance is usually explained by a simple bilinear trend in the upper 100m. Below 100m the gradients have generally become weaker and a

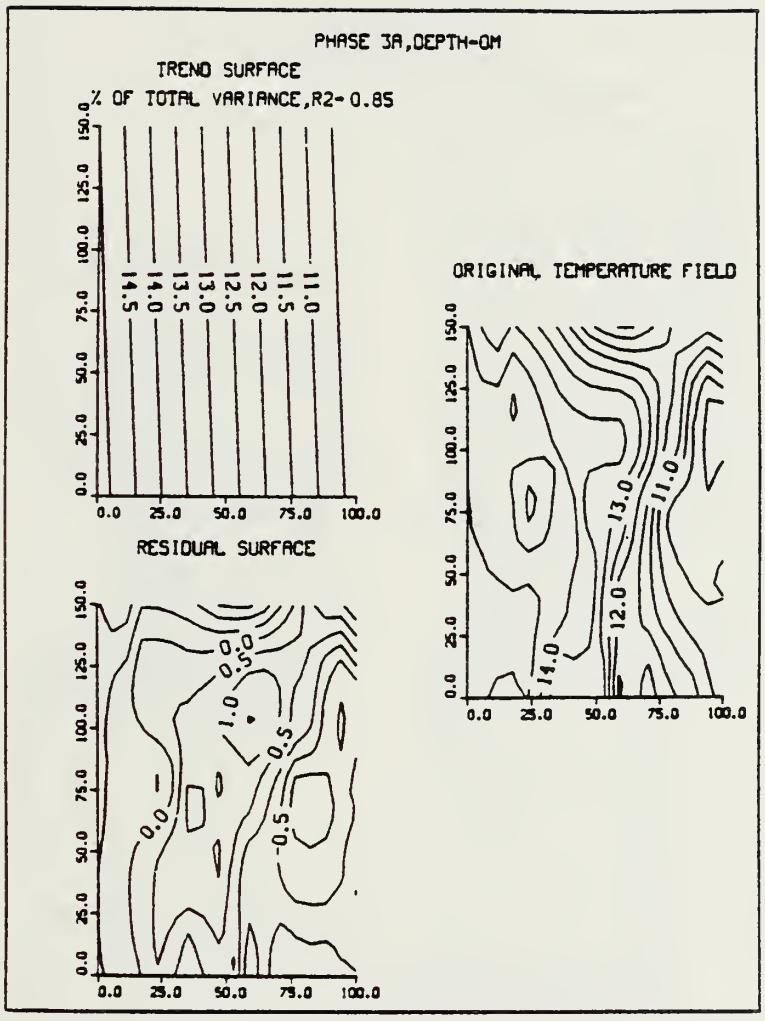

Figure 112. Temperature contour maps for Phase 3A at the surface, produced using the MQS algorithm for two-dimensional interpolation. Panel on R.H.S. shows original temperature field. Upper left panel shows the bilinear trend surface used to detrend original data. Lower left panel shows temperature residuals created by removing bilinear trend surface from original data.

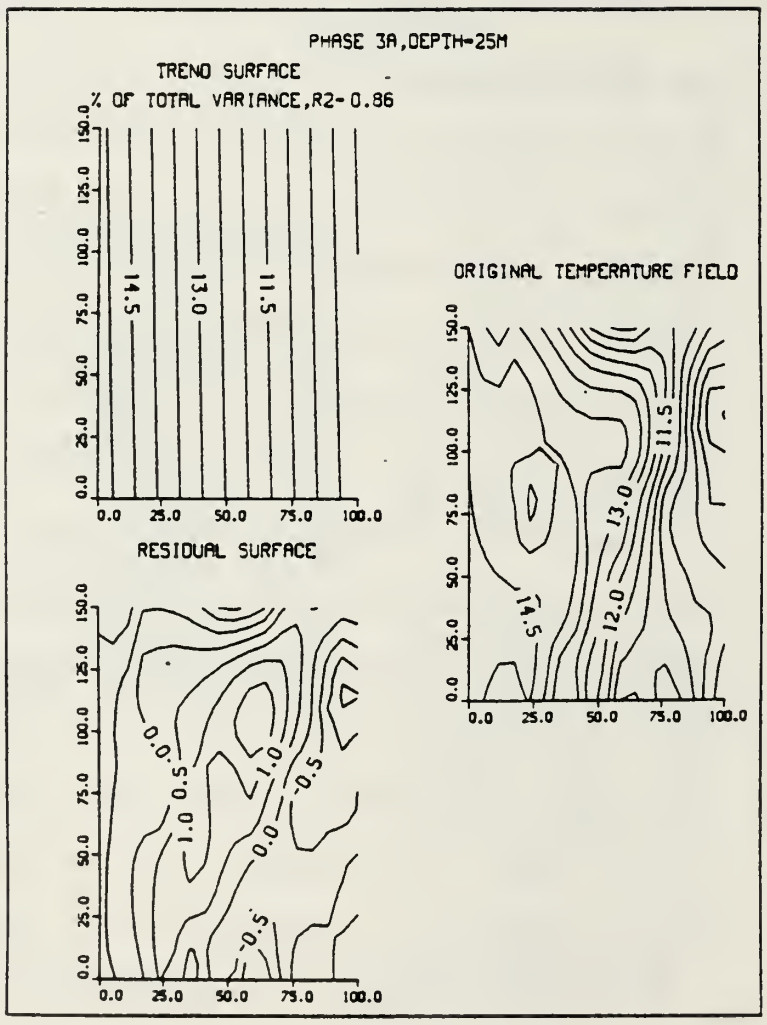

Figure 113. Same as Figure 112 except for a depth of 25m.

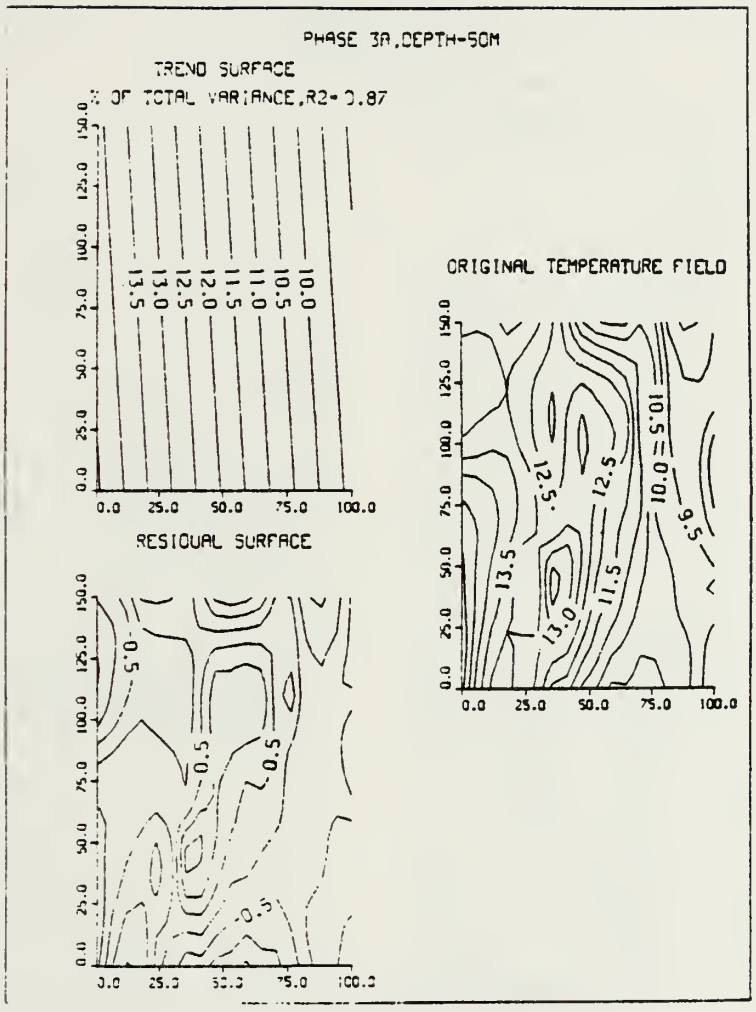

Figure 114. Same as Figure 112 except for a depth of 50m.

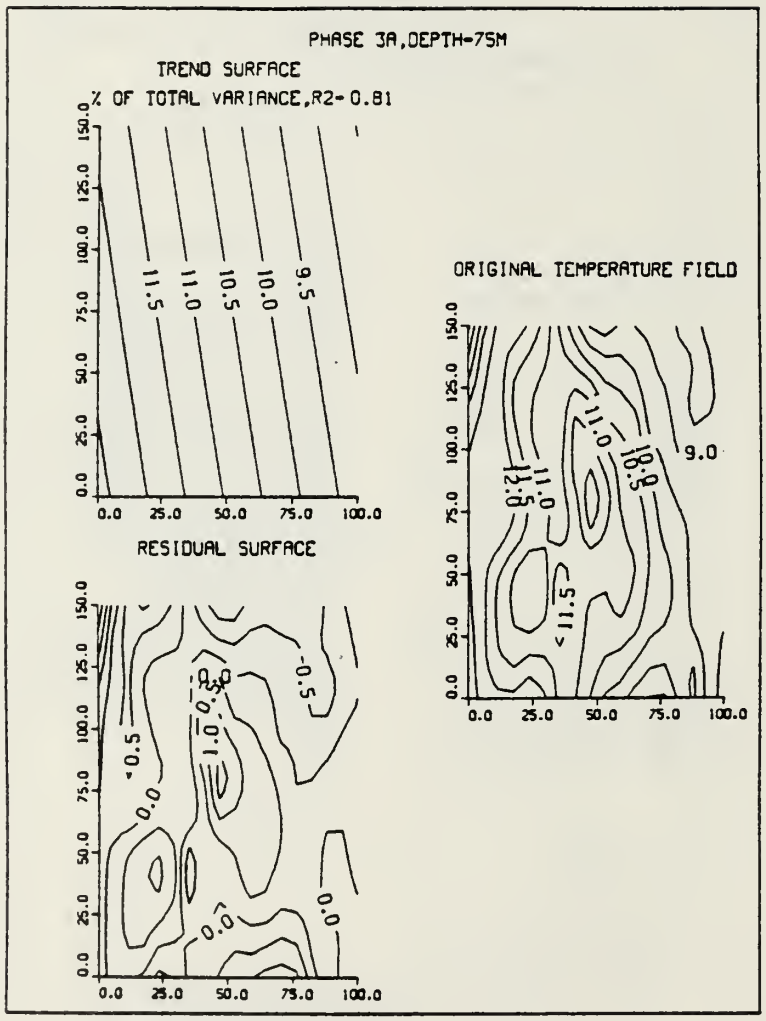

Figure 115. Same as Figure 112 except for a depth of 75m.

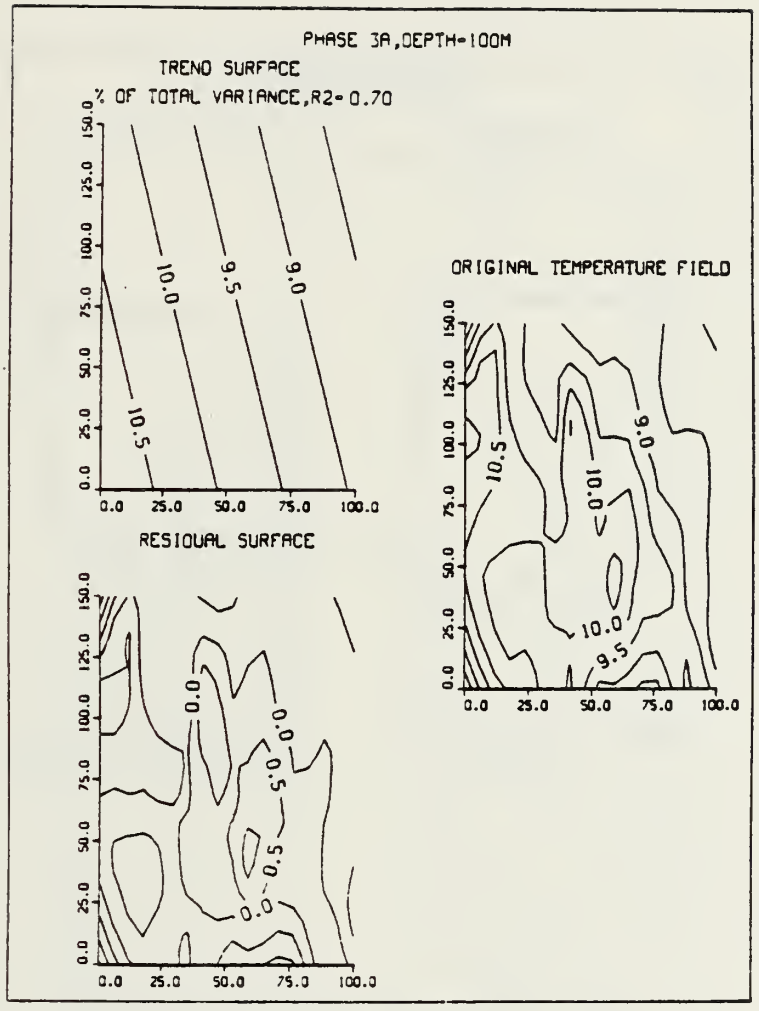

Figure 116. Same as Figure 112 except for a depth of 100m.

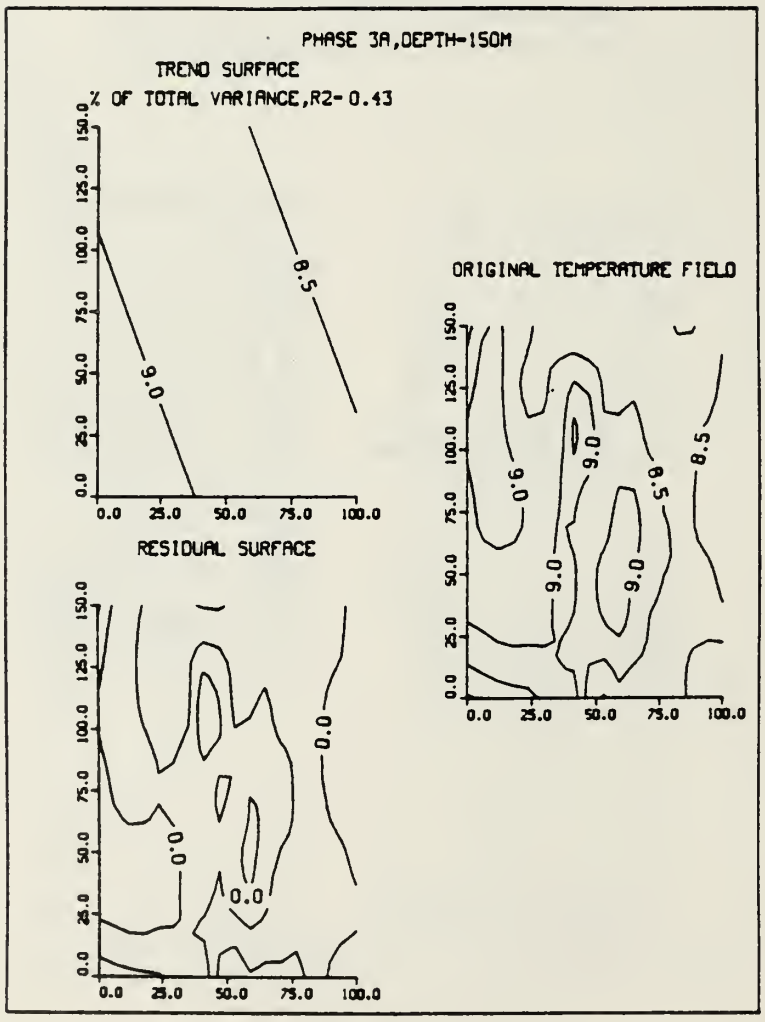

Figure 117. Same as Figure 112 except for a depth of 150m.

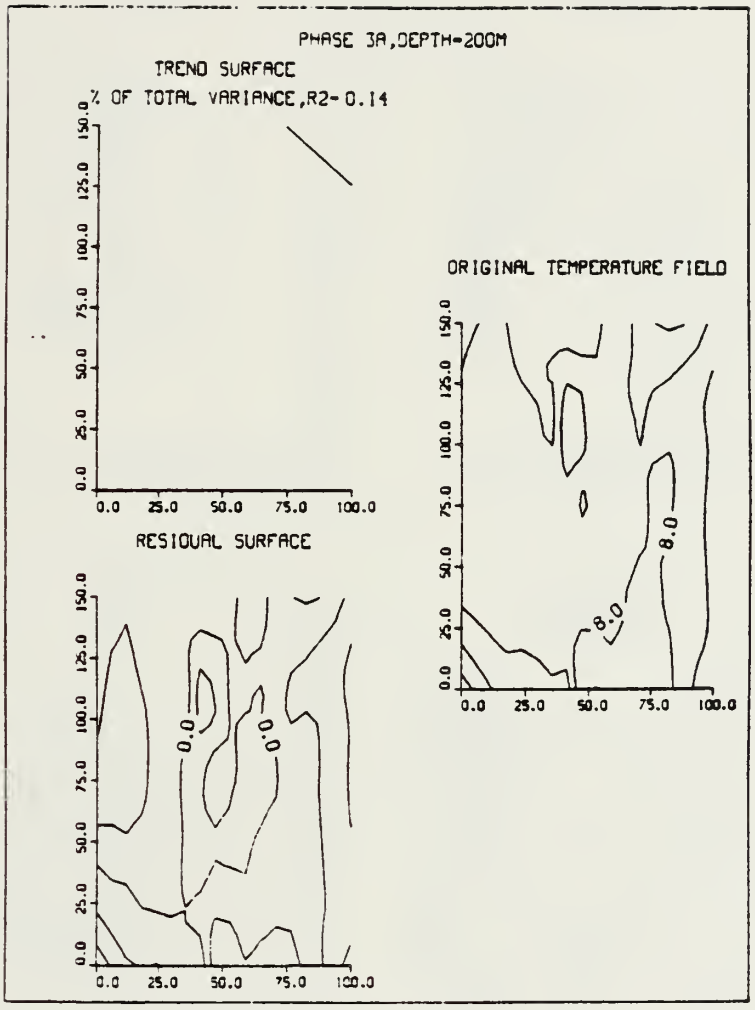

Figure 118. Same as Figure 112 except for a depth of 200m.

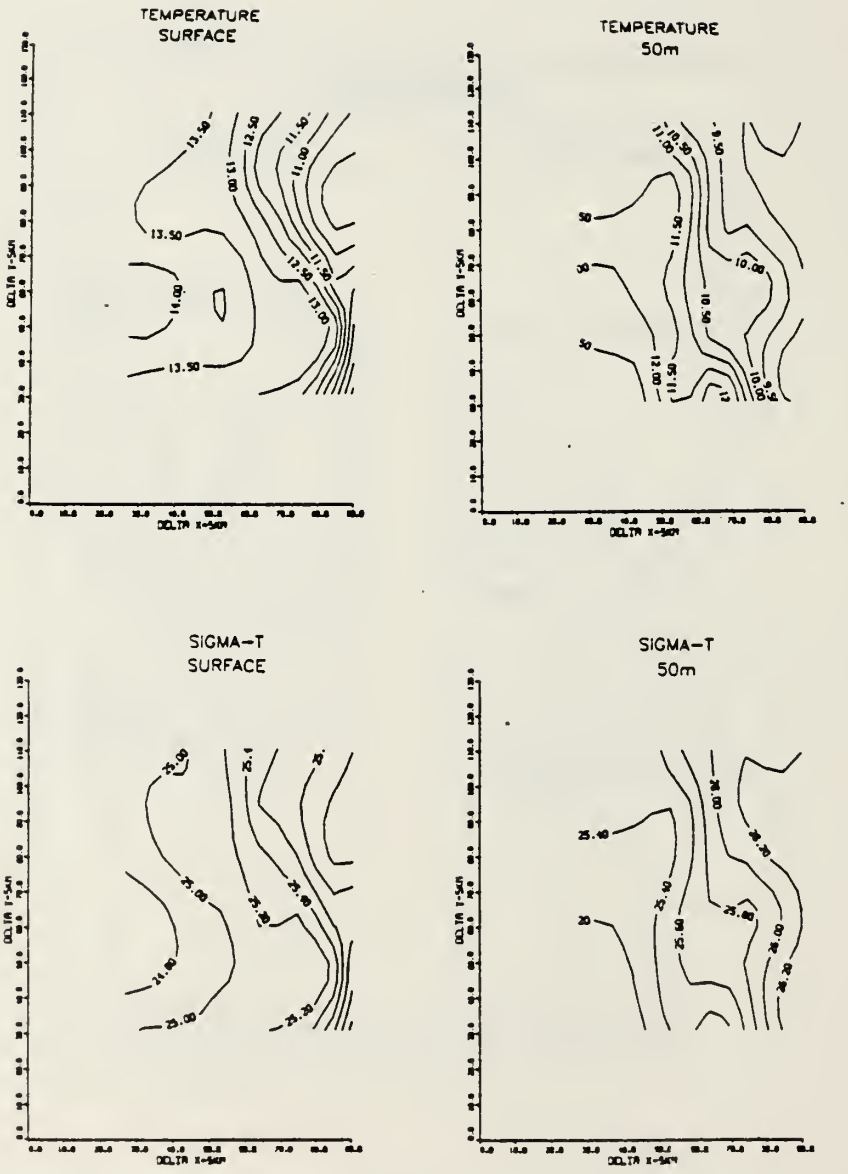

Figure 119. Comparisons of temperature and density maps for Phase 1B, at the surface and at 50m. Maps were produced using the TPS algorithm for two-dimensional interpolation (see Appendix C).

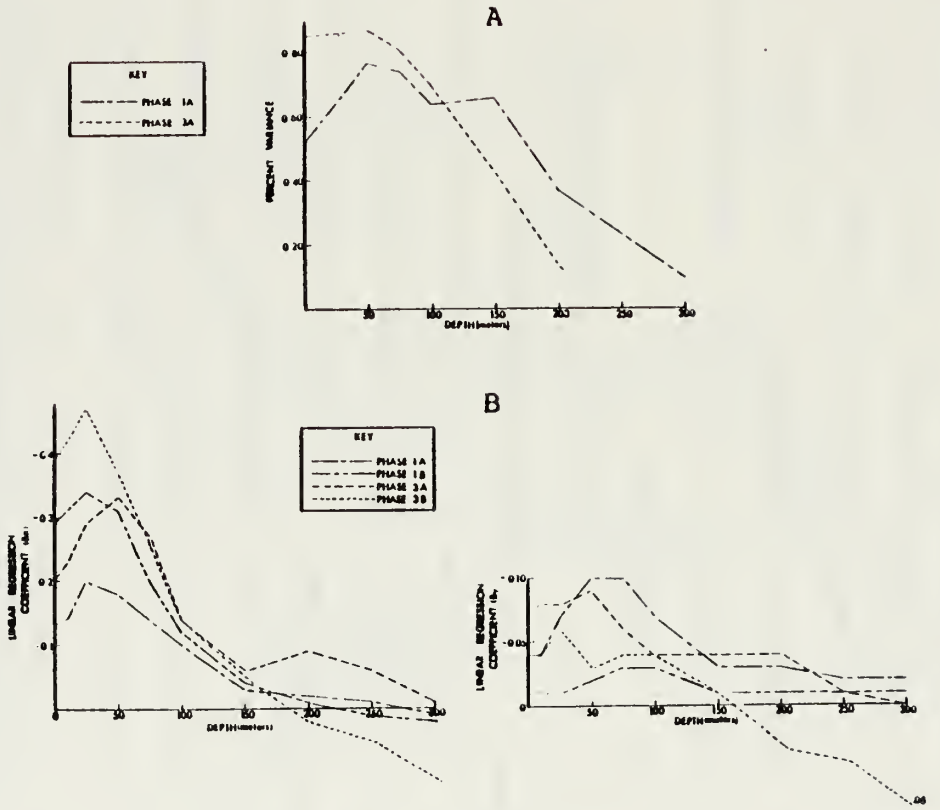

Figure 120. Upper panel shows percent variance in the temperature field accounted for by a bilinear trend versus depth for Phases 1A and 3A. Lower panel shows corresponding alongshore and offshore linear regression coefficients or slopes as a function of depth.

bilinear trend accounts for less of the variability in the internal temperature field.

The slopes of surfaces used in detrending the data have been further examined and show that the depth interval of maximum baroclinicity in the offshore direction lies between 25 and 50m (Fig. 120B). A comparison of the alongshore and offshore regression coefficients used in constructing these trend surfaces, shows that the offshore regression slopes are roughly 4-6 times greater than the alongshore regression slopes between 25 and 50m. Thus the anisotropy associated with the local temperature field is a maximum in this depth range.

Next the pattern correlations themselves are examined. For one phase, 10 reference levels yields $\sum_{i=1}^{n-1} (n-i)$ or 45 possible correlations. These pattern correlations have been calculated using the detrended and non-detrended data for Phases 1A and 3A. Included in Figures 121 and 122 are the correlations using the surface and selected subsurface levels as the primary reference for the detrended data, and the surface only as a primary reference for the non-detrended data. For Phase 1A (Fig. 121), between 10 and 250m, the detrended pattern correlations are significantly lower than the pattern correlations for the non-detrended data. Also the pattern correlations for the 25, 50, 75, and 100m reference levels (i.e., detrended) are quite similar to the

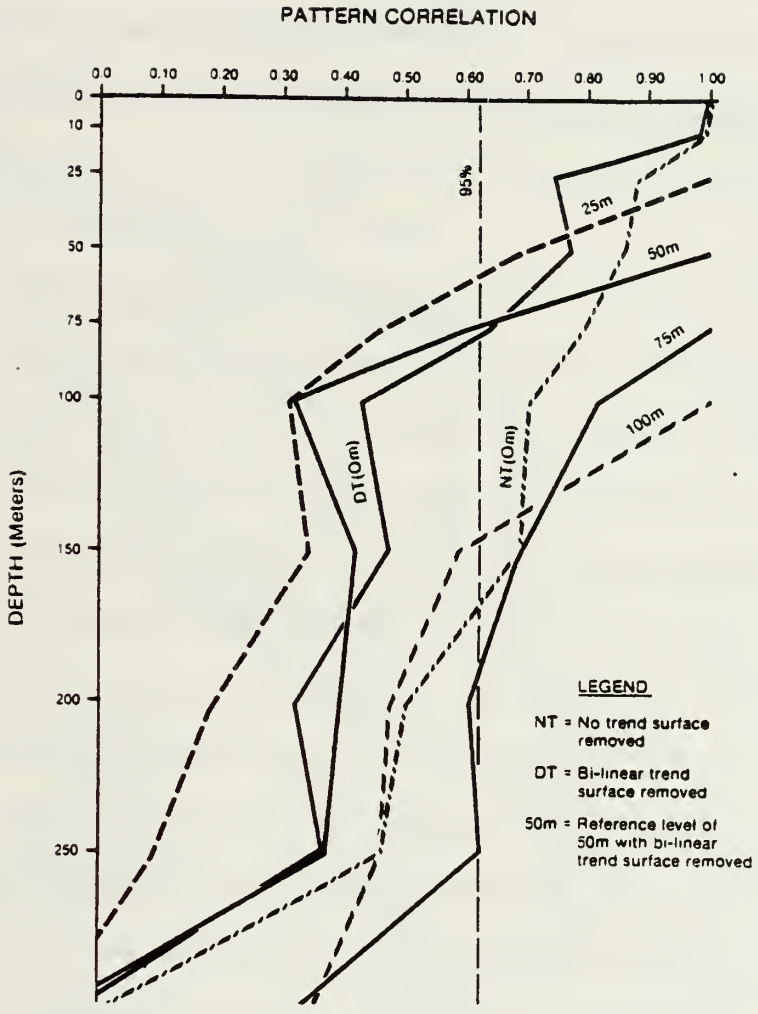

Figure 121. Pattern correlation profiles (PCPs) for Phase 1A. PCPs for reference levels of 0, 25, 50, 75, and 100 meters are shown for detrended surfaces, and for one non-detrended profile (0 meter reference). A 95% confidence limit is included.

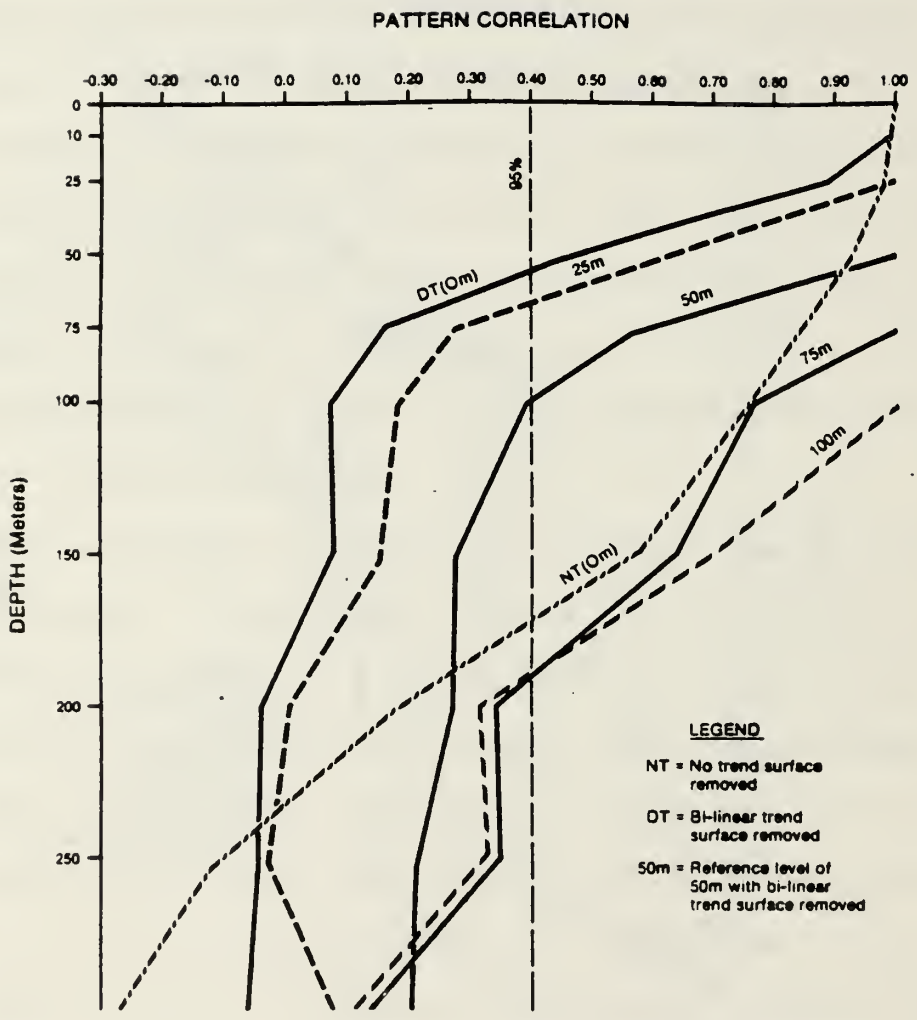

Figure 122. Same as Figure 121 except for Phase 3A.

primary profile (Øm reference), suggesting that the temperature field is relatively homogeneous. A 95% confidence limit has been estimated for $n^* = N / \sum_{j=0}^{N-1} \rho_j(\tau)$ independent values, where N corresponds to the original number of temperature values available at each depth (64 for Phase 1A). Because the resulting number of independent observations is small, the associated confidence limit exceeds 1/e, therefore, it is not possible to confidently estimate an e-folding scale in this case.

The pattern correlations for Phase 3A (Fig. 122) drop off more rapidly with depth than the Phase 1A pattern correlations (Fig. 121). Again, between 1Ø and 25Øm the detrended pattern correlations are significantly lower than those calculated from the non-detrended data for the primary reference. The difference is especially pronounced between about 5Ø and 15Øm. As before, the pattern correlations for reference levels of 25, 5Ø, 75, and 1ØØm are similar to the primary pattern correlation profile, suggesting a homogeneous temperature field. Again, the estimated 95% confidence limit exceeds 1/e and therefore a vertical correlation scale cannot be confidently estimated.

The individual pattern correlation profiles for the detrended data have been adjusted to a common reference level (Øm) and then ensemble averaged to produce mean pattern correlation profiles for both phases (1A and 3A), following the assumption of a vertically homogeneous

temperature field (Fig. 123). The ensemble-averaged profiles are generally similar to the individual profiles shown previously.

Major differences exist in the pattern correlation profiles for Phases 1A and 3A. In comparing both the individual detrended profiles and the ensemble-averaged profiles it is immediately obvious that higher correlations persist over greater depths during Phase 1A than during Phase 3A. For the case of the ensemble averaged profiles, e-folding scales have been estimated. Although the number of DOFs has been increased by ensemble averaging, it is difficult to determine the increase in DOFs precisely because the individual profiles that were averaged, were not independent realizations. However it is assumed that the previous confidence limits in Figs. 121 and 122 have been reduced sufficiently through averaging to justify estimating the e-folding scales. For Phase 1A the e-folding scale is about 170m whereas for Phase 3A, the e-folding scale is about 60m.

One possible explanation for the differences in the pattern correlation profiles and the corresponding e-folding scales is that they are due to increased mixing and upwelling that resulted from the surface winds which intensified significantly over the two-week period between phases.

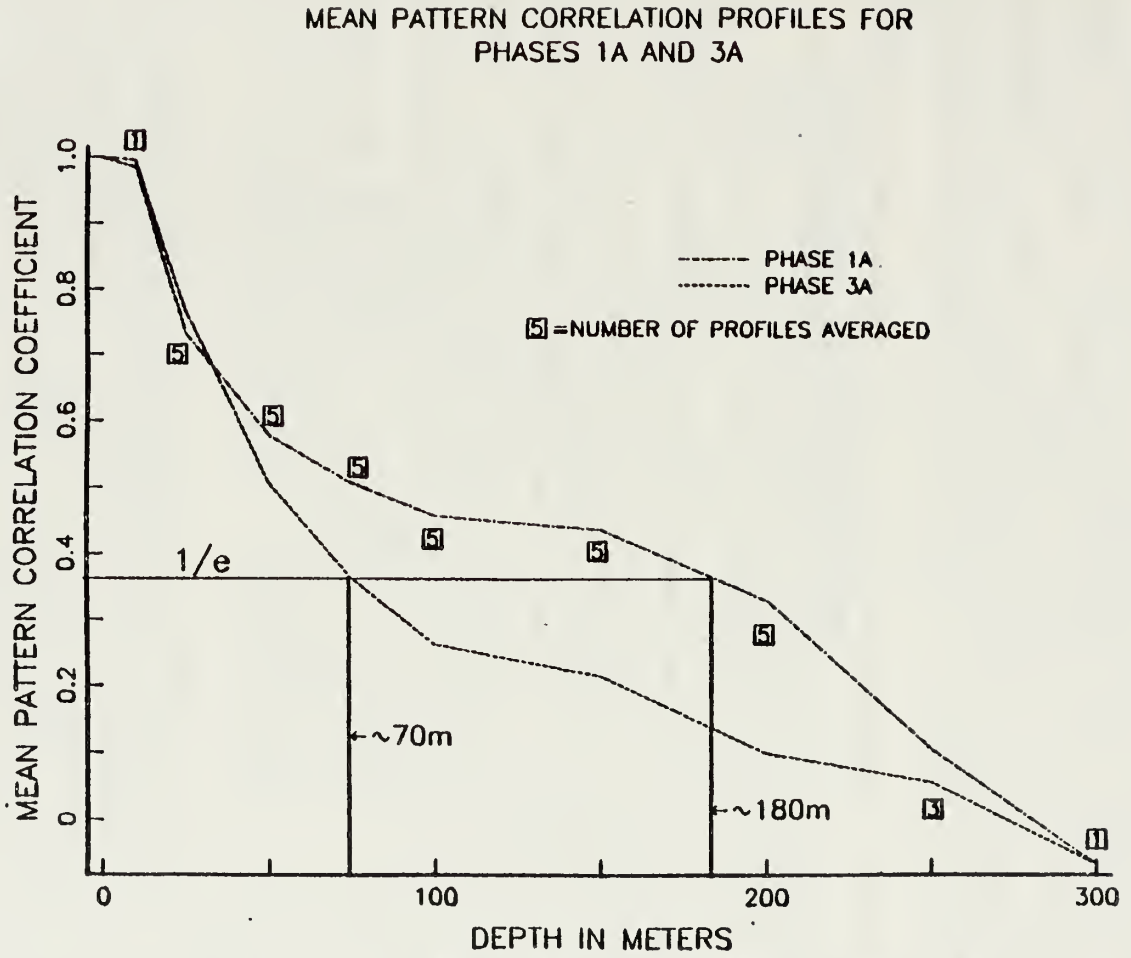

Figure 123. Mean pattern correlation profiles for Phases 1A and 3A. The previous PCPs have been adjusted to a common reference level (Øm) and then ensemble-averaged for each phase. E-folding scales are estimated assuming that the previous confidence limits have been sufficiently reduced, through averaging, to allow significant scale estimates to be obtained.

D. EOF CALCULATIONS

Next, the original temperature profiles are examined using EOF analysis techniques. In calculating EOFs, the corresponding eigenvalues, eigenvectors and principal components may be interpreted as statistical quantities which, as a result, are subject to sampling variability. With certain assumptions about sample size and the form of distribution, confidence limits can be established for these quantities (Morrison, 1976). In practice, it is quite difficult to estimate these confidence limits, and for this reason no attempt is made here to do so.

In Section D.1, EOFs are calculated separately for each phase using the individual deep (300m) profiles initially de-trended using the overall mean transect calculated in Chapter II. The eigenvectors are examined for vertical structure. The principal components are contoured in planview.

In Section D.2, a two-dimensional EOF analysis of the data is undertaken in the offshore - vertical plane. The data are grouped by offshore location in corridors, and since the data are also ordered with respect to alongshore location (and time) a grid is thus established for the subsequent calculations. This framework provides a means

for displaying structure in the temperature field in a vertical plane normal to the coast.

In Section D.3 the data used in Section D.2 are analyzed in the Z dimension allowing the X dependence to be examined separately. Vertical EOFs are calculated in two ways. First, they are calculated after removing a mean X-Z transect, as in previous cases. Second, they are calculated after removing only a simple global mean profile.

1. Preliminary EOF Calculations

EOFs are calculated from the individual deep temperature profiles from each phase. In these calculations the data have been initially detrended by using the overall mean transect calculated previously in Chapter II (Fig. 9). Because the results depend critically on the way in which the data are initially treated before calculating the EOFs, a number of possibilities were considered before deciding on using an overall mean transect to detrend the data. This method of detrending removes the important systematic onshore/offshore changes in profile shape (characteristic of an upwelling regime) from the field of residuals, and thus has a ready physical interpretation. As a result, alongshore variations, and variations in time, are emphasized in the residuals created in this manner. The distribution of variance for the first three eigenvalues for each phase is listed in Table 13. It

Table 13

Variances associated with first three eigenvalues for each phase
Phase (Number of profiles)

EOF	1A(38)	1B(47)	3A(53)	3B(54)
1	76.4%	50.5%	68.0%	83.4%
2	10.1	24.3	18.5	10.7
3	5.0	8.6	4.8	2.6
Total	91.5	83.4	91.3	96.7

is apparent from the table that the variance of these profiles is well represented by the first 3 EOFs. In each case the first eigenvalue accounts for at least 50% of the total variance. However considerable differences in the distributions of variance between EOFs, and between phases for corresponding EOFs, occur. The first three EOFs for Phase 3A are shown in Fig. 124. Most of the important structure in the first EOF occurs between the surface and the upper 100m. This pattern is generally found in the first EOFs for the other phases as well (not shown). The second EOF has a zero-crossing at 50m and displays maximum variation between the surface and about 130m. The 3rd EOF has two zero-crossings, one at 38m and a second at 111m, with a zero-crossing separation of 73m. The maximum amplitude of this EOF occurs between about 50 and 80m. The structures of the 2nd and 3rd eigenvectors were also generally similar between phases.

Next the principal components associated with the first EOF for each phase are plotted in planview (Fig. 125). The resulting patterns are expected to be strongly influenced by the method of detrending employed. Since these principal components represent the influence of the entire profile they cannot be directly compared with the previous temperature maps presented in Chapter II. However, the principal component map for Phase 1A does

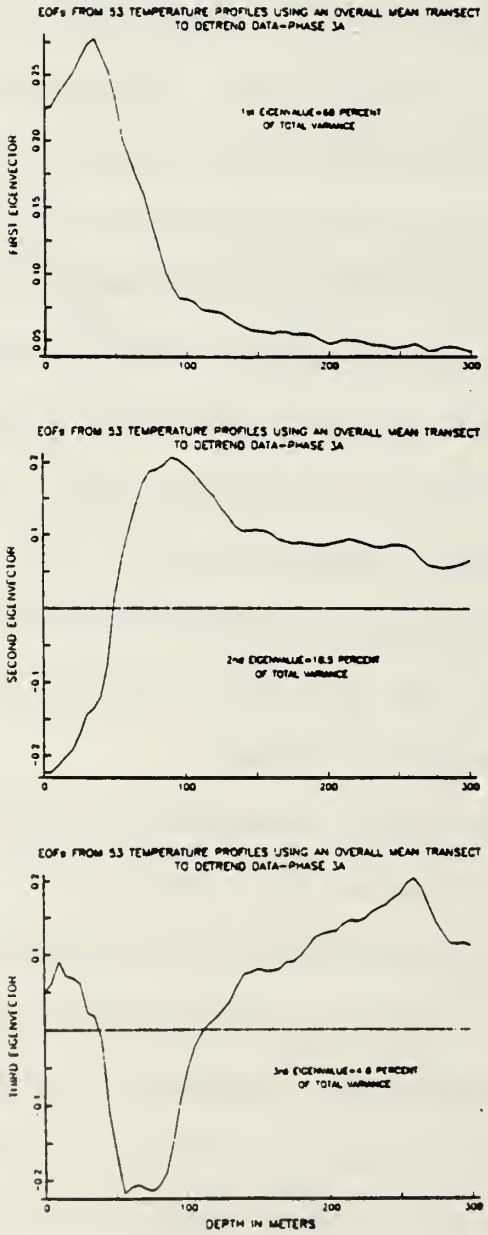

Figure 124. First three EOFs for 53 deep temperature profiles from Phase 3A. An overall mean X-Z transect was first removed from the data.

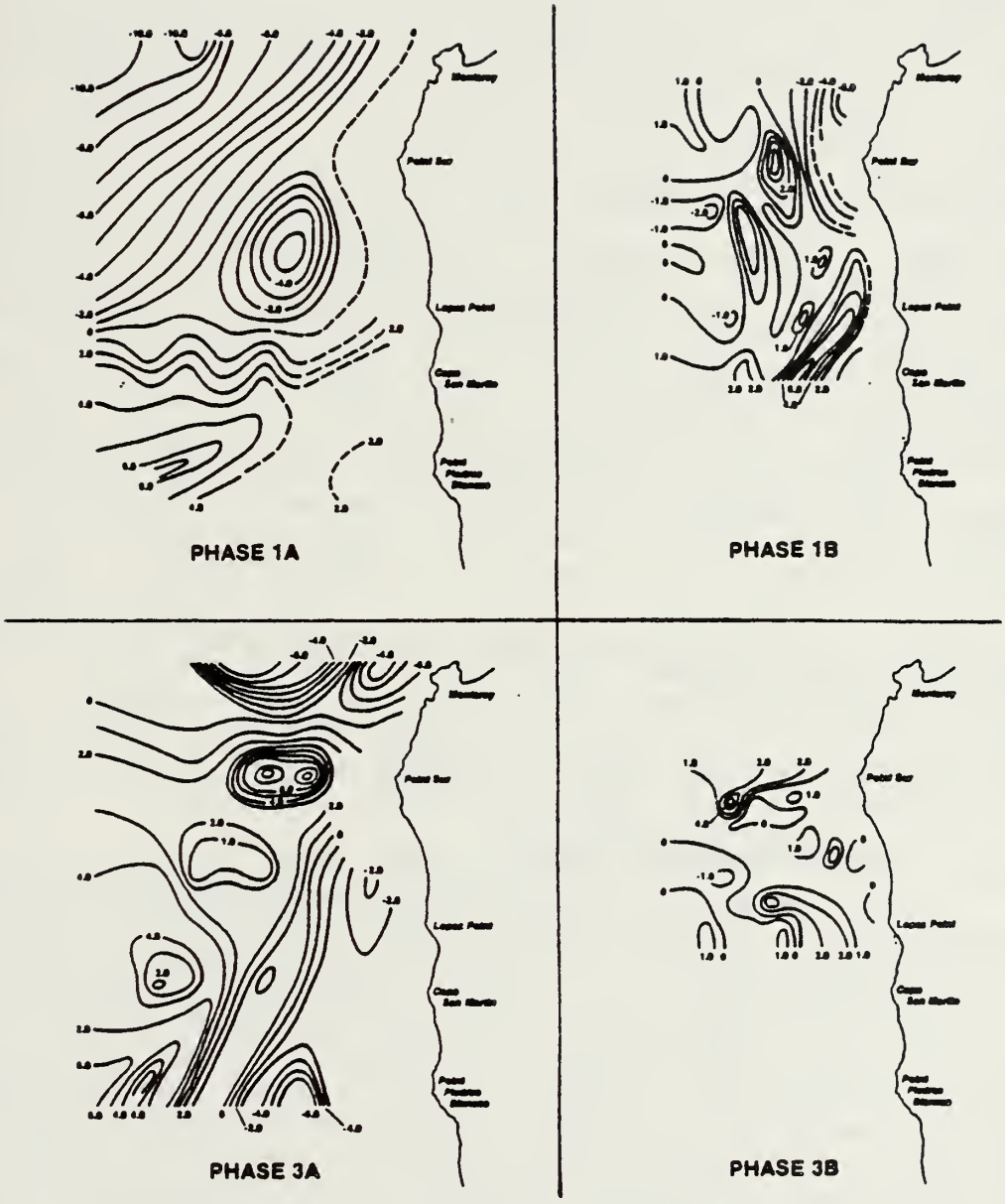

Figure 125. Principal component maps for first EOF for each phase. Principal components are plotted at the respective station locations.

reveal the influence of warm water in the southwest corner as reflected in the principal component contours. The principal component maps for the other phases do not reveal patterns that can be easily related to patterns previously observed in the various surface and subsurface temperature maps. Of more direct interest to the present study however are the space-time scales implied by these patterns. First, these principal component patterns clearly indicate the inhomogeneous nature of the space-time variability over the study area. Local regions of intense variability can be identified in the patterns for each phase. The regions of most intense variability have spatial scales of the order of 25km or less. Also the patterns of variability appear to be distinctly different from one phase to the next (e.g., 1A to 1B, and 3A to 3B), again implying time scales as short as two days (or less).

2. X-Z EOF Calculations

The purpose of calculating two-dimensional EOFs in the X-Z plane is (1) to search for important modes of variability that may be uniquely identified in the offshore/vertical plane, and (2), once identified, to estimate the associated spatial scales. Near the continental shelf it is expected that the variability associated with coastal trapped waves will be important, when they are present.

To compute the X-Z EOFs, the individual profiles from each phase were grouped by trackline and by distance offshore. The five corridors used previously in calculating the mean transects were used again to group the data by offshore location. Thus usually 2 or 3 profiles were averaged within a corridor and the result then assigned to the mid-point of that corridor for a given trackline. Considering all four phases there are 23 points that depend both on alongshore location, and on time since it took the ship approximately 10 hours to occupy the stations along each trackline. To detrend the data before calculating the EOFs, mean profiles were calculated along each corridor and then subtracted from the individual profiles in each case.

In calculating these EOFs, computational problems arose because of the size of the initial data matrix involved. Mid-point profiles were stacked along each trackline and the data matrix that resulted (258 x 23) was too large to calculate the scatter matrix. Two approaches can be used in this case. First, the original matrix can be partitioned into a set of lower-order matrices, with operations performed on the smaller matrices, and the results recombined, or second (when the original data matrix is not square), the scatter matrix can be calculated according to the rank of the data matrix which in practice usually corresponds to the smaller of the two dimensions of

the data matrix. In the present case the second approach can obviously be used to good advantage (23 x 23 vice 258 x 258). However, in using the second approach care must be taken to redefine the scatter matrix by taking into account the necessary scalar multipliers $(n-1)^{-1}$ that are usually ignored in using the standard approach (Morrison, 1976).

The distribution of variance associated with the eigenvalues calculated from the scatter matrix is shown in the upper panel of Fig. 126 (upper panel). The first five EOFs contain about 85% of the total variance and the first eight EOFs contain 91.4%. The selection rule of Craddock was again used to estimate the number of signal-like EOFs from the possible total of 23 (Fig. 126, lower panel). The slopes cross at eigenvalue indices between six and seven.

The first six X-Z EOFs are shown in Figs. 128 to 133. The mean field in the X-Z plane that was used to detrend the data is shown in Fig. 127. First, the two-dimensional EOF patterns are examined for possible physical insight. The first EOF pattern has a shallow (~35m) nodal line running offshore and surfacing about 35km away from the coast (Fig. 128). This EOF pattern has two maxima, the first at the surface near the coast, and the second at about 50km offshore at a depth of 60m. The pattern associated with the first maximum near the coast may be coastally and/or surface-trapped, possibly reflecting the

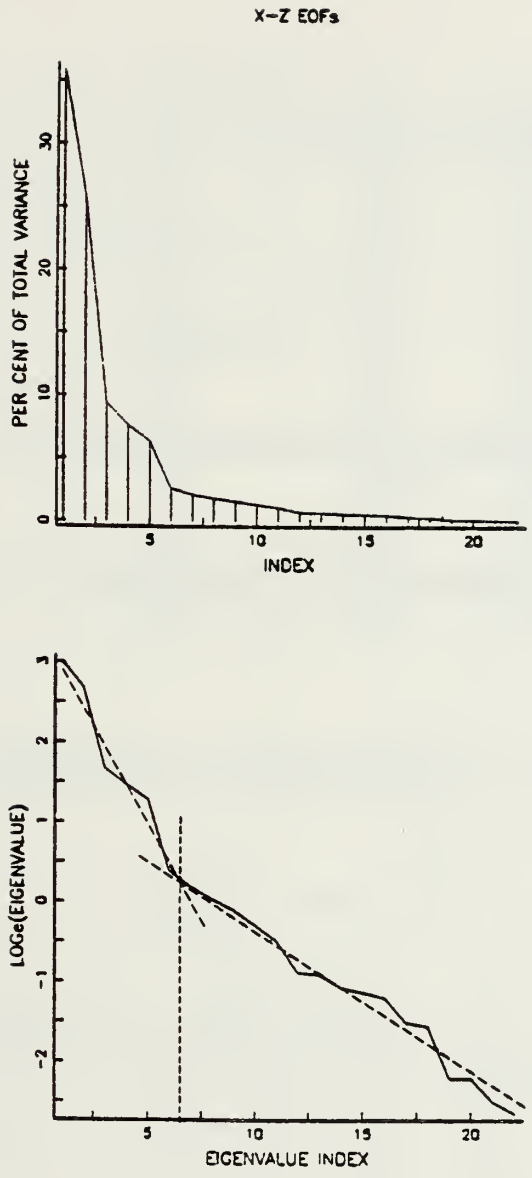

Figure 126. Distribution of variance versus eigenvalue index for X-Z EOFs. Upper panel is a linear plot of variance (i.e., eigenvalues) and the lower panel is the same except with a natural log ordinate. Signal-like EOFs extend over approximately the first 6 EOFs, from the locus of slope intersections.

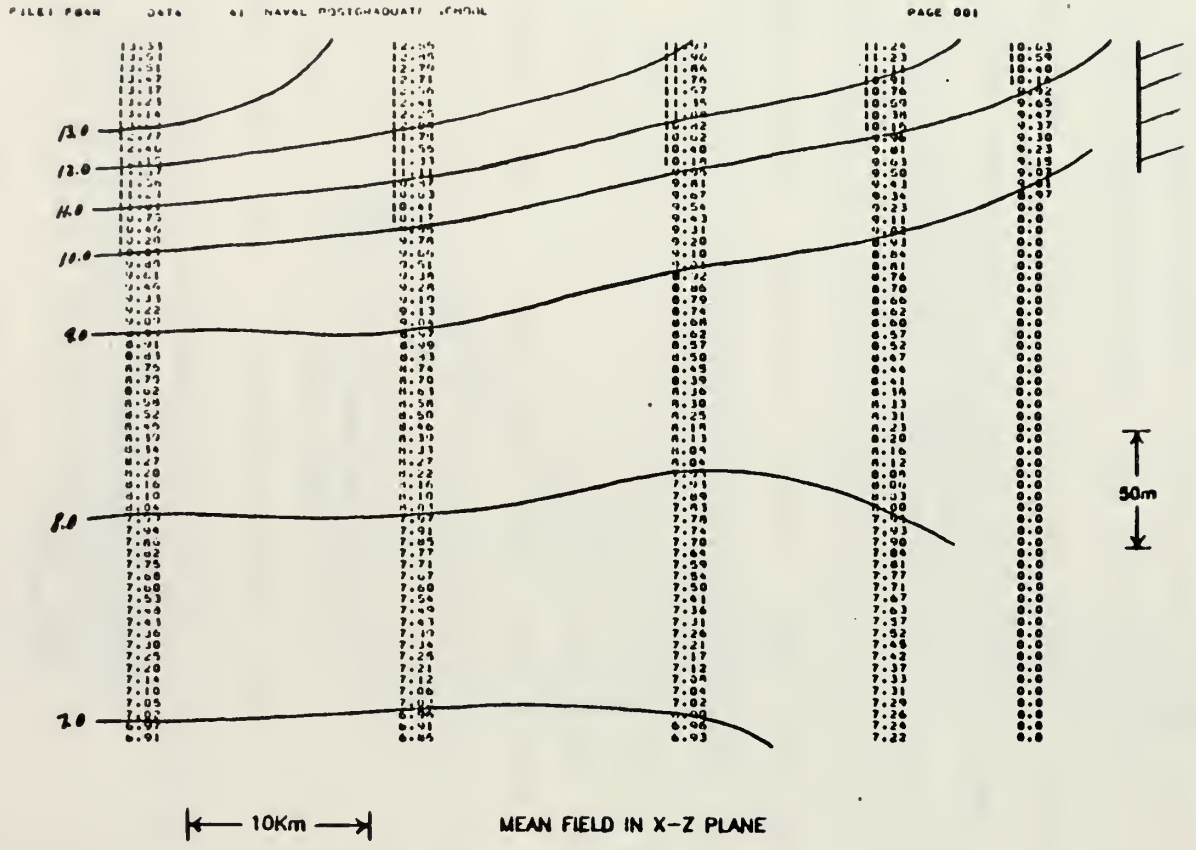

Figure 127. Mean temperature field in X-Z plane from all phases. This field is used to detrend the temperature profiles before calculating the X-Z EOFs.

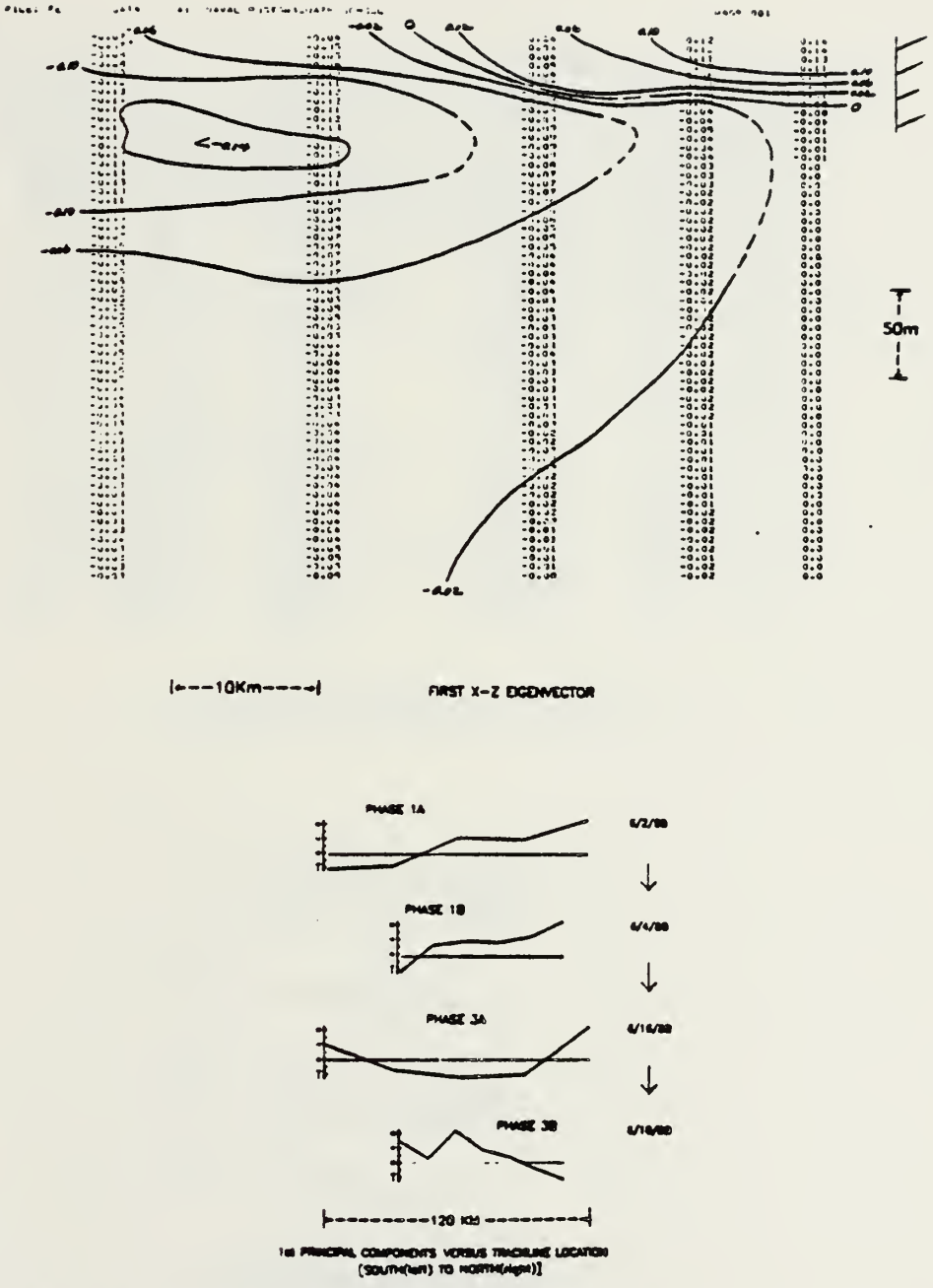

Figure 128. First X-Z EOF (upper panel) and principal components (lower panel). Principal components are both a function of alongshore location, and time.

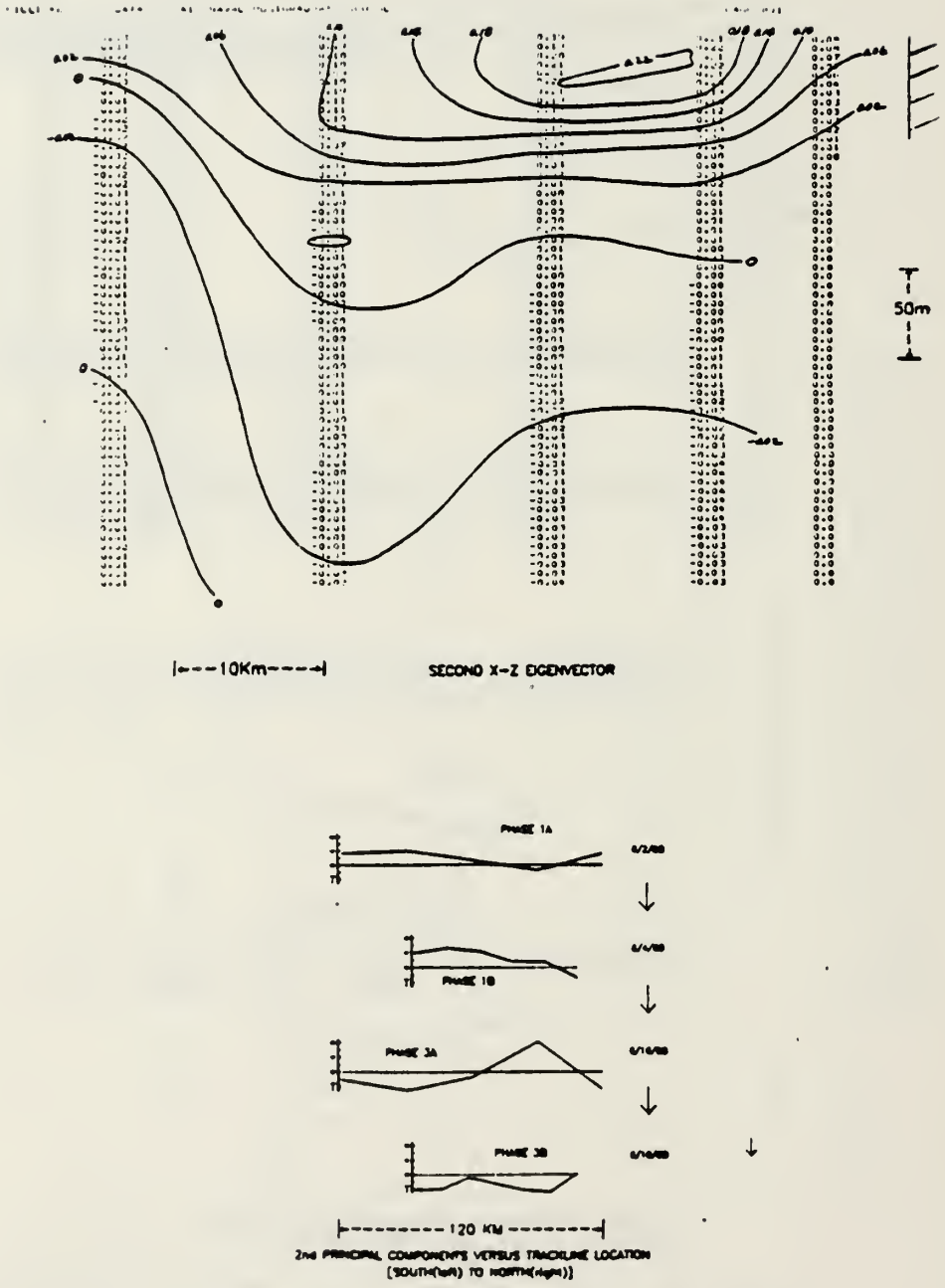

Figure 129. Same as Figure 128 except for second EOF.

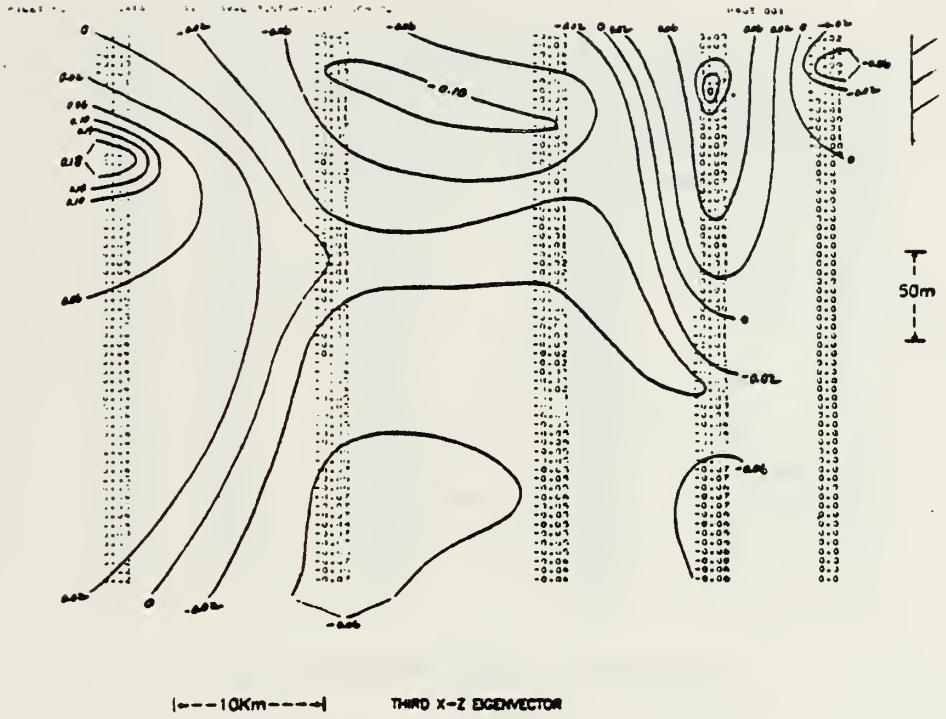

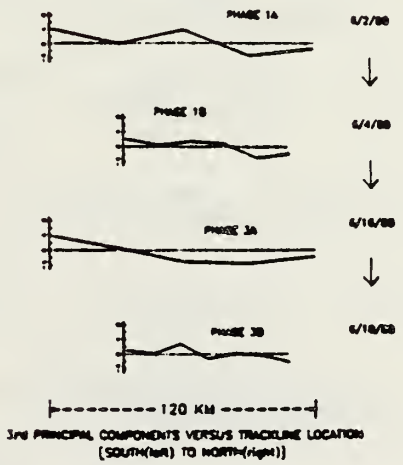

Figure 130. Same as Figure 128 except for third EOF.

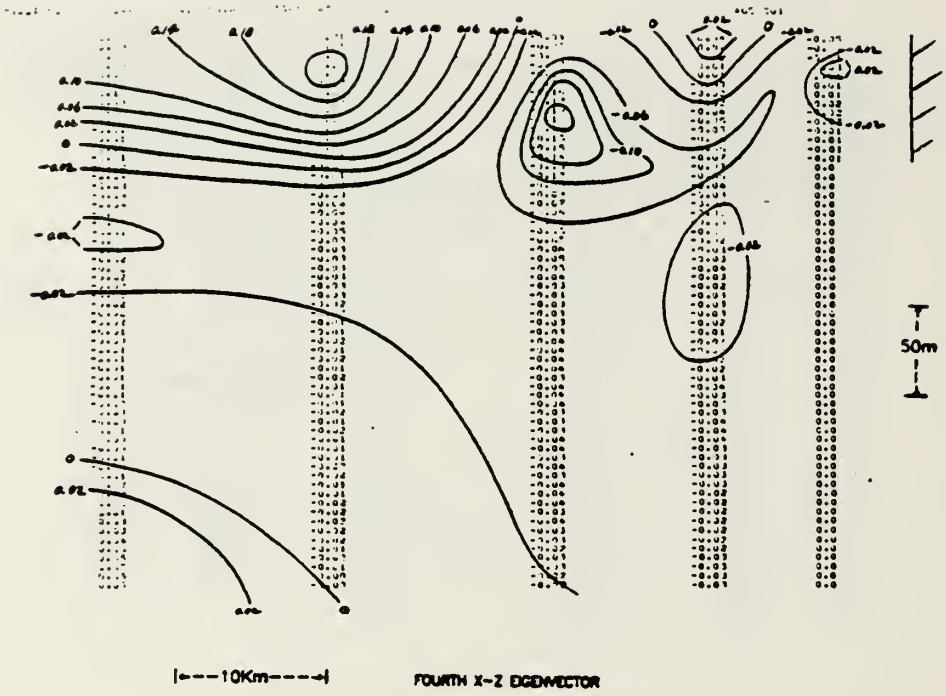

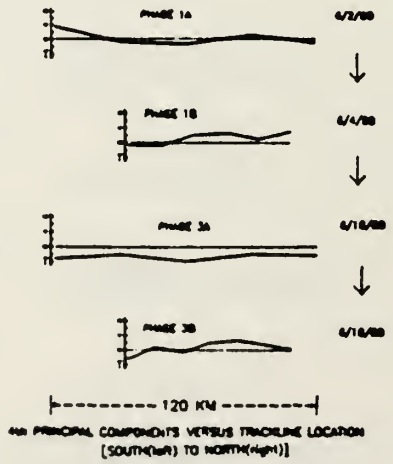

Figure 131. Same as Figure 128 except for fourth EOF.

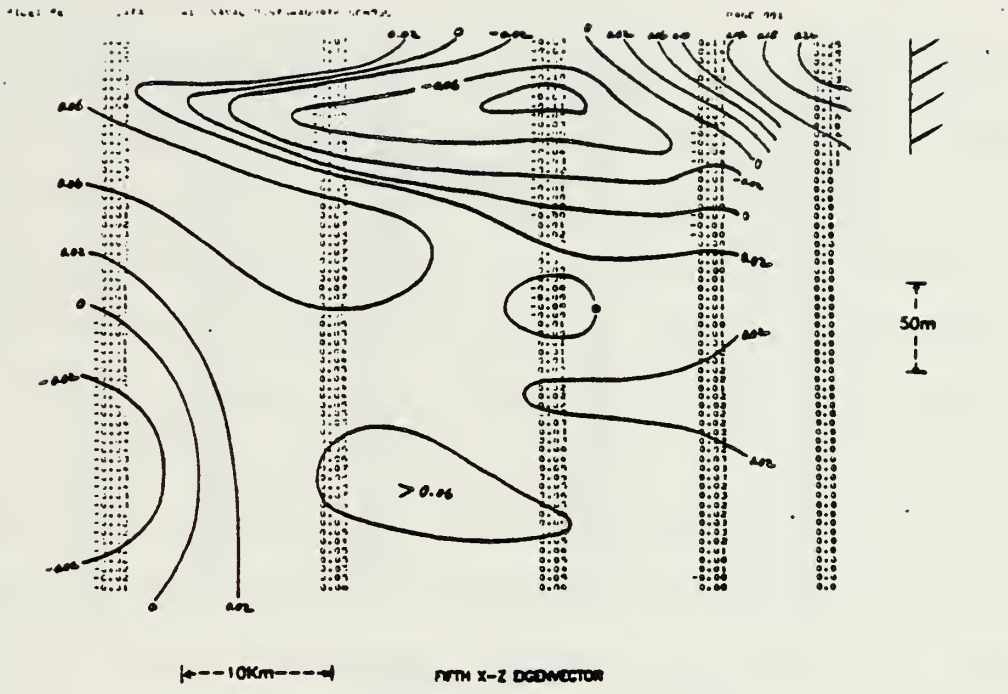

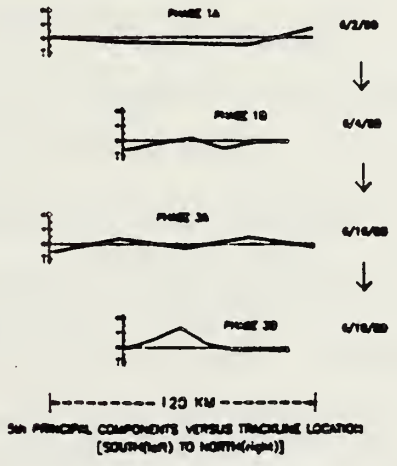

Figure 132. Same as Figure 128 except for fifth EOF.

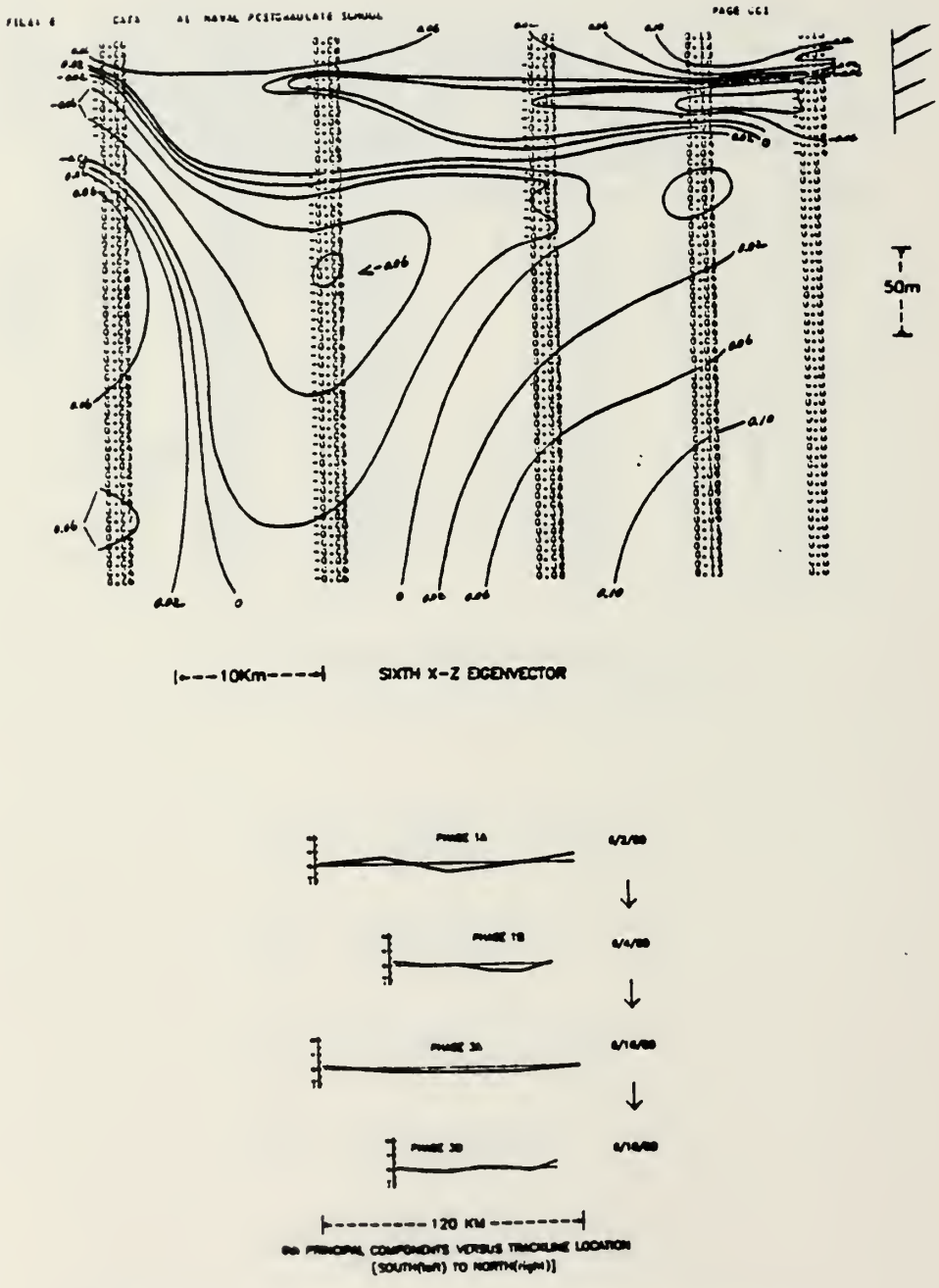

Figure 133. Same as Figure 128 except for sixth EOF.

influence of coastal-trapped waves. The pattern is similar to the first empirical temperature mode calculated off the coast of Peru by Brink et al. (1980). On the Peruvian shelf this mode of variability was attributed to the local winds, however.

The second EOF pattern (Fig. 129) has a major maximum at 20km offshore and at a depth of 15m. This eigenvector could be associated with the coastal jet located approximately within the same region. The third EOF pattern has at least four regions containing antinodes (Fig. 130). At about 14km offshore, one pattern, with an antinode at 30m extends to at least 150m in depth. A major antinode also occurs at the seaward extremity of the area at about 20m and may be related to circulation in the major upwelling frontal boundary generally located in this region. Near the coast a weak antinode occurs at 20m. The fourth EOF pattern possesses a major antinode at 40km offshore and a depth of 15m (Fig. 131). This feature may also be related to some aspect of the equatorward surface jet whose mean location was shown to move rapidly in the onshore/offshore direction over periods of 2 days or less. The 5th EOF pattern shows a strong maximum near the surface at the coast (Fig. 132). This modal pattern is relatively intense and may be coastally trapped thus representing the influence of coastal trapped waves in this region. No major well-defined nodes are seen in the 6th EOF (Fig.

133). From inspection of the first six EOFs, the dominant structures are always contained within the upper 150m and usually within the upper 100m. Again, the EOFs are helpful in identifying inhomogeneous regions. The first six patterns reveal a number of clearly-defined antinodes at various offshore locations and depths where the EOF structures are characterized by closely-spaced contours.

The likelihood of observing the influence of coastal trapped waves in the foregoing two-dimensional EOF analysis is based partly on the fact that it only took half a day or less to occupy the stations along one trackline. Thus several "samples" would have been acquired over a period typical for coastal- trapped waves. However the first corridor for offshore profiles in most cases was located somewhat beyond the shelf margin.

As in Chapter III, estimates of the spatial scales are obtained by comparing intersections of the various X-Z EOF patterns with the mean field. Only the horizontal scales are estimated, however. The vertical scales are estimated in the next section where EOFs of the corridor averaged profiles are calculated. Because the aspect ratio of the X-Z plots is 125/1, nearly-horizontal contours are assumed to be horizontal for the purpose of scale estimation. As in Chapter III, scales are estimated as approximately twice the distance from zero-contour-crossing

to zero contour crossing.[13] Horizontal zero-crossing distances for the first six EOFs are tabulated below along with the locations and intensities of the most prominent EOF structures (Table 14).

The most intense structures (i.e., > 0.20) were shallow (<20m) and within 40km of the coast. The horizontal scales range between 18 and 80km with a mean scale of 48km and a median of 49km. Because the EOFs are subject to sampling variability (if they are treated as statistical quantities), the associated horizontal scales are likewise subject to sampling variability. The horizontal scales do not appear to be clearly depth dependent or dependent on the structure intensity. However there is a slight tendency for the horizontal scales to increase with offshore distance of the feature. There is also a slight tendency for the horizontal scales to decrease with increasing mode number, a common behavior with EOFs.

Since the principal components depend on both space (i.e., distance between tracklines) and time (i.e., data acquisition time between tracklines), they can be interpreted as the space and/or time (y and/or t) varying amplitudes associated with a given eigenvector or mode. The principal components associated with the first six X-Z EOFs are shown in the lower panels of Figs. 128-133. They are plotted here as a function of alongshore location. If

Table 14

Horizontal zero-crossing distances and feature descriptions from the X - Z EOFs

EOF (% Variance)	Intensity[2]	Location Offshore (km)	Depth (m)[1]	Horizontal Zero-Crossing Distance (km)
1 (35.8%)	2.81	6	Ø	32
	3.Ø2	48	6Ø	*
2 (25.8%)	3.18	19	15	4Ø
3 (9.4%)	Ø.95	14	3Ø	9
	Ø.53	32	38	27
	Ø.95	55	7Ø	*
4 (7.6%)	Ø.77	24	45	1Ø
	Ø.94	4Ø	16	3Ø
5 (6.3%)	Ø.89	4	5	18
	Ø.39	25	3Ø	32
6 (2.6%)	Ø.19	11	5	2Ø
	Ø.16	11	35	2Ø

[1] To the center of the feature

[2] Maximum nodal value times appropriate eigenvalue ($^{o}C^{2}$)

* Can not estimate because feature is not completely confined within the study region

they were plotted versus time, the plots for Phases 1B and 3B would be reversed (since they were conducted in reverse order with respect to time) and a 14-day gap would exist between the end of Phase 1B and the start of Phase 3A. The present sample size is too small to analyze the space/time scales of the principal components using correlation analysis techniques.

The principal components for mode 1 for Phases 1A and 1B are closely aligned, with a zero-crossing common to both phases occurring between Cape San Martin and Lopez Point (Fig. 128). The second, third, and fourth principal components for the first mode show little change for Phase 3A; however, zero-crossings occur toward each end of the sequence with a spatial separation of about 90km. The sequences of principal components for Phases 3A and 3B are not similar, suggesting that time dependence in this case may be important.

The principal components for the second mode for Phases 1A and 1B are again somewhat similar except toward the northern end of the sequence (Fig. 129). Both sequences show space/time persistence with successive values tending to be alike. The zero-crossing alongshore separation for Phase 1A is about 25km. The principal component sequences for Phases 3A and 3B are not obviously similar to one another, or similar to the sequences for

Phases 1A and 1B, except that they suggest similar space/time persistence. The Phase 3A alongshore principal component pattern suggests cyclic behavior in its alongshore (time) variability with an approximate wavelength of 50km or period of O(24 hrs).

The principal component sequences for the third mode for Phases 1A and 1B are again generally similar except that the Phase 1A sequence leads 1B by 10-20km (Fig. 130). The zero-crossing separations for 1A and 1B are 45 and 32km, respectively. The Phase 3A principal component sequence has high persistence and, as before, the Phase 3A and 3B sequences are generally dissimilar.

The fourth mode principal components for Phase 1A show cyclic behavior with a wavelength (period) of 30 to 50km (14 to 24 hrs) (Fig. 131). The Phase 3A principal components show high persistence with values remaining between about -2.0 and -4.0(C) over the sequence. The principal component amplitudes for modes 5 and 6 are considerably lower than for the previous modes (Figs. 132, 133). Cyclic behavior is observed for the Phase 3A sequence (5th mode) and for the Phase 1A sequence (6th mode).

In several cases, principal component patterns appeared to be cyclic with wavelengths and periods consistent with those that might be expected for coastal-trapped waves. Because the calculated EOFs do not clearly

resolve the shelf region, and because the expected modal patterns further offshore are not known, perhaps a better way of identifying these waves, if they are present, is through their alongshore time dependence in the associated principal components.

To further examine whether the principal components were in fact statistically independent, the individual sequences for each mode were subjected to run tests assuming that each group of 23 values was a continuous series. The hypothesis tested was whether or not the sequence of signs of the difference between each principal component and the corresponding median for that sequence differ significantly from those that would be obtained from a random sequence. A significance level of Ø.Ø5 was chosen as the acceptance/rejection threshold. To accept the hypothesis that a sequence of principal components is statistically independent, the test statistic must fall between 7 and 18. The results for the first six X-Z modes are summarized in Fig. 134 below. At the 5% level of significance the principal component sequences for modes 2 and 4 are not (marginally) statistically independent. Thus, the previous observations regarding the apparent persistence of these values is at least partially confirmed by an independent objective analysis.

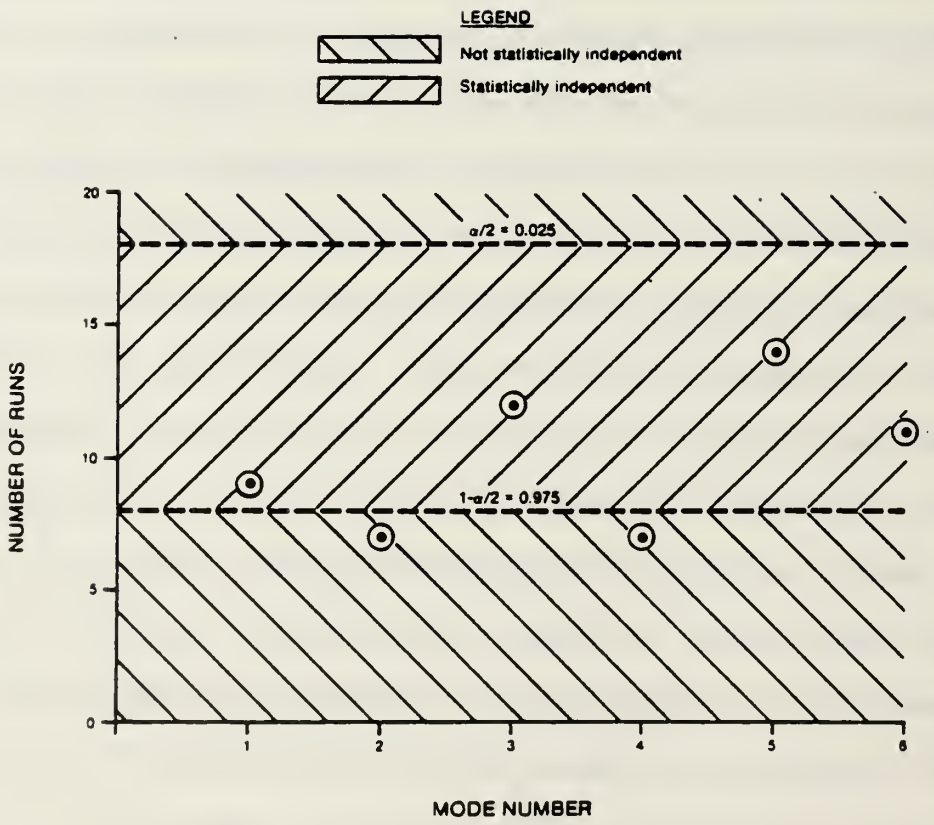

Figure 134. Run tests applied to X-Z principal components to test for statistical independence. Based on run tests for each mode, the principal components for modes 2 and 4 are not statistically independent, at the 0.05 level of significance.

3. Vertical Profile EOF Analysis

The EOF analysis of the previous section is now extended by calculating the one dimensional, vertical EOFs. The same corridor-averaged temperature profiles are used, and the same detrending procedure is initially used. However vertical EOFs are then calculated without first removing a mean X-Z transect. The purpose of the second set of calculations is to examine explicitly the onshore/offshore contribution to the EOFs. In selecting an appropriate sampling procedure for the coastal temperature field, more conservative estimates are likely to be obtained if the onshore/offshore variability, previously modelled as a systematic trend, is now assigned to the field of residuals. Changes in the resulting eigenvalues, eigenvectors, and principal components are examined.

To better resolve the important vertical scales, wavenumber spectra are calculated from the individual vertical eigenvectors. The principal components are also presented in planview for this case with individual values plotted over the grid formed by the intersections of the various tracklines and corridor mid-points. These maps are thus similar in format to those presented in Section D.1. Offshore variability is examined explicity for both the X-Z detrended data and the non-detrended data by calculating individual variances for each corridor.

The distribution of variance associated with the complete set of eigenvalues (i.e.,23) for data with the X-Z mean transect removed is shown in Figure 135 (upper panel). The first four eigenvalues contain almost 94% of the total variance. The normalized entropy for this data set is Ø.35. In attempting to determine the number of significant EOFs in this case Craddock's selection rule, unlike the previous cases, did not provide a clear separation between signal-like and noise-like eigenvalues (Fig. 135, lower panel). In such cases where the slopes derived using Craddock's selection rule are not distinct, other selection rules such as those recommended by Preisendorfer et al. (1981) should be considered. Craddock's rule in this case yields an EOF cutoff somewhere between five and eight. In the following analyses, the first six EOFs are considered (Figures 136-141).

The first EOF possesses significant structure over the upper 1ØØm, and has a maximum at 35m (Fig. 136). The structure of this eigenvector is nearly identical to the first EOF estimated from the individual profiles (Fig. 97, with reversed polarity - a result of using different algorithms in the computations).

The second EOF has significant structure over the upper 1ØØ to 15Øm, with maxima at 1Ø and 8Øm, and a zero-crossing at 48m (Fig. 139). The second eigenvector is again quite similar in shape and magnitude to the second EOF estimated from the individual profiles (Fig.124).

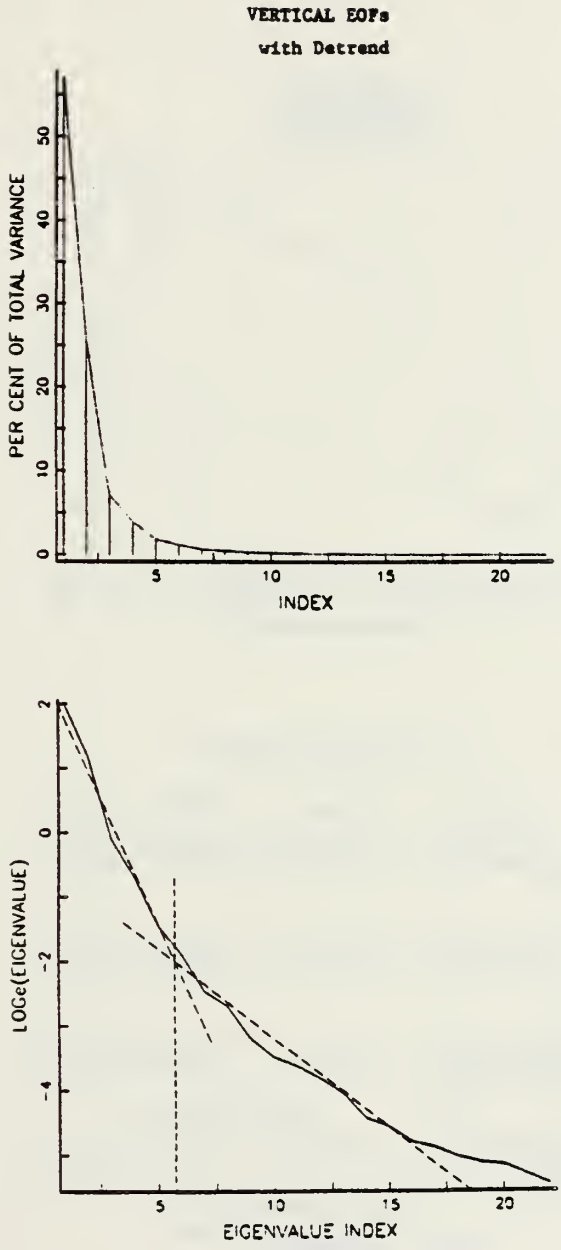

Figure 135. Distribution of variance versus eigenvalue index for the vertical EOFs, with X-Z detrending. Lower panel shows that about the first six EOFs are signal-like.

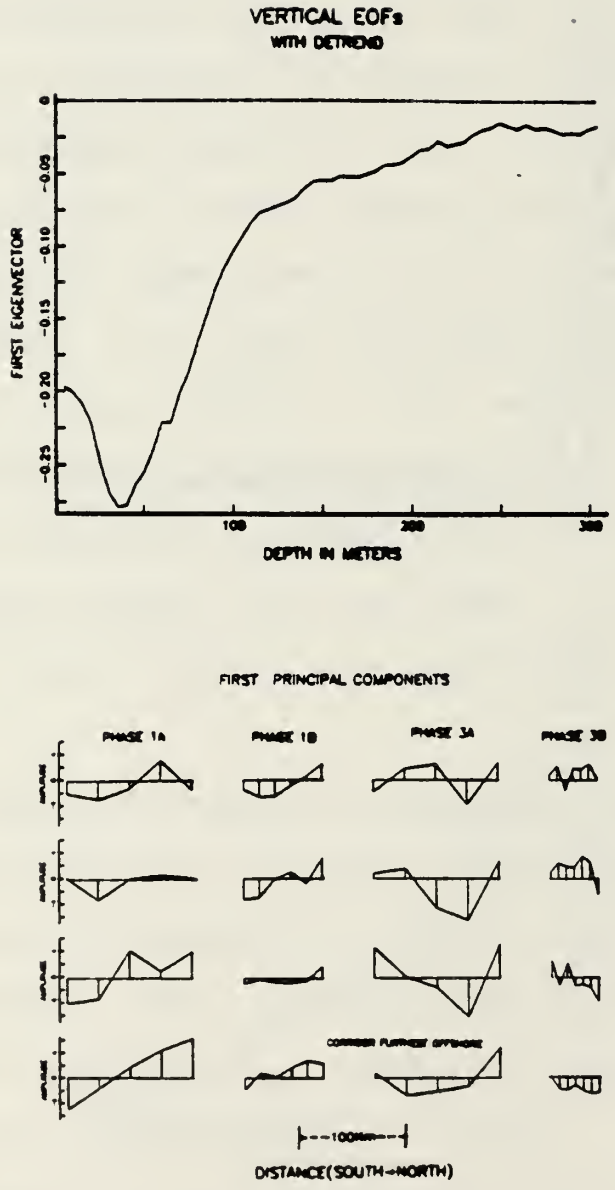

Figure 136. First vertical EOF (upper panel) and principal components (lower panel) with X-Z detrending. Principal components in this case are a function of alongshore and offshore location and time.

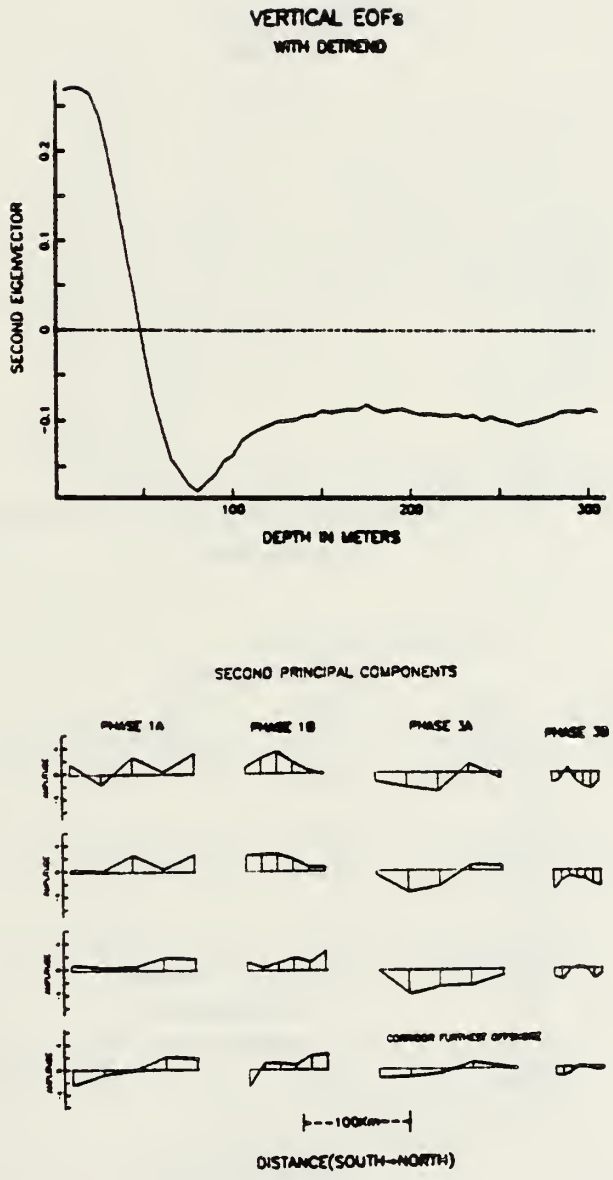

Figure 137. Same as Figure 136 except for second EOF.

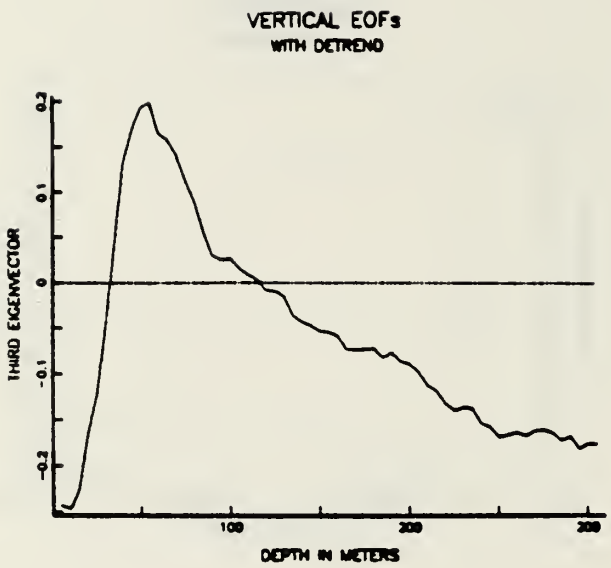

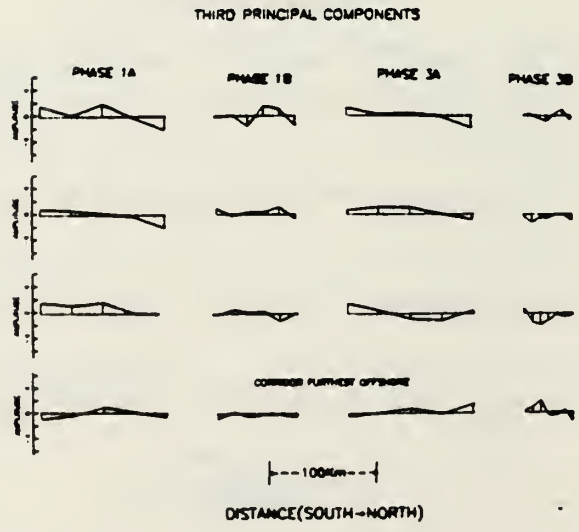

Figure 138. Same as Figure 136 except for third EOF.

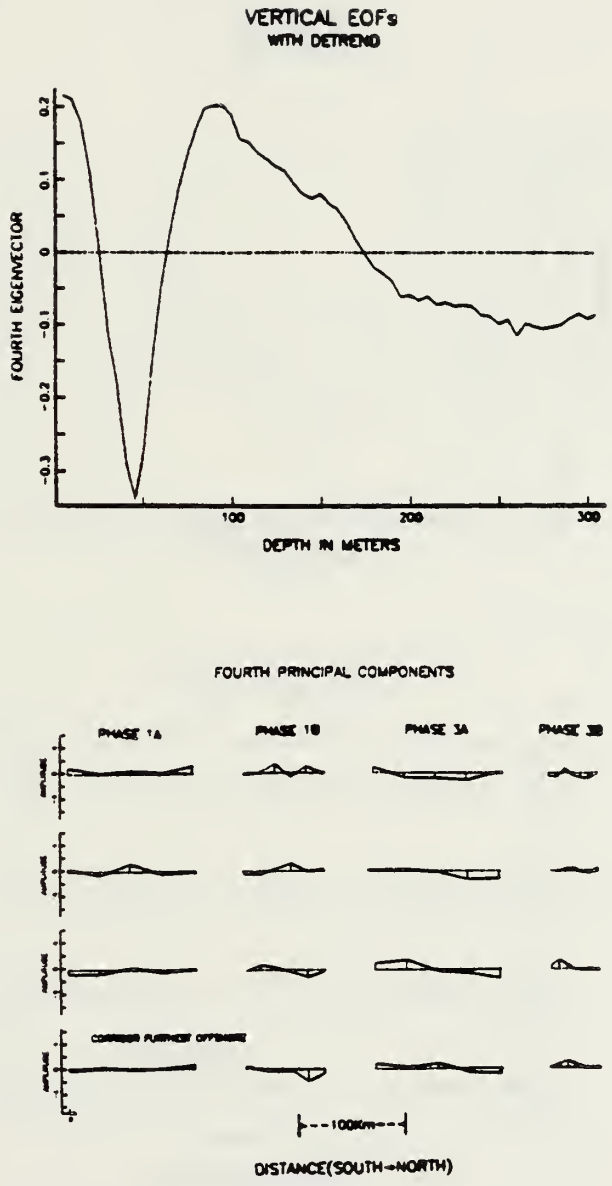

Figure 139. Same as Figure 136 except for fourth EOF.

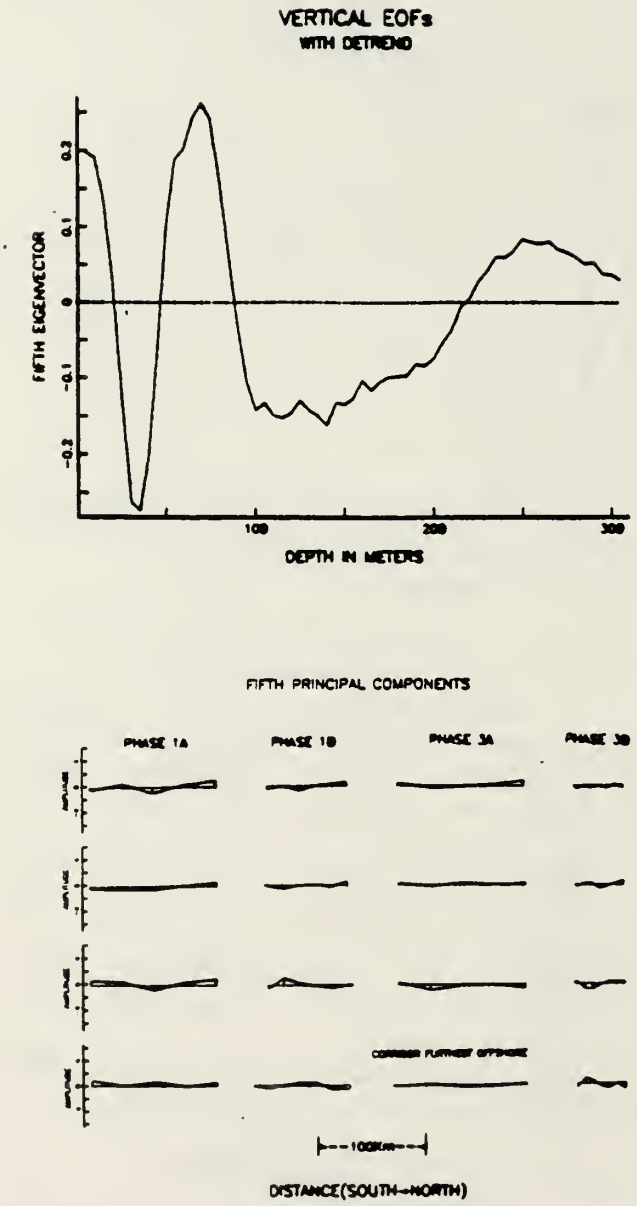

Figure 140. Same as Figure 136 except for fifth EOF.

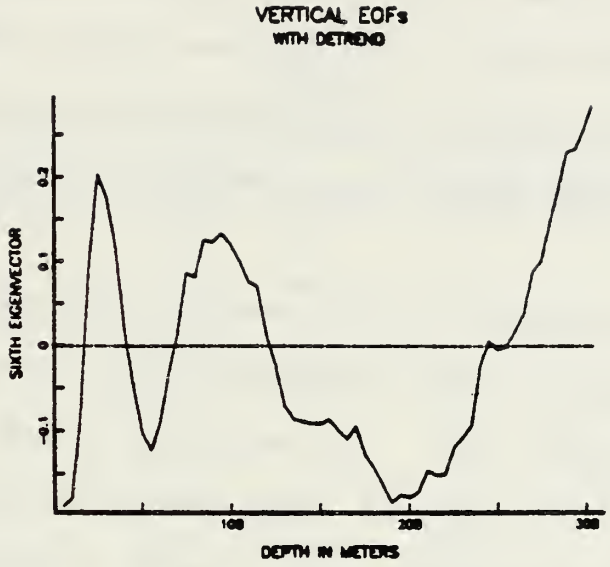

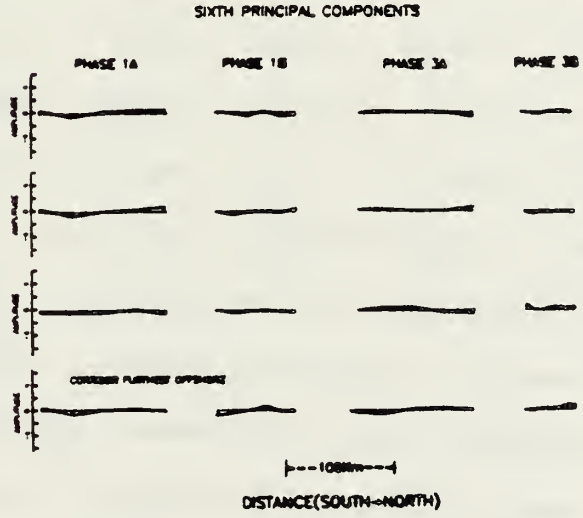

Figure 141. Same as Figure 136 except for sixth EOF.

The third EOF has maxima at 10 and 55m, and zero-crossings at 32 and 117m (Fig. 138). The EOF structure in this case only resembles approximately the corresponding EOF structure from the individual profile analysis.

The locations of EOF maxima, their intensity, their zero-crossing locations, and the zero-crossing intervals for the first six EOFs (Figs. 136-141) are summarized below (Table 15).

The magnitude of EOF maxima clearly decrease with increasing depth, with maximum values usually occurring within the upper 75m. The maximum depth at which EOF maxima are found tend to increase with increasing mode number. Zero-crossings occur over a greater range of depths for the higher modes. Zero-crossing intervals over the first six modes range from 24 to 130m. The EOF structures associated with the higher modes are generally more complex containing more zero-crossings and thus a greater range of zero-crossing intervals. This behavior is also usually exhibited by the dynamical modes that can be calculated from the associated density profiles. The zero-crossing locations and intervals provide a basis for determining where observations should be concentrated. To estimate the spacing of these observations, vertical wavenumber spectra have been calculated for the X-Z

Tabla 15

Vertical Profile EOF Parameters for Detrended Data

EOF(% Variance)	Maxima Intensity[1]	Maxima Depth(m)	Zero-Crossings Depth(m)	Zero-Crossings Interval(m)
1 (57.0%)	1.98	35	-	-
2 (25.7%)	0.86	10	48	
	0.57	80	-	
3 (7.1%)	0.22	10	32	
				85
	0.18	55	117	
4 (3.9%)	0.11	0	25	
				38
	0.17	45	63	
				112
	0.10	96	175	
5 (1.8%)	0.05	0	20	
				27
	0.06	35	47	
				42
	0.06	70	89	
				130
	0.04	140	219	
	0.02	~250		
6 (1.2%)	0.03	0	18	
				24
	0.03	26	42	
				27
	0.02	56	69	
				54
	0.02	97	123	
				127
	0.03	190	~250	

[1]Maximum nodal value times appropriate eigenvalue($^{\circ}C^2$)

detrended data over the first six modes (Figs. 142 and 143). Since the original profiles were digitized (subsampled) at 5m intervals, any significant temperature microstructure (particularly for the STD profiles) occurring over depth intervals of less than 5m will be aliased into these wavenumber spectra. The usual assumption of a "red noise" spectrum is thus implied. Each wavenumber component has been multiplied by the appropriate eigenvalue to make the ordinates proportional to variance. Figure 142 provides another indication of the relative importance of each of the modes. To examine the various wavenumber spectra in more detail, individually scaled periodograms for each mode are also presented (Fig. 143). As expected from the previous eigenvector plots, the higher modes indicate a wider range of important wavenumbers. The sixth mode indicates that wavenumbers as high as seven cycles (per 300m) may be important. As a result, observations should be acquired at least every 10m to adequately resolve the variability contained in the first six EOFs. A conservative sampling strategy consistent with the results of Table 15, and the wavenumber spectra in Fig. 143, suggest that observations should be acquired at least every 10m over the first 100m and then perhaps every 15 or 20m at deeper levels.[14]

The principal components associated with the first six EOFs are shown in the lower panels of Figs. 136-141, as

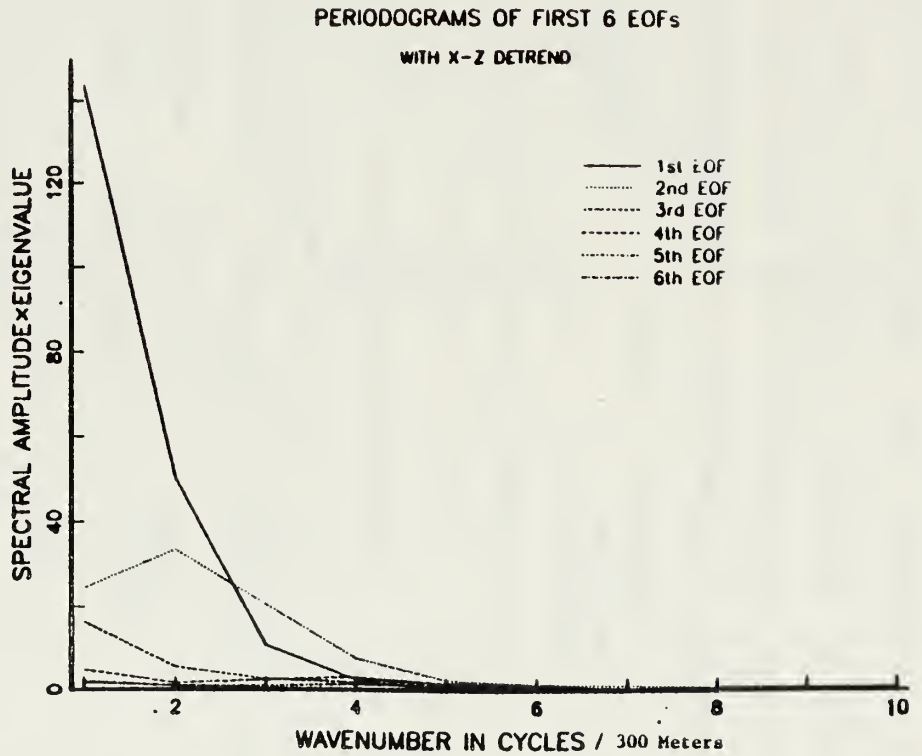

Figure 142. Periodograms for first six vertical EOFs with X-Z detrending. Ordinate is the frequency component times the appropriate eigenvalue. Abscissa is the wavenumber in cycles per 300 meters.

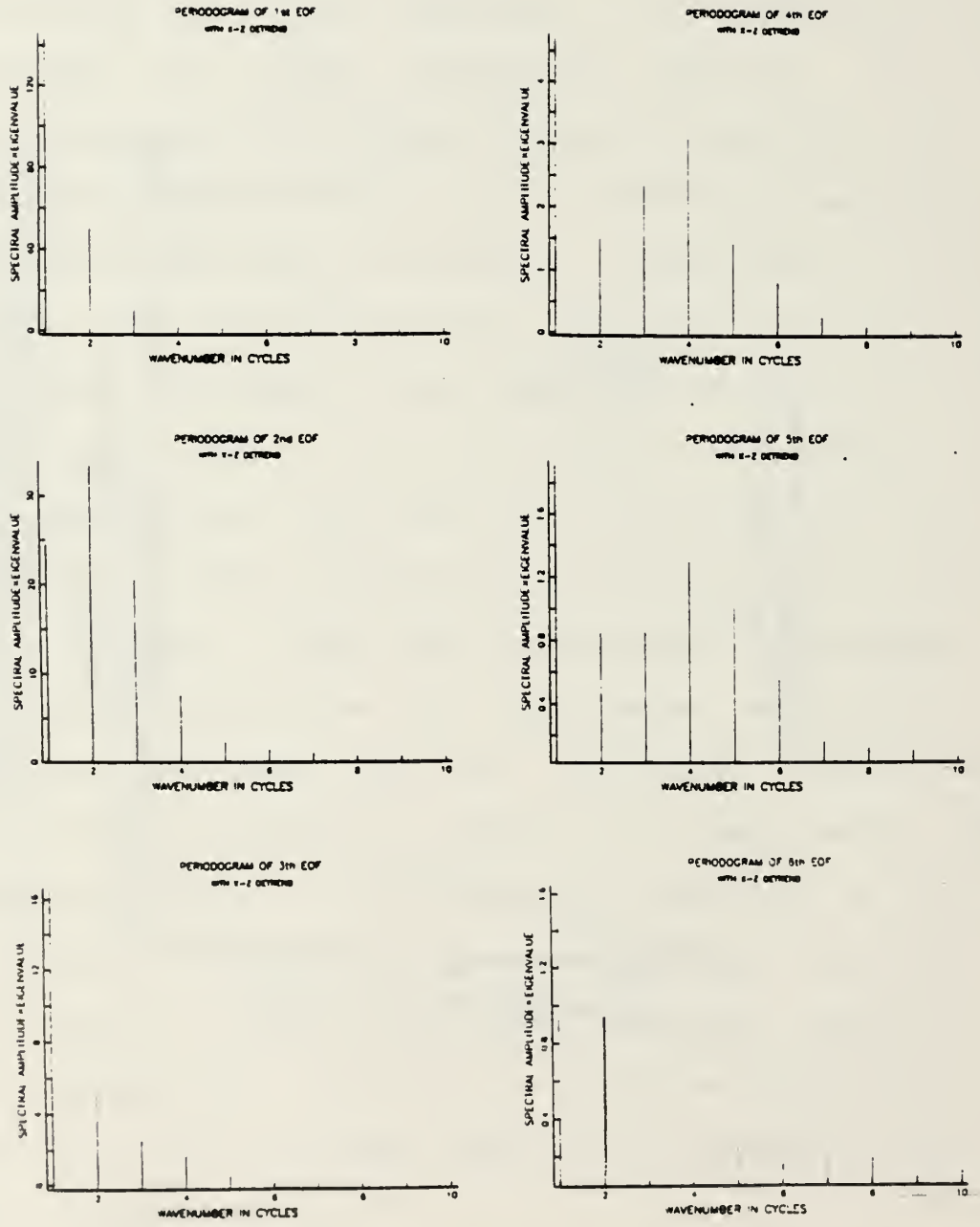

Figure 143. Individually-scaled periodograms for first six vertical EOFs with X-Z detrending.

a function of phase, trackline separation, and offshore location. The important distinction between these principal components and those presented in the previous section is that they are shown explicitly as a function of offshore location. The principal component sequences for mode 1 (Fig. 136) are somewhat similar over the first 3 corridors closest to the coast (i.e., within about 35km). The fourth principal component sequence is distinctly different from the first two sequences and may be due to the influence of oceanic waters beyond the upwelling frontal zone. Overall, a slight increase in amplitude occurs in the seaward direction. The principal components for mode two are generally similar moving offshore; however in this case the amplitudes generally decrease with distance offshore. The principal components also decrease in the offshore direction for mode three; however less similarity between the sequences is now seen. Although principal component amplitudes decrease significantly beyond mode three, less similarity still between the sequences is observed with respect to modes four and five. There may be a tendency for the offshore variability to become uncoupled between the corridors at the higher modes.

To further clarify the offshore dependence of principal component amplitudes, the following calculations are made,

$$V_{jk} = \sum_{i=1}^{23} A^2_{ijk}$$

where A_{ijk} represents the i^{th} principal component for the j^{th} corridor and the k^{th} mode. To obtain the percent variance per corridor per mode, V_{jk} is divided by the quantity $(n-1)\lambda_k$ where n equals the total number of values and λ_K is the k^{th} eigenvalue. These calculations were made for the first six modes and the results are shown in Fig. 144. The first mode shows an increase in variance offshore out to the 3rd corridor, followed by a decrease. The second mode, beyond the 2nd corridor, shows a systematic decrease in variance. The next three modes indicate significant offshore variations in $V_{jk}/(n-1)$ while the sixth mode shows rather constant variance out to the fourth corridor and then an increase.

The final analysis of the principal components consists of plotting these values at their corresponding grid points to construct planview maps in the offshore-alongshore/time plane (Fig. 145). These principal component maps are similar in format to those constructed previously in Section D.1, but here the principal component values are plotted at the appropriate grid point locations whereas before, the principal components were plotted at the individual profile locations. The principal component map for the first EOF for Phase 1A shows a similar warm

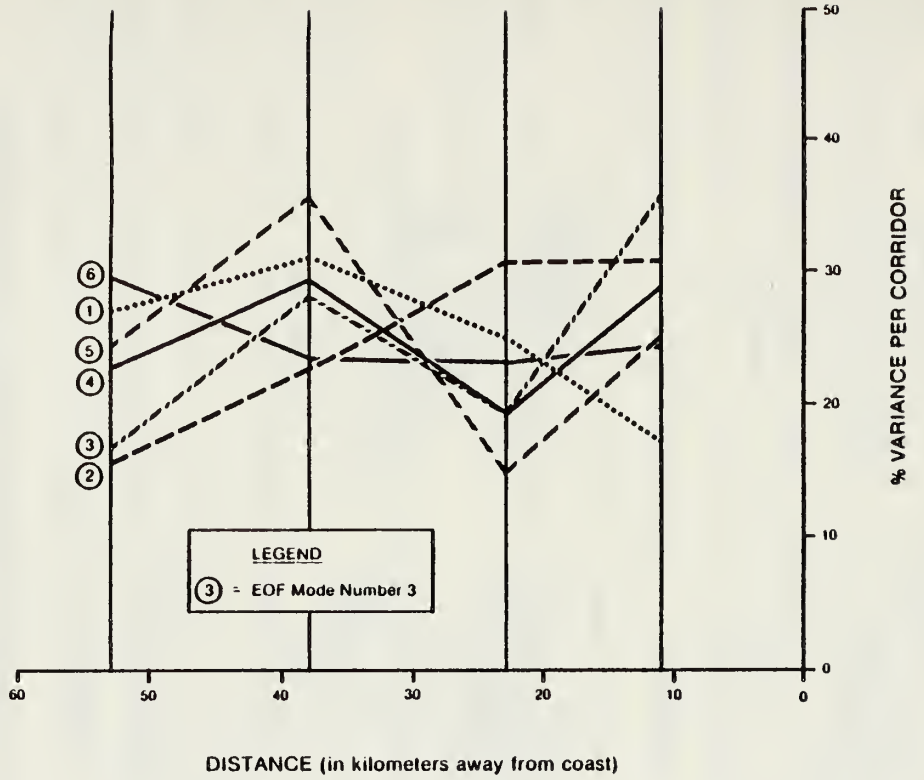

Figure 144. Principal component variance associated with the vertical, X-Z detrended EOFs as a function of offshore distance.

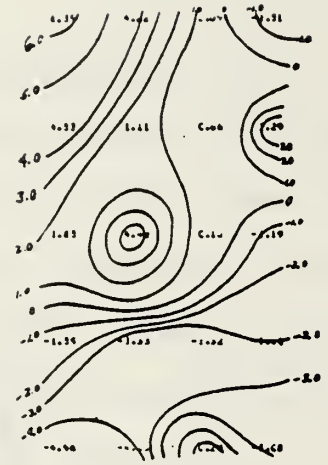

PHASE 1A

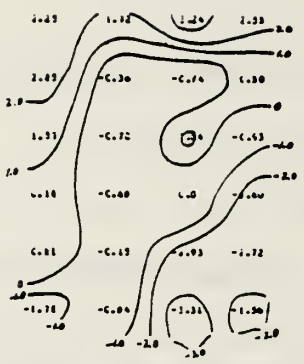

PHASE 1B

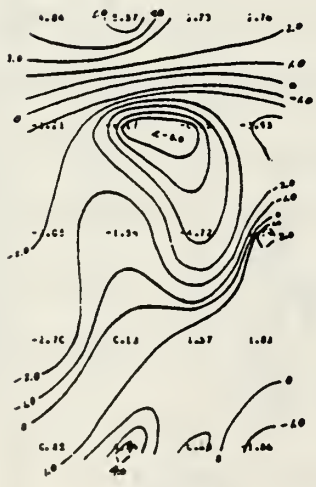

PHASE 3A

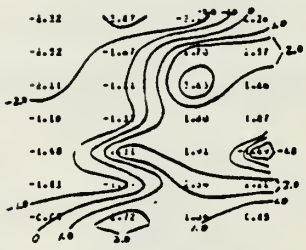

PHASE 3B

Figure 145. Principal component maps for first vertical EOF for each phase. Principal components are plotted at the appropriate grid point locations.

region in the SW corner indicated in the previous planview map (Fig. 125). The map for Phase 1B does not reveal regions with strong gradients but the overall contour pattern is quite different from that indicated for Phase 1B in Fig. 125. Similarity between the Phase 3A principal component map and its previous counterpart is evident, where the gradients are generally strong. Little resemblence is seen between the Phase 3B map in Fig. 145 and the Phase 3B map from Section D.1, and once again the gradients are weak. The final three maps do not provide obvious physical interpretations. However, it is apparent that the similarity between these maps and the previous maps in Section D.1 is greatest when the existing gradients are relatively strong.

Next, vertical EOFs are calculated without first removing an X-Z mean transect. In this case a single global mean profile is calculated and then removed from the individual corridor-averaged profiles. The variability associated with the systematic onshore/offshore changes in profile structure is now contained in the residuals.

The first eigenvalue now contains almost 80% of the total variance (Fig. 146) and the first three eigenvalues contain 95.2% of the total variance. The marked change in the distribution of variance is more easily seen by comparing the actual eigenvalues for both cases (Table 16).

EOFs W/O X-Z DETREND

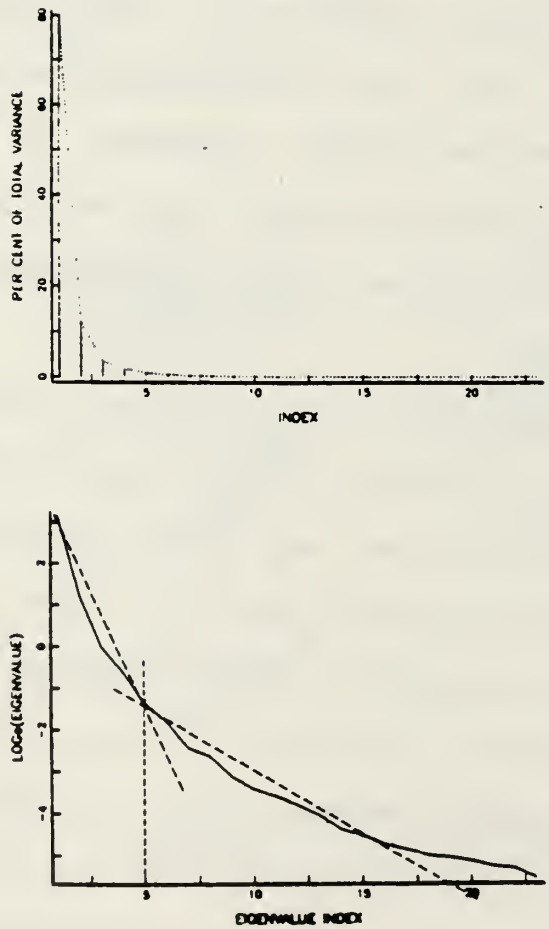

Figure 146. Same as Figure 135 except without X-Z detrending.

Table 16

Comparison of variance distributions for detrended (X-Z), and non (X-Z) detrended data

Mode Number	(with X-Z detrend)	(w/o X-Z detrend)
1	7.Ø9	22.54
2	3.19	3.39
3	Ø.89	Ø.97
4	Ø.49	Ø.52
5	Ø.23	Ø.25
6	Ø.15	Ø.16

Although the overall variance is obviously much greater for the second case (i.e., no X-Z detrend), almost all of the increase in variance is associated with the first EOF. The change in the distribution of variance is also reflected in a lower, normalized entropy of Ø.19, or about 45% less than the entropy calculated for the case with X-Z detrending (Ø.35).

The eigenvectors associated with the first six EOFs are almost identical to the previous EOFs with X-Z detrending. Thus, the vertical eigenvectors for all previous cases including those calculated in Section D.1 are essentially the same (at least over the first three modes) and indicate the robustness of this aspect of the EOF calculations. These eigenvectors have been plotted with respect to the global mean profile for the first six modes (Fig. 147). For dimensional consistency, $(\lambda_i) \cdot e_i(z)$ is actually plotted together with the mean profile in each case. An increasing number of intersections between each eigenvector and the mean profile can be seen for increasing mode number.

Although the structure of the vertical eigenvectors was virtually unaffected by using a global mean profile instead of an X-Z mean transect to detrend the data, it is clear that this modification to the detrending procedure will affect the associated principal components. In particular, the variance associated with the principal

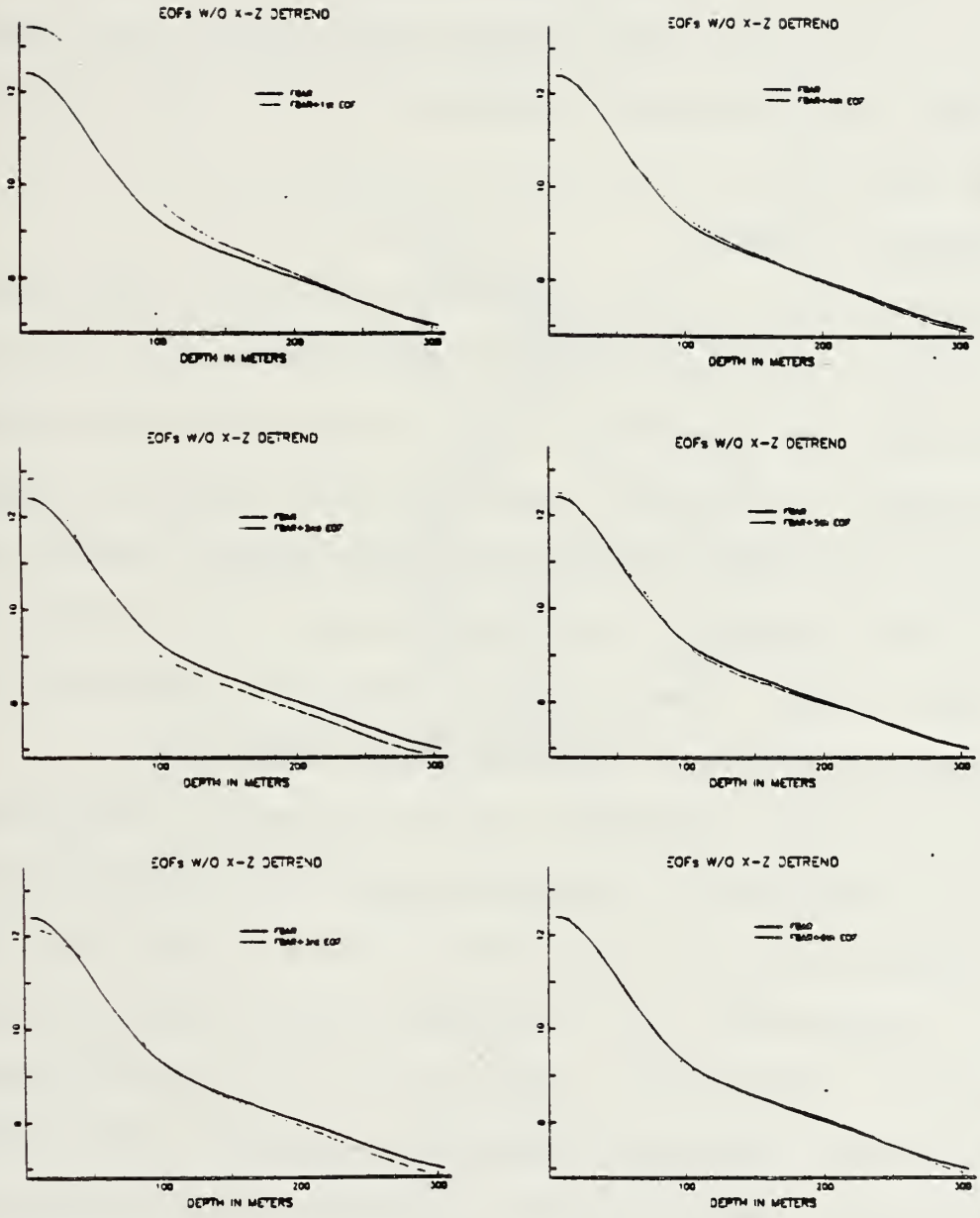

Figure 147. First six eigenvectors without X-Z detrending plotted with respect to global mean profile.

components has again been calculated for each corridor and plotted as a function of offshore position (Fig. 148). The mode one principal component variance is now much greater for the furthest inshore and furthest offshore corridors, a result consistent with first removing a single mean profile. Consistent with previous observations, the second and higher mode principal component variances are about the same as before.

E. SUMMARY OF RESULTS

Length scales in the horizontal plane were estimated from spatial autocorrelations calculated for selected temperature data from Phase 1A. The calculations included the removal of a bilinear trend and were limited to depths of 0, 50, and 100m. Alongshore and offshore scales were similar and generally ranged from about 22 to 37 km over the upper 100m. These results indicated somewhat less alongshore-to-offshore anisotropy than expected.

The vertical dependence of the horizontal temperature field was examined by calculating pattern correlations for the temperature data from Phases 1A and 3A. The data were first interpolated to a standard grid using Modified Quadratic Shepard's method of two-dimensional interpolation. Bilinear trends were removed. The bilinear trend surfaces themselves also provided useful information on the physical characteristics of the local temperature

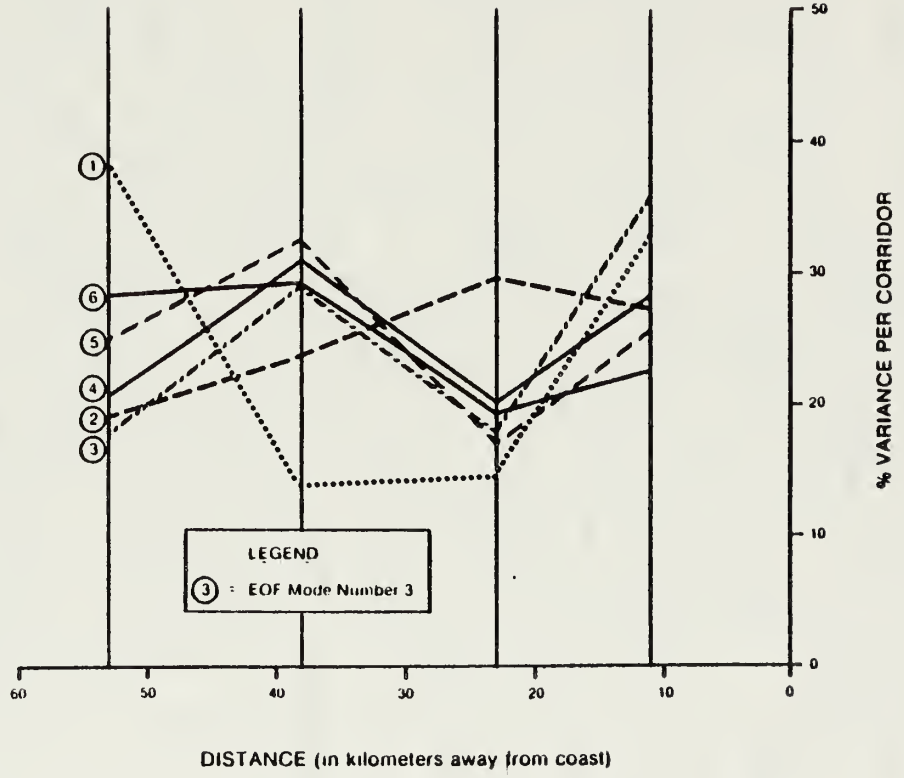

Figure 148. Same as Figure 144 except without X-Z detrending.

field. The trend surface contours tended to rotate counter-clockwise with depth, from an alongshore orientation at the surface to a more onshore/offshore orientation at deeper levels, indicating a change in the predominant direction of flow from equatorward near the surface, to onshore, at deeper levels.

The pattern correlations were calculated for 10 levels between the surface and 300m. Since the actual correlations depended only slightly on the reference levels chosen, the vertical correlation of the temperature field appeared to be approximately homogeneous with depth. As a result, individual pattern correlation profiles (PCPs) calculated at different reference depths for each phase, were ensemble-averaged to obtain mean pattern correlation profiles with greater statistical significance. From these mean PCPs, an e-folding scale of about 170m was obtained for Phase 1A whereas an e-folding scale of about 60m was obtained for Phase 3A. Pattern correlations decreased more rapidly with depth for Phase 3A than for Phase 1A perhaps due to increased wind mixing or upwelling that took place between the phases.

Next, EOFs were calculated for selected temperature profiles from each phase to obtain additional estimates of the important horizontal and vertical scales. EOFs have been used in a few previous studies to obtain estimates of the important scales associated with the internal and

surface temperature fields (Barnett and Patzert, 1980; Halliwell and Mooers 1983). The eigenvectors associated with each EOF are also useful in locating inhomogeneous regions where sampling requirements may be more stringent.

EOFs were calculated for each phase from most of the individual deep profiles available. An overall mean X-Z transect was used to detrend the data. Although the distribution of variance associated with the first three EOFs varied considerably between phases, the associated eigenvectors were similar. Most of the important structure in the first three EOFs was contained in the upper 100-130m. The principal components were plotted in planview for each phase (the first mode only). The resulting patterns could be related to the previous temperature maps for Phase 1A but not for the other phases. The regions of most intense variability in these maps had spatial scales of the order of 25km or less.

In Section D.2, EOFs were calculated in the offshore-vertical (X-Z) plane. A detrending procedure similar to that used in the previous case was employed. The first six EOFs were found to be significant. The resulting two-dimensional eigenvector patterns were examined initially to obtain information on the physical processes that might be revealed. A number of intense nodes were observed in the EOF patterns. Several of the X-Z modes contained patterns

near the coast (within 40km) that suggested the influence of coastal-trapped waves. Also EOF structures perhaps associated with a meandering equatorward near-surface jet were suggested by the location, extent, and depth of certain nodal patterns. The first six eigenvectors generally indicated that most of the important structure occurs within the upper 100-150m.

Estimates of the horizontal scales were obtained by comparing intersections of the various EOF patterns with the mean field. These scales ranged from about 20 to 80km with a mean scale of 48km. The horizontal scales tended to increase with increasing distance offshore, and to decrease with increasing mode number.

The principal components from the two-dimensional EOF analysis were also examined for space/time variability. Cyclic behavior was observed in certain cases with periods and wavelengths often associated with coastal-trapped waves. Since predicted modal patterns beyond the continental shelf and slope are not known, one way in which these waves may be detected from the present analyses, is through their variability alongshore and with time. Inspection of the principal component sequences suggested that adjacent principal components in various sequences were often similar, implying a degree of persistence or autocorrelation in the values. As a result, the principal components were tested separately for statistical

independence. It was found that the principal components for at least two of the modes were not statistically independent thus partially confirming the earlier observations.

As a natural extension of the two-dimensional X-Z EOF analysis, vertical EOFs were calculated from the same data to examine the vertical profile structure. The data were detrended in two ways. First the same mean X-Z transect was removed as before and the associated EOFs calculated. Secondly, a single global mean profile was used to detrend the data before calculating the EOFs. The purpose of the second detrending procedure was to examine the effect of reassigning the onshore/offshore variability, previously modeled as a systematic trend, to the field of residuals.

In the first case (i.e., with X-Z detrending) the first six EOFs were taken to contain useful information. Most of the important structure in the EOFs occurred in the upper 100 to 150m. The EOFs were then subjected to a vertical wavenumber spectral analysis to obtain additional information on the important vertical scales. The results of this analysis suggested that observations be acquired at least every 10m over the first 100m, and then every 15 to 20m at deeper levels.

The principal components associated with the vertical EOFs are presented as a function of offshore location. To emphasize this onshore/offshore dependence, the variance associated with these principal components is plotted versus offshore location. The first mode showed an overall increase in variance in the offshore direction, while the second mode showed an overall decrease in variance offshore. Modes three, four and five showed significant variability in the offshore direction. Planview maps were also prepared from the principal components, similar to those presented in Section D.1 for the individual profiles. These maps were similar to the previous maps only where strong gradients were present. The Phase 1A map once again was physically interpretable in terms of features previously identified in Chapter II.

The distribution of variance associated with the EOFs calculated for the data detrended with a single global mean profile differed considerably from the preceeding case. Although the overall variance associated with the first six eigenvalues was much greater in the second case, most of this additional variance was associated with the first EOF. The eigenvectors in this case were almost identical to those in the previous case; thus, the vertical sampling requirements did not appear to be affected by the change in detrending. The principal components were obviously affected by the change in detrending, and the resulting

variance distribution showed the first mode variance to be much greater in the corridors nearest the coast, and furthest offshore.

VI. A SUMMARY, COMPARISONS, CONCLUSIONS, AND RECOMMENDATIONS

A. INTRODUCTION

The first section of this chapter contains a summary of results from the previous four chapters. The results fall into two general areas, those that relate to the physical characteristics of the study area, and those that relate to the observed space-time scales of variability. In the second section, comparisons are made between those scale estimates obtained in this study and those obtained elsewhere. The final section contains conclusions and recommendations.

B. SUMMARY

1. The Physical Characteristics

The first objective was to establish a regional oceanographic framework within which to evaluate and interpret the space-time scales of variability. Hence, those results that provide information on the physical characteristics of the present study area, are summarized.

During a three-week period in June of 1980 off Pt. Sur, shipboard and coastal winds were consistently from the NNW and, thus were upwelling favorable. Surface winds observed aboard ship indicated a positive wind stress curl extending to at least 50km offshore. The upwelling

associated with positive wind stress curl, however, was estimated to be only about 25% of the expected value for coastal upwelling. There was a relatively strong diurnal variation in the shipboard surface winds.

Based on property distributions of temperature, salinity, and sigma-t, upwelling was active around Pt. Sur during the June period. During the first phase, upwelling was most intense in a zone extending south from Pt. Sur toward Sur Canyon. Also, there was an anticyclonic flow feature in the SW corner of the area near the Davidson Seamount. During the two-week study, the band of upwelled water moved about 15km further offshore, apparently in response to sustained and gradually intensifying alongshore winds.

Individual offshore property transects showed considerable variability. Alongshore averages of these transects retained a smooth version of the expected characteristics of a coastal upwelling regime, including an equatorward surface jet and a poleward undercurrent. A mean transect tendency over a two-week period indicated cooling near the surface within 40km of the coast and warming beyond 60km offshore. T-S analysis near the continental slope off Pt. Sur indicated relatively high temperatures and salinities on sigma-t surfaces, consistent with the poleward flow of Equatorial Water there. In at least one case, a local decrease in SST appeared to be more

the result of intensified mixing than the result of upwelling. Generally however, shoaling internal temperature and salinity fields (i.e., with time) within 20km of the coast, indicated that upwelling was important throughout the study. The thermocline increased in thickness between phases, consistent with an increase in cyclonic vorticity in this depth range, if potential vorticity was conserved. In most of the property maps, the isopleths tended to follow the local bathymetry, particularly inshore of the 1000m isobath. This tendency was observed throughout the study.

The equatorward geostrophic flow at the surface was of the order of 20 cm/sec, to approximately 50km offshore. The poleward, geostrophic subsurface flow (the California Undercurrent) was usually within 20km of the coast. Vertical sections of geostrophic velocity indicated narrow ($\sim$ 20km), equatorward, jet-like flows with axes that appeared to meander rapidly (i.e., often within 2 days).

Since temperature (salinity) generally increased (decreased) away from the coast, the oceanic fronts encountered aboard ship were not usually density compensated. Thus, strong alongfront, baroclinic flows are to be expected.

Several comparisons of IR satellite data with *in situ* temperature data were made. The results of these

comparisons indicated that boundaries observed in the *in situ* data were usually located slightly shoreward (5km, or less) of the boundaries observed in the satellite data. Overall, the results of the comparisons were favorable.

The location of the major upwelling frontal boundary was digitized on a grid extending from about Pt. Piedras Blancas to Cypress Pt. over a sequence of 31 IR satellite images from May 2 to June 13, 1980. The mean shape of this boundary was very similar to that of the underlying bathymetry. The mean frontal boundary however was shifted slightly southward relative to the isobaths near Pt. Sur. The probability of encountering upwelled water around Pt. Sur was highly correlated with the underlying bathymetry. Bathymetric influence was apparent seaward to a depth of at least 1000m.

The satellite-derived frontal boundary locus was decomposed into EOFs to characterize its alongshore variability. The first four EOFs and the mean frontal boundary were lag-correlated with the 100, 500, and 1000m isobaths. In all cases maximum correlations were 0.82 or greater at lags between zero and 14km.

Two sequences of satellite images demonstrated the gradual westward expansion of the upwelling zone on a seasonal time scale. The satellite-derived frontal boundary loci first were interpreted with the aid of a surface Ekman mass transport model. Upwelling surface areas

were estimated from the satellite data and compared with the time integrated local wind stress. The correlation between the upwelling surface area and integrated wind stress was approximately Ø.9Ø. These results are consistent with local wind forcing. However, local wind forcing is not the only possible cause for the observed offshore movement of the upwelling boundary. For example, the speed associated with the frontal movement was estimated to be O(Ø.5cm/sec), a phase speed also consistent with westward propagating Rossby waves. Satellite-derived cloud cover distributions provided additional support for the likely influence of Rossby waves. Based on a scale analysis of the governing vorticity equation, it was concluded that offshore Ekman transport is likely to be dominant on time scales of days to weeks whereas Rossby wave dispersion may be dominant on time scales of approximately two months or more.

The historical satellite imagery was also drawn upon to describe the "typical" seasonal evolution of upwelling along the Central California coast. This description includes at least three stages in the evolution of upwelling over the period from about March to September. Initially, upwelling is restricted to a narrow coastal band of O(1 R_{bc}). This early but visible stage of upwelling may follow the spring transition by at least a month.[15] Within

a few weeks, the zone of upwelled water generally expands offshore, particularly around the major capes. This intermediate phase is characterized by the importance of bathymetric influence. During June, upwelled water may expand considerably further offshore, and extended filaments of cool water often occur. By September, the coastal region out to several hundred km may be influenced by cool upwelled water.

Twelve-year records of SST at three coastal locations along the Central California coast (Granite Canyon, Pacific Grove, and the Farallon Islands) were examined for oceanic and statistical information content. Sudden spring transitions occurred in six out of the 12 years. Decreases in temperature of O(3C) in about seven days were typical. These events were associated with the seasonal transition to sustained coastal upwelling. In at least one case (March 198Ø), this transition was apparently not due to changes in the local wind field, but it was perhaps the result of remote forcing at coastal locations further south. The occurrence, abruptness, and magnitude of the spring transition along the West Coast has only recently been recognized. Preliminary analysis of current meter data on the continental slope just south of Pt. Sur for the transition in March 198Ø indicated that currents reversed briefly from poleward to equatorward over depths from 1ØØ to 5ØØm. The mechanism responsible for these

transitions has not been clearly identified but limited data suggest the likely importance of coastal-trapped waves. It is concluded that a major effort should be devoted to improving our understanding of this phenomenon since existing coastal circulation models (e.g., Allen, 1981) do not account for it.

A well-defined annual cycle in SST was observed at Pt. Sur (Granite Canyon) contrary to the expectations of Reid et al. (1958) and List and Koh (1976). However its range was reduced ($\sim$3C) from that expected for the deep ocean at this latitude. Maximum temperatures also occurred about a month later at Pt. Sur (mid-October) than in the deep ocean at 36N. Four distinct El Nino warming events were identified in the SST data over the 12 year period, 1972-73, 1976-77, 1979-80, and 1982-83. The major spring transitions of 1973, 1977, and 1980 follow El Nino episodes. A possible relationship between El Nino events and the spring transitions is implied.

Spectrum analyses of the SST data did not reveal periodicities that could be clearly related to wind or tidal effects. However, these influences are expected to be important in time-series data acquired at deeper levels in this area (Wickham, 1983). The influence of turbulence on SST was also considered. The slope of the temperature spectrum at higher frequencies was similar to the slope

predicted by classical turbulence theory. However, this apparent agreement may not be highly significant since surface temperature is a non-conservative property and turbulence theories which take this effect into account predict spectral slopes that are somewhat greater than those predicted by classical homogeneous turbulence theory.

2. The Space-Time Scales: Techniques and Results

The results of the previous space-time scale analyses are presented. This includes a summary of the considerations and techniques used in their evaluation.

In Chapter II, space-time scale estimates were obtained mainly through direct observation of the data distributed in space and/or time. Tendency analyses also provided estimates of the important space and time scales. Similarly in Chapter III, these scales were often estimated by direct observation from sequences of satellite images, and from the analyses derived from these images.

In Chapter IV, statistical techniques for estimating time scales were introduced. Spectrum analysis techniques were employed upon occasion to obtain scale estimates. These techniques were used in identifying periodic components in the data. However, once the periodic components were identified, then time domain analysis techniques were required to estimate the scales associated with non-periodic components in the data. The autocorrelation function was used to estimate time scales

from time series of SST at several locations, and subsurface temperature at one location. Several problems arose in the use of autocorrelation functions for estimating these scales. First, the autocorrelation function can be defined in several different ways; second, no universally accepted criterion exists for defining the scales associated with a correlation function; and third, scale estimates from correlation functions are often obtained with data which have not been adequately detrended. In this study, a standard definition for the autocorrelation function recommended by Jenkins and Watts (1968) was used. With respect to the second problem, several criteria were considered in defining correlation scales from the estimated correlation functions. The e-folding scale criterion was adopted because of its consistency and the ease with which it can be applied. Finally, the procedures for detrending the data before calculating the correlation functions were to identify, fit (in the least squares sense), and remove, all major long-term trends and cyclic components in the data. The autocorrelation function was then calculated from these so-called second residuals in each case. The second step was iterative, often requiring calculation of the autocorrelation function several times after selected cyclic components were removed to see if the

autocorrelation function continued to change significantly as more components were removed.

In Chapters III and V, EOF analysis techniques were used to help estimate the important spatial scales. Before calculating EOFs, the data were always centered, in some cases by simply removing a global mean, but more often by removing two-dimensional means. The ways in which the data were initially detrended often influenced the resulting EOFs, particularly the principal components. Thus considerable care was taken in detrending the data before calculating the EOFs. EOF analysis was particularly useful in identifying inhomogeneous regions where sampling requirements are likely to be more stringent. EOF zero-crossing separations were used to provide a basis for establishing adequate sample spacings. It was generally assumed that at least several equally-spaced observations would be required between zero-crossings to retain or reconstruct that mode of variability from the original data. Thus EOF analyses were useful not only in estimating the spatial scales generally, but also in identifying zones where the scales were most likely to change. Vertical scales were also estimated from periodogram analysis of the vertical EOFs associated with temperature profiles acquired over the Pt. Sur study area.

Observed scales were obtained from the various data distributions presented in Chapter II. Geostrophic winds

off Pt. Sur varied on an approximate weekly time scale during June, 1980. Shipboard winds acquired during the Pt. Sur study varied diurnally. Surface property maps for Phase 1A indicated that the offshore width of the coastal upwelling zone was approximately 25km. Property maps from Phase 3A, a mean transect tendency between Phases 1A and 3A, and interprofile correlation maps of temperature profile residuals for Phases 1A and 3A (from Chapter 5), all indicated that the zone of upwelled water expanded offshore about 15km between phases (or to about 40km offshore). SST tendencies over two-day intervals showed rapid trend reversals off Pt. Sur. Thus, sampling intervals of two days or less may be required to capture the significant short-term variations in SST. Vertical sections of geostrophic velocity indicated a meandering near-surface equatorward jet whose (1) core varied between 25 and 50km offshore, (2) vertical extent varied between about 50 and 125m, and (3) width was of the order of 20km. The location of the jet maximum varied over periods as short as two days. Thermalsalinograph data acquired aboard ship during the Pt. Sur study were used to estimate the cross-front scales associated with the temperature and/or salinity fronts encountered during the study. Cross-front scales ranged from about 2 to 5km for temperature, and from about 4 to 7km for salinity.

EOFs were calculated for the upwelling front taken from two sequences of satellite images (May 2, 1980 to June 13, 1980, and April 4, 1981 to July 14, 1981), to estimate the scales of variability in the alongfront direction. The primary EOF for 1980 indicated a meandering front with an alongshore spatial scale of about 80km and a period of 30 to 40 days. Over both years, zero-crossing separations ranged from 4 to 48km. The original data were sampled at 2km intervals; however the results suggest that the satellite-derived frontal locus could probably be sampled once every 5 to 10km to retain most of the important alongfront variability.

Based on the satellite data, significant changes in SST could occur over periods as short as two days. This time scale agrees with previous time scale estimates obtained from the in situ data. Historical satellite data indicated that the R_{bc} was not generally an appropriate offshore length scale for the region influenced by upwelling along the Central California coast, particularly as the upwelling season progressed. Consequently, another scale, based on Rossby wave dynamics, was considered. This latter scale corresponds to the distance travelled by a Rossby wave over a specified time interval. Along the Central California coast, a length scale on the order of 50km is obtained for a period of 100 days. It is difficult to verify this length scale precisely because of the major

alongshore variations that normally occur in the offshore extent of the upwelling frontal boundary. However, the predicted scales are reasonable based on order-of-magnitude estimates.

Historical satellite data have also shown that interannual variability is important. Major changes in the evolution of upwelling along the Central California coast often occur from one year to the next.

In Chapter IV, the time-scales of variability associated with SST at three locations, and subsurface temperature at one location, were estimated. Twelve-year time-series at Granite Canyon, Pacific Grove, and the Farallons were used in estimating the SST time scales. Spectrum analysis of these data revealed a dominant annual cycle and harmonics at six months and about 46 days, in each case. Using detrended data, the calculated autocorrelation functions yielded e-folding time scales of 5.3 days at Pacific Grove, 6.Ø days at Granite Canyon, and 8.4 days at the Farallons. To establish the robustness of these time scale estimates, the series at Granite Canyon was divided into two halves and each half analyzed separately. Time scale estimates for both six-year segments were similar to the one obtained for the entire 12-year record. A 52-day record of hourly temperatures at 175m off Cape San Martin were analyzed using the same

approach. A corresponding segment of SST at Granite Canyon was analyzed similarly, and the results compared. The time scale for the concurrent 52-day segment of daily SST at Granite Canyon was about 30 hours. The corresponding time scale for the hourly subsurface temperature record was about two hours. Also, the periodic semi-diurnal internal tide at 175m was important.

The spatial scales of variability were estimated in Chapters III and V. EOF analysis of frontal variability from IR satellite data in Chapter III yielded alongfront scales ranging from 8 to 96km. In Chapter V, a variety of techniques were used in estimating the spatial scales because the spatial data (i.e., the temperature profile data) were limited due to the number of independent observations available for any given calculation. Also since the data were acquired quasi-synoptically, it was not possible to obtain completely unambiguous estimates of the important horizontal scales. Horizontal spatial autocorrelations of selected temperature fields at 0, 50, and 100m were calculated for the offshore and alongshore directions. Bilinear trends were removed. The results indicate that offshore scales increase from 22 to 33km from the surface to 100m, and alongshore scales generally increase from 33 to 37km. Pattern correlations were calculated between temperature horizons at 10 levels from the surface to 300m. The data were interpolated to a two-

dimensional grid to facilitate the calculations. Bilinear trends were removed before calculating the pattern correlations. The pattern correlation profiles are shown in Figs. 121 and 122. Also, the temperature field was essentially statistically homogeneous with depth, based on calculations using different reference levels. Consequently the individual pattern correlation profiles were ensemble averaged to obtain mean pattern correlation profiles with greater statistical significance (Fig. 123). From these mean pattern correlation profiles, e-folding scales for Phases 1A and 3A were approximately 170 and 60m, respectively. Pattern correlations decreased more rapidly with depth during Phase 3A than during Phase 1A, possibly because of increased wind mixing and upwelling between the phases.

EOFs were next calculated using the individual deep temperature profiles from each phase. A mean offshore-vertical transect was removed before these EOFs were calculated. The resulting eigenvectors indicated that most of the important EOF structure was contained in the upper 100-130m. The principal components were plotted in planview and the resulting distributions indicated (1), the inhomogeneous nature of the study domain, and (2), that the regions of most intense variability had spatial scales of the order of 25km or less. Two-dimensional X-Z EOFs were

calculated to examine variability in the offshore-vertical plane. Again, an X-Z mean transect was first removed from the data. These EOFs were used to locate inhomogeneous regions in the X-Z plane, and to estimate the horizontal scales. The results are summarized in Table 14. Horizontal scales ranged from 18 to 80km with a mean scale of 48km. Also the influence of coastal-trapped waves within 40km of the coast or less was suggested in several of the X-Z modal patterns. The principal components suggested both persistence and cyclic behavior. The degree of persistence could not be evaluated quantitatively because of the limited number of values. However, a separate statistical test confirmed that adjacent values were frequently not independent. The wavelengths and periods associated with the cyclic behavior in the principal components were consistent with coastal-trapped waves, although additional evidence will be required to make a positive identification. In the final section of Chapter V, vertical EOFs were calculated. Two methods of detrending were used. First, an X-Z mean transect was removed as before. Second, a single global mean profile was removed. The second detrending procedure was used to examine the effect on the EOFs of reassigning the important onshore/offshore variability to the field of residuals. The first set of EOFs was further subjected to vertical wavenumber spectrum analysis to obtain improved estimates

of the vertical scales. Again the first set of EOFs indicated that most of the important structure was contained in the upper 100-150m. The vertical EOF spectra indicated that wavenumbers as high as seven cycles per 300m may be important. A conservative sampling strategy in this case suggested that observations should be acquired at least every 10m over the first 100m (below the mixed layer) and every 15 to 20m at deeper levels. Planview maps of the principal components indicated some similarity to previous principal component maps where the gradients were strong. Although the distribution of variance changed dramatically in the second case where EOFs were calculated using only a single global mean profile to detrend the data, the EOF structures were virtually identical; thus the vertical sampling requirements remained the same.

C. COMPARISONS

In this section scale estimates obtained from the present study are compared, where possible, with scale estimates obtained under similar conditions elsewhere.

The alongshore scales in the present study were identified from two sources. First, the possible influence of coastal-trapped waves in a principal component analysis suggests scales of O(50km). Second, spatial autocorrelations in the alongshore direction at 0, 50, and 100m indicate scales of 33, 100, and 37km, respectively.

These values are contrasted with the isotropic spatial scale estimates obtained by Holladay and O'brien (1975) of 16 to 40km from a two-dimensional spectral analysis of SST off the coast of Oregon. In the offshore direction, scales ranged from 20 to 80km to 60km offshore, based on EOF analyses; independent estimates from IR satellite data fell within the same range. Scale estimates obtained from spatial autocorrelations of temperature at 0, 50, and 100m for the offshore direction were 23, 29, and 33km, respectively. All estimates of the offshore spatial scales exceeded the baroclinic radius of deformation. These offshore scales also exceed the value given by Curtin for the upwelling regime off Oregon (O(10km)). Vertical scales were of O(40m) or more depending on what part of the profile was considered. This scale exceeds values indicated by Mooers and Allen (1973) by at least a factor of four. However this scale does not explicitly take into account the surface mixed layer, which in the present case is about 20m. The near-surface, equatorward jet was about 20km wide and 50 to 125m deep. These dimensions differed somewhat from those given by Wickham (1975), who found the jet at this latitude (in August 1972) to be approximately 5km wide, and to extend almost 400m in depth. The surface jet off Oregon is of the order of 10 to 20km in width and 25 to 50m in thickness (Mooers and Allen, 1973). Although the California Undercurrent was clearly detected in the

data from this study, it was not well-resolved spatially because of its proximity to the coast.

Next, the temperature time scales obtained in this study are compared, where possible, with time scales obtained using similar analysis techniques in other areas. Relatively few estimates of temperature time scales however have appeared in the oceanographic literature and those that have appeared, invariably come from deep ocean areas. In MODE-1 (SW of Bermuda), temperature time scales from time-series acquired at 500, 1500, and 4000m were 36.4, 32.4, and 22.8 days respectively (the MODE Group, 1978). The decrease in time scales of temperature with depth was considered significant. Because of the location and depths involved, a direct comparison with the present results cannot be made. However Davis (1973) estimated temperature time scales at the surface with data acquired during MODE-1, obtaining an e-folding time scale from one data set of about six days. In this case a one-day sampling interval was used. This time scale is about the same as the values obtained during the present study for the daily observations at Granite Canyon, Pacific Grove, and the Farallons. However in the thermocline, correlation analysis of isotherm heights yielded time scales which were of O(30 to 40 days). These results differ vastly from the subsurface temperature time scale of about two hours (175m)

found in this study. This discrepancy is probably the result of several factors. First and most importantly, the sample interval used in analyzing Davis' subsurface data was 1.5 days whereas the subsurface data presented in this study were recorded every hour. Thus it is clear that the estimated correlation scales will depend on the original sample spacing used to acquire the data. The problem of aliasing may be important in cases where time scales are compared for series obtained using different sampling rates. The problem of comparing time scales for series initially sampled at different rates can be at least partially addressed through appropriate subsampling of the series acquired at the higher sampling rate.

Second, only a simple polynomial was used to detrend Davis' data and important cyclic components may have been present at subsurface levels which were not removed. Differences in detrending may be an important factor contributing to the difference in time scales and probably reflects a basic difference in objectives. By not first removing important deterministic components in the data, the scales thus obtained will be most suitable for sampling major oceanographic features in the area of interest, but will probably not be suitable for sampling the higher wavenumber random components.

Third, Davis used the unbiased form of the autocorrelation function in his calculations, a form which

leads to higher values particularly where relatively large lags are used. Fourth, in the calculation of subsurface time scales, Davis used isotherm depths instead of actual temperatures. This procedure raises the question of what the equivalent precision in temperature would be. Clearly, if a correlation time scale is estimated from a time series recorded to the nearest Ø.5C, a different result will be obtained than if temperature had been resolved to the nearest Ø.ØlC. Finally, the ocean areas where these data sets were acquired differ considerably, the first representing open ocean conditions SW of Bermuda, and the second, a region 8kms off Cape San Martin just south of Pt. Sur. Thus the difference in time scales in this case undoubtedly has a physical basis as well.

D. CONCLUSIONS AND RECOMMENDATIONS

1. Conclusions

1. The offshore width of upwelled water along the Central California coast exceeds the baroclinic radius of deformation except perhaps during the early stages of upwelling (ca. April). However, the Rossby radius of deformation is expected to provide an estimate for the offshore extent of coastally-trapped waves.

2. AVHRR IR satellite data are well-suited for identifying and delineating thermal boundaries along the Central California coast. Consequently this source of data should

be useful for similar applications in other coastal upwelling regions as well, at similar and higher latitudes.

3. The influence of bathymetry on surface and subsurface property distributions out to at least the 1000m isobath was strong in most cases. Consequently, the oceanic length scales are expected to be similar to the alongshore topographic scales to at least 25km or so offshore. Also, the mechanism(s) responsible for the coupling between the bottom and the upper layers of the water column are not completely understood.

4. Major El Nino warming events occurred in four out of the 12 years of SST examined along the Central California coast. However the higher SSTs associated with El Nino events were mainly observed during the fall and winter seasons. Consequently, the spring transitions that often follow El Nino events are amplified.

These warming events and their possible influence on climate and fisheries as far north as Central California has been generally overlooked. Hence, these data, previous data, and data from other locations along the California coast should be examined with these factors in mind. Also other properties such as the coastal winds, sea level, and dynamic height should be included in such analyses.

5. The spring transition, in the years that it occurs, should provide a time-zero reference for the offshore expansion of the coastal upwelling zone. In 1980, a time

delay of approximately 3 months between the spring transition and the westward expansion of cool water associated with coastal upwelling was observed. In other years this delay may be closer to one or two months.

6. Evidence was found for offshore mass compensation in the upwelling region off Pt. Sur. Also a region of warming at the base of the pycnocline was observed during a two-week period of upwelling favorable winds. These phenomena should be examined in greater detail when additional data become available.

7. The likely importance of offshore Ekman transport in the short term (days to weeks), and Rossby wave dispersion in the longer term (several months) on circulation in the California Current along the Central California coast was indicated. That Rossby wave dispersion may be an important influence on circulation in this region is a relatively new concept. Because of the general complexity of the circulation in this region, and because of previous disagreements between earlier theories and observations, existing and future data should be reviewed in the light of Rossby wave dynamics. Other mechanisms such as baroclinic instability as described by Ikeda et al. (1983) off Vancouver Island may also be important in contributing to the variability observed in this region, particularly with

respect to the long filaments of cool water that frequently occur off the major capes.

8. The spatial scales resulting from this study should be used in grid design for numerical circulation models along the Central California coast. For example, an alongshore grid spacing of 10 to 15km (between 10 and 60km offshore), and an offshore grid spacing of 5km (out to 60km offshore), are indicated (Table 17).

The space-time scales should also be useful in objective analysis schemes such as so-called optimum interpolation that require correlation distances and/or times for their implementation.

9. The ratio of alongshore-to-offshore length scales obtained from this study indicate a degree of anisotropy slightly less than expected. The original alongshore-to-offshore station spacing aspect ratio was approximately 3:1, whereas the observed aspect ratio was closer to 2:1.

10. Based on vertical pattern correlations of temperature between the surface and 300m, correlation coefficients of 0.2 or less were usually observed. However, the overall similarity of the bottom topography and SST patterns was strong. These results, which are not necessarily inconsistent, should be compared in greater detail.

11. Although it is obviously desirable to extend the present results to other coastal upwelling regions, limited IR satellite coverage of the other major coastal upwelling

areas indicates that the offshore extent of waters influenced by coastal upwelling may not be as great as it is off the Central California coast (Breaker, 1982).[16]

12. The estimated space-time scales are summarized in terms of recommended sample intervals (Table 17). When several scale estimates were derived, the recommended sample spacing was dictated by the shortest scale estimate obtained. Thus the overall recommended sampling rates are often determined by the inhomogeneities in the region. An exception arises with respect to the surface mixed layer where enough observations were not acquired to completely resolve this complex region (this was not an objective of the original study). The criterion used for the spatial scales is, $s = S/4$ (Monin et al., 1974). S is the scale in this case, and s, the sample interval. Thus a sampling rate of approximately four samples per "cycle" is considered satisfactory.[17] For sampling in time, e-folding times per se are recommended since they usually provide smaller, and thus more conservative scale estimates than the other time scale criteria considered.

2. Recommendations

1. The approach to ocean sampling given by Davis (1974) which uses spectral techniques, should be considered in cases where sufficient data are available. Davis' approach additionally provides estimates of the errors that arise

Table 17

Overall recommended spatial and temporal sample spacings for the Central California coast and other coastal upwelling regions at similar latitudes

RECOMMENDED SPATIAL SAMPLING

Feature or Location	Orientation	Recommended Sample Interval	Comments
Central California Coast	Alongshore	12km	Between 10 and 60km offshore
"	Offshore	5km	Out to 60km
"	Vertical a) < 100m b) > 100m	100m 15 to 20m	Excluding the surface mixed layer
Major Upwelling front	Alongfront	10km	
Major Upwelling front	Cross-front	1km	For temperature, salinity and density
Equatorward surface jet	Cross-section (alongshore)	5km or less	
Equatorward surface jet	Vertical	100m	
Horizontal temperature patterns	Vertical	∿50m	i.e., the vertical separation of horizontal patterns

RECOMMENDED TEMPORAL SAMPLING

Location or Event	Depth	Recommended Sample Interval	Comments
Central California Coast	Surface	5 days	
Pt. Sur Study Area	175m	∿2 hrs	Coincident SSTs at Pt. Sur yielded a time scale of one-to-two days
Pt. Sur Study Area	Entire water column	∿2 days	
Spring Transition	"	∿0.5 days	Between February and April
Annual cycle in SST	Surface	∿12 days	Annual cycle in SST has major 1st and 3rd harmonics at 6 months and 46 days respectively

due to aliasing, and to the effects of discrete versus continuous sampling.

2. The technique of analyzing data in space-time coordinates shows promise for interpreting the variability of data acquired in coastal regions.

3. A number of aspects relating to space-time scales should be examined in greater detail. These include:

   (1) Dependence on depth, location, and season.

   (2) Robustness of the scale estimates, and sensitivity to changes in their methods of calculation.

4. The spring transition off Central California is an important event that occurs in many years. Data should be acquired to better resolve this phenomenon in space and time. Observations between about February and April for coastal SSTs should be acquired at least twice per day to better resolve these transitions in time. A better understanding of this phenomenon is needed to improve our knowledge of coastal circulation and, in particular, the onset of coastal upwelling. The results presented here indicate that major spring transitions may frequently follow El Nino events. The possible relationship between El Nino events and the spring transition should be explored.

5. In estimating correlation space-time scales associated with the random components in a given data set, the following procedures are recommended:

(1) Remove deterministic-like components initially. This includes long-term trends and major cyclic components.

(2) Calculate the biased form of the auto (cross) correlation function.

(3) Use the e-folding scale criterion.

6. Space-time scales should be estimated for other physical and dynamical properties as well as for temperature.

7. In estimating the spatial scales, the calculations were usually limited by the amount of data available. Both correlation and EOF analysis techniques were used in attempting to estimate these scales. To provide further support for using EOFs in estimating the scales of variability, comparisons between the two techniques should be made.

8. Pattern correlations were calculated as a function of depth interval for selected temperature data. By incorporating calibrated and earth-located IR satellite data into such pattern correlations, it may be possible to develop procedures for predicting subsurface temperature structure from satellite data directly.

9. In previous studies often too little attention has been given to initial detrending procedures, since a slight change in detrending may alter the remaining variance structure drastically. It is recommended in future studies

of this type that more emphasis be placed on how the data are detrended, and on how much detrending is appropriate. Whenever possible, physically meaningful models should be used to establish a basis for detrending; thus that portion of the variance which is initially removed is assumed to be separable and understood on physical grounds.

10. Numerical sampling experiments should be conducted, applying candidate space-time sampling plans to simulated data sets having statistical properties similar to those obtained from the present study. Such experiments would determine the tradeoffs between spatial resolution and temporal synopticity, for example.

The results of these simulation experiments would then be applied to future field measurement programs designed, for example, to test the resulting statistics for stationarity with respect to the present results, and to examine the importance of variability at scales not resolved in the present study.

APPENDIX A

CALCULATION OF THE BAROCLINIC ROSSBY RADIUS OF DEFORMATION FROM CONTINUOUS VERTICAL PROFILES OF DENSITY

It is often difficult to obtain reliable estimates of the first mode baroclinic Rossby radius of deformation (R_{bc}) using the two-layer approximation given in Chapter I (1.1, p. 17), because the selection of a thickness for the upper layer may be ambiguous for typical profiles of density. As a result, the vertical velocity equation for internal waves is considered, for continuous density distributions.

Consider the following partial differential equation governing the propagation of inertial-internal waves on a rotating earth,

$$\frac{\partial^2 \psi}{\partial x^2} - \left(\frac{\sigma^2 - f^2}{N^2 - \sigma^2}\right) \frac{\partial^2 \psi}{\partial z^2} = 0 \qquad \text{(A.1)}$$

where ψ is the streamfunction given by

$$u = -\frac{\partial \psi}{\partial z}, \quad w = \frac{\partial \psi}{\partial x}$$

and N is the Vaisala-Brunt (VB) frequency where

$$N^2(z) \simeq -\frac{g}{\bar{\rho}} \left(\frac{\partial \rho}{\partial z}\right), \qquad \text{(A.2)}$$

g is the acceleration due to gravity, ρ is the density, $\bar{\rho}$

the mean density, f is the Coriolis parameter, and σ is the internal wave frequency. Since N is only a function of depth (in this case), using separation of variables, and assuming plane wave propagation, then A.1 can be expressed as

$$\frac{d^2\phi}{dz^2} + \left(\frac{N^2 - \sigma^2}{\sigma^2 - f^2}\right) K^2\phi = 0 \qquad (A.3)$$

where

$$\psi = \phi(z)e^{i(\sigma t - kx)}$$

K is the first-order horizontal wavenumber $2\pi/L$ where L represents the horizontal wavelength. For a rigid sea surface, the following kinematic boundary conditions apply:

$$\phi(z) = 0 \text{ at } z = 0 \text{ and at } z = -D$$

where -D is the bottom depth. Thus it is required that the vertical velocity vanish at the surface and at the bottom.

Equation A.3 must be solved numerically since N(z) is a continuous, arbitrary function of depth. The solution of A.3 represents an eigenvalue problem. A first-guess is made for the eigenvalue and then an initial value problem is solved from the surface down. The bottom boundary condition must also be satisfied and as a result the final solution is obtained by iteration. Solutions for A.3 can be obtained for an infinite number of modes, but in the present case only the first (baroclinic) mode is of interest.

Four VB2 (VB squared) profiles were calculated from density profiles taken from each phase at a common location (Fig. 149). The location is approximately 40km off Lopez Point in a water depth of 1500m. Beyond this distance offshore, the vertical property distributions do not change significantly. Since in situ data during the Pt. Sur upwelling center study were only acquired to a depth of 300m, the VB2 profiles were extrapolated to the bottom using an exponential fit to data acquired in the area during other field studies. These exponential "tails," and the calculated VB2 profiles were then catenated. The depth of catenation was 248m. In the calculation, a depth increment of 5m was used. A mean VB2 profile has also been included in these calculations and it was obtained by averaging the four density profiles originally selected (Fig. 150). Because the solutions to A.3 are depth dependent, two additional depths were included, 1000 and 2000m. These depths fall within the range of depths encountered over the study area but occur far enough offshore that the VB2 profiles are still representative.

Results of these computations include the phase speed, c, and horizontal velocity versus depth (for each mode). Phase speeds were used to calculate R_{bc}, where

$$R_{bc} = c/|f|$$

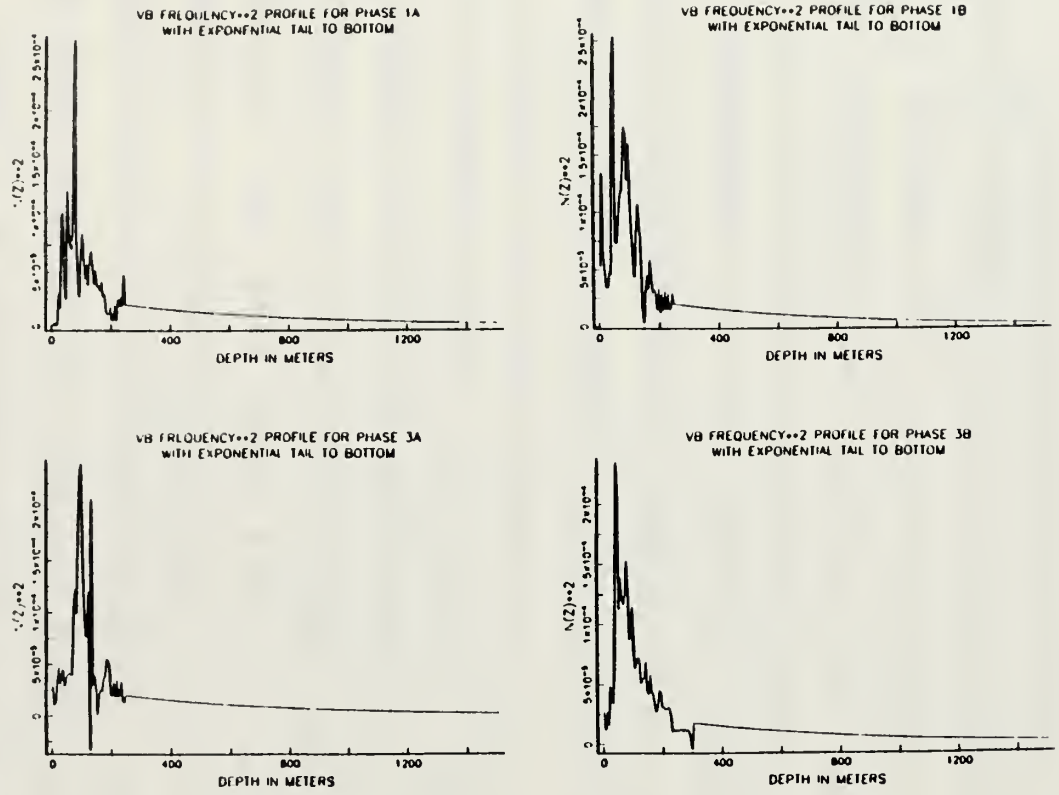

Figure 149. Individual Brunt-Vaisala frequency squared profiles for each phase for a location approximately 40km off Lopez Point. Profiles have been extended to the bottom by catenating an exponential "tail" in each case.

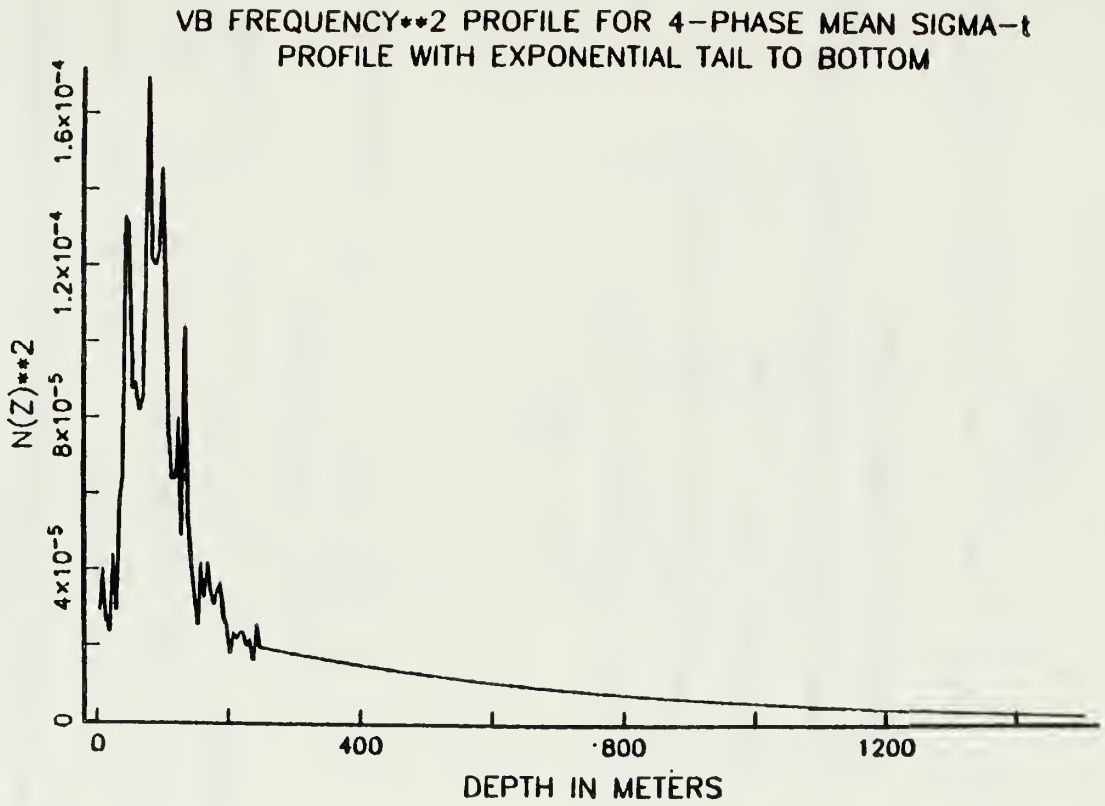

Figure 150. Four-phase mean Brunt-Vaisala frequency squared profile. Same exponential tail has been catenated in this case as in Fig. 149.

However the phase speeds as calculated are dispersive and to obtain the non-dispersive equivalent phase speed, the following relation was used

$$C_{nd} = [1 - (\frac{T}{T_i})^2]^{1/2} C_d$$

where

C_d = Dispersive phase speed

C_{nd} = Non-dispersive equivalent phase speed

T = Selected wave period

T_i = Inertial period (20.42 hours at 36N)

R_{bc} can also be estimated from

$$R'_{bc} = \frac{\bar{N}D}{\pi f}$$

where

$$\bar{N} = \frac{1}{n} \sum_{i=1}^{n} N_i(z), \quad n = \text{total number of depths}$$

D = Total water depth

As a result, R'_{bc} has also been included in these calculations for comparison (Table 18). Zero-crossing depths for the vertical distribution of horizontal velocities (first mode) have also been extracted to obtain an estimate for the depth of the upper layer for the two-layer approximation given in equation 1.1. This depth, and the corresponding R_{bc}, are then used to estimate the corresponding equivalent density differences between the

Table 18

Rossby radius of deformation(R_{bc}) and its approximation(R'_{bc}) versus depth and phase

	PHASE				
Depth(m)	1A	1B	3A	3B	Mean
1000	14.5[1]	15.2	15.4	14.9	15.0
	14.7[2]	16.1	15.5	15.7	15.8
1500	17.9	18.3	18.5	18.1	18.2
	18.2	19.6	18.9	19.2	19.2
2000	19.1	19.6	19.8	19.6	19.7
	20.4	21.8	21.2	21.4	21.5

[1] R_{bc} (km)

[2] $R'_{bc} = \frac{\bar{N}D}{\pi f}$ (km)

upper and lower layers for the two-layer approximation (Table 19).

From Table 18 several observations can be made. First, R_{bc} (and R'_{bc}) increase from about 15km at 1000m, to about 18.5km at 1500m, and finally to about 20km at 2000m. Second, the ranges about the four-phase means for R_{bc} are 0.9, 0.6, and 0.7km for 1000, 1500, and 2000m respectively. Finally, R'_{bc} exceeds R_{bc} in all cases. The mean difference between R'_{bc} and R_{bc} is about 1km. As a result of these calculations, it is concluded that R_{bc} is probably known to within at least $\pm$ 10% of its true value.

Finally, the upper layer thicknesses and the density differences indicated in Table 19, may provide useful order-of-magnitude estimates for calculating the two-layer R_{bc} in future studies of the region.

Table 19

Density differences for two-layer approximation for R_{bc}

Total water depth (m)	Upper layer thickness (m)	$\Delta\rho x10^{-4}$(gm/cm3)
1000	400	7.2
1500	590	7.1
2000	680	6.7

APPENDIX B

CORRELATION ANALYSES OF THE VERTICAL TEMPERATURE PROFILES ACQUIRED OFF PT. SUR

A. INTRODUCTION

This appendix serves as a prelude to Chapter 5. In this appendix, vertical temperature profiles are cross-correlated to examine the space-time variability in thermal structure over the Pt. Sur study area. The results are presented as a function of spatial separation, location, separation in time, and in space-time coordinates.

B. PRELIMINARY CALCULATIONS

To examine changes in vertical temperature structure over distance (alongshore and offshore) and time, temperature profiles over the Pt. Sur area have been cross-correlated. Because a few stations were re-occupied to within a km or less between Phases 1A and 1B, it has also been possible to estimate temperature profile correlation time scales. However it has not been possible to isolate the spatial influence on profile correlation scales completely because the measurements were not synoptic.

The cross-correlations, $E\{T_i(x,y,z,t) \cdot T_j(x,y,z + h_3,t)\}$ calculated according to:

$$r_{ij}(h_3) = \sum_z (T_i'(z) \cdot T_j'(z + h_3)) \; / \; NF \qquad \text{(B.1)}$$

where,

$$T_k'(z) = T_k(z) - \bar{T}(z), \; \begin{matrix} z = 1, \ldots, N \\ k = 1, \ldots, n \end{matrix}$$

and,

$$\bar{T}(z) = \frac{1}{n} \sum_{j=1}^{n} T_j(z), \quad z = 1, \cdots, N$$

$r_{ij}(h_3)$ = Sample cross-correlation coefficient at lag h_3 between the ith and jth temperature profiles

N = Number of points in profile

$\sigma^2_{T_i}$ = Variance of ith profile

n = Total number of profiles

The temperature profiles used in the following analyses have been first smoothed and then subsampled at 5m intervals. The smoothing has removed high wavenumber components from the data and probably caused the subsequent correlations to be higher than otherwise; the subsampling has introduced aliasing. The calculations are made to Ø.ØlC although the accuracy of the XBTs may be somewhat less than this value ($\sim \pm$Ø.Ø2C). In these calculations the only method of detrending the data has been to remove the global mean at each depth. The mean profiles used in calculating the temperature profile residuals (TPRs) are shown in Fig. 151. Because of the considerable variability found over the area it is somewhat surprising how similar the mean temperature fields were between Phases 1A and 1B.

Although this procedure is considered to be a necessary first step, it may not be sufficient to entirely remove deterministic-like components from the individual profiles;

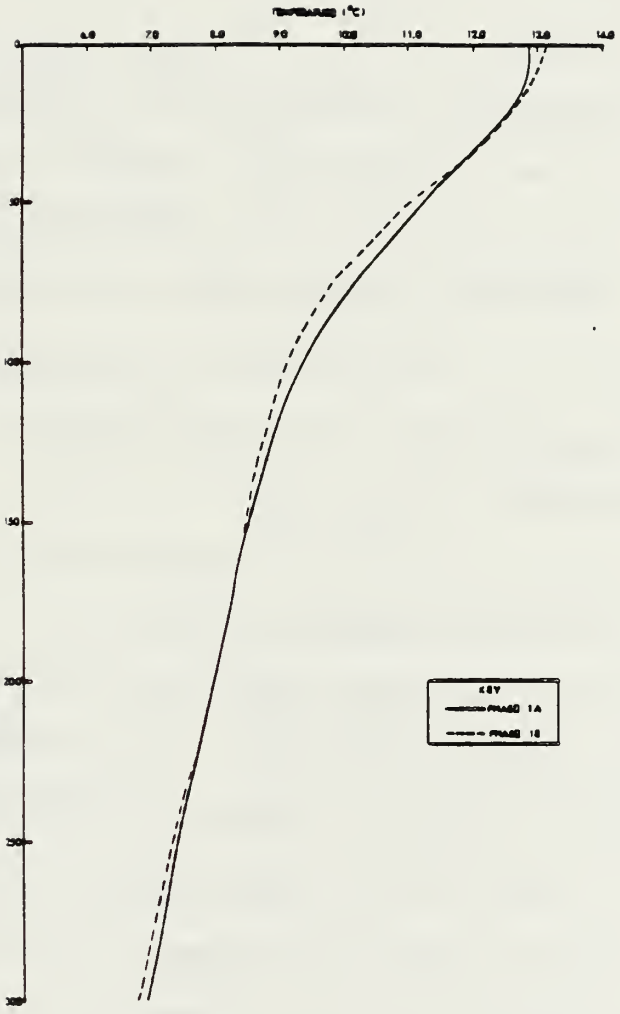

Figure 151. Mean temperature profiles for Phases 1A and 1B. Only deep (300m) profiles from each phase are included.

hence the resulting correlations computed in this manner may exceed the true values. The lag increment in the calculated cross-correlations was 5m in depth and the maximum number of lags was 10 (or 50m). Only deep profiles were used in the computations (i.e., to 300m), thus excluding profiles over the continental shelf and upper continental slope.

The correlation structure of temperature profile residuals in the alongshore and offshore direction has been examined through the cross-correlation of selected profiles. However because data were acquired far less synoptically in the alongshore direction, only cross-correlation results for the offshore direction are considered here.

Approximately 10 hours (per leg) was taken to acquire data in the onshore/offshore direction. Figure 152 shows the correlation of TPRs along leg C of Phase 1A, starting with the station farthest from the coast. TPR correlations decreased gradually to about 0.75 over a distance of about 40 km, approaching the coast. At this distance from the coast and closer, the correlations become strongly negative with respect to stations further offshore. This abrupt change in the pattern of TPR correlations is probably due to the change from oceanic water to water located within the zone of active coastal upwelling. As shown by the 5th, and the last plot in the

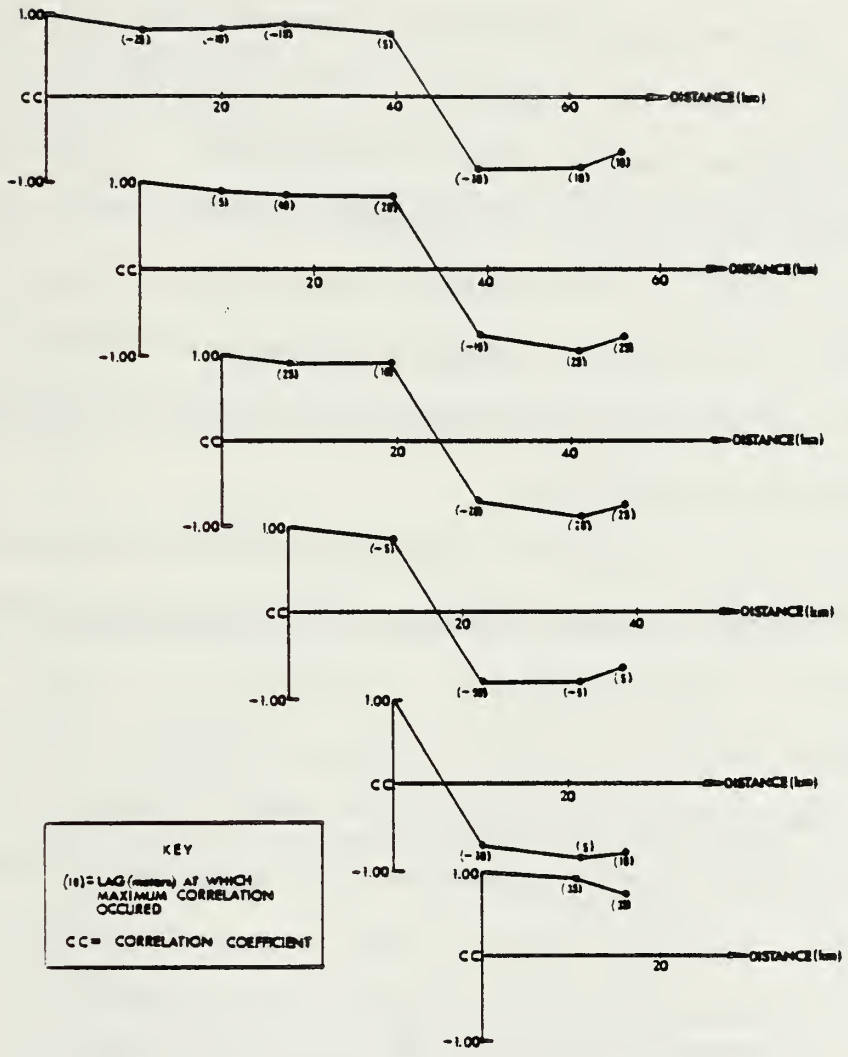

Figure 152. Offshore correlation transect of temperature profile residuals for Phase 1A along Leg C. Numbers in parentheses indicate the vertical depth lag at which the maximum correlation occurred.

sequence, the TPRs nearer the coast (and all presumably within the coastal upwelling zone) are themselves highly correlated (Ø.75 over 16 km). The offshore correlation structure may be approximately homogeneous since the correlation transects appear to be independent of the reference profiles used in the calculations. In principle, the offshore correlation transects could be ensemble averaged to obtain a more reliable estimate of the offshore correlation structure. However, this has not been done here because the number of points that could be averaged at each location is different.

Onshore TPR correlations were also calculated for legs B and D of Phase 1B (not shown). TPR correlations along legs B and D were similar. Similar to Leg C, TPR correlations became negative with respect to stations farther off the coast at about the same distance offshore. TPR correlations were calculated for <u>each</u> leg of Phase 3A (Fig. 153). Correlations at zero lag have been plotted here and are generally only slightly less (1Ø-2Ø%) than the maximum correlations observed at lags other than zero. As before, TPR correlations changed sign at some point along each transect in the offshore direction. Over the 5 legs, the offshore distance at which the profile correlations changed sign ranged from 35km (Leg D) to 55km (Leg E). The

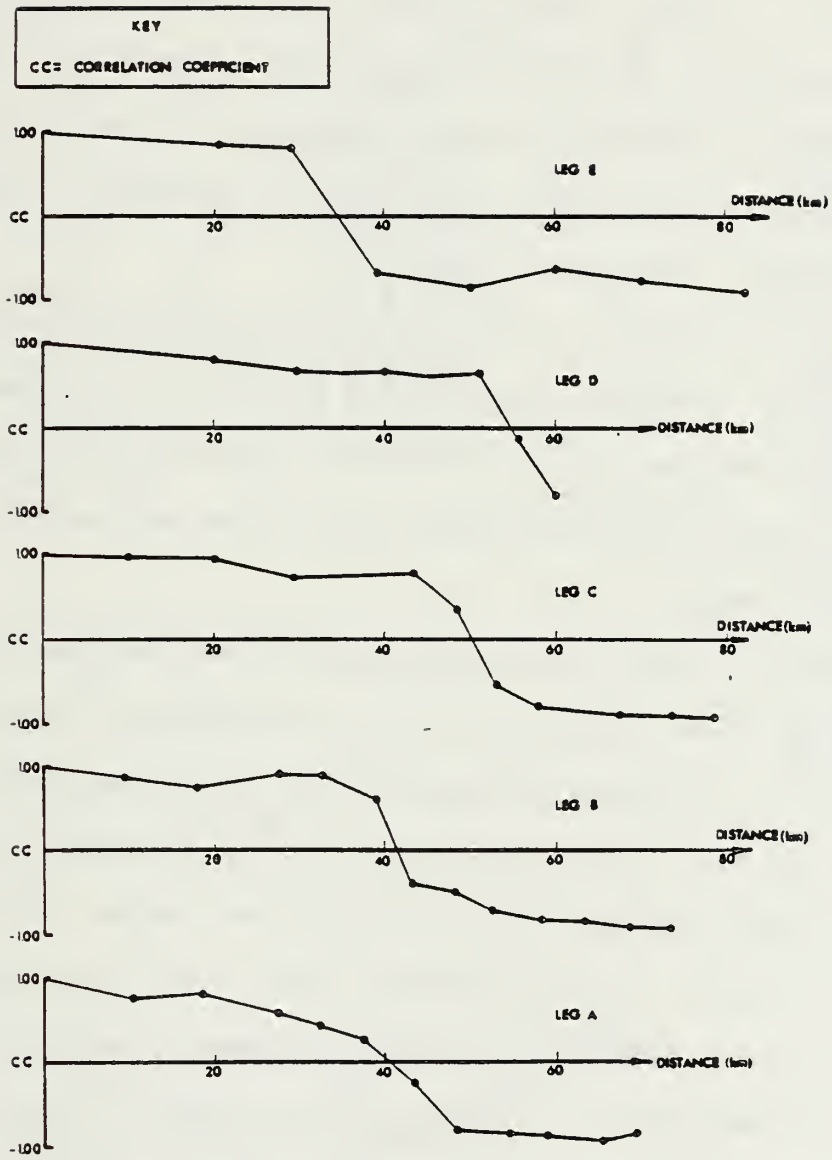

Figure 153. Offshore correlation transect of temperature profile residuals for all Legs (A through E) of Phase 3A. Correlation coefficients in this case correspond to zero depth lag.

leg C sign change for Phase 3A occurred within 5km of the location found on leg C during Phase 1A.

Because of the procedure used in detrending the data originally, these results may not be suitable for estimating actual correlation scales. However they have been helpful in identifying and resolving the major changes in thermal structure that may reflect changes in vertical motion, mixing, and water types.

Because the entire vertical structure enters into the calculation in profile correlation analysis, this technique may provide better estimates on the location of physical boundaries than can be obtained from planview property maps at a single depth.

TPR correlations were also calculated between stations taken at the same locations but at different times for all four phases. Between Phases 1A and 1B, 1Ø stations were re-occuppied to within about 1km of the original stations. Between Phases 3A and 3B, four stations were re-occuppied to within 1km. Times between stations which were re-occuppied range between 17.5 and 74 hours. In this case it should be possible to isolate the influence of time on the correlation of TPRs. The correlations are shown both at zero lag, and at the lags producing maximum values (Fig. 154). Both sets of values produce similar mean curves with a maximum in correlation occurring between about 42 and 52 hours.

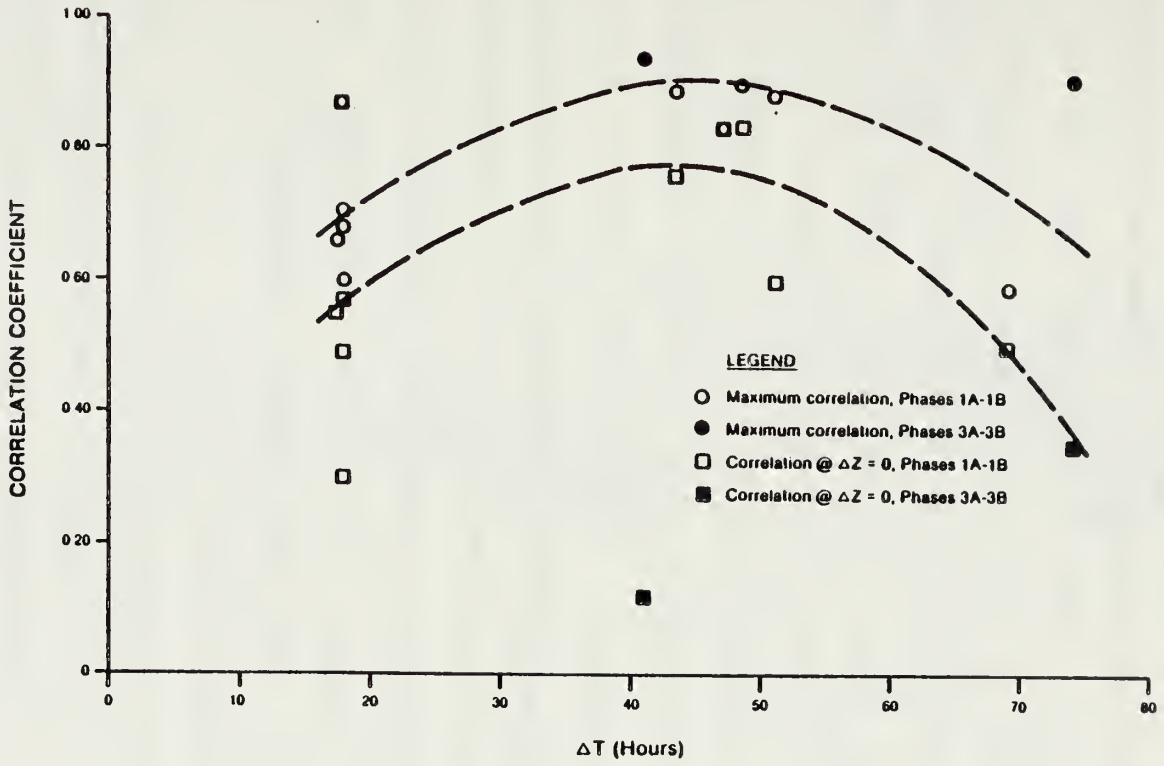

Figure 154. Temperature profile residual correlation times for stations re-occuppied (to within ∿ 1km) between Phases 1A and 1B, and 3A and 3B. Maximum correlations and correlations at zero depth lag are included.

Interprofile correlation maps of TPRs in the offshore direction for Phases 1A and 3A have been constructed. In each case adjacent profiles were correlated and the zero lag values plotted at the mid-points between the respective station locations. These values were then contoured in planview. A band of low correlations occurs paralleling the coast at a distance of 25-40km offshore in the Phase 1A map (not shown). Both closer to the coast and further offshore the adjacent TPR correlations were much higher. Away from the boundary region the TPR correlations were typically 0.80 or greater. In the Phase 3A interprofile correlation analysis, the boundary region is clearly oriented in the alongshore direction, and is continuous over the length of the domain (Fig. 155). The regions away from the major thermal boundary are also better delineated, with slightly higher correlations on average. The TPR correlation field was clearly better organized during Phase 3A than during Phase 1A.

The offshore interprofile TPR correlation maps for Phases 1A and 3A add support to previous interpretations with respect to the presence of two thermally distinct regions separated by a boundary zone approximately 25km in width. Also the boundary region moved 10-15km further offshore between Phases 1A and 3A, consistent with observations in Chapter II, which indicated that the

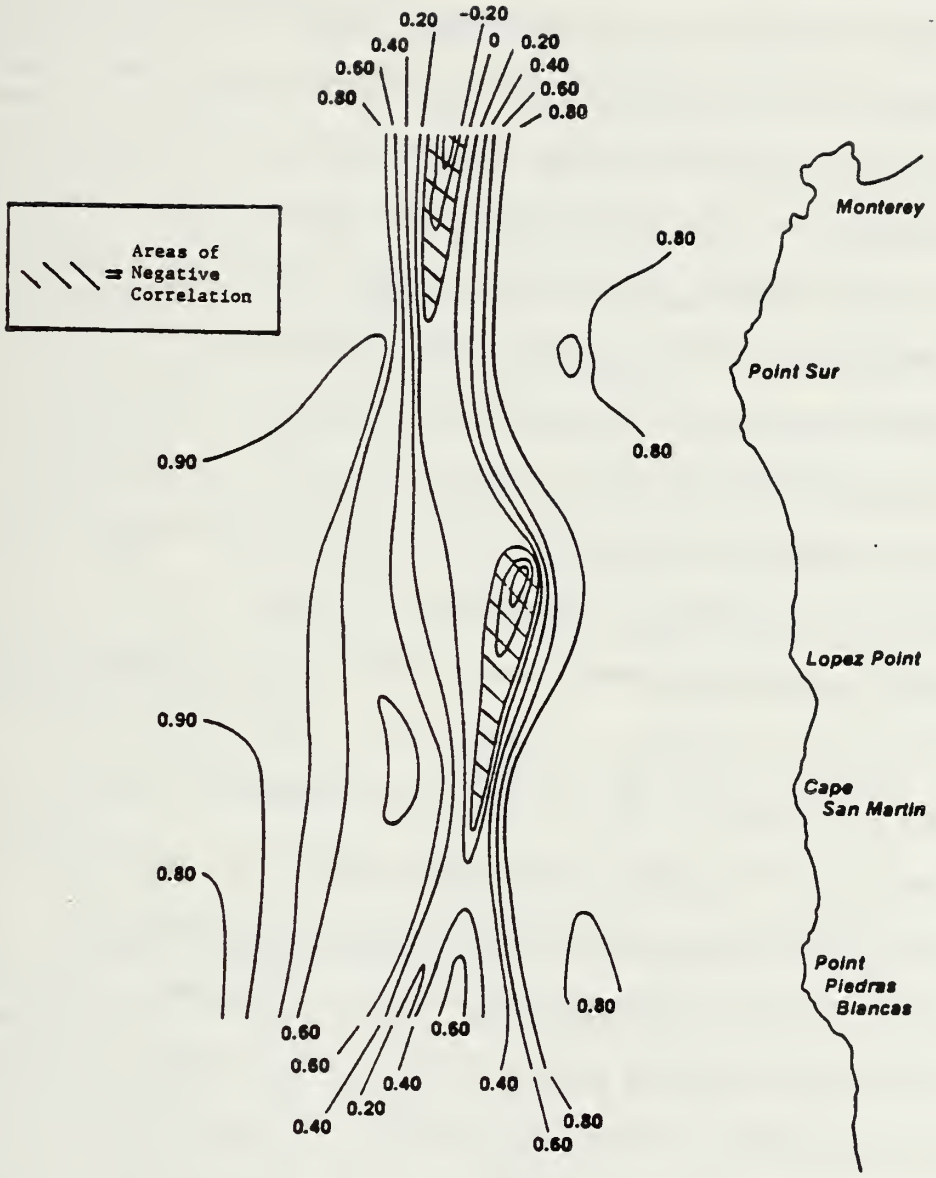

Figure 155. Interprofile correlation map of temperature profile residuals for Phase 3A. These correlation coefficients were obtained by cross-correlating adjacent profiles along each leg and plotting the result at the station mid-points. Values shown are for zero vertical depth lag.

surface baroclinic zone had moved seaward over the same two-week period.

To examine the space-time variability of TPR correlations explicitly, a presumed homogeneous subregion was selected from the offshore TPR correlations just shown. In particular, a subset of profiles located south of Pt. Sur and inside the upwelling zone was chosen from the data acquired during Phases 3A and 3B. These data provided the greatest number of observations that could be assembled in one homogeneous area (arbitrarily assumed to be one with correlation coefficients equal to Ø.8Ø or greater). Twenty-five profiles were used in the calculations which assumed local isotropy, providing a total of $\sum_{i=1}^{n-1} (n-i)$ independent correlations (i.e., 3ØØ). ΔT extends to 6Ø hours and ΔR to 4Økms. Values of ΔT up to 3Ø hours correspond to profile correlations from Phase 3A only, with values beyond 3Ø hours corresponding to correlations between profiles acquired during Phases 3A and 3B. The correlations are at zero depth lag in all cases. Over the entire field the values range from Ø.55 to Ø.99. Because of the non-uniform distribution of values in space-time coordinates, and because of the rapid and apparently random variations in magnitude of these values, these data were averaged to extract possible spatial and/or temporal trends. First the values were averaged in 5 hr x 5km blocks over the domain, and the resulting averages plotted

at the mid-points of each block (Fig. 156). A slight decrease in correlation is seen with increasing $\triangle R$, for values of $\triangle T$ less than about 25 hours. An increase in TPR correlation is seen for increasing $\triangle T$ at $\triangle T$'s of 35 hours or greater. To test the robustness of this averaging procedure and to take into account the possibility that higher values of TPR correlation might be more representative of population values than lower values at similar space-time displacements, a second averaging procedure was used. In the second case TPR correlations located within adjacent 4 hr x 4km blocks were averaged (Fig. 157). However, a non-linear weighted average was used in this case, favoring the higher values. The weighting used is,

$$WA(\Delta T,\Delta R) = (\overline{CC^2})^{-1} \sum_{i=1}^{n} CC_i^3 \ (\Delta T,\Delta R)$$

where,

$$\overline{CC^2} = \sum_{i=1}^{n} CC_i^2 \ (\Delta T,\Delta R)$$

the weights corresponding to the square of the correlation coefficients themselves. For correlation coefficients of Ø.8Ø and Ø.9Ø, for example, WA is Ø.856, while for correlation coefficients of Ø.5 and Ø.9Ø, WA is Ø.8Ø6. Thus, for adjacent values which are similar, WA differs little from the linear average used previously. Results of the second analysis show patterns in the corresponding space-time diagram that are somewhat similar to those indicated in the

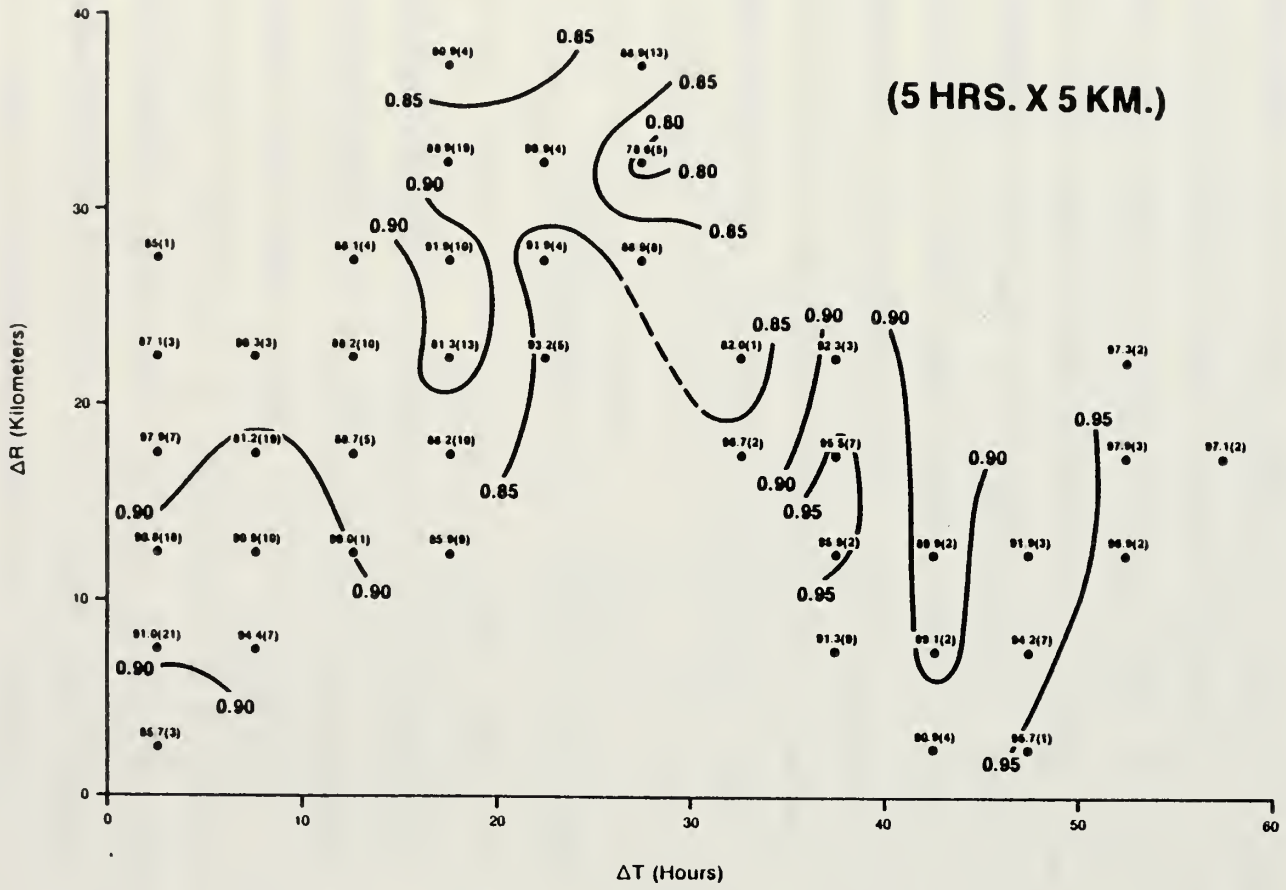

Figure 156. Contoured space-time correlation map of temperature profile residuals. Values have been averaged in 5km x 5hour blocks before being contoured.

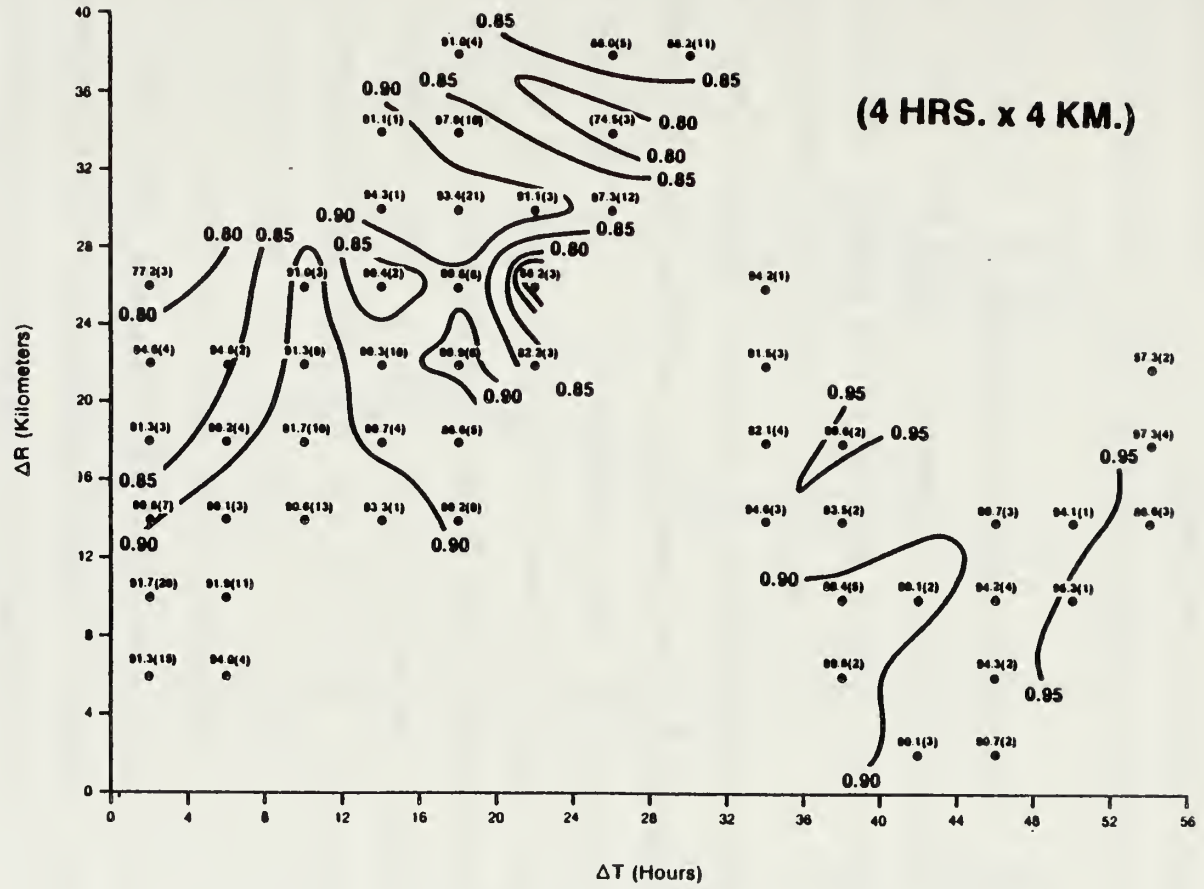

Figure 157. Contoured space-time correlation map of temperature profiles residuals. Means in this case have been calculated using a non-linear weighted average favoring higher correlations. Also the block size in this case is 4km x 4 hours.

previous 5 hr x 5km analysis. Again a slight decrease in TPR correlation occurs with increasing ΔR for small values of ΔT. Also relatively high values (≥ 0.90) occur again beyond a ΔT of about 40 hours. However differences exist in the details of the corresponding space-time structure. For example, greater variability is seen in the region delimited by $\Delta R > 25$km and for ΔT's between 12 and 30 hours.

Further averaging has been applied to these data in order to detect separate trends in space and time (Figs. 158 and 159). In these figures, the block correlations (both the 5 x 5 and the 4 x 4 analyses) have been averaged again, first, horizontally, to obtain a separate measure of range dependence, and second, vertically, to obtain a separate measure of time dependence.[18] A gradual decrease in TPR correlation is seen with increasing ΔR (Fig. 158). This trend becomes more apparent when the 5 x 5 and 4 x 4 block averages are smoothed (a 3-point running mean). TPR correlations vs. ΔT for the vertically averaged block values show first, a decrease in correlation with increasing ΔT and then beyond about 25 hours, an increase in correlation out to at least 55 hours (Fig. 159). This correlation pattern is quite consistent with the previous pattern of TPR correlations versus time for the stations which were re-occuppied between phases where relatively low

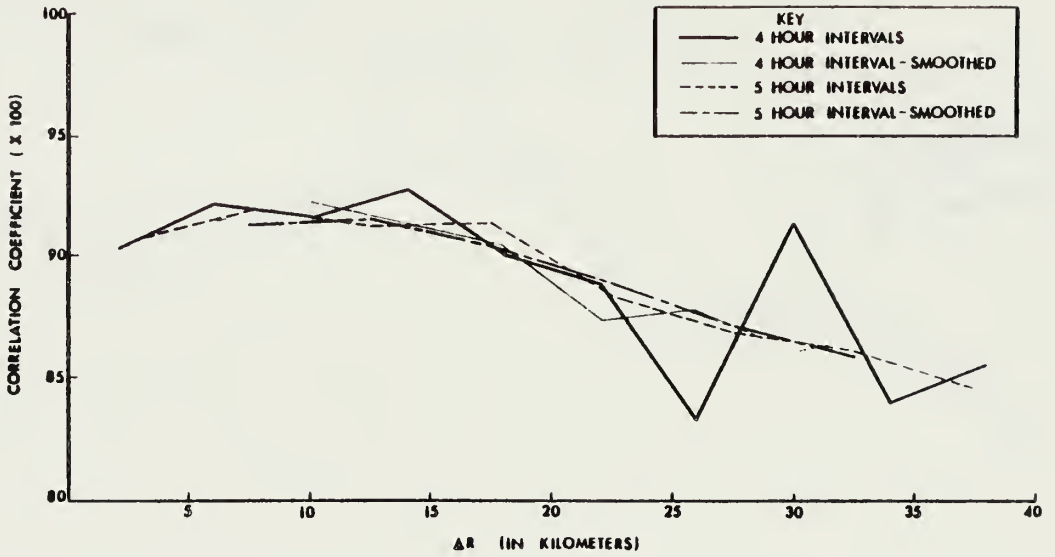

Figure 158. Space-time temperature profile residual correlations averaged over time to isolate range dependence.

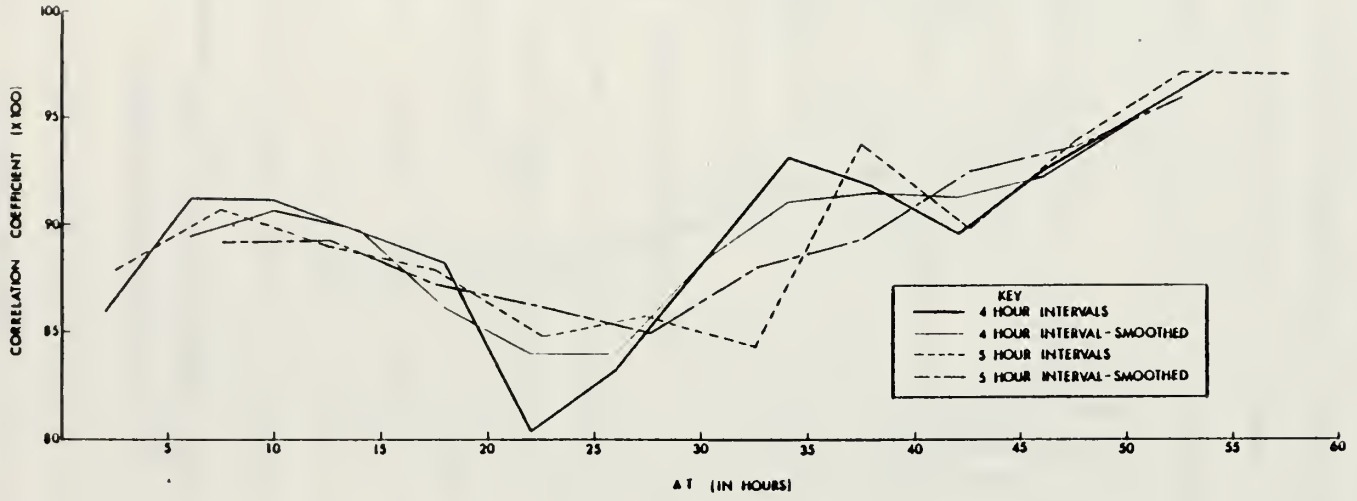

Figure 159. Space-time temperature profile residual correlations averaged over space to isolate time dependence.

values near 20 hours were followed by higher correlations between 42 and 52 hours.

APPENDIX C

IMPLEMENTATION AND COMPARISON OF TWO METHODS OF TWO-DIMENSIONAL INTERPOLATION

Many of the existing methods for two-dimensional interpolation of scattered data on the plane have recently been compared in detail (Franke, 1979). A number of the methods tested were found to be unsatisfactory with respect to the criteria employed. Two of the most promising interpolation algorithms that were evaluated in this study have been implemented locally on the NPS IBM 370 computer (Franke, 1982a). They both provide continuous lower order partial derivatives everywhere with respect to the spatial coordinates (i.e., x and y) except at the input data locations. These interpolation schemes have been applied to the Pt. Sur data at selected levels and compared in various ways. The first algorithm, Modified Quadratic Shepard's method (MQS), is an inverse distance weighted least squares method of interpolation. The method provides a smooth interpolant with the property that interpolated values correspond to observed values at the points where actual data exist. First, a nodal or basis function, $Q_i(x,y)$, is employed which provides a local approximation to the observed values in regions not far from the observed

values. The Q_i's are calculated in local regions from an inverse distance weighted least squares fit to the observations. Inherent in calculating the nodal functions is the selection of a distance function which determines the radius of influence and a "distance decay rate" for the Q_i's. The manner in which these last two parameters are specified in MQS makes the technique unique, and significantly improves the results (Franke and Nielson, 1980). The Q_i's are then combined with appropriate weight functions to provide the local interpolant.

The second method of interpolation is the Thin Plate Spline method (TPS). As in the MQS method, a basis function, Q_i, is determined which provides an approximation to the desired interpolated data field in a local region. Rectangular subregions are used. These local approximations are the thin plate splines and are determined from a linear system of N + 3 equations(where N equals the number of points in a local region). The values that enter into these equations are the locations of the initial data in a pre-defined local region, and the distances between these points. The solved equations then provide the coefficients needed to calculate the local approximation. The actual basis functions used in determining Q_i are of the form $d_k^2 \text{ Log } d_k$

where

$$d_k = [(x-x_k)^2 + (y-y_k)^2]^{1/2}$$

The local approximations are then combined with weighting functions to provide the overall interpolant. The weighting functions in this method are Hermite cubic polynomials. These weighting functions are related to the specification of a computational grid which, in practice, depend on the spacing of the input data. The way in which this grid is specified is important in the subsequent calculations of the interpolated data field.

The ways in which these interpolation schemes are implemented determines to a great extent the quality of the interpolated data fields that result. In MQS, two radii of influence may be specified, and, by selecting these radii according to the density and distribution of existing observations, it is often possible to improve the quality of the interpolation. In the present case however because the overall distribution of data was generally quite uniform, default values were found to provide satisfactory results. The associated radii of influence that apply in this case are determined as follows (Franke and Nielson, 1980).

$$R_q = 1/2\ D(N_q/N)^{1/2} \qquad (C.1)$$

$$R_w = 1/2\ D(N_w/N)^{1/2} \qquad (C.2)$$

where R_q is the radius of influence associated with the nodal functions, R_w is the radius of influence associated with the weight functions, D corresponds to the maximum dimension of the domain, N is the number of observations, and N_q and N_w correspond approximately to the number of data points contained within circles of radii R_q and R_w respectively. With $N_q \approx 2N_w$ and substituting the appropriate values into C.1 and C.2, R_q is approximately equal to 41km and R_w, 29km. Equations C.1 and C.2 also indicate that as the total number of observations available at a given depth decrease, the radii of influence increase (since N_q and N_w remain essentially constant). Considering the number of observations available for all phases and levels, R_q varies between 36 and 50km, while R_w varies between 25 and 36km.

In the implementation of MQS, in situ observations of temperature and location, with respect to a fixed grid, provided the basic input. The initial machine-contoured interpolated temperature fields did not compare favorably with previous hand-drawn analyses based on the original data (Fig. 160). Gradients in the alongshore direction were much too high. Since the data were acquired on a grid with closer spacing in the x-direction, particularly near the coast, the input data in this direction were scaled by a factor approximately equal to the average y/x data

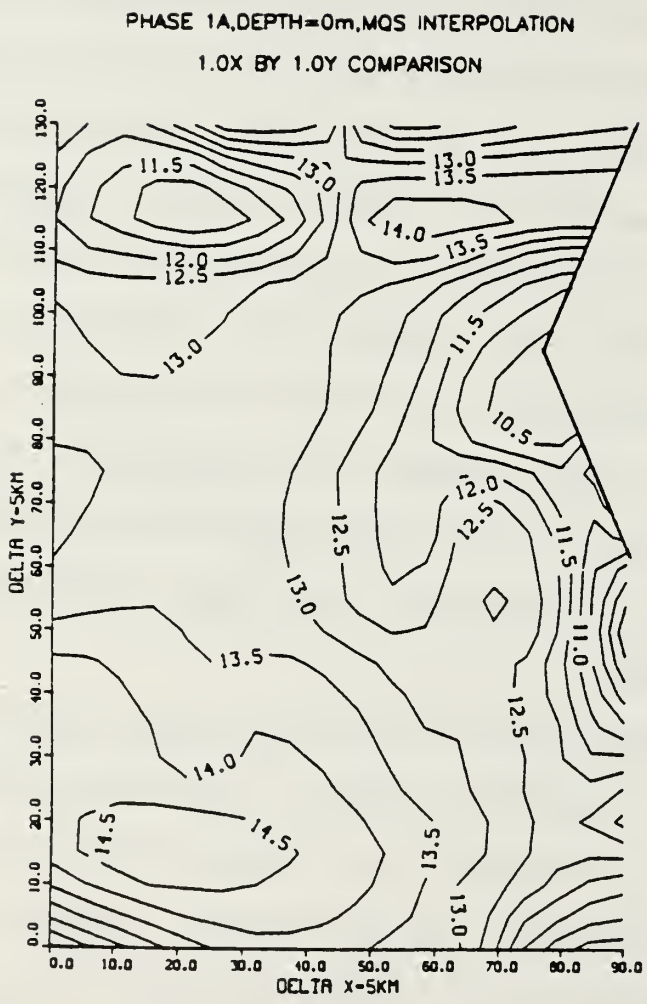

Figure 160. Two-dimensional interpolation of surface temperature data from Phase 1A using the Modified Quadratic Shepard (MQS) algorithm. Data are scaled equally in the X and Y directions, yielding poor results because data were not acquired with equal spacing in both directions.

acquisition aspect ratio which was about 3 to 1 for each phase. The effect of "data stretching" in the offshore direction was to change the computational areas of influence from circles to ellipses. The results of this input scaling were satisfactory (Fig. 161).

Implementation of the TPS method of interpolation was slightly more involved. In this algorithm a pre-determined number of input observations is sought for each rectangular subregion used in calculating the local approximations. Franke (1982b) has found that about 10 points per subregion yields satisfactory results and hence this approximate number of values (also the default value in this version) was used in the calculations described here. As mentioned, a computational grid can be specified in this version; this option was taken. The computational grid was taken initially to approximate the grid on which the input data were acquired. This configuration was then varied stepwise to check the sensitivity of subsequent interpolations to slight changes in the computational grid. When the input grid and computational grids were about the same, the results of the interpolation appeared to be highly satisfactory (Fig. 162). When smaller intervals in x and y were specified for the computational grid, the resulting interpolations quickly became erratic. Little change in output was found for intervals in the computational grid larger than the input grid. Thus it was concluded that a

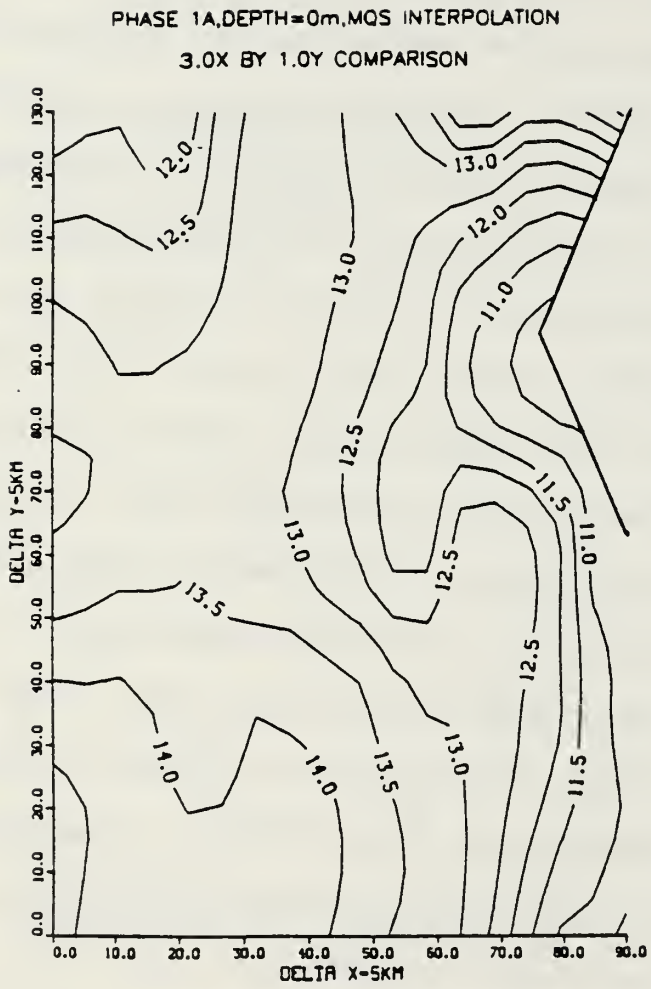

Figure 161. Same as Figure 161 except that the input data have been expanded by a factor of 3 in the offshore direction to more closely approximate the actual data acquisition alongshore/offshore aspect ratio.

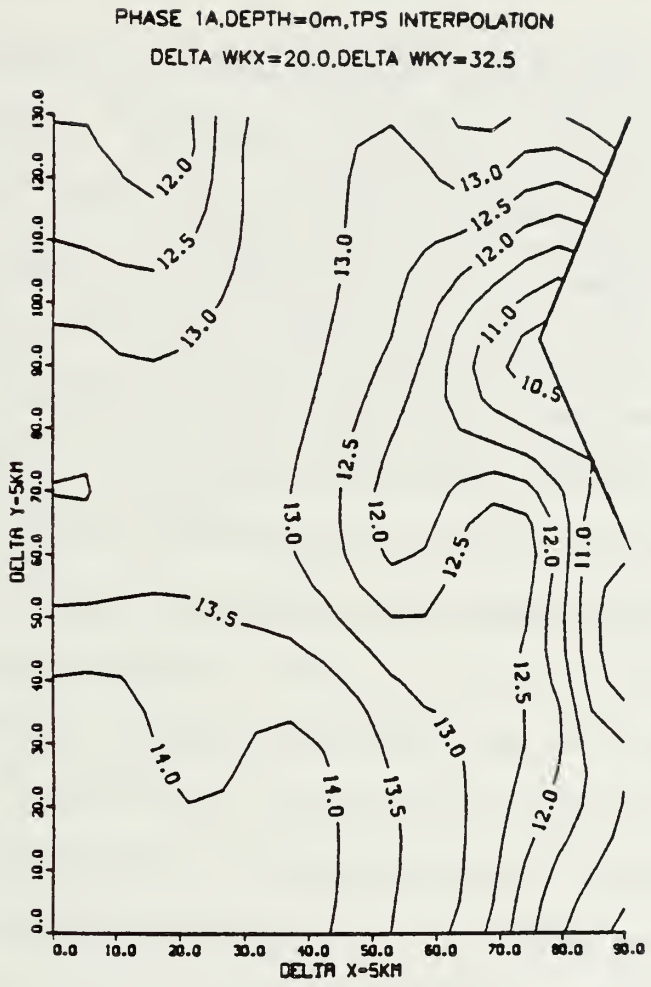

Figure 162. Two-dimensional interpolation of surface temperature data from Phase 1A using the Thin Plate Spline (TPS) algorithm. This map is satisfactory.

computational grid approximately equal to the input grid, or somewhat larger in either or both dimensions, provided satisfactory results. Further calculations using this method employed a computational grid approximately equal to the input grid.

After both interpolation algorithms were evaluated, the results were compared, and again compared with previous hand-drawn analyses based on the original data (Mooers et al., 1983). In general, the agreement between the two machine-produced contour fields was equal to, or better than, the agreement between either machine-drawn analysis, and the corresponding hand-drawn analysis. Differences between machine-produced and hand-drawn analyses at this point are probably more the result of imprecise hand contouring than a result of poor interpolation. Both methods were found to work best when the initial data were somewhat uniformly distributed in space, and the observations did not vary too rapidly in amplitude. On one occasion anamolous behavior was observed using MQS that was not found using TPS. Surface salinities were interpolated for Phase 1B using both methods. Near the offshore edge of the area, MQS produced a strong gradient in sea-surface salinity that was not found in the corresponding TPS analysis. The original data supported the contours produced using TPS. Such edge effects may be more common

to MQS since this algorithm appears to be slightly more responsive to changes in the input than TPS, but by the same token, MQS can go astray more easily where data are not available on all sides to control the behavior of the local interpolant.

Since both methods provided equivalent results for most comparisons, additional criteria were adopted in deciding which technique was best-suited to the task at hand. For the data sets employed, both methods required approximately the same amount of computer time. The MQS method was finally chosen since this method is slightly easier to implement than TPS, and the supporting theory is considerably simpler.

LIST OF FOOTNOTES

1. For exceptions, see Hasselman, Munk and MacDonald (1963), and Roden and Bendiner (1973).

2. Improved estimates for R_{bc} are presented in APPENDIX A where calculations based on continuous density profiles are used, rather than the two-layer approximation given in (1.1).

3. Mixed layer depth was generally taken as the depth at which the surface isothermal layer intersected the seasonal thermocline. In ambiguous cases, mixed layer depth was taken as the depth at which the temperature was Ø.2C less than its surface value, a procedure commensurate with XBT resolution.

4. A more sophisticated procedure would have weighted each image inversely with its time displacement relative to the shipboard data.

5. The recommended sample spacing is then established by taking at least four samples per cycle where one cycle in this case is twice the zero-crossing distance, following Monin et al., 1974.

6. In situ verifications of these offshore upwelling features have recently been made (Huyer, 1982; Mooers and Robinson, 1983).

7. As pointed out by Leipper (1982) the formation of stratus is complex, and although the conditions expressed above are necessary, they may not be sufficient to initiate low cloud formation.

8. These cloud contours also roughly correspond to, and parallel, the region of positive wind stress curl (Nelson, 1977).

9. Gaps in the Farallon Island data were more prevalent.

10. During leap years (1972, 1976, and 198Ø) SSTs for February 29th have been removed, providing a total of 12 x 365 or 438Ø values.

11. In jackknifing, the original series is divided into two halves; the autocorrelation function is then calculated for each half, and the resulting values compared with the original correlation function. By a suitable combination of all three correlations, the overall bias in the estimate is reduced.

12. Independent current measurements acquired off Cape San Martin during the 1980 spring transition also suggest that this disturbance possessed characteristics similar to those expected for coastally-trapped waves (Breaker, 1983).

13. In practice, distances were usually taken somewhat less than this because the gradients often became weak and poorly defined as the zero contours were approached.

14. This recommended sampling strategy does not include the surface mixed layer where observations should be acquired on a finer scale.

15. The spring transition is an abrupt decrease in temperature along the coast that indicates the onset of coastal upwelling.

16. This conclusion relates to offshore length scales in particular and not necessarily to the other space and time scales obtained as a result of this study.

17. Actually Monin et al. recommend that s S/4, or, a sampling rate of at least four samples per cycle.

18. It should be noted, however, that when these data are collapsed onto either axis, a somewhat distorted representation will be obtained since the data are not uniformly distributed with respect to the other dimension.

LIST OF REFERENCES

Allen, J.S., 1980: Models of wind-driven currents on the continental shelf. Ann. Rev. Fluid Mech., 12, 389-433.

Allen, J.S., and R.D. Romea, 1980: On coastal trapped waves at low latitudes in a stratified ocean. J. Fluid Mech., 98, 555-585.

Anderson, D.L.T., and A.E. Gill, 1975: Spin-up of a stratified ocean, with applications to upwelling. Deep-Sea Res., 22, 583-596.

Anderson, T.W., 1958: An Introduction to Mutivariate Statistical Analysis. Wiley, 374pp.

Andrews, W.R.H., and L. Hutchings, 1980: Upwelling in the Southern Benguela Current. Prog. in Oceanogr., 9, 81pp.

Angell, J.K., D.H. Pack, L. Machta, C.R. Dickson, and W.H. Hoecker, 1972: Three dimensional air trajectories determined from tetroon flights in the planetary boundary layer of the Los Angeles Basin. J. Appl. Met., 11, 451-471.

Arthur, R.S., 1965: On the calculation of vertical motion in eastern boundary currents from determinations of horizontal motion. J. Geophys. Res., 70, 2799-2803.

Atkinson, B.W., 1981: Meso-scale Atmospheric Circulations. Academic Press, 495pp.

Baker, D.J., 1981: Ocean instruments and experiment design. Evolution of Physical Oceanography, B.A. Warren and C. Wunsch, Eds., MIT Press, 396-433.

Bakun, A., 1975: Daily and weekly upwelling indices, west coast of North America, 1967-73. NOAA Tech Rpt. NMFS SSRF-693, 114pp.

Bakun, A., 1980: Personal communication.

Barnett, T.P. Knox, R.A., and R.A. Weller, 1977: Space-time structure of the near-surface temperature field during the NORPAX Pole experiment. J. Phys. Oceanogr., 7, 572-579.

Barnett, T.P., and W.C. Patzert, 1980: Scales of thermal variability in the tropical Pacific. J. Phys. Oceanogr., 10, 529-540.

Bartlett, M.S., 1946: On the theoretical specification and sampling properties of autocorrelated time-series. Roy. Stat. Soc., 27-41.

Batchelor, G.K., 1953: The Theory of Homogeneous Turbulence. Cambridge Univ. Press, 197pp.

Bendat, J.S., 1958: Principles and Applications of Random Noise Theory. Wiley, 431pp.

Bernstein, R.L., L.C. Breaker, and R. Whritner, 1977: California Current eddy formation: ship, air, and satellite results. Science, 195, 353-359.

Bernstein, R.L., and W.B. White, 1981: Stationary and traveling mesoscale perturbations in the Kuroshio Extension Current. J. Phys. Oceanogr., 11, 692-704.

Black, C.F., 1965: The turbulent distribution of temperature in the ocean. The Bissett-Berman Corp., Santa Monica, California.

Bloomfield, P., 1976: Fourier Analysis of Time Series: An Introduction. Wiley, 258pp.

Blumberg, R.E., 1975: Mesoscale spatial and temporal variations of water mass characteristics in the California Current region off Monterey Bay in 1973-1974. M.S. Thesis, Naval Postgraduate School, Monterey, 140pp.

Bowden, K.F., 1977: Heat budget considerations in the study of upwelling. A Voyage of Discovery, M. Angel, Ed., Pergamon Press, 277-290.

Box, G.E.P., and G.M. Jenkins, 1976: Time Series Analysis: Forecasting and Control. Holden-Day, 575pp.

Breaker, L.C., 1982: Upwelling off coastal capes. Eastern Pacific Oceanic Conference (EPOC), Oral Presentation.

Breaker, L.C., 1983: Observations on the spring transition along the Central California coast. Eastern Pacific Oceanic Conference (EPOC), Oral Presentation.

Breaker, L.C., J.C. Arvesen, D. Friedenlund, and K. Short, 1984: A remote sensing experiment off Cape Mendocino. NASA AMES Tech. Rpt., (in press).

Breaker, L.C., and R.P. Gilliland, 1981: A satellite sequence on upwelling along the California coast. Coastal Upwelling, F.A. Richards, Ed., an AGU Publication, 87-94.

Breaker, L.C., P.A.W. Lewis, and E.J. Orav, 1983: Analysis of a 12-year record of sea-surface temperatures off Pt. Sur, California. Naval Postgraduate School Tech. Rep. NPS55-83-Ø18, Monterey, 62pp.

Brekhovskikh, L.M. Fedorov, K.N., Fomin, L.M., Koshlyakov, M.N., and A.D. Yampolsky, 1971: Large-scale multi-buoy experiment in the tropical Atlantic. Deep Sea Res., 18, 1189-12Ø6.

Bretherton, F.P., Davis, R.E., and C.B. Fandry, 1976: A technique for objective analysis and design of oceanographic experiments applied to MODE-73. Deep Sea Res., 23, 559-581.

Bretschneider, D.E., 198Ø: Sea level variations at Monterey, California. M.S. Thesis, Naval Postgraduate School, Monterey, 1Ø5pp.

Bretschneider, D.E., and D.R. McLain, 1983: Sea level variations at Monterey, California. NOAA Tech. Rpt. NMFS SSRF-761, 5Øpp.

Brink, K.H., D. Halpern, and R.L. Smith, 198Ø: Circulation in the Peruvian upwelling system near 15S. J. Geophys. Res., 85, 4Ø36-4Ø48.

Brink, K.H., B.H. Jones, J.C. VanLeer, C.N.K. Mooers, D.W. Stuart, M.R. Stevenson, R.C. Dugdale, and G.W. Heburn, 1981: Physical and biological structure and variability in an upwelling center off Peru near 15 S during March, 1977. Coastal Upwelling, F.A. Richards, Ed., An AGU Publication, 473-495.

Brink, K.H., D.W. Stuart, and J.C. VanLeer, 1983: Observations of the coastal upwelling region near 34.5N off California: spring 1981. WHOI Contribution No. 5319, Woods Hole, 29pp.

Broenkow, W.W., 1982: A direct comparison of geostrophic and current meter observations in a California Current eddy. Deep Sea Res., 29, 13Ø3-1311.

Brown, R.L., 1974: Geostrophic circulation off the coast of Central California. M.S. Thesis, Naval Postgraduate School, Monterey, 265pp.

Burkov, V.A., and Y.V. Pavlova, 1980: Description of the eddy field of the California Current. Oceanology, 20, 272-278.

Chatfield, C., 1980: The Analysis of Time Series: An Introduction. Chapman and Hall, 268pp.

Chelton, D.B., P.A. Bernal, and J.A. McGowan, 1982: Large-scale interannual physical and biological interaction in the California Current. J. Mar. Res., 40, 1095-1125.

Conrad, J.W., 1980: Relationships between sea surface temperature and nutrients in satellite detected oceanic fronts. M.S. Thesis, Naval Postgraduate School, Monterey, 114pp.

Cox, D.R., and P.A.W. Lewis, 1966: The Statistical Analysis of Series of Events. Methuen and Co., 285pp.

Craddock, J.M., 1972: Problems and prospects for eigenvector analysis in meteorology. The statistician, 22, 133-145.

Curtin, T.B., 1979: Physical dynamics of the coastal upwelling frontal zone off Oregon. Ph.D. Dissertation, Univ. of Miami, Coral Gables, 317pp.

Davis, J.C., 1973: Statistics and Data Analysis in Geology. Wiley, 550pp.

Davis, R.E., 1975: Statistical methods. Dynamics and the Analysis of MODE-1, A.R. Robinson, Ed., 1-26.

Davis, R.E., 1976: Predictability of sea-surface temperature and sea level pressure anomalies over the North Pacific Ocean. J. Phys. Oceanogr., 6, 249-266.

Davis, R.E., 1977: Techniques for statistical analysis and prediction of geophysical fluid systems. Geophys. Astrophys. Fluid Dyn., 8, 245-277.

Davis, T.M., 1974: Theory and practice of geophysical survey design. NAVOCEANO Ref. Pub. 13, 125pp.

Davis, T.M., 1982: Personal Communication.

Defant, A., 1950: Reality and illusion in oceanographic surveys. J. Mar. Res., 9, 120-138.

deSzoeke, R.A., and J.G. Richman, 1981: The role of wind-generated mixing in coastal upwelling. J. Phys. Oceanogr., 11, 1534-1547.

Dreves, D.A., 1980: Sea levels and metered currents off Central California. M.S. Thesis, Naval Postgraduate School, Monterey, 94pp.

Duthie, W.D., 1968: Notes on the analysis of weather charts. Naval Postgraduate School informal publication, Monterey.

Edinger, J.G., and R.A. Helvey, 1961: The San Fernando convergence zone. Bull. Am. Met. Soc., 42, 626-635.

Enfield, D.B., and J.S. Allen, 1980: On the structure and dynamics of monthly mean sea level anomalies along the Pacific coast of North and South America. J. Phys. Oceanogr., 10, 557-578.

Franke, R., 1979: A critical comparison of some methods for interpolation of scattered data. Naval Postgraduate School Tech. Rep. NPS-53-79-003, 373pp.

Franke, R., and G. Nielson, 1980: Smooth interpolation of large sets of scattered data. International Journal for Numerical Methods in Engineering, 15, 1691-1704.

Franke, R., 1982a: Scattered data interpolation: tests of some methods. Mathematics of Computation, 38, 181-200.

Franke, R., 1982b: Smooth interpolation of scattered data by local thin plate splines. Comp. and Maths. with Appls., 8, 273-281.

Freeland, H.J., and W.J. Gould, 1976: Objective analysis of meso-scale ocean circulation features. Deep-Sea Res., 23, 915-923.

Friehe, C.A., and C.D. Winant, 1982: Observations of wind and sea surface temperature structure off the Northern California coast. First International Conference on Meteorology and Air/Sea Interaction of the Coastal Zone, Amer. Meteorol. Soc., The Hague, 209-214.

Gandin, L.S., 1965: Objective analysis of meteorological fields. Israel Program for Scientific Translations, 242pp.

Garrett, C., and W. Munk, 1972: Space-time scales of internal waves. Geophys. Fluid Dyn., 2, 225-264.

Garrett, C.J.R., and R.H. Loucks, 1976: Upwelling along the Yarmouth Shore of Nova Scotia. J. Fish. Res. Board Can., 33, 116-117.

Gerst, A.L., 1969: Correlation of sea-surface temperature with cloud patterns off the west coast of North America during the upwelling season. M.S. Thesis, Naval Postgraduate School, Monterey, 124pp.

Gill, A.E., and A.J. Clarke, 1974: Wind-induced upwelling, coastal currents, and sea-level changes. Deep-Sea Res., 21, 325-345.

Greenspan, H.P., 1968: The Theory of Rotating Fluids. Cambridge Univ. Press, 327pp.

Greer, R.E., 1975: Mesoscale components of the geostrophic flow and its temporal and spatial variability in the California Current off Monterey Bay 1973-1974. M.S. Thesis, Naval Postgraduate School, Monterey, 177pp.

Griggs, G.B., 1974: Nearshore current patterns along the Central California coast. Estuarine Coastal Mar. Sci., 2, 395-405.

Hagan, D., 1983: Personal communication.

Halliwell, G.R., and J.S. Allen, 1983: Large scale sea level response to atmospheric forcing along the west coast of North America. (Submitted to Journal of Physical Oceanography).

Halliwell, G.R., and C.M.K. Mooers, 1979: The space-time structure and variability of the shelf water-slope water and Gulf Stream surface temperature fronts, and associated warm-core eddies. J. Geophys. Res., 84, 7707-7726.

Halliwell, G.R., and C.N.K. Mooers, 1983: Meanders of the Gulf Stream downstream from Cape Hatteras. J. Phys. Oceanogr., 13, 1275-1292.

Halpern, D., 1974: Summertime surface diurnal period winds measured over an upwelling region near the Oregon coast. J. Geophys. Res., 79, 2223-2230.

Hanson, W.E., 1980: Nutrient study of mesoscale thermal features off Point Sur, California. M.S. Thesis, Naval Postgraduate School, Monterey, 182pp.

Hasselmann, K., Munk, W., and G. MacDonald, 1963: Bispectra of ocean waves. Time Series Analysis, M. Rosenblatt, Ed., 125-139.

Hawkins, J.D., 1977: A study of the mesoscale wind circulation in a land-sea breeze regime. Bull. Am. Met. Soc., 58, 1289-1295.

Hickey, B.M., 1979: The California Current system-hypotheses and facts. Prog. in Oceanogr., 8, 191-279.

Hinze, J.O., 1959: Turbulence: An Introduction to its Mechanism and Theory. McGraw-Hill, 586pp.

Holladay, C.G., and J.J. O'brien, 1975: Mesoscale variability of sea-surface temperature. J. Phys Oceanogr., 5, 761-772.

Hughes, J.G., 1975: The spatial and temporal variation of sound speed in the California Current system. M.S. Thesis, Naval Postgraduate School, Monterey, 108pp.

Huthnance, J.M., 1981: Waves and currents near the continental shelf edge. Prog. in Oceanogr., 10, 193-226.

Huyer, A., 1982: Hydrography in Code-2, Twenty ninth Eastern Pacific Oceanic Conference (EPOC), Minutes of the 29th EPOC, Pacific Grove.

Huyer, A., E.J.C. Sobey, and R.L. Smith, 1979: The spring transition in currents over the Oregon continental shelf. J. Geophys. Res., 84, 6995-7011.

Ichiye, T., 1972: A theory of coastal upwelling based on a two-layer ocean model and its application to the eastern Pacific Ocean. IV Congreso Nacional de Oceanografia, Memorias, Mexico, 13-36.

Ikeda, M., W.J.Emery, and L.A. Mysak, 1983: Seasonal variability in meanders of the California Current System off Vancouver Island. Submitted to the Journal of Geophysical Research.

Jennings, F.D., and R.A. Schwartzlose, 1960: Measurements of the California Current in March 1958. Deep Sea Res., 7, 42-47.

Johnson, A., and J.J. O'Brien, 1973: A study of an Oregon sea breeze event. J. Appl. Met., 12, 1267-1283.

Johnson, J.E., 1980: Subsurface dynamical properties of variable features seen in satellite IR imagery off Pt. Sur and their acoustic significance. M.S. Thesis, Naval Postgraduate School, Monterey, 239pp.

Johnson, W.R., Van Leer, J.C., and C.N.K. Mooers, 1976: A cylesonde view of coastal upwelling. J. Phys. Oceanogr., 6, 556-574.

Jones, P.G.W., 1972: The variability of oceanographic observations off the coast of NW Africa. Deep Sea Res., 19, 405-431.

Katsaros, K.B., 1980: The aqueous thermal boundary layer. Bound. Lay. Met., 18, 107-127.

Kelley, J.C., 1971: Sampling considerations in upwelling studies. Inves. Pesq., 35, 251-260.

Kelley, J.C., 1976: Sampling the sea. The Ecology of the Seas, D.H. Cushing and J.J. Walsh, Eds., W.B. Saunders Company, 361-387.

Labyak, P.S., 1969: An oceanographic survey of the coastal water between San Francisco Bay and Monterey Bay, California. M.S. Thesis, Naval Postgraduate School, Monterey, 311pp.

LeBlond, P.H., and L.A. Mysak, 1978: Waves in the Ocean. Elsevier, 602pp.

Legeckis, R.V., and J. Pritchard , 1976: Algorithm for correction of VHRR imagery for geometric corrections due to earth curvature, earth rotation and spacecraft roll attitude errors. NOAA Tech. Memo, NESS 77, 31pp.

Leipper, D.F., 1980: Day to day and place to place changes in low level atmospheric temperature structure off Southern California. Second Conference on Coastal Meteorology, Amer. Meteorol. Soc., Los Angeles, 58-62.

Lighthill, M.J., 1969a: Dynamic response of the Indian Ocean to onset of the southwest monsoon. Phil. Trans. Roy. Soc., 265, 45-92.

Lighthill, M.J., 1969b: Unsteady wind-driven ocean currents. Quart. J. Roy. Met. Soc., 95, 675-688.
lo

Linder, D., and L.C. Breaker, 1983: Warm sea-surface temperatures along the California coast. Coastal Oceanography and Climatology News, 5, 31-32.

List, E.J., and R.C.Y. Koh, 1976: Variations in coastal temperatures on the southern and Central California coast. J. Geophys. Res., 81, 1971-1979.

Lorenz, E.N., 1956: Empirical orthogonal functions and statistical weather prediction. Report No. 1, Statistical Forecasting Project, Dept. Meteorology, MIT, 49pp.

Lumley, J.L., 1970: Stochastic Tools in Turbulence. Academic Press, 194pp.

Maul, G.A., P.W. DeWitt, A. Yanaway, and S.R. Baig, 1978: Geostationary satellite observations of Gulf Stream meanders: infrared measurements and time series analysis. J. Geophys. Res., 83, 6123-6135.

Maul, G.A., and M. Sidran, 1973: Atmospheric effects on ocean surface temperature sensing from the NOAA satellite scanning radiometer. J. Geophys. Res., 78, 1909-1916.

McCreary, J.P., 1977: Eastern ocean response to changing wind systems. Ph.D. Thesis, Univ. of California, San Diego, 156pp.

Miller, R.G., 1974: The jackknife--a review. Biometrika, 61, 1-16.

Monin, A.S., V.M. Kamenkovich, and V.G. Kort, 1974: Variability of the Oceans. Wiley-Interscience, 241pp.

Mooers, C.N.K., 1976: Physical variability of the continental shelf. Mem. Soc. Roy. des Sciences de Liege, 6, 27-30.

Mooers, C.N.K., L.C. Breaker, B. Hunter, and R. Koob, 1982: Oceanographic data acquired in support of the June 1980 study of the upwelling center off Pt. Sur, California. Naval Postgraduate School Data Report, Monterey, 145pp.

Mooers, C.N.K., C.A. Collins, and R.L. Smith, 1976: The dynamic structure of the frontal zone in the coastal upwelling region off Oregon. J. Phys. Oceanogr., 6, 3-21.

Mooers, C.N.K., Flagg, C.N., and W.C. Boicourt, 1978: Prograde and retrograde fronts. Oceanic Fronts in Coastal Processes, M.J. Bowman and W.E. Esaias, Eds., Springer-Verlag, 43-58.

Mooers, C.N.K., and A.R. Robinson, 1983: Turbulent jets and eddies in the California Current and inferred cross-shore transports. (submitted to Science).

Morrison, D.F., 1976: Multivariate Statistical Methods. McGraw-Hill, 413pp.

Namias, J., 1972: Space scales of sea-surface temperature patterns and their causes. Fish. Bull., 70, 611-617.

Navrotskiy, V.V., 1969: The statistical analysis of spatial temperature fluctuations in the ocean surface layer. Izv., Atm. and Ocean Physics, 5, 94-110.

Navrotskiy, V.V., L.I. Kazachkina, and S. Ye. Navrotskaya, 1968: A study of spatial temperature variations. Okeanologiya, 8, 9-16.

Navrotskiy, V.V., V.T., Paka, and E.I. Karabasheva, 1972: Characteristics of thermal inhomogeneities on sections in the Atlantic Ocean. Izv., Atm. and Ocean Physics, 8, 307-320.

Nelson, C.S., 1977: Wind stress and wind stress curl over the California Current. NOAA Tech. Rpt. NMFS SSRF-714, 89pp.

O'Brien, J.J., and R.D. Pillsbury, 1974: Rotary wind spectra in a sea breeze regime. J. Appl. Meteorol., 13, 820-825.

Panchev, S., 1971: Random Functions and Turbulence. Pergamon Press, 444pp.

Pedlosky, J., 1974: Longshore currents, upwelling, and bottom topography. J. Phys. Oceanogr., 4, 214-226.

Phillips, O.M., 1977: The Dynamics of the Upper Ocean. Cambridge Univ. Press, 336pp.

Pilie, R.J., E.J. Mack, C.W. Rogers, U. Katz, and W.C. Kocmond, 1979: The formation of marine fog and the development of fog-stratus systems along the California coast. J. Appl. Meteorol., 18, 1275-1286.

Pirie, D.M., M.J. Murphy, and J.R. Edmisten, 1975: California nearshore surface currents. Shore and Beach, 43, 23-34.

Preisendorfer, R.W., Francis W. Zwiers, and Tim P. Barnett, 1981: Foundations of principal component selection rules. SIO Ref. Series 81-4, Scripps Institution of Oceanography, 191pp.

Reid, J.L., 1962: Measurements of the California Countercurrent at a depth of 250 meters. J. Mar. Res., 20, 134-137.

Reid, J.L., G.I. Roden, and J.G. Wyllie, 1958: Studies of the California Current system. CalCOFI Rep., 1 July 1956-1 January 1958, 28-56.

Reid, J.L., and R.A. Schwartzlose, 1962: Direct Measurements of the Davidson Current off Central California. J. Geophys. Res., 67, 2591-2597.

Richman, J.G., C. Wunsch, and N.G. Hogg, 1977: Space and time scales of mesoscale motion in the western North Atlantic. Rev. Geophys. and Space Physics, 15, 385-420.

Rhines, P.B., 1977: The dynamics of unsteady currents. Marine Modeling, E.D. Goldberg, I.N. McCave, J.J. O'Brien, and J.H. Steele, Eds., Wiley-Interscience, 189-318.

Robinson, M.K., 1976: Atlas of North Pacific Ocean monthly mean temperatures and mean salinities of the surface layer. Naval Oceanogr. Office, Washington, D.C., Rep. No. NOO RP-2, i-xix, 173 Figs.

Robinson, M.K., 1957: Sea temperature in the Gulf of Alaska and in the Northeast Pacific ocean, 1941-1952. Bull. Scripps Inst. Oceanogr., 7, 1-98.

Roden, G.I., 1963: On statistical estimation of monthly extreme sea-surface temperatures along the west coast of the United States. J. Mar. Res. 31, 172-190.

Roden, G.I., and D.J. Bendiner, 1973: Bispectra and cross-bispectra of temperature, salinity, sound velocity and density fluctuations with depth off Northeastern Japan. J. Phys. Oceanogr., 3, 308-317.

Rooth, C., 1973: On eddy diffusion versus "criticality" in turbulent transport processes. Final report of the coastal upwelling ecosystems analysis summer 1973 theoretical workshop, C.N.K. Mooers and J.S. Allen, Eds., C-31B-C31B1.

Rouse, L.J., 1952: Infrared transmittance of marine atmospheres. Processes in Marine Remote Sensing, F.J. Vernberg and F.P. Diemer, Eds., Univ. of South Carolina Press, 67-76.

Saunders, P.M., 1972: Space and time variations of temperature in the upper ocean. Deep Sea Res., 19, pp. 467-480, 1972.

Saunders, P.M., 1973: Tracing surface flow with surface isotherms. Mem. Soc. Roy. des Sciences de Liege, 6, 99-118.

Sauvel, J., 1983: Some oceanic effects of diurnal wind off the California coast. Naval Postgraduate School seminar, Monterey.

Schwartzlose, R.A., 1963: Nearshore currents of the western United States and Baja California as measured by drift bottles. CalCOFI Rpt. No. 9, 15-22.

Schwartzlose, R.A., and J.L. Reid, 1972: Nearshore circulation in the California Current. CalCOFI Rpt. No. 16, 57-65.

Sciremammano, F., Jr., 1979: A suggestion for the presentation of correlations and their significance levels. J. Phys. Oceanogr., 9, 1273-1276.

Shaffer, G., 1976: A mesoscale study of coastal upwelling variability off NW Africa. Meteor "Forsch.-Ergebn. A," 17, 21-72.

Shepard, A.B., 197Ø: A comparison of oceanic parameters during upwelling off the central coast of California. M.S. Thesis, Naval Postgraduate School, Monterey, 2Ø9pp.

Silva, M.F.P.S., 1981: Thermal calibration of satellite infrared images and correlation with sea-surface nutrient distribution. M.S. Thesis (in writing), Naval Postgraduate School, Monterey, 76pp.

Simon, R.L., 1976: The summertime stratus over the Eastern Pacific Ocean. M.S. Thesis, San Jose State University, San Jose, 77pp.

SIO Reference 81-8Ø, 1981; Data report surface water temperatures at shore stations - United States West Coast. Marine Life Research Committee and Marine Life Research Group, Univ. of California, Scripps Institution of Oceanography, La Jolla, 45pp.

Skogsberg, T., 1936: Hydrography of Monterey Bay, California thermal conditions, 1929-1931. Am. Phil. Soc. Trans., 29, 152pp.

Squire, J.L., 1971: Measurements of sea-surface temperature on the Eastern Pacific continental shelf using airborne infrared radiometry: August 1963-July 1968. U.S. Coast Guard Oceanographic Rpt. No. 47, Washington, D.C., 229pp.

Stevenson, M.R., and F.R. Miller, 1974: Application of satellite data to the study of oceanic fronts in the Eastern Pacific. CUEA Tech. Rpt. 17, 111pp.

Stewart, R.W., 1969: Turbulence and waves in a stratified atmosphere. Radio Science, 4, 1269-1278.

Stommel, H., 1963; Varieties of oceanographic experience. Science, 139, 572-576.

Swallow, J.C., 1957: Some further deep current measurements using neutrally buoyant floats. Deep Sea Res., 4, 93-104.

Taylor, G.I., 1938: The spectrum of turbulence. Proc. R. Soc. London, ser. A, 164, 476-490.

The CODE Group, 1983: Coastal ocean dynamics. EOS, 64, 538-540.

Tibby, R.B., 1941: The water masses of the west coast of North America. J. Mar. Res., 4, 112-121.

Tomczak, M., 1978: Ecosystem analysis and the definition of boundaries in upwelling regions. Upwelling Ecosystems, R. Boje and M. Tomczak, Eds., Springer-Verlag, 3-11.

Traganza, E.D., J.C. Conrad, and L.C. Breaker, 1981: Satellite observations of a cyclonic upwelling system and giant plume in the California Current. Coastal Upwelling, F.A. Richards, Ed., An AGU publication, 228-241.

Traganza, E.D., D.A. Nestor, and A.K. McDonald, 1980: Satellite observations of a nutrient upwelling off the coast of California. J. Geophys. Res., 85, 4101-4106.

Traganza, E.D., V.M. Silva, D.M. Austin, W.L. Hanson, and S.H. Bronsink, 1983: Nutrient mapping and recurrence of coastal upwelling centers by satellite remote sensing: its implication to primary production and the sediment record. Coastal Upwelling, Pt. A, E. Suess and J. Thiede, Eds., Plenum Pub. Corp, 61-83.

Tukey, J.W., 1967: An introduction to the calculations of numerical spectrum analysis. Spectral Analysis of Time Series, B. Harris, Ed., Wiley, 25-46.

Van Patten, B.D., 1980: Long term spectra of wind and temperature in the vicinity of the marine inversion. Second Conference in Coastal Meteorology, Amer. Meteorol. Soc., Los Angeles, 262-265.

Wang, D.-P., and C.N.K. Mooers, 1976: Coastal-trapped waves in a continuously stratified ocean. J. Phys. Oceanogr., 6, 853-863.

White, W.B., 1982: Traveling wave-like mesoscale perturbations in the North Pacific Current. J. Phys. Oceanogr., 231-243.

White, W.B., and R.L. Bernstein, 1979: Design of an oceanographic network in the mid-latitude North Pacific. J. Phys. Oceanogr., 9, 592-606.

White, W.B., and J.F.T. Saur, 1981: A source of annual baroclinic waves in the eastern subtropical North Pacific. J. Phys. Oceanogr., 1452-1462.

Wickham, J.B., 1975: Observations of the California Countercurrent. J. Mar. Res., 33, 325-340.

Wickham, J.B., and S.P. Tucker, 1979: Currents on the Central California slope. EOS, 60, 855-856.

Woods, J.D., 1974: The local distribution in Fourier space-time of variability associated with turbulence in the seasonal thermocline. Mem. Soc. Roy. des Sciences de Liege, 7, 171-189.

Woods, J.D., 1973: Space-time characteristics of turbulence in the seasonal thermocline. Mem. Soc. Roy. des Sciences de Liege, 6, 109-130.

Wooster, W.S., and J.L. Reid, 1963: Eastern boundary currents. The Sea, 2, M.N. Hill, Ed., Krieger, 253-276.

Yaglom, A.M., 1962: An Introduction to the Theory of Stationary Random Functions. R.A. Silverman, translator and editor, Prentice-Hall, 235pp.

Yoshida, K., 1980: The coastal undercurrent - a role of longshore scales in coastal upwelling dynamics. Prog. in Oceanogr., 9, 83-131.

INITIAL DISTRIBUTION LIST

		No. Copies
1.	Defense Technical Information Center Cameron Station Alexandria, VA 22314	2
2.	Library, Code 0142 Naval Postgraduate School Monterey, CA 93943	2
3.	Chairman (Code 68Mr) Department of Oceanography Naval Postgraduate School Monterey, CA 93943	32
4.	Chairman (Code 63Rd) Department of Meteorology Naval Postgraduate School Monterey, CA 93943	1
5.	Commander Naval Oceanography Command NSTL Station Bay St. Louis, MS 39522	1
6.	Commanding Officer Naval Oceanographic Office NSTL Station Bay St. Louis, MS 39522	1
7.	Commanding Officer Fleet Numerical Oceanography Center Monterey, CA 93943	1
8.	Commanding Officer Naval Ocean Research and Development Activity NSTL Station Bay St. Louis, MS 39522	1
9.	Commanding Officer Naval Environmental Prediction Research Facility Monterey, CA 93943	1
10.	Professor E. B. Thornton (Code 68Tm) Department of Oceanography Naval Postgraduate School Monterey, CA 93943	1

11. Adjunct Professor J. L. Mueller (Code 68Ms) 1
Department of Oceanography
Naval Postgraduate School
Monterey, CA 93943

12. Associate Professor R. H. Franke (Code 53Fe) 1
Department of Mathematics
Naval Postgraduate School
Monterey, CA 93943

13. Professor P. A. W. Lewis (Code 55Lw) 1
Department of Operations Research
Naval Postgraduate School
Monterey, CA 93943

14. Laurence C. Breaker (Code 68) 1
Department of Oceanography
Naval Postgraduate School
Monterey, CA 93943

15. Bureau of Land Management 1
Pacific OCS Office
300 N. Los Angeles T.
Los Angeles, CA 90012
ATTN: Mr. Sigurd Larson

16. Office of Oceanic and Atmospheric Research 1
NOAA
6010 Executive Blvd.
Rockville, MD 20852
ATTN: Dr. William Sprigg

205396

Thesis
B8024
c. 1

Breaker
The space-time scales of variability in oceanic thermal structure off the Central California Coast.

17 MAR 88

31507

205396

Thesis
B3024
c.

Breaker
The space-time scales of variability in oceanic thermal structure off the Central California Coast.

AMERICAN BINDERY
TOPEKA KANSAS

thesB8024
The space-time scales of variability in
3 2768 000 66634 1
DUDLEY KNOX LIBRARY